THE CRYOGENIC PUMPING SECTION OF THE KATRIN EXPERIMENT

–

DESIGN STUDIES AND EXPERIMENTS FOR THE COMMISSIONING

Zur Erlangung des akademischen Grades eines

DOKTORS DER NATURWISSENSCHAFTEN

von der Fakultät für Physik
des Karlsruher Instituts für Technologie
genehmigte

DISSERTATION

von

Dipl. Phys. Alexander Jansen

aus Karlsruhe

Erstgutachter: Prof. Dr. G. Drexlin
                  Institut für Experimentelle Kernphysik, KIT
Zweitgutachter: Prof. Dr. U. Husemann
                  Institut für Experimentelle Kernphysik, KIT

Tag der mündlichen Prüfung: 13. Februar 2015

Declaration of authorship

I declare that I have developed and written the enclosed thesis completely by myself, and have not used sources or means without declaration in the text.

Erklärung der Selbständigkeit

Ich versichere wahrheitsgemäß, die Arbeit selbstständig angefertigt, alle benutzten Hilfsmittel vollständig und genau angegeben und alles kenntlich gemacht zu haben, was aus Arbeiten anderer unverändert oder mit Abänderungen entnommen wurde.

Karlsruhe, 22.01.2015

. . . .
        (Alexander Jansen)

Zusammenfassung

Neutrinos spielen eine fundamentale Rolle in der Teilchenphysik und in der Kosmologie. Seit ihrer Postulierung durch W. Pauli sind sie fester Bestandteil im Standardmodell der Teilchenphysik. Dort sind sie als masselose, neutrale, nur schwach wechselwirkende Leptonen mit Spin 1/2 (Fermionen) eingeordnet. Nachdem mehrere Schlüsselexperimente, insbesondere zur Untersuchung von Neutrinooszillationen, gezeigt haben, dass Neutrinos eine nicht verschwindende Masse besitzen, bietet die Untersuchung der Eigenschaften von Neutrinos einen idealen Zugang zur Physik jenseits des Standardmodells. Massenbehaftete primoridale Neutrinos sind primäre Kandidaten für die heiße dunkle Materie mit großem Einfluss auf die Entwicklung des frühen Universums und der Bildung der großräumigen Strukturen. Das Gebiet der Neutrinophysik und der Astroteilchenphysik, inklusive Kosmologie, sind damit vor allem über Neutrinos und ihre Eigenschaften sehr eng miteinander verbunden. Beide Gebiete profitieren von den Erkenntnissen aus dem jeweils anderen Gebiet. So können zum Beispiel Eigenschaften von Neutrinos aus kosmologischen Beobachtungen (modellabhängig) abgeleitet werden, andererseits können diese Eigenschaften in Laborexperimenten modellunabhängig bestimmt werden und damit zur Verbesserung kosmologischer Modelle beitragen. Eine besondere Eigenschaft von Neutrinos ist die noch unbekannte Skala ihrer Ruhemasse. Mit diesem Parameter lässt sich die Entwicklung und die Formation großflächiger Strukturen im Universum erklären. Er kann zudem zum tiefgreifenden Verständnis von masseerzeugenden Prozessen für Elementarteilchen beitragen.

Die zentrale Motivation des **Ka**rlsruher **Tri**tium **N**eutrino (KATRIN) Experiments ist die Bestimmung der effektiven Masse des Elektronantineutrinos. Das 70 m lange Experiment wird zur Zeit auf dem Gelände des Karlsruher Instituts für Technologie (KIT) aufgebaut. Zur Massenbestimmung macht sich das KATRIN Experiment die Kinematik des Tritium-Beta-Zerfalls zu Nutze, indem es das Zerfallsspektrum nahe am Energieendpunkt mit bisher unerreichter Genauigkeit analysiert. Mit einer Sensitivität von $200\,\mathrm{eV}/c^2$ bei 90% C.L. wird es in der Lage sein, eine absolute Neutrinomasse von $350\,\mathrm{eV}/c^2$ zu bestimmen mit einem Entdeckungspotential von $5\,\sigma$. Im Falle einer geringeren Masse wird es eine neue Obergrenze definieren von $m(\nu_\mathrm{e}) < 200\,\mathrm{meV}/c^2$.
Der experimentelle Aufbau kann in drei große funktionale Einheiten unterteilt werden. Jede umfasst ein ausgedehntes Vakuumsystem, eine Anordnung supraleitender Magnete und einen Hochspannungsteil. Gasförmiges Tritium wird zunächst in eine fensterlose, gasförmige Tritiumquelle (WGTS) injiziert. Der zentrale Teil des komplexen Quellkryostaten besteht im Wesentlichen aus einem 10 m langen Strahlrohr mit zwei offenen Enden, in

dem Tritiummoleküle zerfallen können, während die Moleküle zu beiden Enden heraus driften. Die Zerfallselektronen werden adiabatisch mit Hilfe von Solenoiden von der Quelle in die Spektrometer geführt. Dort wird durch Variation eines Hochspannungsretardierungspotentiales das Energiespektrum der Zerfallselektronen analysiert. Elektronen mit einer genügend hohen Energie können die Potentialbarriere überwinden und werden anschließend am Detektor gezählt. Um zu verhindern, dass nicht zerfallenes Tritium in die Spektrometer gelangt, wo es Untergrundereignisse erzeugen könnte, ist eine komplexe Transport- und Pumpstrecke zwischen der Quelle und den Spektrometern platziert. Ihre Aufgabe ist es, den Gasfluss von der Quelle in die Spektrometer um mehr als 14 Größenordnungen zu reduzieren und dabei gleichzeitig die Zerfallselektronen adiabatisch zu führen. Das Tritiumunterdrückungssystem besteht aus einer differentiellen (DPS) und einer kryogenen (CPS) Pumpstrecke. Mit der DPS soll der Gasfluss durch aktives Pumpen mit Turbomolekularpumpen um fünf Größenordnungen reduziert werden. Mit der nachfolgenden CPS soll durch Kryosorption der verbleibende Tritiumfluss um mindestens 7 weitere Größenordnungen reduziert werden. Das zentrale Kryosorptionselement ist dabei eine 3 K kalte Argonfrostschicht. Das Verständnis dieser beiden Komponenten ist von höchster Wichtigkeit für das gesamte KATRIN Experiment. Dementsprechend ist das Kernthema der vorliegenden Dissertation eine Optimierung der Tritiumpumpperformance und der Sicherheit der CPS. Ein besonderes Augenmerk wurde dabei auf die Optimierung der vakuumphysikalischen Auslegung der CPS gelegt, hierzu zählen insbesondere die Präparation der Argonfrostschicht und der daraus resultierende Gasreduktionsfaktor. Weiterhin wurden die Aktivierungsbedingungen für die Getterpumpe am Ende der CPS optimiert. Zusätzlich wurden die Beipassdioden des Magnetsicherheitssystemes konzipiert, aufgebaut und unter realitätsnahen Bedingungen getestet.

Die Schutzdioden stellen den wichtigsten Teil des CPS Magnetsicherheitssystemes dar. Sie sind parallel zu den supraleitenden Magneten montiert und dienen als elektrischer Schalter. Für den Fall, dass ein Magnet quencht, d.h. während des Betriebes vom supraleitenden in den normalleitenden Zustand übergeht, leiten sie den Strom um den quenchenden Magneten herum und entladen die Energie, die im kompletten Magnetsystem gespeichert ist. Dabei müssen die Dioden einem maximalen Strom von 200 A standhalten und mit maximal 3.5 MJ gespeicherter Energie sicher umgehen können. Um die Dioden vor Überhitzung zu schützen, sind sie zwischen massiven Kupferblöcken, sogenannten heat sinks, montiert. Um die Zuverlässigkeit dieses Aufbaus zu gewährleisten, wurden die Diodenstacks intensiven Stresstests unterzogen. Dazu zählen Vorselektionstests der Dioden, das Fahren von Temperaturzyklen, elektrische Funktionstests, und fünf Zyklen von Dauerbestromungstests bei 77 K (nicht adiabatisch) und bei 4.5 K (quasi-adiabatisch) in einem speziell instrumentierten Kryostaten. Dabei wurde der nominelle Strom von 200 A für 253 s durch die Dioden geleitet. Dies entspricht der gleichen Energie, die im Quenchfall in der CPS frei wird mit einem 30 prozentigen Sicherheitsfaktor. Alle Dioden haben den Test in flüssig Stickstoff bestanden. Ihre Temperatur blieb unter 120 K, die der Kupferblöcke unter 80 K. Diese Tests wurden mit einer kontinuierlichen Kühlung durchgeführt. Bei den quasi-adiabatischen Bestromungstests bei 4.5 K Anfangstemperatur wurden die Arbeitsbedingungen im CPS Kryostaten simuliert. Die Diodentemperatur stieg auf 240 K an, die Temperatur der Kupferblöcke blieb unter 200 K. Alle sieben plus zwei Ersatzdiodenstacks wurden erfolgreich getestet und an den industriellen CPS Partner, die Firma ASG in Genua, ausgeliefert.

Die CPS wird bei den Langzeitmessungen mit KATRIN in drei Arbeitszyklen operieren: a) Präparation der Argonfrostschicht, b) Neutrinomassenmessung mit ganz KATRIN (Standard Modus). Nachdem sich eine Aktivität von 1 Ci auf der Argonschicht angesammelt

hat, erfolgt c) das Regenerieren (Erneuern der Argonfrostschicht). Die Präparation der Frostschicht, besonders die Injektion von Argon durch die neun beheizbaren Kapillare im CPS Kryostaten wurde im Rahmen dieser Dissertation detailliert untersucht. Hierfür wurde eine originalgetreue Kapillare nachgebaut und anschließend ihre Vakuumeigenschaften in einem Teststand bestimmt. Unter isothermischen Bedingungen wurden der Leitwert und der Gasdurchfluss von Argon und Helium bestimmt. Beide Werte waren in guter Über-einstimmung mit den durchgeführten vakuumphysikalischen Simulationen. Diese Ergebnisse wurden anschließend auf die CPS angewendet. Zunächst wurde die missionskritische Temperaturverteilung entlang einer Kapillare während des Argoneinlasses simuliert. Das erzielte Temperaturprofil variiert je nach Wärmeeintrag an der Kapillarfixierung in der CPS. Auf der elektrisch beheizten Gaseinlassseite ergibt sich eine Temperatur von 76 K. Auf der gegenüberliegenden Seite wird sich eine Temperatur zwischen 17 K (maximaler Wärmekontakt) und 69 K (kein Wärmekontakt) einstellen. Da die Verankerung dort einem lose aufgelegten Kontakt entspricht, kann der Wärmeübertrag an dieser Stelle vernachlässigt werden. Somit ist eine Endtemperatur zwischen 60 K und 69 K zu erwarten.

In einem zweiten Schritt wurde die Temperaturverteilung als Ausgangspunkt für eine nichtisotherme Gasflusssimulation von Argon durch die Kapillare im molekularen Strömungsbereich verwendet. Der Druck in der Kapillare fällt zwischen der ersten und der letzten Öffnung fast um einen Faktor 100 ab. Folglich ist zu erwarten, dass die Argonfrostschicht in jedem der vier Strahlrohrelemente 2-5 der CPS nicht homogen verteilt sein wird. Dieser Druckabfall bewirkt aber positiv, dass der Druck in der Kapillare zu jeder Zeit unterhalb des Dampfdruckes von Argon sein wird, sodass kein Einfrieren des Kapillarinneren zu erwarten ist. Es ergibt sich sogar ein Sicherheitsfaktor von mindestens zwei Größenordnungen im Druck.

Das Ziel der Argonfrostpräparation ist es, eine Anzahl von 1000 bis 3000 Lagen Argonfrost zu präparieren. Mit dem maximalen Gasdurchlass durch alle neun Kapillare im Bereich 10^{-3} mbar ℓ/s (molekularer Bereich) würde die Einlassprozedur etwa 3-4 Wochen dauern. Um die Präparationszeit zu verkürzen, muss der Einlassdruck um maximal zwei Größenordnungen erhöht werden. Damit wird in den Kapillaren eine Übergangsströmung herrschen. Da Berechnungen in diesem Strömungsbereich nur groben Näherungen entsprechen muss die genaue Argonpräparationsprozedur, speziell in Bezug auf die Einlasszeit bei der Inbetriebnahme der CPS, experimentell ermittelt werden.

Im Rahmen dieser Dissertation wurde auch der Reduktionsfaktor der neuen differentiellen Pumpstrecke (DPS) simuliert. Für eine voll instrumentierte DPS ergibt sich ein Reduktionsfaktor von $4.46 \cdot 10^5$ unter Verwendung der Definition des Bauteilleitwertes. Dieses Resultat liegt im spezifizierten Bereich, folglich wird der Gasfluss in die CPS ebenfalls im spezifizierten Bereich von 10^{12} T_2 Molekülen pro Sekunde liegen. Auf der Basis von Literaturwerten konnte in dieser Arbeit gezeigt werden, dass die kapazitive Sorptionsfähigkeit der CPS einen Wert von 60 Ci erreicht. Dies entspricht einem Sicherheitsfaktor von 60 während des Standard-Operationsmodus.

Schließlich wurde auch die Durchgangswahrscheinlichkeit für einströmendes Tritium für die CPS simuliert. Dabei wurden Desorptionsprozesse sowie die durch den Betazerfall tritiierter Moleküle induzierten Diffusionsprozesse vernachlässigt. Damit ergibt sich eine Durchgangswahrscheinlichkeit in der Größenordnung 10^{-17}, gemäß der Definition des Bauteilleitwertes. Diese optimistische, theoretische Transmissionswahrscheinlichkeit wurde anschließend mit den Ergebnissen des TRAP-Experiments verglichen, einem früheren Testexperiment zum Pumpen mit Argonfrost. Dabei wurde eine Diskrepanz von sieben Größenordnungen ermittelt, entsprechend einer berechneten Durchgangswahrscheinlichkeit basierend auf TRAP von 10^{-10}. Da jedoch die Betriebstemperatur der CPS deutlich unterhalb des Wertes von TRAP liegt, ist zu erwarten, dass die Durchgangswahrscheinlichkeit der CPS zwar größer als 10^{-17} ist, aber dennoch kleiner als der TRAP-basierte Wert von 10^{-10}. Die CPS wird somit mindestens drei Größenordnung über ihrer Spezifikation

operieren. Der exakte Reduktionsfaktor muss bei der Inbetriebnahme experimentell bestimmt werden.

Die letzte Pumpstufe der Transportstrecke bildet eine sogenannte Non-Evaporable Getter (NEG) Pumpe in der letzten Sektion der CPS. Die Pumpe wird während des Ausheizens der CPS indirekt durch Wärmestrahlung aktiviert. Die durchgeführten thermischen Simulationen ergaben, dass eine maximale Aktivierungstemperatur von $336°$C und eine durchschnittliche Arbeitstemperatur von $-23°$C erreicht werden. Die Haftwahrscheinlichkeit der Getterpumpe wurde in einem dezidierten Teststand bestimmt, speziell in Bezug auf die simulierte Aktivierungstemperatur. Es ergab sich eine maximale Haftwahrscheinlichkeit von $\alpha = 0{,}013$. Im Verglich dazu beträgt die maximal mögliche Wahrscheinlichkeit $\alpha = 0{,}029$. Falls die Aktivierungstemperatur auf $260°$C gesenkt werden würde, ergäbe sich eine Haftwahrscheinlichkeit von $\alpha = 0{,}010$.

Um die Auswirkung von verschiedenen Aktivierungstemperaturen auf die Gasflussreduktion der CPS zu untersuchen wurden spezifische vakuumphysikalische Simulationen durchgeführt. Dabei ergaben sich nur sehr geringe Unterschiede im Bereich der analysierten Aktivierungstemperaturen von $260°$C bis $336°$C. Beide Szenarien verbessern den Gesamtreduktionsfaktor um eine halbe Größenordnung. Aus kapazitiven Gründen sollte die Pumpe jedoch so hoch wie möglich ausgeheizt werden. Es wird empfohlen, die CPS Getterpumpe neu zu designen. Speziell der Innenradius sollte erweitert werden, um die Gefahr zu vermindern, dass der transportierte magnetische Flussschlauch die NEG-Pumpe berührt. Zusätzlich sollte die Pumpe mit einer elektrischen Heizung ausgestattet werden. Dies würde es erlauben, lokal höhere Temperaturen zu erreichen, wodurch die CPS Temperaturzyklen unabhängig von der NEG-Pumpe gefahren werden können.

Zusammenfassend lässt sich festhalten, das im Rahmen dieser Dissertation wesentliche Beiträge zur Optimierung des Tritiumrückhaltevermögens der DPS und der CPS geleistet wurden. Die durchgeführte Arbeit umfasst wichtige Hardwareaspekte sowie vakuumphysikalische Simulationsarbeiten, die es in ihrer Gesamtheit erlauben, das komplexe Gesamtsystem aus DPS und CPS vollständig zu charakterisieren und bei den in naher Zukunft erfolgenden Inbetriebnahmemessungen zu optimieren.

Introduction and Objective

Neutrinos play a fundamental role in particle physics and cosmology. They are established in the Standard Model of particle physics as neutral, only weakly interacting massless fermions. Several experiments have given clear evidence that neutrinos have a non-vanishing mass, which points to physics beyond the Standard Model. Massive neutrinos from the Big Bang are good candidates for hot dark matter, having a distinct influence on the evolution of large-scale structures in the universe. Neutrino physics and astroparticle physics, including cosmology, are thus connected in a multiple way. Neutrino properties can be predicted with the help of cosmological observations, and, vice versa, cosmological models can benefit from laboratory-based values for intrinsic neutrino properties. One of the most important open issue in these fields is the mass of the neutrino, since this key parameter will improve the understanding of structure evolution in our universe, as well as open up a new understanding of mass generation mechanism for elementary particles.

The **Ka**rlsruhe **Tri**tium **N**eutrino (KATRIN) experiment is targeted to determine the effective mass of the electron anti-neutrino. It is currently under construction at the Karlsruhe Institute of Technology (KIT). KATRIN takes advantage of the well-known kinematics of tritium β-decay. A high precision energy analysis of the decay electron spectrum near its end point allows the experiment to access an absolute neutrino mass of $m(\nu_e) = 350 \, \text{meV}/c^2$ with $5\,\sigma$, equivalent to a sensitivity of $200 \, \text{meV}/c^2$ at 90% C.L. [1]. In case neutrinos would be lighter than this value, KATRIN will improve the current mass limits by one order of magnitude to $m(\nu_e) < 200 \, \text{meV}/c^2$.

The experimental set-up can be subdivided into three major functional parts, each featuring a dedicated vacuum system, an assembly of superconducting magnets, and a high voltage part. Gaseous tritium is injected into a Windowless Gaseous Tritium Source (WGTS), consisting of a complex cryostat with a central beam tube with open ends. A small fraction of injected tritium molecules will decay while drifting out of the source. The huge flux of decay electrons is adiabatically guided to the spectrometer, where electron energies are analysed by variation of a high voltage retarding potential. Only electrons passing this barrier are counted at a detector. In order to avoid tritium molecules to reach the spectrometer and cause background there, an intermediate transport and pumping section is placed between the source and the spectrometer. Its target is to reduce the tritium flow from the source by more than 14 orders of magnitude, while adiabatically guiding the electrons to the spectrometer. This section consists of two major components: the Differential Pumping Section (DPS) and the Cryogenic Pumping Section (CPS). For

the first element a gas flow retention of five orders of magnitude is specified, the second element is specified for further reduction of the tritium flux by another seven orders of magnitude. The understanding of all relevant tritium retention processes and in particular the highest degree of reliability of both components is of utmost importance for the entire KATRIN experiment. The theoretical principles of physics form the methodological base for all commissioning measurements as well as for the long-term KATRIN operation. The efficiency of tritium retention relies crucially on the efficiency of differential pumping and on the mechanism of croygenic pumping with argon frost. In the latter case especially the preparation of an active argon frost layer is mission-crucial. Also, the mechanism of getter pumping is of importance. In order to investigate the performance of the CPS, and respectively of the DPS, a suite of key test experiments was performed in the framework of this thesis, yielding for the argon preparation procedure, as well as for the activation conditions for getter pumping. With this experimental input the overall pumping performance of the CPS and DPS was investigated by means of dedicated vacuum simulations, verifying the ambitious goal of tritium retention of more than 14 orders by combining active (DPS) and passive (CPS) tritium pumping methods.

The present thesis is subdivided into seven main chapters. It starts with a short outline of the present status of neutrino physics and in particular neutrino masses (chapter 1), which forces the central motivation for the KATRIN experiment. The experiment itself is explained in more detail in chapter 2. Since the main focus of this thesis is on the physics processes and optimisation of the performance of the CPS tritium retention techniques, this prominent topic is subdivided into four specific parts. The basics of vacuum physics and technology, as well as the tritium retention of the DPS and a detailed summary on the CPS are presented in chapter 3. Chapter 4 focuses on the magnet safety system of the CPS, while chapters 5 and 6 focus on the preparation and the vacuum performance of the argon frost layer of the CPS, the most critical component of the entire tritium retention system. The last pumping stage inside the CPS will be a non-evaporable getter pump presented in chapter 7. Finally the thesis concludes with chapter 8.

Contents

List of Figures

List of Tables

1. Neutrino physics and current neutrino mass limits

Neutrinos play a fundamental role in particle and astro-particle physics, as well as in cosmology. Due to the well-known fact that they are extremely light particles with an extremely small cross section, they are very difficult to detect. As a consequence their physical properties such as their exact masses are not known even today. Apart from their mass scale a key open question in neutrino physics is: are neutrinos Dirac or Majorana particles?

This chapter will give a short overview on the physical properties of neutrinos and highlight key experimental results. It also focuses on the broader physical context of the KATRIN experiment. After a short comment on the history of the discovery of neutrinos and the classification of neutrinos in the Standard Model of particle physics (section 1.1), neutrino properties are discussed in scenarios involving physics beyond the standard model (section 1.2). Finally, a short description on current methods aiming for a direct neutrino mass determination is given in section 1.3.

1.1. Neutrinos in the Standard Model of particle physics

In 1930 W. Pauli postulated a novel neutral particle in order to explain the experimentally observed continuous electron spectrum of β-decays to guarantee conservation of energy and momentum [2]. Only two years later E. Fermi formulated his famous theory of β-decays based on Pauli's neutral and massless particle, called neutrino [3]. Making use of the inverse beta decay reaction at a nuclear reactor,

$$\bar{\nu}_e + p \rightarrow n + e^+ \quad , \tag{1.1}$$

the first (electron anti-) neutrinos were detected in 1956 by C. Cowan and F. Reines [4]. The positron in equation 1.1 annihilates with an electron emitting two gamma rays which are detected. The free neutron is captured emitting gamma radiation as well. The delayed coincidence of both signals at the same position is a strong indication for an anti-neutrino interaction. Today three different neutrino species are known, namely the electron-, the muon-, and the tau-neutrino (ν_e, ν_μ, ν_τ). The ν_μ was detected in 1962 at the Brookhaven National Laboratory (BNL) by a Nobel prize winning experiment headed by L. M. Lederman, M. Schwartz, and J. Steinberger [5]. In 2000 the ν_τ was finally detected by the

Table 1.1.: The Standard Model of particle physics (SM). Natural units have been used ($c = \hbar = 1$). In the SM, the Higgs boson generates the mass of the particles. The table and physical properties are based on [7] and [8].

Name	Symbol	Mass	Electric charge	Spin
Quarks				
Up	u	2.3 MeV	+2/3	1/2
Down	d	4.8 MeV	−1/3	1/2
Charm	c	1.275 GeV	+2/3	1/2
Strange	s	95 MeV	−1/3	1/2
Top	t	173.07 GeV	+2/3	1/2
Bottom	b	4.18 GeV	−1/3	1/2
Leptons				
Electron	e	0.511 MeV	−1	1/2
Muon	μ	105.66 MeV	−1	1/2
Tau	τ	1.78 GeV	−1	1/2
Electron-neutrino	ν_e	< 2.2 eV	0	1/2
Muon-neutrino	ν_μ	< 0.17 MeV	0	1/2
Tau-neutrino	ν_τ	< 15.5 MeV	0	1/2
Gauge bosons				
Photon	γ	0	0	1
Gluon	g	0	0	1
Z-Boson	Z	91.2 GeV	0	1
$W^\pm$-Boson	$W^\pm$	80.4 GeV	±1	1
Higgs Boson	H	126 GeV	0	0

DONUT experiment at Fermilab [6].

The physical interactions of massless neutrinos are defined in the framework of the Standard Model (SM) of particle physics. This model describes the properties of all known quarks and leptons together with their interactions, as well as the properties of the interaction particles (gauge bosons), as listed in table 1.1. In this model, neutrinos are assumed to be massless neutral particles, as originally defined by W. Pauli and E. Fermi. They are the neutral partners of the charged leptons with spin 1/2 (fermions). They only interact via the weak force by exchange of $W^\pm$ and Z^0 gauge bosons. As the corresponding neutrino cross sections are extremely small, it is very difficult to directly detect neutrinos.

Historically, the observation of electron neutrinos coming from the sun provided a first crack in this model by showing a deficit between the experimentally detected and theoretically predicted neutrino flux. This 'loss' of neutrinos is called the 'solar neutrino problem'. It is described in section 1.2.1. The solution of this problem is based on the phenomenon of neutrino oscillations (section 1.2.2). Neutrinos, when travelling through space, are changing their flavour state in a periodical manner, therefore they must have a non-vanishing mass. However, as neutrinos are only weakly interacting, light particles, their exact masses have not been determined yet, and only upper limits can be stated as described in section 1.3.

1.1.1. Sources of neutrinos

Neutrinos are the second most abundant particles in the universe after the cosmic microwave background (CMB) photons with a present number density of $339\,\nu/\mathrm{cm}^3$ [9]. They were produced during the Big Bang by thermal processes caused by the weak interaction. A selection of processes is given below. In general, neutrino sources can be grouped into terrestrial (atmospheric and nuclear) and extraterrestrial (primordial and solar) ones.

Atmospheric neutrinos have their origin in the decay chain of pions and kaons when high-energy cosmic rays hit the upper earth atmosphere. The largest part of the primary cosmic radiation are hadrons (98%), mainly protons, while the remaining part are electrons. The cosmic ray spectrum produced in the atmosphere has been investigated with balloon-based experiments as well as by extensive air shower experiments such as KASCADE-Grande [10], Auger [11], and others. Neutrinos originate in the decay of mesons and muons. The dominant reactions are:

$$\begin{aligned}
\pi^+ &\to \mu^+ + \nu_\mu \to e^+ + \nu_e + \nu_\mu \\
\pi^- &\to \mu^- + \bar{\nu}_\mu \to e^- + \bar{\nu}_e + \bar{\nu}_\mu \quad .
\end{aligned} \tag{1.2}$$

Nuclear reactors are the strongest terrestrial source of neutrinos. A typical commercial nuclear power reactor will produce about 10^{20} neutrinos per second during the β-decays of heavy fission fragments, resulting also in a huge number of neutrons. Reactor neutrinos have served as powerful sources in long baseline experiments to proof and to determine properties of neutrino oscillations (see section 1.2.2).

Primordial neutrinos introduced already above are a thermal relict from the Big Bang, which were created by weak interactions in the very early universe. In thermal equilibrium, electrons and their anti-particles, positrons, were annihilating to create photons as well as neutrinos:

$$\gamma + \gamma \leftrightarrow e^+ + e^- \leftrightarrow \bar{\nu}_i + \nu_i \quad , \tag{1.3}$$

where the index i denotes for the three different neutrino species. After $1\,\mathrm{s}$ the early universe had cooled to a temperature of $10^{10}\,\mathrm{K}$, so that the creation of charged lepton/anti-lepton pairs stopped, so that the reactions in equation 1.3 took place only from left to right. From that time on neutrinos were produced only via neutron decays:

$$n \to p + e^- + \bar{\nu}_e \quad . \tag{1.4}$$

All these neutrinos are known today as the cosmic neutrino background with a temperature of $1.9\,\mathrm{K}$ and a density of $339\,\nu/\mathrm{cm}^2$ [9]. Since the cross sections of the primordial neutrinos are extremely small, this background radiation has not been detected yet.

Solar neutrinos are produced in main sequence stars like the sun during fusion of hydrogen inside the stellar core. This fusion is started via two branches, the pp-chain (99.75%) and the pep-chain (0.25%). In the first stage two protons and one electron fuse to form a deuterium nucleus and an electron-neutrino:

$$\begin{aligned}
p + p &\to D + e^+ + \nu_e + 0.42\,\mathrm{MeV} \qquad \text{(pp-chain)} \\
p + e^- + p &\to D + \nu_e + 1.44\,\mathrm{MeV} \qquad \text{(pep-chain)} \quad .
\end{aligned} \tag{1.5}$$

In the following reactions heavier elements are formed by fusion of D to ^{3}He and helium to beryllium to lithium and boron. During these reactions more (higher energy) electron-neutrinos are emitted.
After all fuel has been fused, a star reaches its final configuration, either transforming to a white dwarf (for star masses less than eight solar masses), or exploding as a supernova (with a mass of more than eight solar masses). During the core collapse of a supernova,

electrons are captured by the ambient matter, creating neutrons (neutronisation) and electron-neutrinos, forming a hot proton-neutron star. During cooling, almost 100% of the explosion energy is transported by a strong neutrino flux. At the Kamiokande II detector, as well as at the IMB experiment, the first extragalactic neutrinos from the supernova SN1987 were observed in 1987 [12].

Since the cross sections of neutrino interactions are extremely small, they can escape the core of a star without significant interactions, carrying information about the processes inside. This opens the opportunity to investigate solar and stellar models by observing neutrinos coming from a stellar core.

1.2. Neutrinos beyond the Standard Model

The observation and finally the solution of the solar neutrino problem via the phenomenon of neutrino flavour oscillations has proved that neutrinos possess a non-vanishing mass. Although they are part of the Standard Model particle zoo, the non-zero masses of neutrinos clearly points to new physics beyond the SM. This section will focus on the 'solar neutrino problem' and its solution.

1.2.1. The solar neutrino problem

The Homestake experiment in 1970 [13] was intended to confirm the theoretical solar neutrino flux, calculated by Bahcall et al. in the framework of the Standard Solar Model (SSM) [14] [15]. Solar neutrinos were detected in a radiochemical method with a tetrachloro-ethylene-based detector in the following reaction:

$$\nu_e + {}^{37}\text{Cl} \leftrightarrow {}^{37}\text{Ar} + e^- \quad . \tag{1.6}$$

After a few weeks of solar exposure, the radioactive ^{37}Ar (half-life of 35 days) was extracted by a dedicated radiochemical process. The few extracted ^{37}Ar atoms were identified via electron capture (equation 1.6 from right to left), resulting in an exited chlorine nuclei. Its deexcitation via Auger electrons allowed to identify the number of ^{37}Ar atoms produced by solar neutrinos. The Homestake experiment obtained a neutrino flux of roughly 1/3 of the expected SSM flux [16]. This deviation is called the 'solar neutrino problem'. It was at first attempted to be explained by uncertainties in the SSM. However, with the successor experiments GALLEX, SAGE, and GNO [17] [18] [19] the observed deficit in solar neutrinos was confirmed.

With the onset of new real-time detectors, such as Kamiokande [20], Super-Kamiokande [21], and SNO [22], the solar neutrino problem has been investigated in more detail. These detectors made use of several tonnes of high-purity H_2O (D_2O in case of the SNO detector) as target material together with a huge amount of photomultipliers to detect Cerenkov-radiation from neutrino interactions with the target material. Neutrino interactions comprise elastic scattering with electrons (ES), neutral currents (NC), and charged currents (CC) in the expample of SNO:

$$\begin{aligned}
\text{ES:} \quad & \nu_i + e^- \rightarrow \nu_i + e^- \\
\text{NC:} \quad & \nu_i + D \rightarrow p + n + \nu_i \\
\text{CC:} \quad & \nu_e + D \rightarrow p + p + e^- \quad ,
\end{aligned} \tag{1.7}$$
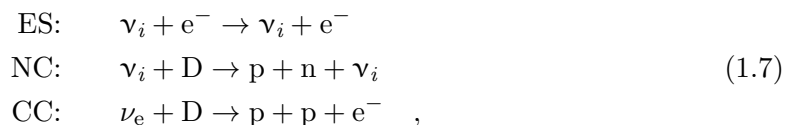
with the index i representing the three neutrino species (ν_e, ν_μ, ν_τ). By detecting the Cerenkov light cones, the primary energy of the neutrino, its direction, and its arrival time can be determined. In case of neutral currents the released neutron has to be captured by a suitable nucleus, emitting thus photons with known energies. These characteristic photons then represent a neutrino NC signal. Via the charged current, the rate of electron

neutrinos from the sun can be determined. In the case of SNO, again a ν_e-specific deficit ($\Gamma(\nu_e)_{exp} \approx 1/3 \cdot \Gamma(\nu_e)_{theo}$) was observed. However, via the neutral currents, which are sensitive to all neutrino flavours, the SNO detector in 2001 observed a total solar neutrino rate equivalent to the expected theoretical rate [23], thus solving the 'solar neutrino problem'.

A few years earlier, in 1998, the Super-Kamiokande detector observed oscillations of atmospheric neutrinos. The rate of atmospheric muon-neutrinos travelling a long distance through the earth varies significantly from the rate of muon-neutrinos travelling only a short distance from the upper atmosphere [24]. The solar neutrino problem and the atmospheric muon-neutrino zenith angle distribution together give clear proof of the existence of flavour changing process of neutrinos, the so called neutrino oscillations. The observation of these oscillations implies that flavour eigenstates of neutrinos are not identical to mass eigenstates. Hence neutrinos must possess a non-vanishing mass, pointing to physics beyond the Standard Model.

1.2.2. Neutrino oscillations

The theory of neutrino oscillations describes a periodic flavour change of neutrinos, by defining three flavour eigenstates ($|\nu_\alpha\rangle$ with $\alpha = $ e, μ, τ), which can be expressed by a mixture of three different mass eigenstates ($|\nu_i\rangle$ with $i = 1, 2, 3$):

$$|\nu_\alpha\rangle = \sum_{i=1}^{3} U_{\alpha i} |\nu_i\rangle \quad , \tag{1.8}$$

correlated by a unitary PMNS neutrino mixing matrix $U_{\alpha i}$ (PMNS = Pontecorvo-Maki-Nakagawa-Sakata matrix). The PMNS matrix can be parametrised by three Euler angles (Θ_{12}, Θ_{13}, and Θ_{23}) and a complex phase (ϕ) for CP violation:

$$U = \begin{pmatrix} U_{e1} & U_{e2} & U_{e3} \\ U_{\mu 1} & U_{\mu 2} & U_{\mu 3} \\ U_{\tau 1} & U_{\tau 2} & U_{\tau 3} \end{pmatrix} = \begin{pmatrix} 1 & 0 & 0 \\ 0 & 1 & 0 \\ 0 & 0 & e^{i\phi} \end{pmatrix} \cdot \begin{pmatrix} 1 & 0 & 0 \\ 0 & \cos\Theta_{23} & \sin\Theta_{23} \\ 0 & -\sin\Theta_{23} & \cos\Theta_{23} \end{pmatrix} \cdot$$
$$\cdot \begin{pmatrix} \cos\Theta_{12} & \sin\Theta_{12} & 0 \\ -\sin\Theta_{12} & \cos\Theta_{12} & 0 \\ 0 & 0 & 1 \end{pmatrix} \cdot \begin{pmatrix} 1 & 0 & 0 \\ 0 & \cos\Theta_{13} & \sin\Theta_{13} \\ 0 & -\sin\Theta_{13} & \cos\Theta_{13} \end{pmatrix} \tag{1.9}$$

The square of the absolute value of one matrix element ($|U_{\alpha i}|^2$) gives the probability to find the neutrino in the mass eigenstate i for a given flavour α. Neutrinos, when created in weak interactions, thus have a well defined flavour eigenstate. When propagating through space this initial flavour will change.

The evolution in time of the propagating mass eigenstates can be expressed in quantum mechanics as:

$$|\nu_i(t)\rangle = e^{-\frac{i}{\hbar}(E_i t - \vec{p}_i \vec{x})} |\nu_i(t = 0)\rangle \quad , \tag{1.10}$$

with the neutrino plane wave given by the energy E_i and the momentum $\vec{p}$. In the relativistic limit neutrinos are travelling almost with the speed of light, so that their masses can be neglected compared to their energies. Thus, the relativistic relation between energy and momentum can be approximated by:

$$p = \frac{1}{c}\sqrt{E_i^2 - m_i^2 c^4} \approx \frac{1}{c}\left(E - \frac{m_i^2 c^4}{2E}\right) \quad . \tag{1.11}$$

Inserting this approximation into equation 1.10 and expressing the parameter t via the distance in travelling $t = L/c$, the wave function of a neutrino mass eigenstate as function of distance is obtained:

$$|\nu_i(t)\rangle \approx e^{-\frac{i}{\hbar c} \cdot \frac{m_i^2 c^4}{2E} \cdot L} |\nu_i(L = 0)\rangle \quad . \tag{1.12}$$

Due to their different masses m_i, these eigenstates will evolve differently over distance and hence in time. Thus a phase difference will occur during propagation. The interference of the three mass eigenstates is the reason why a different flavour eigenstate will be observed at a distance L from the origin, or respectively at a time t. Only for specific values of L the actual state will be identical to the initial state.

The probability of a neutrino created in the flavour eigenstate $|\nu_\alpha\rangle$, to be found at $t > 0$ in the state $|\nu_\beta\rangle$ can thus be calculated via:

$$P(\alpha \to \beta,\ t) = |\langle \nu_\beta(t)|\nu_\alpha(0)\rangle|^2 = \left| \sum_{i,j} U_{\alpha i} U_{\alpha j}^* U_{\beta j}^* U_{\beta j} e^{-\frac{i}{\hbar c} \frac{\Delta m_{ij}^2 c^4}{2E} L} \right|^2 \quad , \qquad (1.13)$$

where equation 1.8 was used. It can clearly be seen that the probability P of finding a neutrino with flavour β, created with flavour α, depends on the difference of the mass squares, the distance L, and energy E. Hence neutrino oscillation experiments only yield the mass differences of the neutrino flavours, but do not allow to define the absolute mass scale.

Two flavour oscillations

Assuming only two flavours (ν_α, ν_β) and two massive eigenstates (ν_1, ν_2) to couple, the neutrino mixing matrix can be simplified with one mixing angle Θ only. This simplifies equation 1.8 to:

$$\begin{pmatrix} \nu_\alpha \\ \nu_\beta \end{pmatrix} = \begin{pmatrix} \cos\Theta & \sin\Theta \\ -\sin\Theta & \cos\Theta \end{pmatrix} \cdot \begin{pmatrix} \nu_1 \\ \nu_2 \end{pmatrix} \quad . \qquad (1.14)$$

The probability of detecting a neutrino with flavour β, created with flavour α then is:

$$P(\alpha \to \beta,\ t) = |\langle \nu_\beta(t)|\nu_\alpha(0)\rangle|^2 = \sin^2(2\Theta) \cdot \sin^2\left(\frac{\Delta m^2 c^4}{2E} \cdot \frac{L}{\hbar c} \right) \quad , \qquad (1.15)$$

with $\Delta m^2 = m_1^2 - m_2^2$. The first term describes the amplitude, and the second term the frequency of oscillation. The latter depends on the difference in the mass squares, on the distance L between source and detector, and on the neutrino energy E [25].

Calculations for the more general case of three mixing flavours are somewhat more complicated, since differences of three mass squares have to be taken into account, as well as the MSW (Mikheyev-Smirnow-Wolfenstein) effect in case of propagation in matter. More details on neutrino oscillations and the MSW effect can be found in [26].

Experimental results for mixing angles and squared mass differences

A large set of experiments has verified the existance of neutrino oscillations by typically detecting neutrinos at two different distances from a source. By doing so, the mixing angles and the square of the mass differences were determined. To investigate electron-neutrino oscillations, the experiments KamLAND [27], Daya Bay [28], RENO [29], and Double Chooz [30] made use of nuclear reactors as neutrino source. The experiments MINOS [31] and T2K [32] used a beam of muon-neutrinos, produced at a particle accelerator to investigate muon-neutrino flavour oscillations. The present data (mixing angles and mass differences) are listed in table 1.2.

As stated above, only the square of the neutrino masses can be determined via oscillation experiments, so no information is available yet on the mass hierarchy or the absolute mass scale. Three possible scenarios exist:

Table 1.2.: Experimentally determined parameters of neutrino oscillation. Since the oscillation depends only on the square of the neutrino masses no statement on the hierarchy and on their absolute values can be made. The sign of Δm_{32}^2 is yet unknown. Taken from [8].

Parameter	Value	
$\sin^2(2\Theta_{12})$	0.846 ± 0.021	
Δm_{21}^2	$(7.53 \pm 0.18) \cdot 10^{-5} \, \text{eV}^2/c^4$	
$\sin^2(2\Theta_{23})$	$0.999^{+0.001}_{-0.018}$	normal mass hierarchy
$\sin^2(2\Theta_{23})$	$1.000^{+0.000}_{-0.017}$	inverted mass hierarchy
Δm_{32}^2	$(2.44 \pm 0.06) \cdot 10^{-3} \, \text{eV}^2/c^4$	normal mass hierarchy
Δm_{32}^2	$(2.52 \pm 0.07) \cdot 10^{-3} \, \text{eV}^2/c^4$	inverted mass hierarchy
$\sin^2(2\Theta_{13})$	$(9.3 \pm 0.8) \cdot 10^{-2}$	

1. **Quasi-degenerate hierarchy:** The absolute mass m_i is much larger than the square of the mass differences Δm_{ij}^2.

2. **Normal hierarchy:** The masses are ordered as defined by $m_1 < m_2 < m_3$.

3. **Inverted hierarchy:** Since the sign of Δm_{32}^2 is yet unknown, it is possible that $m_3 < m_1 < m_2$.

With the determination of the absolute mass scale and the sign of Δm_{32}^2, all neutrino mass parameters will be fixed.

1.3. Determination of neutrino masses

Only a few approaches exist which allow to determine the absolute neutrino masses. An interesting approach is provided by cosmology, based on analysis of fluctuations in the cosmic microwave background (CMB). This represents however a model-dependent way to estimate the sum of all three neutrino masses (see section 1.3.1). Another approach to determine neutrino masses is based on detecting and counting the number of events in searches for neutrino-less double beta decay, as presented in section 1.3.2. The most promising and most precise approach is however direct neutrino mass measurements relying only on the kinematics of β-decays, as outlined in section 1.3.3 and described in more detail in section 2.1.

1.3.1. Cosmological approach

The cosmic microwave background (CMB) is a relict from the early universe. It pictures the moment of last scattering of photons before their decoupling from matter. At the very beginning, the temperature of all particles was so hot that processes such as $e^- + e^- \leftrightarrow \gamma + \gamma$ occurred rapidly. The matter density was so high that the early universe was opaque to the high energetic photons. After roughly $380\,000$ years, the universe expanded and cooled down to values which allowed ionised matter to became neutral. This implied that photons decoupled from matter at that time, where the temperature was about $3\,000\,\text{K}$. The decoupled photons cooled down independently from the residual matter, today forming a black body radiation with a temperature of $(2.72548 \pm 0.00057)\,\text{K}$ [33], still carrying a fingerprint of the early universe structure. Since the first discovery of the CMB by Penzias and Wilson in 1965 [34], a set of satellite missions has investigated the exact nature and properties of the CMB, namely COBE, WMAP, and Planck. All of

them investigated tiny CMB anisotropies in temperature of significantly less than $1\,\text{mK}$. These are caused by the following processes before the decoupling of photons in the early universe:

- Baryonic acoustic oscillations: Fluctuations in the primordial matter density grew due to the gravitational accumulation of more matter until the radiation pressure dominated, causing overdense spots to expand again. The CMB carries information about these early density fluctuations.

- Sachs-Wolfe effect: When photons escape from a large-scale denser region, they lose energy in the gravitational potential, thus getting more red-shifted with respect to photons from less dense regions.

- Silk damping: This effect dampens small-scale acoustic oscillations, since photons diffuse readily thereby carrying energy from hotter regions to colder regions.

The observed black body spectrum with its fluctuations can be fitted within the standard ΛCDM model of cosmology, taking the different matter contributions (vacuum energy Ω_Λ, baryons Ω_b, and cold dark matter Ω_DM) into account. The Planck mission found an upper limit for the sum of all three neutrino species of [35]:

$$m(\nu) = \sum_{i=1}^{3} m(\nu_i) \approx 0.23\,\text{eV}/c^2 \quad . \tag{1.16}$$

Note that this method is however extremely model-dependent.

Another way of estimating neutrino masses is by investigating the large-scale structures (LSS) of the universe. Although the universe is assumed to be homogeneous, it shows a clumpy filament-like structure on larger scales. Neutrinos play an important role in the evolution of these filament structures. Neutrinos with a comparably higher mass will transport more energy from denser regions to regions with lower densities, thus levelling structures on smaller scales more efficiently than lighter neutrinos. Therefore, massless neutrinos would have led to a more clumpy structure. With the ΛCDM model these structure formation scenarios can be simulated. By comparing the results with the observed large-scale structures a mass limit for all three neutrinos was found to be [36]:

$$m(\nu) = \sum_{i=1}^{3} \leq 0.5\,\text{eV}/c^2 \quad . \tag{1.17}$$

Cosmology thus opens up great opportunities to investigate the impact of different neutrino masses on LSS and thus allows to obtain limits for the sum $m(\nu)$. By varying the different free parameters of the ΛCDM-model, specific neutrino mass limits are obtained. However, turning the argument around, the a priori knowledge of neutrino masses will positively affect cosmology as well. Laboratory values for neutrino masses, for example, will tighten the ΛCDM-model, since one free parameter, the neutrino masses, would be fixed. This is a strong motivation for laboratory experiments aiming to determine the neutrino mass, especially for the KATRIN experiment, since its way of determination will be completely model-independent.

1.3.2. Neutrinoless double beta decay

The process of neutrinoless double beta ($0\nu\beta\beta$) decay is a beyond SM process giving the opportunity to investigate the intrinsic nature of neutrinos, a well as providing access to their masses. If this decay would be detected, neutrinos are identical to their own

antiparticles, which defines them to be Majorana particles.

Within the normal double beta ($2\nu\beta\beta$) decay mode, two neutrons decay at the same time into two protons emitting two electrons and two anti-neutrinos:

$$2\mathrm{n} \to 2\mathrm{p} + 2\mathrm{e}^- + 2\bar{\nu}_\mathrm{e} \quad . \tag{1.18}$$

The electron energies of this allowed and observed SM process follow a continuous spectrum. Double beta decays can, in principle appear in all beta emitters. However, due to their nature as second order weak interaction, the $\beta\beta$-probabilities typically are negligible compared to single beta decays. Therefore, only specific elements are suitable to investigate this double transition. The most promising elements are ^{76}Ge and ^{136}Xe with single decay being energetically forbidden. In case of a $0\nu\beta\beta$-decay process, antineutrinos will not be emitted, violating lepton number conservation. In this case both electrons share the complete decay energy, so that a sharp electron energy peak will be observed, thus proving the Majorana nature of neutrinos. At present several experiments, such as GERDA [37] and EXO [38], are taking data. However, no $0\nu\beta\beta$-signal was observed until now, yielding limits on the effective Majorana neutrino mass of the order of $0.2 - 0.4\,\mathrm{eV}$ (95% C.L.) [39].

1.3.3. Single beta decay

Weak nuclear β-decays of first order can be subdivided into three reactions:

$$\begin{aligned} \beta^- &: & \mathrm{n} &\to \mathrm{p} + \mathrm{e}^- + \bar{\nu}_\mathrm{e} \\ \beta^+ &: & \mathrm{p} &\to \mathrm{n} + \mathrm{e}^+ + \nu_\mathrm{e} \\ \mathrm{EC} &: & \mathrm{p} + \mathrm{e}^- &\to \mathrm{n} + \nu_\mathrm{e} \quad . \end{aligned} \tag{1.19}$$

The β^+-decay channel takes only place in proton-rich nuclei, while β^--decays occur in neutron-rich nuclei. The latter is thus well suited to investigate the electron (anti-) neutrino mass by a detailed analysis of the energy spectrum of the emitted electrons near the end point. Since this is the basic idea of the KATRIN experiment, it is described in detail in section 2.1.

Currently only a upper limit for the 'electron-neutrino mass' has been found at the Troitsk and Mainz experiments, and likewise for the 'muon-neutrino mass' at PSI, and for the 'tau-neutrino mass' at the LEP accelerator:

$$\begin{aligned} \text{Troitsk-Experiment (90\% C.L.) [40]:} \quad & m(\nu_\mathrm{e}) < 2.2\,\mathrm{eV}/c^2 \\ \text{PSI (90\% C.L.) [41]:} \quad & m(\nu_\mu) < 190\,\mathrm{keV}/c^2 \\ \text{LEP (95\% C.L.) [42]:} \quad & m(\nu_\tau) < 18.2\,\mathrm{MeV}/c^2 \quad . \end{aligned} \tag{1.20}$$

It should be noted however, that these old 'flavour-based' masses do not make sense due to the results of recent oscillation experiments.

2. Neutrino mass measurement with the KATRIN Experiment

The **Ka**rlsruhe **Tri**tium **N**eutrino experiment (KARTIN) is designed to determine the absolute neutrino mass scale by measuring the effective 'electron antineutrino mass' $m(\bar{\nu}_e)$ in a direct and model-independent way with a sensitivity of $0.2\,\text{eV}/c^2$ (90% C.L.) [1]. It is the direct successor of experiments at Troitsk [40] and Mainz [43] with one order of magnitude better sensitivity. The upper limits of these experiments are given by:

$$\text{Troitsk experiment:} \qquad 2.2\,\text{eV}/c^2 \text{ (95\% C.L.) [40]} \qquad (2.1)$$

$$\text{Mainz experiment:} \qquad 2.3\,\text{eV}/c^2 \text{ (95\% C.L.) [43]} \qquad (2.2)$$

KATRIN will take advantage of the well-known tritium β-decay kinematics (section 2.1) to improve these limits by one order of magnitude. To do so it will analyse the shape of the β-electron spectrum with unprecedented precision in a region close to the kinematic end-point at about $18.6\,\text{keV}$.

The experiment is currently being assembled at Karlsruhe Institute of Technology (KIT). There, it benefits from infrastructure and expertise of Tritium Laboratory Karlsruhe (TLK) which offers unique knowledge in handling and processing of tritium on large scales. The KATRIN assembly is shown in figure 2.1. The beam line is roughly $70\,\text{m}$ long and features many technological challenges and breakthroughs such as its UHV system. It not only pushes spectroscopic possibilities to their current limits, it also pushes especially the tritium retention units to unprecedented levels. In section 2.1 the basics of the tritium beta decay are outlined. Sections 2.2 and 2.3 describe the experimental set-up from the tritium source, via the transport section, to the spectrometer and detector system. A detailed view on the MAC-E filter principle is given in subsection 2.3.1. In sections 2.4 and 2.5 the KATRIN sensitivity, its limits, and the monitoring of the key parameters are described.

2.1. Kinematics of the tritium beta decay

The KATRIN experiment makes use of the kinematics of tritium β-decay to determine the effective 'electron antineutrino mass' $m(\bar{\nu}_e)$ in a direct and model-independent way. The process of tritium β-decay provides optimal conditions for high-sensitivity neutrino mass measurement, as:
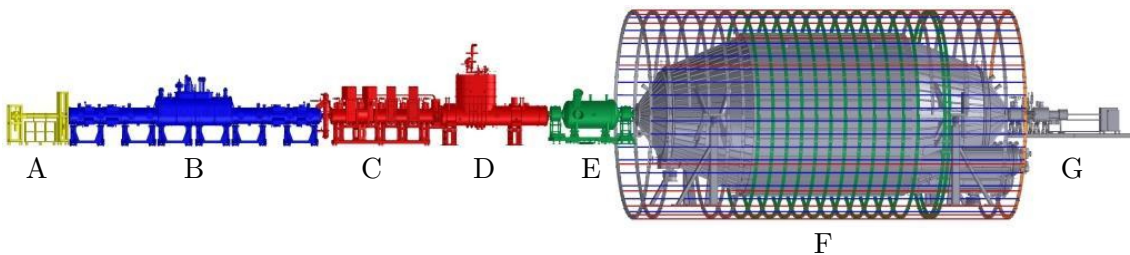
Figure 2.1.: KATRIN assembly. Yellow, A: Rear section. Blue, B: Windowless gaseous tritium source (WGTS). Red, C+D: Transport section, C: Differential pumping section (DPS), D: Cryogenic pumping section (CPS). Green, E: Pre-spectrometer. Grey, F: Main spectrometer and air coils. Grey, G: Detector. The magnetic field inside the vacuum system points south, from the detector to the rear section.

1. It is a β-emitter with a rather low end-point energy E_0 of 18.6 keV, which is of distinct technological advantage.

2. Since the end-point energy is low, the phase space for an electron antineutrino to be emitted into the last few eVs below the end-point is rather large. Also, tritium features a high decay rate. About 10^{-10} particles per decay fall into the interval between $[E_0 - 10\,\text{eV}, E_0]$.

3. Tritium has a short half life time of 12.3 years and hence a high specific activity. This allows a source with a rather low tritium density and thus rather small low inelastic scattering effects within this source.

4. The electron configuration is one of the simplest of all β-active elements. This minimises atomic physics corrections, such as inelastic scattering in the source or final states, all of which have to be taken into account when calculating β-electron energies.

5. The tritium β-decay is a super-allowed transition, so that the transition matrix element is independent of the energy ($|M|^2 \neq f(E)$).

The KATRIN experiment will analyse the integrated β-spectrum in the vicinity of the end-point energy with ultra-high precision. Electrons are produced in the β-decay of molecular tritium:

$$\text{T}_2 \rightarrow {}^3\text{HeT}^+ + \text{e}^- + \bar{\nu}_{\text{e}} \quad . \tag{2.3}$$

The transition rate for β-electrons emitted from this decay can be calculated with Fermi's Golden Rule:

$$\frac{d^2N}{dtdE} = \frac{2\pi}{\hbar}|M|^2\rho(E) \quad , \tag{2.4}$$

with the transition matrix element M and the final states density $\rho(E)$. For tritium, the nuclear mass is much larger than the electron mass and neutrino energies. The nucleus can thus be assumed to balance the leptonic momenta, however, in doing so, it does not receive a large fraction of recoil energy. The final state densities of the electron and neutrino can be considered to be independent.

$$\rho(E) = \frac{dn_{\text{e}}}{dE_{\text{e}}}\frac{dn_{\nu}}{dE_{\nu}} = \frac{p_{\text{e}}E_{\text{e}}p_{\nu}E_{\nu}V^2}{4\pi^4\hbar^6} \quad , \tag{2.5}$$

with the electron and neutrino momenta p_{e} and p_{ν}, respectively, their kinetic energies $dE_{\text{e}/\nu}$, and the phase space volume V. With $E_{\nu} = E_0 - E$ and the relativistic energy-

momentum relation, one obtains:

$$\rho(E) = \frac{p_e(E + m)\sqrt{(E_0 - E)^2 - m^2(\nu_e)}\,(E_0 - E)\,V^2}{4\pi^4 \hbar^6} \quad . \tag{2.6}$$

The matrix element M in equation 2.4 consists of a leptonic M_{lep} and a hadronic part M_{had}:

$$M = G_F \cos \Theta_C M_{\text{lep}} M_{\text{had}} \quad , \tag{2.7}$$

with the Cabibbo angle Θ_C, and the Fermi coupling constant G_F. The leptonic matrix transition element leads to [44]:

$$|M_{\text{lep}}|^2 = \frac{1}{V^2} F(E, Z + 1) \quad , \tag{2.8}$$

where $F(E, Z+1)$ describes the Fermi function, which parametrises the interaction between the outgoing electron and recoiling daughter nucleus. With the hadronic matrix element [44]

$$|M_{\text{had}}|^2 = 5.55 \hbar^6 \quad , \tag{2.9}$$

and equation 2.4 and 2.7 the energy dependent transmission rate can be calculated. Taken electronic excitation of the daughter nucleus into account leads to [44]:

$$\begin{aligned}
\frac{d^2 N}{dt dE} = &\frac{G_F^2 \cos^2 \Theta_C}{2\pi^3 \hbar^7} \cdot F(E, Z + 1) \cdot p(E + m) \times \\
&\times \sum_j W_j \epsilon_j \left(\sum_i |U_{ei}^2| \sqrt{\epsilon_j^2 - m^2(\nu_i)} \cdot \Theta(\epsilon_j - m(\nu_i)) \right) \quad ,
\end{aligned} \tag{2.10}$$

with the energy differences $\epsilon_j = (E_0 - V_j - E)$, the excitation energies V_j, and the probabilities W_j of the daughter nucleus to be in an excited state j, and the neutrino mixing matrix U_{ei}. The theoretical spectrum is shown in figure 2.2. By measuring the decay energies of electrons, the square of the effective 'electron antineutrino mass' is determined:

$$m^2(\bar{\nu}_e) = \sum_i |U_{ei}|^2 m^2(\bar{\nu}_i) \quad , \tag{2.11}$$

with the neutrino mixing matrix U_{ei}.

2.2. Source and Transport section

The tritium source is a key component of the KATRIN set-up. It must provide a constant β-decay activity with highest luminosity. In the case of KATRIN, a windowless gaseous tritium source (WGTS) was chosen in order to minimise energy losses inside the source. Since this type of source contains no window acting as barrier for migration of tritium molecules, the injected gas could proceed to the spectrometer region. This is prohibited by a transport section, where the gas flow has to be reduced by at least 14 orders of magnitude so that background processes due to tritium decay in the spectrometer section are avoided during the neutrino mass measurements. To reach that goal, a differential pumping section (DPS) and a cryogenic pumping section (CPS) are planed.
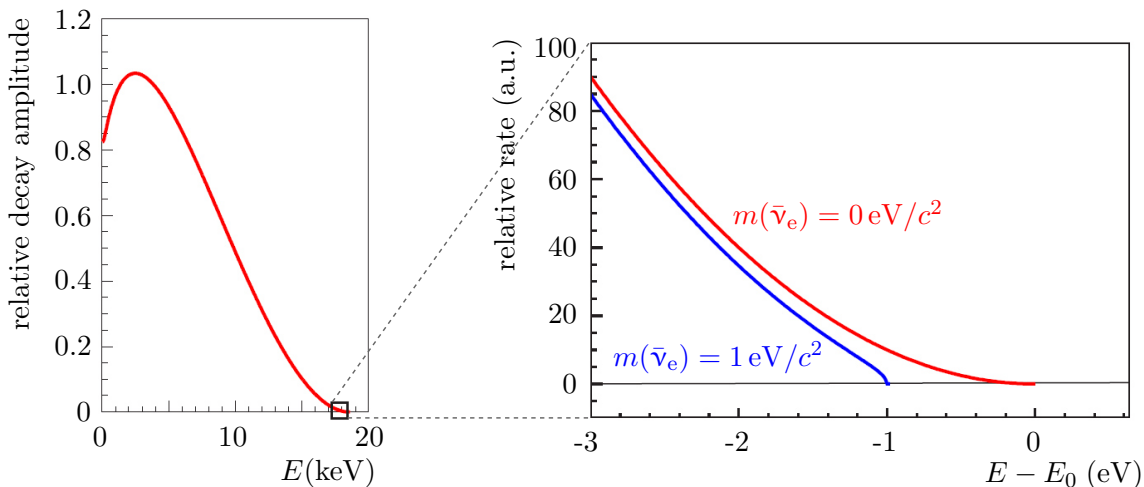
Figure 2.2.: Tritium β-decay spectrum. Left: Entire spectrum, with an end-point energy of about $18.6\,\mathrm{keV}$. Right: Spectrum close to the end-point. Sketched are a vanishing and a non vanishing neutrino mass with $1\,\mathrm{eV}/c^2$. Based on [45].

2.2.1. Windowless gaseous tritium source (WGTS)

The WGTS cryostat (figure 2.1 B) contains a $10\,\mathrm{m}$ long and $90\,\mathrm{mm}$ wide vacuum beam tube with open ends. High purity tritium ($\epsilon > 95\%$) is injected through capillaries with a flow rate of $q = 1.853\,\mathrm{mbar}\,\ell/\mathrm{s}$ into the vacuum system in the centre of the source. This leads to a column density of $\rho d = 5 \cdot 10^{17}\,\mathrm{molecules} \cdot \mathrm{cm}^{-2}$, which must be stabilised on the 10^{-3} level. This comes from the fact that changes in the column density will have a direct influence on the signal electron rate and their energies due to different scattering processes. Additional systems are installed at the WGTS cryostat to monitor key source parameters (see section 2.4 below and [46]).

Figure 2.3 illustrates the WGTS pumping scheme. The injected tritium molecules are pumped out at both ends of the $10\,\mathrm{m}$ long tube, via the so called DPS1-F and DPS1-R elements (differential pumping section 1 - front/rear). Both units feature two pumping chambers with a total of 12 turbo molecular pumps (TMPs) with a pumping speed of $\approx 2400\,\ell/\mathrm{s}$ for T_2 each. The pumped out gas enters the 'Inner Loop System', where it is partially cleaned and injected back into the WGTS [47]. The tritium source has to deal with a large nominal gas throughput, which results in a source activity of $1.7 \cdot 10^{11}\,\mathrm{Bq}$. The gas flow reduction in this first active stage is designed to be 10^2 as described in detail in [48]. Since the electron energies depend on the thermal velocity of tritium molecules, it is important to stabilise the WGTS at a low temperature, which has to be sufficiently high to avoid forming of extended cluster molecules. By means of a novel two-phase neon cooling system, operated between $1\,\mathrm{bar}$ and $10\,\mathrm{bar}$, the temperature can be adjusted in the range from $27\,\mathrm{K}$ to $33\,\mathrm{K}$ [49]. In order to minimise commissioning risks, the WGTS cooling system was tested in the large-scale Demonstrator test experiment [50] [51] [52]. There, the temperature could be stabilised with a relative deviation of $\pm 3 \cdot 10^{-4}\,\mathrm{K}$ [53].

In order to guide the signal electrons into the spectrometer the WGTS features seven superconducting magnets. The source field, as well as the DPS1-R field, is nominally at $B_\mathrm{S} = 3.6\,\mathrm{T}$. The maximum magnetic field of the DPS1-F is higher with $5.6\,\mathrm{T}$.

Ion production and reactions inside the source

Inside the WGTS beam tube, β-electrons are produced according to equation 2.3. On average a single keV-range β-decay electron will scatter about 15 times off residual gas
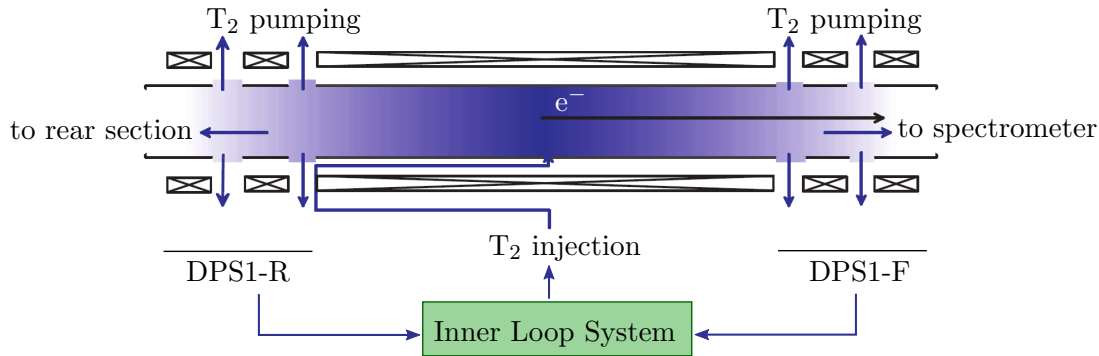
Figure 2.3.: Schematic drawing of the WGTS pumping set-up. Molecular tritium is injected at constant flow rate from the Inner Loop System into the centre of the source. The β-decay electrons are guided magnetically out of the source into the spectrometer and rear section, respectively. The tritium gas thermally diffuses to both ends of the 10 m long tube. At both ends, one pumping station each (DPS1-R/F) is pumping out neutral tritium molecules. A small part of the pumped-out gas is cleaned in the infrastructure of tritium laboratory and injected back into the source.

molecules until reaching a free molecular flow regime. During these collisions a number of different ions are produced by:

- **Ionisation:** Electrons hitting neutral T_2 can produce T_2^+ (95%) and T^+ (5%).

$$\begin{aligned} e^- + T_2 &\rightarrow e^- + e^- + T_2^+ \\ e^- + T_2 &\rightarrow e^- + e^- + T^+ + T \quad . \end{aligned} \tag{2.12}$$
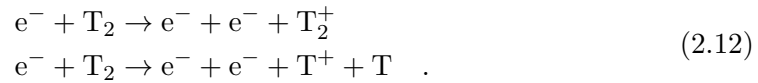
- **Chemical reactions:** Ions and neutral particles react and can form tritium clusters.

$$\begin{aligned} He^+ + T_2 &\rightarrow He + T + T^+ \\ He^+ + T_2 &\rightarrow He + T_2^+ \\ T^+ + T_2 + T_2 &\rightarrow T_3^+ + T_2 \\ T_3^+ + T_2 + T_2 &\rightarrow T_5^+ + T_2 \quad . \end{aligned} \tag{2.13}$$
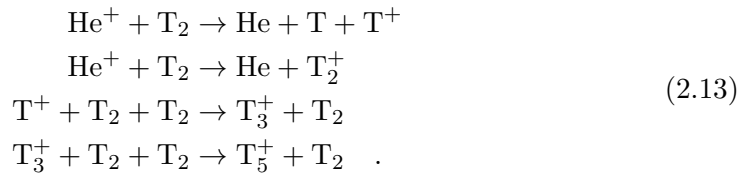
- **Recombination:** Electrons and ions which are produced in the WGTS can recombine via the following channels:

$$\begin{aligned} A^+ + e^- &\rightarrow A^* + \gamma \\ A^+ + e^- + e^- &\rightarrow A^* + e^- \\ T_3^+ + e^- &\rightarrow T_2 + T \\ T_5^+ + e^- &\rightarrow T_2 + T_2 + T \quad . \end{aligned} \tag{2.14}$$
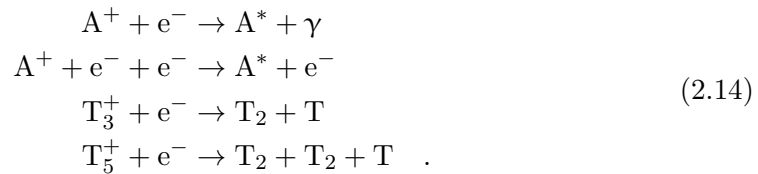
Altogether, a current of 27 nA of positive ions is expected to be generated inside the source. Negative tritium ions will occur as well within the following dissociative attachment reaction:

$$e^- + T_2 \rightarrow T^- + T \quad . \tag{2.15}$$

Their current is expected to be about 2 nA. All reactions and numbers are taken from [54], [55] and [56].

Both, negative and positive ions are magnetically guided out of the WGTS to the spectrometer region. When entering the spectrometer, they would produce significant background during neutrino mass measurement [57]. A dedicated system for ion reduction is therefore installed in the KATRIN transport section (see section 3.2.4).

2.2.2. Differential pumping section (DPS)

The differential pumping section (DPS) constitutes the first tritium-pumping stage of the transport section (figure 2.1 C). Its target is to reduce further the tritium gas flow by at least five orders of magnitude [1] while also guiding the β-decay electrons adiabatically towards the spectrometer section. In parallel the DPS should block and eliminate the positive ion flow.

The DPS can be approximated by a roughly 6.5 m long vacuum tube (100 mm diameter) which is bent along its five elements to form a chicanery of 20°. The connection to the WGTS is achieved via the so called pump port 0 (PP0), consisting of a cylindrical chamber with two TMPs. Along the chicanery four TMPs with individual pumping speeds of about $2400 \, \ell/s$ for T_2 are installed at so called pumping chambers. Owing to the chicanery, neutral particles hit the chamber walls, where the TMPs are installed. A further element is formed by the electric dipoles, which are placed inside the vacuum system for ion suppression (see section 3.2.4). In order to analyse ions, both quantitatively and qualitatively, a Penning trap based unit, a FT-ICR (Fourier Transform - Ion Cyclotron Resonance) element, is placed at the beginning of the DPS (compare section 3.2.3).

The DPS is designed as a modular system. Five superconducting stand-alone magnets with magnetic fields of up to 5.5 T from CryoMagnetics shape the magnetic flux tube in order to guide the electrons to the spectrometer. The DPS is designed to transport at least a value of 191 Tcm^2 flux tube through its vacuum system [1]. The value of the magnetic flux tube is caused by the geometry and the specifications of the KATRIN main spectrometer, as described in sections 2.3.1 and 2.3.3. A detailed description of the DPS properties and its vacuum performance is given in section 3.2.

2.2.3. Cryogenic pumping section (CPS)

The cryogenic pumping section (CPS) is the second and last stage of the KATRIN transport section (figure 2.1 D). Since the working principle of the CPS is the major topic of the this thesis, only a short overview is given here, before a detailed account is given later. The CPS is a key component of KATRIN and also one of the most challenging parts. It plays a special role in the tritium safety concept, in particular with respect to tritium retention. The CPS is specified to reduce the residual gas flow coming from the DPS by at least seven orders of magnitude. Again, as in case of the DPS, the unit has to guide signal electrons in the 191 Tcm^2 flux tube adiabatically to the spectrometers [1] [58]. It consists of a vacuum system (roughly 7 m long, inner diameter: ≥ 75 mm) assembled with a 15° chicanery in its centre. There, an argon frost layer will be prepared and cooled down to 3 K with an external cooling station. Incoming neutral tritium will be adsorbed onto the cold surface with a sticking probability of 0.7 [59]. The electrons are guided through the vacuum system by seven superconducting magnets with central fields up to 5.7 T. The magnet safety system inside the closed cryostat must be as reliable as possible. Therefore the magnet protection diodes have been tested in detail, as described in chapter 4.

At the end of the CPS a condensed krypton source, serving as calibration system for the spectrometer, and a semiconductor detector, monitoring the electron flux, can be installed. Both are described in sections 3.3.5 and 3.3.6 .
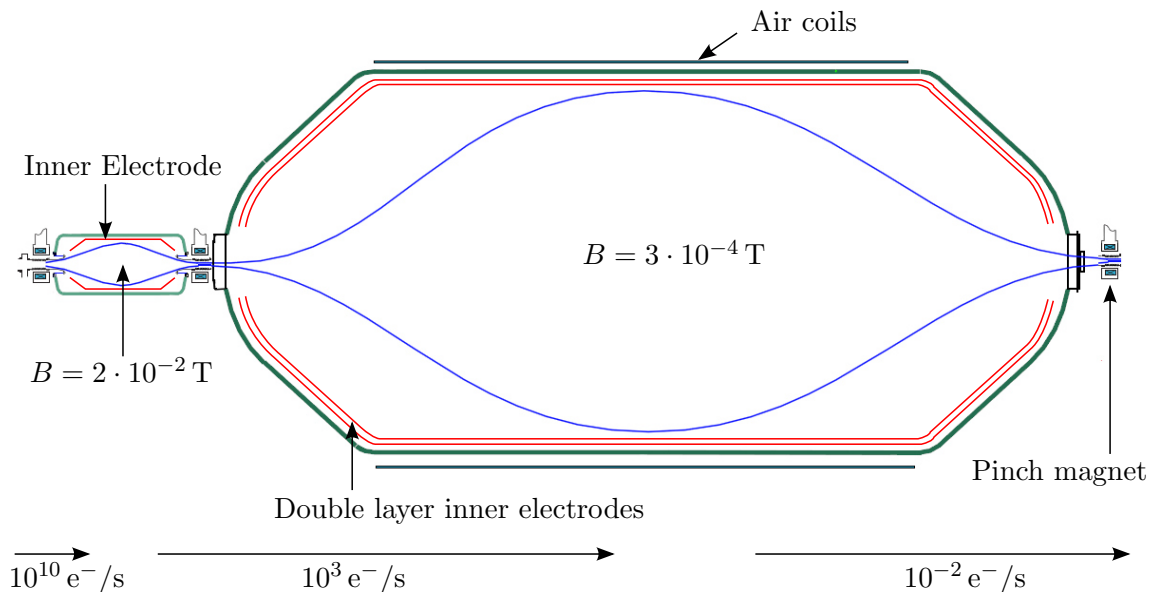
Figure 2.4.: Schematic drawing of the tandem spectrometer. Blue: Magnetic flux tube. Red: Inner electrodes. The magnetic field is reduced by two orders of magnitude in the pre-spectrometer (left), and by four orders of magnitude in the main spectrometer (right).

2.3. Spectrometer and Detector system

In the spectrometer and detector system (figure 2.1 E, F, G), the high-precision β-spectroscopy takes place. This functional unit consists of the pre-spectrometer (section 2.3.2), allowing to be operated as a pre-selection device, and the main spectrometer (section 2.3.3), where the high-precision analysis takes place. Finally, a semiconductor detector (Focal Plane Detector) will count the transmitted electrons (section 2.3.4). Both spectrometers, as illustrated in figure 2.4, are operated as MAC-E Filter, as described in section 2.3.1.

2.3.1. Neutrino mass analysis with a MAC-E-Filter

The KATRIN experiment will analyse the β-decay spectrum (compare figure 2.2) by means of a 23 m long MAC-E filter (Magnetic Adiabatic Collimation combined with an Electrostatic filter), with a diameter of 10 m. This size pushes the MAC-E filter principle to its technological limits. Again electrons are guided adiabatically from the point of entry to the point of exit by a magnetic field. With an electric retarding potential electrons are selected according to their longitudinal energy. Figure 2.5 shows a schematic drawing of the MAC-E filter principle. Two solenoids provide an inhomogeneous, axially symmetric magnetic field which reaches its minimum strength in the centre between both magnet units. The plane where the magnetic field is minimal is called the analysing plane. In general two motions have to be considered, the longitudinal motion, which is parallel with respect to the field lines, and the transversal cyclotron motion, which is, according to Lorentz law, perpendicular to the field lines. The total kinetic energy can thus be described as:

$$E_{\text{kin}} = E_{\parallel} + E_{\perp} \quad . \tag{2.16}$$

Since the magnetic moment μ of the electrons is conserved

$$\mu = \frac{E_{\perp}}{|\vec{B}|} = const. \quad , \tag{2.17}$$

their transversal energy $E_{\perp}$ will be transformed into longitudinal energy $E_{\parallel}$ along the decreasing magnetic field. The minimal field thus defines the maximum longitudinal energy.
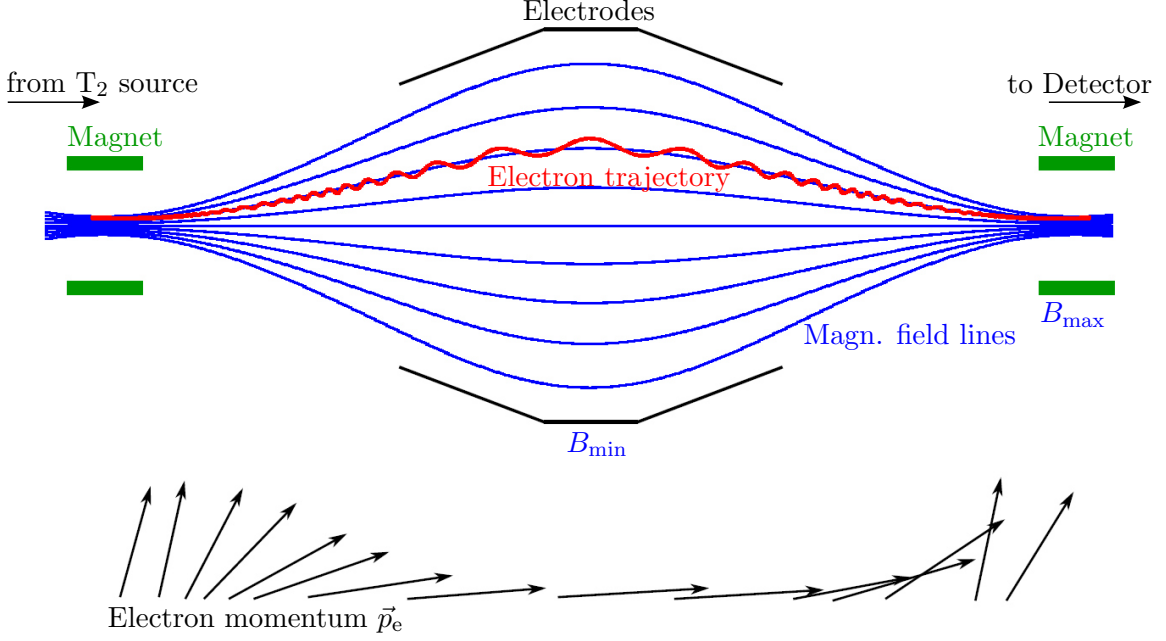
Figure 2.5.: Principle of a MAC-E Filter. Top: Two solenoids (green) provide a magnetic
            guiding field (blue) with its minimum in the centre of both magnets. Electrons
            are guided along the field lines (red). An electrostatic retarding potential is
            used to filter out electrons below the retarding potential. Bottom: Electron
            momentum vector. The transversal component is transformed into the longi-
            tudinal component due to the decreasing magnetic field. Only electrons with
            $E_\perp > q \cdot U$ are transmitted. Based on [1].

The spectrometer vessel walls are set to a negative potential with respect to the grounded
spectrometer entrance. Thus the magnetic guiding field is superimposed by an electric
retarding potential. In the centre of the spectrometer the electric field is directed against
the longitudinal motion of the electrons. The MAC-E filter acts as a high-pass filter, sensi-
tive only to the longitudinal electron energy. In case of a perfect filter only electrons with
$E > q \cdot U$ are transmitted. Since the real filter has a finite resolution

$$\Delta E = \frac{B_{\min}}{B_{\max}} \cdot E_0 \quad , \tag{2.18}$$

the transmission function must be written as:

$$T(E, U) = \begin{cases} 0 & \text{for } E - qU < 0 \\ 1 - \sqrt{1 - \frac{E - qU}{E} \cdot \frac{B_{\min}}{B_{\max}}} & \text{for } 0 \leq E - qU \leq \frac{B_{\min}}{B_{\max}} \cdot E \\ 1 & \text{for } E - qU > \frac{B_{\min}}{B_{\max}} \cdot E \end{cases} \tag{2.19}$$

The resolution for the specifications of KATRIN is $\Delta E = 0.93 \, \text{eV}$.
For the KATRIN assembly, the magnetic mirror effect has to be taken into account, in
particular in case of the huge field variation along the main spectrometer. Only particles
with a maximum acceptance angle $\theta_{\max}$ with respect to the magnetic field lines of

$$\theta_{\max} = \arcsin \sqrt{\frac{B_S}{B_{\max}}} \quad , \tag{2.20}$$

are transmitted to the detector. Here B_S denotes the source field and $B_{\max}$ the maximum
field in the KATRIN assembly (Pinch magnet with 6 T). Electrons, emitted in the source
with an angle greater than $\theta_{\max}$ are reflected back into the direction of the source. The

maximum angle will be $\theta_{\mathrm{max}} = 51.7°$ for the specified magnetic field strengths.

In order to investigate the electron anti-neutrino mass with a sensitivity of $200\,\mathrm{meV}/c^2$, the maximum and the minimum magnetic field strengths of the MAC-E filter were specified, as well as its geometrical dimensions. As mentioned above, the maximum field strength was defined to $6\,\mathrm{T}$, the minimum field strength to $3 \cdot 10^{-4}\,\mathrm{T}$. The maximum inner diameter of the spectrometer, as described in more detail in section 2.3.3, was chosen to $10\,\mathrm{m}$, with respect to mechanical and technical limitations. Taking some safety margin into account, this results in an analysing plane of $A_{\mathrm{A}} = 63.6\,\mathrm{m}^3$ [1], thus defining the magnetic flux tube to a value of:

$$\Phi = \int B dA = B_{\mathrm{min}} \cdot A_{\mathrm{A}} = 191\,\mathrm{Tcm}^2 \quad . \tag{2.21}$$

This value specifies the minimal geometrical dimensions of the vacuum system of all other sections and components of the entire KATRIN assembly.

2.3.2. Pre-spectrometer

The main task of the pre-spectrometer (figure 2.1 E) is to provide a possibility to reduce the electron flux into the main spectrometer from $10^{10}\,\mathrm{e}^-/\mathrm{s}$ to $10^3\,\mathrm{e}^-/\mathrm{s}$, i.e. to filter out those electrons which do no carry information on the neutrino mass. It also works as a high-pass filter, as explained in section 2.3.1. The pre-spectrometer is formed by a roughly $3.4\,\mathrm{m}$ long and $1.7\,\mathrm{m}$ wide vacuum vessel with two superconducting magnets ($4.5\,\mathrm{T}$) at its ends. The vacuum there is created by two TMPs (type Leybold MAG-W 1300) and with about $90\,\mathrm{m}$ of SAES ST707 getter strips providing a pumping speed of $6 \cdot 10^5\,\ell/\mathrm{s}$ for hydrogen. During commissioning measurements a final pressure of $p = 4.8 \cdot 10^{-11}\,\mathrm{mbar}$ was reached [60].
Inside the vessel an electrode system is mounted. It is adjusted to the shape of the vessel and is set to $-18.3\,\mathrm{kV}$. The vessel wall itself is set to a potential of $-18.5\,\mathrm{keV}$. Cosmic particles, like muons, produce electrons when interacting with the vessel walls. These secondary electrons are reflected back to the vessel wall due to the axially symmetric magnetic field, but also due to the potential difference between the vessel wall and the wire electrode system. The pre-spectrometer features an energy resolution (according to equation 2.18) of $\Delta E \approx 70\,\mathrm{eV}$.

2.3.3. Main spectrometer

The main spectrometer (figure 2.1 F) is a much larger version of the pre-spectrometer. It works as a high-pass filter according to the MAC-E principle. It is $23.8\,\mathrm{m}$ long and features an inner diameter of $9.8\,\mathrm{m}$ (central cylindrical part). The inner surface is $690\,\mathrm{m}^2$, the volume $1450\,\mathrm{m}^3$ [61]. It is designed to operate at a pressure lower than $10^{-11}\,\mathrm{mbar}$ [1]. Inside the three pump ports a total of $3000\,\mathrm{m}$ getter strips (SEAS ST707) are mounted. Since 2014, these strips can be baked out electrically and thus be activated directly. The two outer pump ports are equipped with a total of six TMPs (type Leybold MAG-W 2800). In front of each getter pump, a copper baffle is positioned, which is cooled to a temperature of $77\,\mathrm{K}$ with liquid nitrogen. The baffles are designed to adsorb radon, which is mostly emitted from the huge getter pumps, in order to reduce background inside the main spectrometer. More details on radon-induced background are given in [62] [63] [64] and [65].
Inside the vacuum vessel a double layer of wire electrodes is mounted. The electric potential of $-18.5\,\mathrm{kV}$ is typically about $100\,\mathrm{V}$ more negative than the vessel wall. The electrode system helps to reduce, as in case of the pre-spectrometer, the background from cosmic rays. The retarding potential will reduce the signal electron flux to the detector to a value
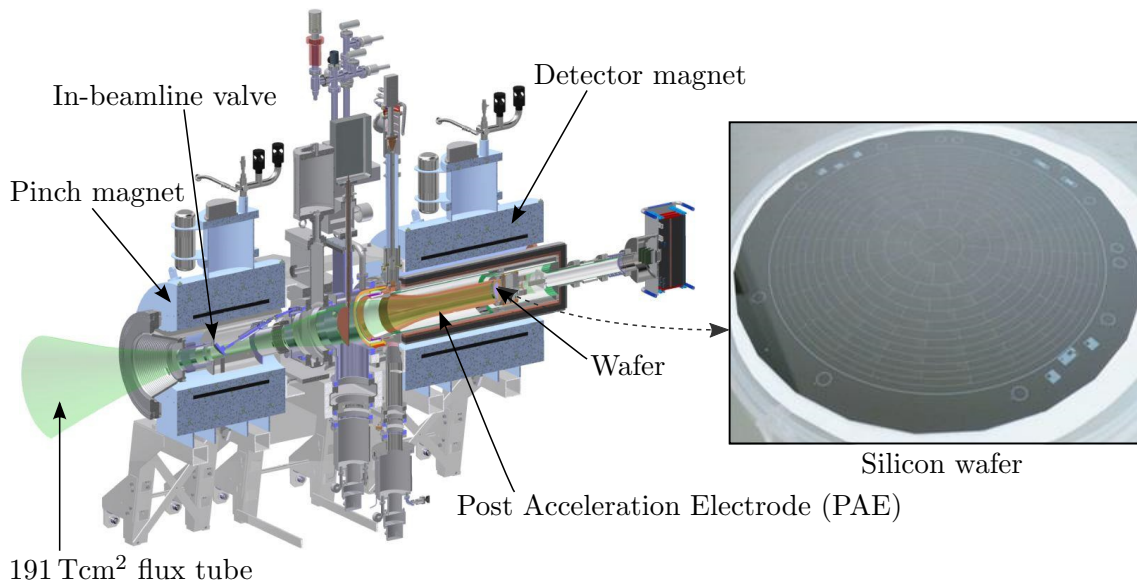
191 Tcm^2 flux tube

Figure 2.6.: Focal-Plane-Detector assembly: The 191 Tcm^2 flux tube is guided into the detector assembly with the Pinch magnet (B = 6 T) and focussed on the silicon wafer with the detector magnet (3.6 T). The signal electrons are accelerated in front of the wafer with the post acceleration electrode (PAE). The wafer itself is a segmented PIN diode with 148 pixels.

of 10^{-2} electrons per second when operating close to the end-point energy. In order to guide the electrons, two superconducting magnets are placed at each end. The first one provides a guiding stray field for the pre-spectrometer as well. The second one, called Pinch magnet, has a maximum field of 6 T thus defining θ_{max}. In the centre of the main spectrometer the magnetic field is reduced to $3 \cdot 10^{-4}$ T. Therefore the resolution according to equation 2.18 is $\Delta E = 0.93$ eV. Air coils are mounted around the spectrometer in order to tune the magnetic field and to compensate the earth's magnetic field.

2.3.4. Focal Plane Detector

The β-decay electrons are analysed with respect to their longitudinal energies when passing the main spectrometer. The target of the down stream Focal Plane Detector (FPD) (figure 2.1 G) is thus to count the transmitted electrons. The detector assembly is shown in figure 2.6. The FPD is detachable from the main spectrometer by an in-beamline valve. The detector system itself is operated in an ultra high vacuum (UHV) chamber with a design value of $p < 10^{-10}$ mbar. The 191 Tcm^2 flux tube is focused on a circular silicon PIN (Positive Intrinsic Negative) diode array (90 mm diameter) by means of a separate detector magnet. The 148 pixels are separated by 50 μm and feature a dead layer of 100 nm [61]. The array is positioned in the centre of the detector magnet with a maximum field of 3.6 T. The custom-made data acquisition system is attached at the back side of the detector, operating in the vicinity of the detector magnet under high vacuum (HV) conditions. The silicon wafer itself is segmented into 148 pixels. These form 12 rings, with 12 pixels each. The centre is formed by four pixels. This assembly allows to track the detected electrons back to their pointed origin inside the WGTS. Thus possible density inhomogeneities of the source can be detected. The detector energy resolution is ≈ 2 eV at an electron energy of 18.6 keV [66], with a detection efficiency of > 0.9. The detector system features a post acceleration electrode in front of the wafer, which can be elevated up to 10 kV, in order to accelerate the decay electrons. This can improve the signal-to-background ratio in the detector region of interest, while also allowing to detect electrons with thermal energies.

One of the biggest challenges is the reduction of background, since the expected signal count rate is 10^{-2} cps (counts per second). Thus the combined spectrometer and detector background rate must be in the same range. In order to differentiate between cosmic signals and β-decay signals in the FPD, a muon veto is installed. The detector system has been commissioned and is described in detail in [66] [67] [68].

2.4. Monitoring and calibration devices

The measurement of a neutrino mass in the sub-eV range requires devices which allow to adequately monitor and calibrate key parameters in order to limit systematic uncertainties. Correspondingly the source activity is monitored by a dedicated component, the rear section. The tritium purity specification as well as the high voltage stability of the main spectrometer are monitored with two external components, the LARA-system and the monitor spectrometer, respectively.

Rear section

The rear section (figure 2.1 A) is a large component located at the rear side of the WGTS. Its task is to monitor the source activity. To do so a gold plated so called rear-wall is installed, where source electrons will produce X-rays. With a custom-made high-resolution solid state detector system this high energy radiation will be monitored. The source activity will be measured over time intervals of $100\,\mathrm{s}$ with a precision of 0.1% [69]. In addition the rear section features an electron gun in order to calibrate the entire KATRIN assembly and to measure the column density of the source. Therefore control magnets and electrodes are implemented. More detail on the set-up and the physics basics can be taken from [69].

LARA-System

With a dedicated laser based Raman system (LARA) the tritium purity is monitored over single time intervals of $60\,\mathrm{s}$. The system is integrated into the inner loop system. It makes use of the inelastic Raman scattering process to determine the gas composition. The laser based LARA system continuously monitors the gas to be injected into the WGTS through vacuum optics. A large body of LARA-related results has already been published, e.g. [70] [71] [72].

Monitor spectrometer

The monitor spectrometer is the smallest MAC-E filter in the KATRIN assembly, however, featuring a precision of $\Delta E = 1\,\mathrm{eV}$ [73] for a small source region. It is formed by the former Mainz spectrometer, a $3\,\mathrm{m}$ long and $1\,\mathrm{m}$ wide vacuum vessel, again featuring a set of electrodes in its inner part. Here the vessel wall is set to ground potential, while the inner electrodes are electrically connected to the high voltage of the main spectrometer. The purpose of the monitor spectrometer is to detect long-term shifts in the high voltage. Therefore it permanently monitors conversion electrons from the transition of ^{83m}Kr to its ground state. To do so, a krypton source is placed at the entrance of the monitor spectrometer. Since the ^{83m}Kr electron energy $(17824.3 \pm 0.5)\,\mathrm{eV}$ [74] is slightly smaller than the tritium end-point energy, the krypton source has to be set to a non-zero potential. By varying the source potential, the transmission function and thus the K32-line position can be determined. Line shifts over time are an evidence for high voltage instabilities. More details are given in [73] and [75].

2.5. Sensitivity and Uncertainties

The KATRIN experiment will require extremely low systematic uncertainties over the entire measuring time of five calendar years. The key parameters with regard to systematics are the source activity, the energy resolution inside the spectrometer, and the background rate at the detector. The origin of systematic uncertainties is listed below:

Source related uncertainties

Most systematics are related to the source. These include:

- **Final states distribution:** This is the largest contribution to the uncertainty budget. Decaying tritiated molecules (HT, DT, T_2) can leave the daughter nucleus ($^3HeH^+$, $^3HeD^+$, $^3HeT^+$) in an exited electronic final state and/or in excited vibration and rotational final states. These effects will shift the detectable electron end-point energy down to lower values [76].

- **Electron scattering:** Signal electrons can scatter elastically or inelastically off residual gas. These scattering effects are the second major contribution of uncertainties. The scattering cross sections are rather small (of the order of $10^{-18}\,cm^{-2}$, and less for 18.6 keV electrons [77]) but not negligible. Since scattering effects are unavoidable, they have to be at least constant in time.

- **Doppler broadening:** Since the tritium molecules propagate with thermal velocities in the source, their non-vanishing field causes a spectral broadening by the Doppler effect.

The Doppler related uncertainties are temperature-dependent, while the electron scattering depends on the integrated column density (amount of gas). In order to reduce these systematic effects as much as possible, the tritium source is cooled down to a level of 30 K, which has to be stabilised at the 10^{-3} K level. As the column density has to be stabilised on the 10^{-3} level as well, a constant inlet pressure is of utmost importance. Finally, a tritium purity of $> 95\%$ should be provided.

In the past, complex simulation packages have been developed to take into account all systematics. These simulations include the tracking of electrons through the entire set-up including the emission of synchrotron radiation and interactions of electrons with the residual gas, elastic scattering, electronic excitation, and collisions with ionisation. In addition the final states distribution, the Doppler broadening, and the scattering in the source are taken into account [48] [49] [76] [78].

Spectrometer related uncertainties

Beside source-related effects, the high voltage stability plays an important role. It has to be stabilised at the 10^{-6} V level in order to reach the KATRIN goal [61]. The spectrometer and detector sections are a considerable source of background effects, if the source and transport section operates within specifications:

- **Cosmic muons:** These particles produce secondary electrons, when interacting with the main spectrometer vessel walls. The resulting low-energy electrons are reflected back onto the vessel wall by the axially symmetric magnetic field, and to a lesser extent by the inner electrode system, whereas high-energy electrons can pass this inner potential barrier [79].

- **Ionisation of residual gas:** Even though the pressure inside the main spectrometer is less than 10^{-11} mbar, stored high-energy electrons can ionise residual gas particles. The tertiary electrons and ions can than propagate to the detector.

- **Stored electrons:** If electrons are stored in electric or magnetic Penning traps in a spectrometer region they can produce a large number of charged particles by ionisation. Due to the excellent UHV conditions, the mean storage time of trapped particles can be in the order of hours [61].

- **Radioactive decay:** The main source of primary electrons in the inner volume of the spectrometer arises from radioactive decays of ^{219}Rn and ^{220}Rn, and, potentially, from T_2 inside the spectrometer. The tritium flow from the source to the spectrometer thus must be suppressed by 14 orders of magnitude. The radon-induced background has its origin in the large getter pumps of the main spectrometer, as well as the vessel walls. The material emits small amounts of different radon isotopes. With a liquid nitrogen baffle in front of each pump the radon will be pumped out. [64] [80]

- **Detector background:** Cosmic muons, as well as intrinsic radiation following radioactive decays from the detector material leads to background. The required overall background count rate must be less than 10^{-2} cps.

The limit for the quadratic sum over all known systematic uncertainties is $\sigma_{\text{sys, tot}} = 0.017\,\text{eV}^2/c^4$ [81]. Within three 'full beam' years of operation, the expected statistical uncertainty will be of the same order $\sigma_{\text{stat, tot}} = 0.018\,\text{eV}^2/c^4$ [81]. Both parameters will lead to a total uncertainty for the KATRIN experiment of $\sigma_{\text{tot}} = 0.025\,\text{eV}^2/c^4$ at 90% C.L. [61]. Thus KATRIN can determine a neutrino mass of $m_\nu = 350\,\text{meV}/c^2$ at $5\,\sigma$. In case of no spectral distortion, a new upper mass limit for the neutrino mass of $m_\nu \leq 200\,\text{meV}/c^2$ (90% C.L.) will be established [61].

3. Tritium Retention of the Transport Section and its instrumentation

The main focus of the present thesis is on the KATRIN transport section, consisting of the differential and the cryogenic pumping section. The two main units have already been briefly outlined in the previous chapter 2. Here, they will be discussed in detail in sections 3.2 (DPS) and 3.3 (CPS). Theoretical studies on the specifications and the general design of both components are presented there. The raison d'être of the transport section is the reduction of the tritium flow from the WGTS by at least 14 orders of magnitude. Two orders of magnitude are expected to be achieved after the first stage, the DPS1-F, which is integrated into WGTS cryostat. A further five orders of magnitude is the design target for the DPS, while the missing seven orders of magnitude are the challenge for the CPS. The mass flow of tritium at the end of the CPS is specified to be less than 10^{-14} mbar ℓ/s [1]. Details about background effects, caused by tritium, can be taken from [65]. The main principles of vacuum generation, pumping, and pressure measurements are described in section 3.1.

Inside the DPS also the critical task of ion suppression will take place. Ions are produced during the interactions of electrons from tritium β-decay. These ions will be guided, as well as the signal electrons, towards the spectrometer, where they would produce significant levels of background during the neutrino mass measurements [57]. An analysis of the existing ion species was already given in section 2.2.1, now an ion retention system is introduced in section 3.2.4.

3.1. Basics of vacuum technology and vacuum simulations

Vacuum is in general defined as a pressure inside a system which is lower than 300 mbar. It is usually subdivided into five ranges, as listed in table 3.1. The different vacuum conditions can be reached by various types of vacuum pumps. The most commonly used are described in section 3.1.1. The different vacuum conditions provide different gas flow behaviours. Particles in a closed system interact either with other particles (viscous flow regime) or with the vacuum vessel walls (molecular flow regime), depending on their mean free path:

$$\bar{l} = \frac{k_B T}{\sqrt{2} \cdot \pi \cdot d^2} \cdot \frac{1}{p} \quad , \tag{3.1}$$

with the Boltzmann constant k_B and the particle diameter d. In the viscous regime properties such as heat transfer, gas flow angular/velocity distributions, etc. are formed by the

Table 3.1.: Subdivision of vacuum and its corresponding pressure and mean free path conditions [82].

Pressure range	Pressure (mbar)	Mean free path (m)
Low vacuum	$300 > p \geq 1$	$10^{-8} < \bar{l} \leq 10^{-4}$
Medium vacuum	$1 > p \geq 10^{-3}$	$10^{-4} < \bar{l} \leq 10^{-1}$
High vacuum (HV)	$10^{-3} > p \geq 10^{-7}$	$10^{-1} < \bar{l} \leq 10^{3}$
Ultra high vacuum (UHV)	$10^{-7} > p \geq 10^{-12}$	$10^{3} < \bar{l} \leq 10^{8}$
Extra high vacuum (XHV)	$p < 10^{-12}$	$\bar{l} \geq 10^{8}$

particle flow itself, whereas in the molecular flow regime these properties are determined by the vacuum system design. Both regimes are distinguished by the dimensionless Knudsen number K_n:

$$K_n = \frac{\bar{l}}{d_s} \quad , \tag{3.2}$$

with the mean free path $\bar{l}$ and the diameter of the vacuum system d_s:

- Molecular flow: $Kn > 0.5$

- Knudsen / transitional flow: $0.5 > Kn > 0.01$

- Viscous flow: $Kn < 0.01$

The molecular flow is predominantly observed in the XHV and UHV regime and partially for the HV conditions, while the viscous flow is predominantly observed in the low vacuum regime. The latter shows a deeper structure. The gas flow can be either laminar or turbulent or blocked. For more details see [82] [83]. The medium vacuum range is dominated by a mixture of particle-particle and particle-wall interactions.

An important parameter, when designing a vacuum system, is the conductance of a component. The conductance is defined as the amount of gas flowing through a component per unit time interval:

$$C = \frac{q_{pV}}{\Delta p} \quad , \tag{3.3}$$

with the pV-flow rate $q_{pV} = pV/t$ and the pressure difference along the component Δp. For the molecular flow regime the conductance can be calculated with [83]:

$$C = C_B \cdot P = \frac{1}{4} \cdot \bar{c} \cdot A \cdot P \quad , \tag{3.4}$$

where $\bar{c} = (8RT/(\pi M))^{-1/2}$ denotes the mean velocity according to the Maxwell-Boltzmann distribution, with the universal gas constant R, the gas temperature T, and the molar mass M. The parameter A denotes the entrance surface and P the transmission probability. The conductance is defined in two different ways. It is subdivided into the built-in and the stand-alone conductance.

- The **Built-in conductance** is defined as the conductance of a component in a larger assembly. Its value depends on the geometry of the components around the region of interest. When gas flows for example through a tube, it forms a flow profile. Depending on the geometry, this profile can be significantly peaked forward. The strength of this peak depends on the ratio between length and diameter [84]. By calculating the built-in conductance, the incoming gas flow with its particular angular distribution has to be taken into account, as well as backscattering from the component which is located behind the component of interest.

- The **Stand-alone conductance** is defined as the conductance when the component of interest connects two large vessels. Here, large means that the conductance of each vessel is much higher than the one of the connecting component. As a result, this parameter describes a component-characteristic quantity. In such an assembly, the incoming gas flow follows a cosine-like angular distribution, such as the one of Lambertian emitters [83] [85]. The backscattering effect is defined to be zero, hence the conductance is independent of the components in front of and behind the one of interest.

For an assembly of normal tubes in series, each characterised by a stand-alone conductance of C_i, the total conductance can be calculated with the approximated formula [83]:

$$\frac{1}{C_{\text{tot}}} = \sum_i \frac{1}{C_i} \quad . \tag{3.5}$$

For an assembly of normal tubes in parallel, the total conductance is given by [83]:

$$C_{\text{tot}} = \sum_i C_i \quad . \tag{3.6}$$

Within the molecular and the viscous flow regime, conductances can be calculated very precisely as a function of temperature, via experimental observations and numerical simulations. The basics of vacuum simulations in the molecular flow regime are given in section 3.1.2. Nevertheless, within the transitional flow regime, only rough estimations are possible when determining the flow properties of a vacuum system/component. Even with experimental observations, no simple models exist which can describe temperature-dependent flow rates, conductances, transport phenomena, etc. in a precise way.

Along the extended vacuum system of the KATRIN beam line, both the transitional and the molecular flow regime can be found. The medium vacuum will be predominant in the tritium source (transitional flow). Simulations and analysis for this specific geometry are under investigation in [48]. Between the differential pumping section (DPS) and the focal plane detector the vacuum pressure will decrease to nearly XHV conditions.

3.1.1. Vacuum generation and vacuum measurements

This section gives an overview of commonly used vacuum pumps and gauges at the KATRIN experiment and at the test set-ups used in the framework of the underlying thesis. These include turbo molecular pumps (TMPs), scroll pumps, roots pumps, and cryopumps, as well as hot and cold cathode gauges, Pirani gauges, capacitive gauges, and residual gas analysers (RGAs).

Mechanism of vacuum pumps

Turbo molecular pumps (TMPs) are used to generate and to maintain high vacuum conditions or better. They are purely mechanical pumps. TMPs consist of a stacking of fast spinning, tilted, metallic (aluminium-steel-alloy) rotor blades which rest on stator blades, as illustrated in figure 3.1. Particles, when hit by a supersonically spinning rotor blade, will be reflected forwards onto a tilted stator blade. Caused by the tilt, the most probable desorption direction is pointing onto the next rotor stage, and so on. This pumping mechanism leads to a final pressures less than 1.0×10^{-9} mbar. The pumping speed of a specific TMP depends on the gas species, especially on their different velocities for a given temperature. The final pressure is limited by the gaps in the TMP assembly and by the process of back-diffusion. Some TMPs feature a Holweck stage, which is a pre-stage
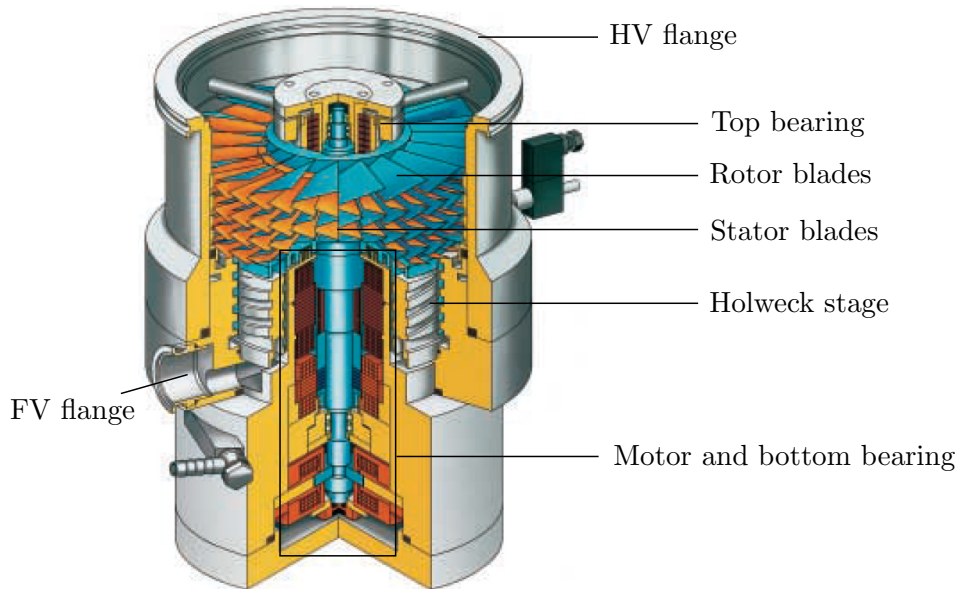
Figure 3.1.: Assembly of a turbo molecular pump. Blue: Rotor with shaft, rotor blades, and Holweck stage. Orange: Stator blades. FV = forevacuum, HV = high vacuum. The picture is taken from [86].

behind the rotor blades, spinning with the same velocity as the rotor itself. It is formed by a cylinder with spiral grooves connecting the last rotor stage with the forevacuum. It allows a higher gas throughput. Depending on the size of the pump, it can have a magnetic, a ceramic, or a hybrid (combination of both) bearing of the rotor.

When operating turbo molecular pumps in magnetic fields, some boundary conditions have to be considered. Pumps with a magnetic bearing will fail if the external magnetic field parallel to the rotor axis increases above a pump-specific value. This value depends on the mounting position of the pump and the direction of the field (parallel or anti-parallel to the rotor axis). The field limits have to be determined for each pump individually [87] [88] [89]. For TMPs with a ceramic bearing this point is not an issue. When operating a TMP in a magnetic field (either inhomogeneous or with a field component perpendicular to the rotor axis), eddy currents are induced into the fast spinning rotor, which causes a heating of the rotor. The maximum rotor temperature must not exceed a specific value, which is, for most of the TMPs used at the KATRIN experiment, limited to 90°C. The behaviour of different turbo molecular pumps in magnetic fields perpendicular to their rotor axis and the modelling of the rotor temperature have been investigated and measured in detail in [87] [88] [90] [91] [92] [93].

TMPs can be operated in vacua better than 10^{-3} mbar, thus they need a backing-pump to provide an adequate forevacuum. In general these backing-pumps belong to the class of displacement pumps. The most common type used at the KATRIN experiment are **scroll pumps** and **roots pumps**. Both operate with the same principle. They consist of one (scroll pump) or more (roots pump) rotating parts, with only tiny gaps between each other. During rotation the moving parts form a closed volume at the vacuum end. This volume is guided to the forevacuum end (commonly the atmosphere). On its way it is compressed and opened again at the forevacuum end. Figure 3.2 shows the pumping principle using the example of a roots pump. Both pump types (scroll and roots pump) feature the advantage of a huge throughput of several cubic metres per hour. They can provide a vacuum pressure in the order of 10^{-3} mbar against atmosphere, limited only by the gaps between the moving parts.
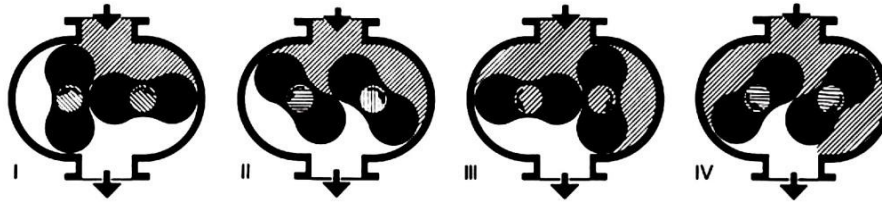
Figure 3.2.: Working principle of a roots pump. The pistons rotate in opposite directions. I: Inlet of gas from the vacuum end. II: Sealing the gas in a volume. III: Compressing the volume and guiding it towards the forevacum end. IV: Discharging the sealed gas volume into the forevacuum (atmosphere). Taken from [83].

Two other important types of pumps are getter pumps and cryopumps. Since these units are the main topic of the underlying thesis, they are described in more detail in chapter 6 and chapter 7.

Pressure and partial pressure measurements

There are two ways of measuring pressure inside a system: direct and indirect. The direct measurement is independent of the specific kind of gas, whereas the indirect measurement is influenced by different gas species. The whole vacuum range to be measured includes 15 orders of magnitude. Evidently, there is no pressure gauge which can measure the entire range. Thus, always a combination of different gauges is necessary to monitor the pressure of a system between atmospheric and (extra high) vacuum pressure. Very precise instruments, which are independent of the gas species are formed by **capacitive gauges**. They consist of a capacitor with one static plate and one dynamic plate, commonly a ceramic membrane. The membrane seals the second capacitor plate from the vacuum system. It is pushed towards the static plate when it is hit by residual gas particles. This changes the capacitance of the gauge. The change in capacitance is proportional to the amount of gas inside the system and hence proportional to the vacuum pressure. Capacitive gauges can be used from atmospheric pressure down to 10^{-6} mbar, with a precision of 0.01% full scale range [83]. This type was used in the test set-up during determination of the argon capillary conductance described in chapter 5.

With **Bayard-Alpert** (hot cathode) gauges a pressure range from 10^{-3} mbar down to 10^{-13} mbar can be measured [82]. They consist of an emission cathode, an acceleration electrode, and an ion collector. Emitted electrons from the hot cathode are accelerated onto the anode. On their way they ionise the residual gas. The ions are accelerated towards the ion collector. The measured ion current is proportional to the gas density and hence to the pressure. Gauges following the Bayard-Alpert principle are almost linear in pressure, but since they are based on gas ionisation, they depend on the residual gas species inside the vacuum via the individual cross sections of ionisation. These gauges have been used to determine the sticking coefficients of the NEG pumps of the CPS in a dedicated test set-up, as described in chapter 7.

Descriptions of other pressure-measuring devices, such as the Pirani sensor, or the inverted magnetron unit, can be take from literature [82] [83] [94].

In order to analyse the gas composition inside the vacuum, a **residual gas analyser (RGA)** is used. It consists of two parts, namely a Quadrupole-Mass-Spectrometer (QMS), and a detector. The QMS is an assembly of four electrodes (long cylindrical tubes) which are positioned parallel to each other at the edges of an imaginary square. At one end, the residual gas is ionised by emitted and accelerated electrons. The gas ions are accelerated along the electrode assembly. An electric quadrupole field is generated with the four electrodes, as well as an alternating field, forcing the ions to move in helically trajectories. If the amplitude of this movement is less than the field radius, the ions reach the detector. The amplitude of movement, or ion mass respectively, is proportional to the electrode voltage at constant frequency of the alternating field. The residual gas can therefore be analysed by variation of the electrode voltage. The transmitted ions are detected with a Faraday cup or a Secondary Electron Multiplier (SEM). The Faraday cup measures and amplifies the incoming ion current. It is approximately linear in pressure (ion current). The SEM uses an array of dynodes. Ions hitting a dynode will release a couple of secondary electrons which are accelerated onto the next dynode, were they release again more electrons and so on, so that an electron avalanche is detected. The SEM is more sensitive than a Faraday cup, but it is not linear in pressure. Residual gas analysers, in the Faraday mode, have been used to determine the sticking coefficient of the CPS NEG pump (see chapter 7).

3.1.2. Gas flow simulations in high vacuum systems

In the high vacuum regime particles do not further interact with each other, but only with the walls of the vacuum chamber. Thus all properties, such as thermal velocity, heat transfer, pressure, etc. are determined by the vacuum chamber itself, which means by its design. In the present thesis two simulation programs have been used in order to determine physical properties within the molecular flow regime, namely MolFlow+ (Version 2.4.1) and COMSOL Multiphysics (Version 4.4).

Vacuum simulations with MolFlow+

MolFlow+ is a Monte-Carlo based, free software tool, developed at CERN [95], to calculate the isothermal gas flow in the molecular flow regime. Any geometry can be simulated there. To do so, no volume elements exist, as only surface elements are defined, called facets. These polygon facets form the surface of the vacuum system. If the edges of two neighbouring polygons do not exactly fit each other, leaks might occur. On each facet a set of properties can be defined, including desorption, adsorption (given by a sticking factor or directly by a pumping speed), opacity, and so on. Particles can be desorbed with a pre-defined angular distribution. Such a particle is tracked through the vacuum system until it is adsorbed (pumped) or in the worst case eliminated after hitting a leaky facet connection. When the particle hits a facet without adsorption, it is reflected with a cosine-like angular distribution. Only after adsorption (and leakage), the next particle is desorbed and tracked. The more facets are needed to built the geometry, the longer it will take to track a gas particle until it is removed from the simulation (adsorbed). Tiny and complex geometries extend the tracking time and thus the simulation time as well. The software counts the hits of all tracked particles on every facet.

Transmission probabilities through a system and relative pressures can be determined by the ratio of hits on two different facets. When calculating relative pressures the facet surface has to be taken into account. The statistical uncertainties can be improved by running long-term simulations. Counting a number 10^4 hits on a facet will lead to an uncertainty of 1%. Since MolFlow+ does not include any time information only stationary solutions within the statistical uncertainties can be simulated. Nevertheless, it provides an easy and quick way to analyse isothermal, non-complex vacuum systems.

Vacuum simulations with COMSOL Multiphysics

COMSOL Multiphysics is a commercial software tool [96] featuring a complex set of different modules in order to simulate various physical problems with the finite element method (FEM). The 'free molecular flow' module (fmf) includes simulations in the molecular flow regime. Vacuum systems of any geometry can be simulated. In general, geometries in COMSOL consist of volumes and surfaces, however, for the molecular flow simulations only surfaces are taken into account. After designing the vacuum system, a set of properties can be defined on a surface including gas flow, vacuum pumps, reservoirs (which corresponds to an buffer with constant pressure), etc. The simulation package includes the dependency between gas flow and temperature. By coupling different modules the molecular flux can be combined with heat transfer phenomena, for example.
Calculations in COMSOL are performed via the angular coefficient method. Therefore the entire geometry has to be discretised by a mesh into small elements of triangular or quadrangular shape. Subsequently the incident flux on each surface is calculated by summing up the flux arriving from all other surfaces in the line of sight [96]. All physical properties, such as the pressure, can be derived from the incident flux. A detailed description of the variables and equations used in the 'free molecular flow' module is given in section 5.3. In COMSOL the time is implemented as a parameter, so that time-dependent simulations, as well as stationary problem can be performed.

MolFlow+ yields isothermal, relative pressure ratios and transmission probabilities, whereas COMSOL yields relative and absolute pressures but no transmission probabilities, which have to be calculated out of the determined flux. The angular coefficient method requires more computational power, but significantly less time when simulating more complex vacuum systems. Within this thesis the most adequate software tool was used, according to the underlying problem.

3.2. Differential Pumping Section

The differential pumping section (DPS) is the first stage of the KATRIN transport section. It is designed to reduce the tritium flow from the source to the spectrometer by five orders of magnitude [1]. The 6.5 m long component is built up in a modular system. Figure 3.3 illustrates the differential pumping section. The vacuum system is made out of five approximately one metre long single tube segments (called beam tubes) with an inner diameter of at least 100 mm. They are arranged in an Ω-like shape forming a chicane, with an angle of 20 degrees to each other. Four pump ports are located at the connection points between the beam tube elements. They can be approximated as simple cylinders, with 322 mm in diameter and roughly 715 mm in length. The beam tubes are fixed to the pump ports in the upper half. At the lower end of each cylinder, a gate valve, a bellow and a turbo molecular pump (TMP) are mounted. Each TMP of type MAG-W 2800 manufactured by Leybold features a pumping speed of about $2100\,\ell/s$ for hydrogen [97] and roughly $2400\,\ell/s$ for tritium. More details on the pumping principle are given in section 3.2.1. The efficiency of the differential pumping section is simulated in section 3.2.2.
Five stand-alone magnets, each with a maximal centre field of 5.5 T, guide the signal electrons through the vacuum system, from the WGTS to the CPS. The magnets are assembled in coaxial alignment to the vacuum system. The beam tubes are positioned in the warm bore of the magnets. Installation of the magnet modules and first measurements on the magnetic field are ongoing in the framework of a master thesis [98].
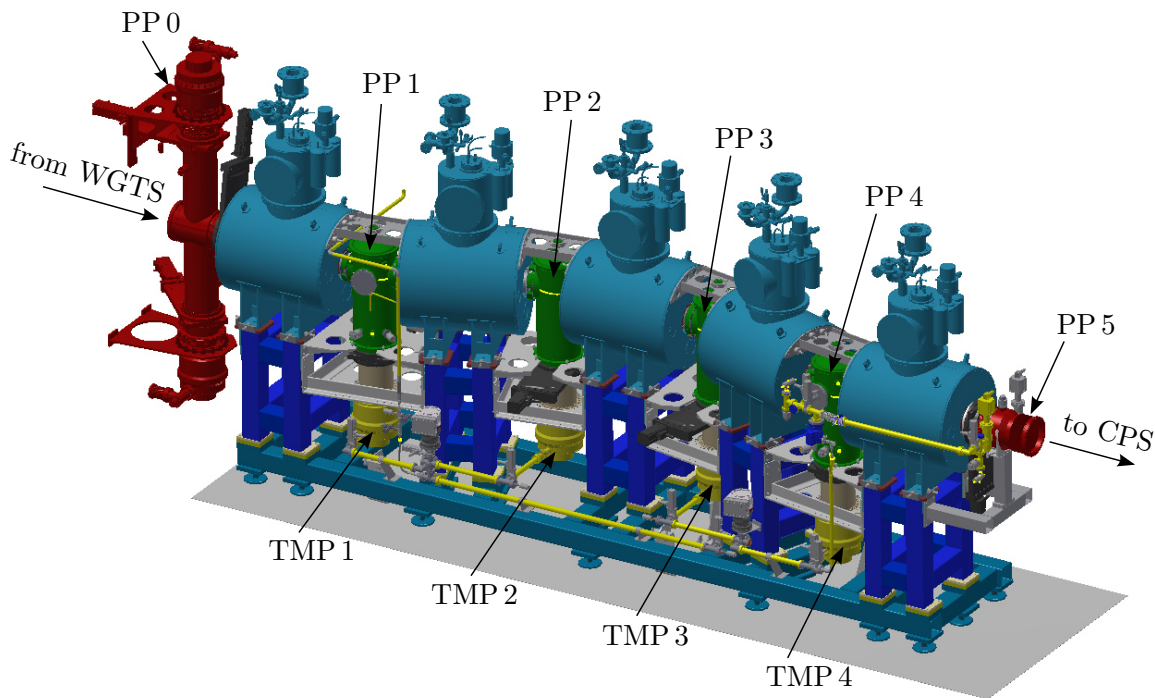
Figure 3.3.: DPS assembly. Red: Connection to the WGTS pump port 0 (PP 0) and to the CPS PP 5. Light blue: Magnets. Green: Pump ports (PP) 1-4. Yellow: Turbo molecular pumps (MAG-W 2800). The beam tubes are inside the magnets and cannot be seen here.

3.2.1. Pumping principle of the DPS

The DPS vacuum system consists of five 980 mm metre long beam tube segments, connected via four pump ports, as mentioned above. The beam tubes are tilted with an angle of 20° to each other. The tilting avoids direct gas beaming effects from the KATRIN source into the spectrometer. At each pump port a Leybold MAG-W 2800 TMP is installed. These TMPs have a final pressure of 1.0×10^{-10} mbar and a compression ratio of 1.0×10^9 [97]. They offer a pumping speed of approximately $2400\,\ell/s$ for tritium, calculated by J. Wolf [99]. Since TMPs cannot run against atmospheric pressure, an adequate forepump is necessary.

The TMPs are located 1040 mm below the centre of the beam tube. Hence they will be operated in the stray fields of the superconducting magnets. As described in section 3.1, the operation of TMPs in strong magnetic fields might lead to overheating by induced eddy currents or to a failure of the magnetic bearing. Since the MAG-W 2800 has a pure magnetic bearing, its behaviour in external magnetic fields has been investigated (see [88]). Magnetic fields running parallel / antiparallel to the rotor axis forces the 11.4 kg heavy rotor, with full spinning velocity (480 Hz), to drop into a ceramic emergency bearing. Parallel here describes a field pointing from the forevacuum flange to the high vacuum flange. Table 3.2 summarises the limits of the MAG-W 2800 magnetic bearing. These performance limits are an artefact of magnetic bearings, since other TMPs, such as the MAG-W 2200 [87] or the MAG-W 600 iP [69], show a similar behaviour with different, specific limits.

The stray fields of the DPS magnets contain a perpendicular component at the TMP position. If conducting materials, such as the rotor, are moving (spinning) in a constant magnetic field, eddy currents will increase the rotor temperature. The TMP is running safely as long as a specific temperature is not exceeded. For long-term operation of the TMPs in use here, this limit amounts to 90°C. The behaviour of different TMPs in magnetic fields perpendicular to their rotor axis and the modelling of the rotor temperature

Table 3.2.: Magnetic field limits of the MAG-W 2800 magnetic bearing. "Parallel" describes magnetic fields pointing from the forevacuum flange to the high vacuum flange. In the upright mounting position, the high vacuum flange is on top.

Mounting direction	Field direction	Max. magnetic field
Upright	parallel	12.5 mT [88]
	anti-parallel	15.7 mT [89]
Upside down	parallel	21.2 mT [88]
	anti-parallel	18.8 mT [89]
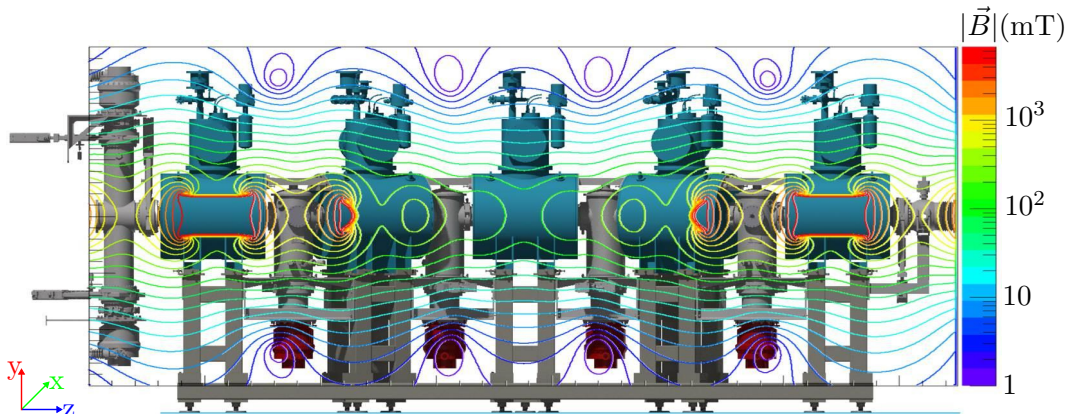
Figure 3.4.: DPS stray fields in the y-z plane. Under normal DPS operation conditions, the TMPs will run in a magnetic field up to 5 mT. The stray fields will increase if one single magnet will quench. Thanks to R. Combe for the magnetic field calculations.

have been previously investigated by the author and measured in detail in [87] [88] [90] [91] [92] [93]. Hereby, [88] focuses on the turbo molecular pumps of the DPS. A maximum perpendicular magnetic field of 3 mT was determined to not exceed 90°C. Figure 3.4 shows that each TMP is exposed to magnetic fields higher than this given limit. An adequate shielding is therefore essential to guarantee safe operation. Shieldings for turbo molecular pumps have been investigated in [89] [100] [101]. A cylindrical shielding out of common ST-37 steel, 10 mm in thickness, appears to be sufficient to guarantee a magnetic field less than 3 mT. A detailed analysis and the final design of the shield are under preparation. Adequate shielded TMPs must guarantee a gas flow reduction of five orders of magnitude, as specified for the differential pumping section. This challenging efficiency number is simulated in the next section 3.2.2.

3.2.2. Simulation of the tritium retention inside the DPS

The transmission probability and hence the reduction factor of the stand-alone DPS unit has been simulated with MolFlow+. For a definition of the stand-alone conductance, transmission probability respectively, see section 3.1. The vacuum system of the DPS, excluding pump port 0 and 5, has been implemented in MolFlow+ by M. Krause. Figure 3.5 shows the model with all necessary definitions. The basic model includes the five beam tube sections with DN 250 flanges at both ends, the four pump ports, and the bellows at the beam tube - pump port connections. The bellows, which separate the turbo molecular pumps from the pumping chambers, have been approximated by a cylinder with equal conductance. The basic model does not include any beam tube instrumentation such as the ion detection system (FT-ICR, see section 3.2.3) or the ion reduction system (dipole
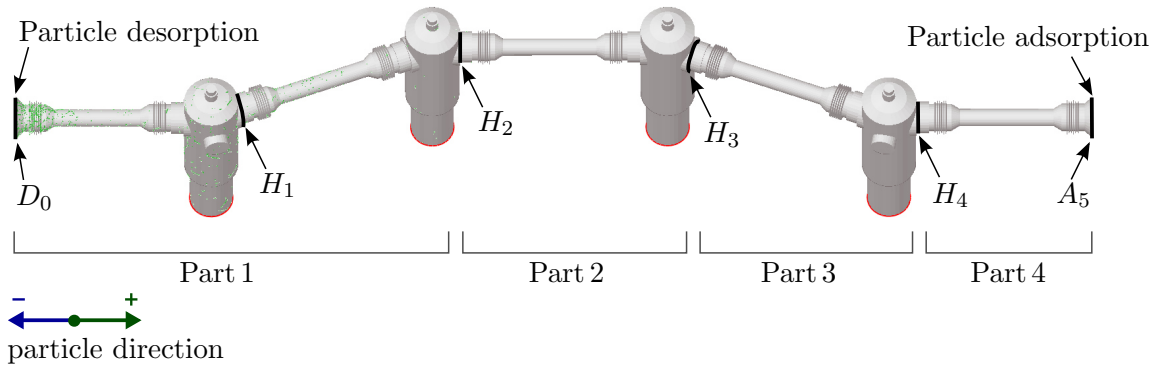
Figure 3.5.: Model of the DPS vacuum simulation in Molflow+. The black lines mark surfaces inside the beam tube elements. At the red facets turbo molecular pumps have been defined. There are two directions the particles move in, either from the desorption facet to the adsorption one (+ direction) or the opposite way (- direction).

electrodes, see section 3.2.4), hence the basic simulation aims to obtain the 'bare' DPS reduction factor only. The instrumentation has been implemented in a second, extended model. This extended simulation aims to give the fully equipped DPS reduction factor.

The basic principle of this simulation is to start particles with a cosine-like angular distribution at the inlet flange (left end in figure 3.5), and to track them through the entire geometry. The reduction factor is then simply given by the ratio between the number of particles reaching the end flange (right end in figure 3.5) and the number of desorbed particles. To get a statistical uncertainty of less than 1%, at least 10^4 hits at the outlet of the DPS have to be counted. With an expected design reduction factor of 10^5, at least 10^9 particles have to be tracked through the geometry until they are adsorbed, either at the facets, representing the turbo molecular pumps, or at the outlet / inlet. By definition, according to the stand alone conductance, the outlet and inlet must have a sticking factor which is equal to a pumping probability of unity.

In order to shorten the simulation time, the DPS has been simulated in sections. Therefore the geometry has been subdivided into four virtual parts, bounded by six facets given by the definitions in figure 3.5. Each of these analysing surfaces consists of a pair of facets, with equal dimensions and positions, but opposite orientation of the surface normal. When defining each of these to a different structure (for definition see MolFlow+ users guide [85]), it is possible to count only particles passing through the facet against the direction of its normal vector. Hence the combination of such identical facets gives the number of particles at a specific position inside the geometry, that move from left to right (+ direction), and from right to left (- direction).

The basic idea of calculating the overall transmission probability is by using the following identity:

$$P_{tot} = \prod_i P_i = \frac{H_{2+}}{D_{0+}} \cdot \frac{H_{3+}}{H_{2+}} \cdot \frac{H_{4+}}{H_{3+}} \cdot \frac{A_5}{H_{4+}} = \frac{A_5}{D_{0+}} \quad . \tag{3.7}$$

P_i describes the single pseudo-probability for one section. The indices + and - separate between particles passing through the facets D_0, H_2, H_3, H_4, and A_5 in the + or the - direction. The single ratios are called pseudo-probabilities, since back- and forth-scattering effects are taken into account and hence ratios greater than one can occur.

For each simulation part, the desorbing facet has been shifted towards the section of interest. Even in case of the molecular flow regime, which is given inside the DPS, a gas flow profile occurs. The longer a tube is, the more forward peaked the gas profile is at constant radius [84]. Since the angular distribution of the gas inside the DPS is unknown,

Table 3.3.: Settings for the DPS reduction factor simulation (basic and extended version). For the definitions of the single facets see figure 3.5. In the general settings of MolFlow+ a particle mass of 6 g/mol was chosen.

Part	Section of interest		Desorption	Adsorption
	Inlet facet	Outlet facet	(cosine)	($\alpha = 1$)
1	D_0	H_2	D_0	D_0, A_4
2	H_2	H_3	H_1	H_1, A_4
3	H_3	H_4	H_2	H_2, A_4
4	H_4	A_4	H_3	H_3, A_4

Table 3.4.: Simulation results for the DPS transmission probability. The parts have been defined in table 3.3. The hits on the different facets in the + direction are listed as "Counts through". Basic simulation means without instrumentation, extended means with instrumentation.

Part	Counts through		Leaks	Ratio P	Uncertainty	
	Inlet	Oulet		(outlet/inlet)	σ_P	Δ_P
Basic simulation						
1	8100739	78831	778	$9.73 \cdot 10^{-3}$	$3.47 \cdot 10^{-5}$	$9.60 \cdot 10^{-5}$
2	584859	78034	25	$1.33 \cdot 10^{-1}$	$4.78 \cdot 10^{-4}$	$4.27 \cdot 10^{-5}$
3	748814	99235	370	$1.33 \cdot 10^{-1}$	$4.21 \cdot 10^{-4}$	$4.94 \cdot 10^{-4}$
4	829001	40365	0	$4.87 \cdot 10^{-2}$	$2.42 \cdot 10^{-4}$	0.00
Extended simulation						
1	9042184	50942	658	$5.63 \cdot 10^{-3}$	$2.50 \cdot 10^{-5}$	$7.28 \cdot 10^{-5}$
2	464988	51462	13	$1.11 \cdot 10^{-1}$	$4.88 \cdot 10^{-4}$	$2.80 \cdot 10^{-5}$
3	450036	50353	158	$1.12 \cdot 10^{-1}$	$5.00 \cdot 10^{-4}$	$3.51 \cdot 10^{-4}$
4	635674	20347	0	$3.20 \cdot 10^{-2}$	$2.24 \cdot 10^{-5}$	0.00

it has to be ensured that the desorbing facet is far enough from the section of interest, during simulation, in order to avoid direct beaming effects between the desorbing facet and the facets which limit the region of interest. For the simulations given here, the distance between desorbing facet and section of interest was chosen to be one beam tube length. The desorbing gas flow profile there has been set to be cosine-like. Since the region of interest is open ended, this type of simulation considers backscattering effects. Table 3.3 gives the setting for the simulation, while table 3.4 lists the results. During the simulation runs a couple of leaks were observed for high statistics. Leaks corresponds to areas where particles reach the outside of the implemented geometry through holes or edges, which have not been closed in the underlying MolFlow+ geometry. If these leaks did occur inside the section of interest, they were treated as systematic uncertainties. The statistical uncertainties arise from the count rate at the outlet of the region of interest. With the conservative approach of the maximal possible systematic uncertainty and with the Gaussian error propagation
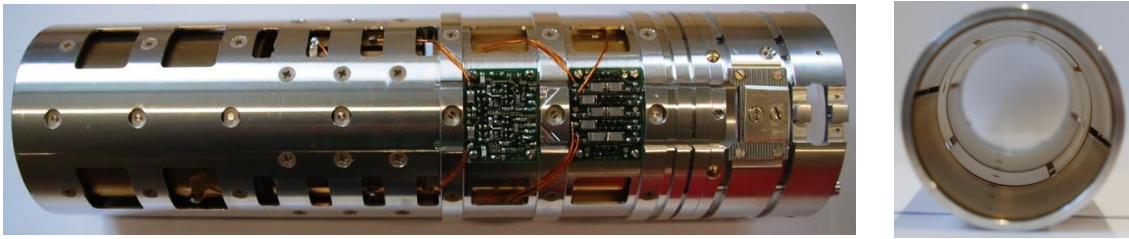
Figure 3.6.: FT-ICR used inside the DPS. They can be positioned in the first and in the last beam tube section to determine the ion species inside the source and transport section. Left: Top view on the FT-ICR. Right: View on the FT-ICR electrode structure.

the overall transmission probability (equation 3.7) is determined to be:

$$\text{Basic DPS:} \quad P_{\text{tot,b}} = \prod_i P_{i,b} = (8.38 \pm 0.07_{\text{stat}} \pm 0.86_{\text{sys}}) \cdot 10^{-6}$$
$$\text{Extended DPS:} \quad P_{\text{tot,e}} = \prod_i P_{i,e} = (2.24 \pm 0.02_{\text{stat}} \pm 0.04_{\text{sys}}) \cdot 10^{-6} \quad . \tag{3.8}$$

The reduction factor can be achieved by inverting the transmission probability:

$$\text{Basic DPS:} \quad R_{\text{DPS,b}} = \frac{1}{P_{\text{tot,b}}} = (1.19 \pm 0.01_{\text{stat}} \pm 0.12_{\text{sys}}) \cdot 10^{5}$$
$$\text{Extended DPS:} \quad R_{\text{DPS,e}} = \frac{1}{P_{\text{tot,e}}} = (4.46 \pm 0.01_{\text{stat}} \pm 0.73_{\text{sys}}) \cdot 10^{5} \quad . \tag{3.9}$$

This fits perfectly the estimated design value of five orders of magnitude. The fully equipped DPS (extended) will reduce the gas flow from the WGTS significantly better than the bare DPS (basic) without instrumentation.

3.2.3. Ion detection inside the DPS with the FT-ICR

During the interaction of β-decay electrons with the tritium molecules, a variety of different ion species will be created which propagate into the source and transport section. For a quantitative determination of the ion species, the DPS features up to two Penning traps. These FT-ICR (Fourier Transform - Ion Cyclotron Resonance) devices can be positioned in the homogeneous region of the magnetic field inside beam tube one, and potentially also in beam tube element five. They have been built by Stahl Electronics [102] and characterised in the theses [103] [104] [105]. These powerful mass spectrometers, which operate with a superposition of an electric quadrupole field and a homogeneous magnetic field, are shown in figure 3.6. Each unit is 256 mm long, features an inner diameter of 70 mm, and consists of two 89 mm long ring electrodes. These are divided into two parts with a small gap each, to avoid high induced eddy currents in case of a DPS magnet quench. Between these two trapping electrodes, a four-segmented electrode arrangement, with a length of 56 mm, is positioned. This assembly allows to detect and to distinguish different ion species. Each electrode (1 mm in thickness) is made out of oxygen-free copper, covered with a diffusion barrier of 50 µm silver and a gold plating with a thickness between 0.5 µm and 1 µm [106]. The electrode assembly is fixed to an aluminium housing, which is insulated with PEEK (Polyetheretherketone). On top of the housing a pre-amplifier and a signal filter unit are mounted and connected to the electrode system via a Kapton-isolated cable. Both existing units are designed to operate in a large pressure range between 10^{-4} mbar and 10^{-8} mbar [107]. All signals, both inwards and outwards, have to be fed through the pump ports

of the DPS. Outside the vacuum system, the signals are amplified and digitized. The Penning traps are used to determine the respective anion and cation-type ion species, and to draw conclusions about the ionising attachment and detachment radioactive processes inside the source.

The physics conditions in a Penning trap are well known and can be described exactly. The ions are trapped inside the electric potential which is created by the two ring electrodes (given in polar coordinates) [108]:

$$V(\rho, z) = \frac{V_0}{2d^2} \left(z^2 - \frac{\rho^2}{2} \right) \quad . \tag{3.10}$$

These ring elements pick up the common motions of charged particles in electro-magnetic fields, namely the modified cyclotron motion, the magnetron motion and the harmonic oscillation along the symmetry axis, caused by the electric potential. Solving the equation of motions, given by Lorentz law, yields three eigenfrequencies [108]:

$$
\begin{aligned}
\text{Harmonic oscillation:} \quad & \nu_z = \frac{1}{2\pi} \sqrt{\frac{qV_0}{md^2}} \\
\text{Modified cyclotron:} \quad & \nu_+ = \frac{1}{2} \left(\nu_c + \sqrt{\nu_c^2 - 2\nu_z^2} \right) \\
\text{Magnetron:} \quad & \nu_- = \frac{1}{2} \left(\nu_c - \sqrt{\nu_c^2 - 2\nu_z^2} \right) \quad ,
\end{aligned}
\tag{3.11}
$$

with the cyclotron frequency $\nu_c = (2\pi)^{-1} \cdot qB/m$, the ion mass m, and d acting as a geometrical trap dimension parameter.

With a four-segmented electrode system, surrounding the centre of the trap (figure 3.7), ions can be excited with their cyclotron frequency by two opposite electrodes (dipolar excitation). After excitation the ions will rotate in phase as packages and induce an image current on the two pick-up electrodes. Assuming two parallel pick-up electrodes, the image current I_{ic}, which is of the order of pico amps, is given by [103]:

$$I_{ic} = 2\pi \cdot q \cdot \frac{\nu_{ion} r_{ion}(t)}{D} \quad , \tag{3.12}$$

with the distance D between the two electrodes, the ion frequency ν_{ion}, and the projection of the radial motion perpendicular to the electrodes $r_{ion}(t)$ [103]. If the ion species inside the Penning trap are unknown, a cosine-like broad band frequency spectrum can be applied for excitation. Only these ions will rotate in resonance, for which the cyclotron frequency matches the excitation frequency. Table 3.5 gives the eigenfrequencies of the most common ions, expected inside the source and transport section, calculated for the magnetic field of the DPS of $B = 5.6\,\text{T}$ [103].

A global pulse-delay generator triggers a measurement cycle. The two end cap electrodes then will be ramped up to a maximum value of $250\,\text{V}$ (technical specification). Since power supplies are not fast enough, a high voltage switch will be used for setting the electrodes under voltage. The switching delay is in the order of nanoseconds. When trapping ions, the "hot" (high energy) ions will escape from the potential. After a time delay of about $5\,\text{ms}$, the amount of captured ions will be constant inside the Penning trap. The electric excitation field can then be applied via an arbitrary wave form generator. The duration will depend on the actual amount of ions and on the ion species, commonly it is about $10\,\text{ms}$. When stopping the excitation, a short time period ($2\,\text{ms}$) has to pass by until the capacitive influence of the excitation onto the pick-up electrodes vanishes. Then an image current analysis can be started, which will take about $10\,\text{ms} - 130\,\text{ms}$, depending
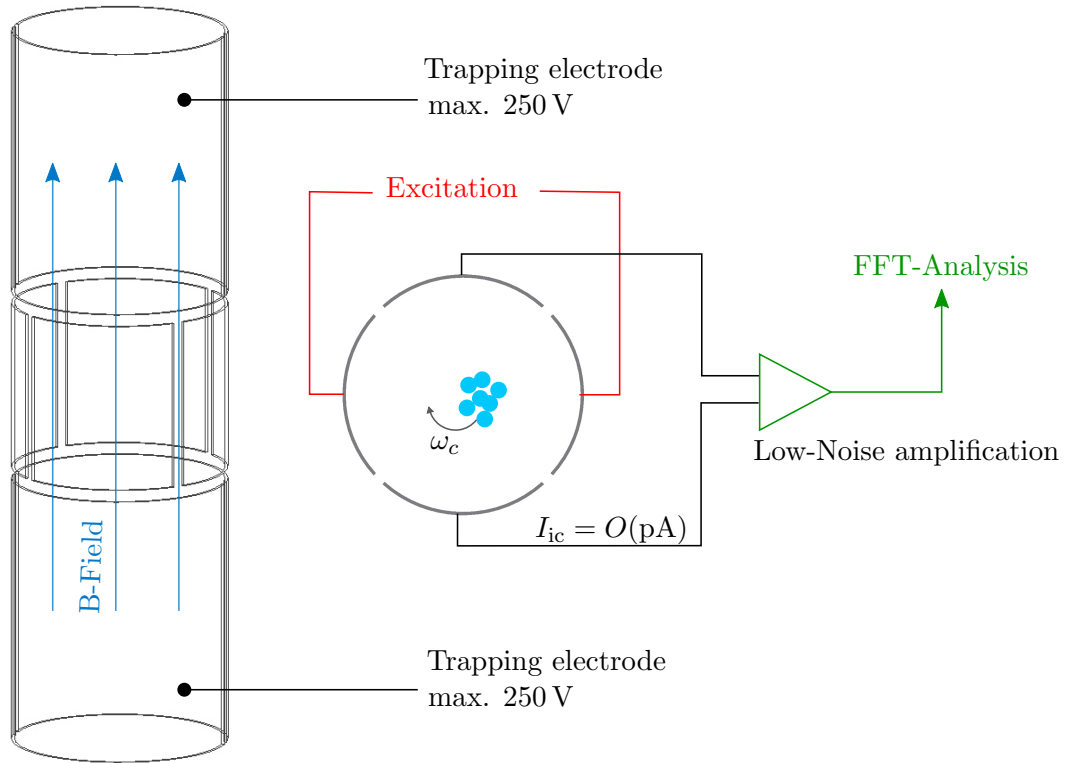
Figure 3.7.: Schematic drawing of the Penning traps used at the KATRIN experiment. Two electrodes trap the ions inside. With a four fold segmented electrode system around the centre of the trap, the ions can be excited (excitation electrodes), and subsequently detected by their induced image current I_{ic} (pick-up electrodes).

Table 3.5.: Cyclotron frequencies of the most common ions expected in the transport section, calculated with a magnetic field of $B = 5.6\,\text{T}$. Taken from [103].

Ion species	Cyclotron frequency (MHz)
H_2^+	38.39
$^3\text{He}^+$, T^+	25.59
DT_2^+	9.60
T_3^+	8.53
T_5^+	5.12

Figure 3.8.: DPS electric dipole system. The dipoles are placed inside the DPS beam tube
module two, three, and four. Left: CAD model inside one beam tube element.
Right: Dipole prototype.

on the ions captured inside. The signal of the image current is pre-amplified with a
low noise pre-amplifier, which is positioned directly on the Penning trap. With a post-
amplifier the signal is guided to a down-converter which shifts the high frequency signal
(MHz) down into the kHz range. An FFT-Analyser (Fast Fourier Transform Analyser)
subsequently converts the amplitude over time signal into an amplitude over frequency
spectrum. For higher accuracy the excitation and analysis can be run in a cycle with
subsequent averaging over the spectra. At the end of the cycles the ring electrodes have
to be switched off. Depending on the order of the off-switching, the captured ions can be
released in a well-defined direction.

During commissioning tests at the University of Heidelberg the FT-ICR sensitivity was
determined with lithium ions. The ions ^{6}Li$^+$ and ^{7}Li$^+$ have a mass-to-charge (m/q) ratio
similar to the m/q ratio of T$_2^+$ and T$_3^+$. The sensitivity depends on the residual gas
pressure and the ion species. For lithium and thus for tritium, about 1000 ions (single
ionised) are needed to differentiate between background and signal. The upper charge
limit corresponds to more than 10^6 charges [107].

3.2.4. An electric dipole system for ion suppression

The transport section is the ideal location to eliminate the different ion species coming
from the WGTS (see section 2.2.1). It is absolutely necessary to get rid of these ions,
because ions are trapped between the gas flux from the WGTS and the ring-shaped ion
reflection electrodes [57]. These cylindrical reflection electrodes are installed at the end of
the DPS (one end cap of the FT-ICR could serve as the ring electrode there), between the
CPS and the pre-spectrometer, and between both spectrometers. The latter ones serve for
redundancy. The DPS ring electrode is designed to operate with a value of about +100 V.
Thermal ions guided out of the WGTS will be reflected in the last DPS section and pass
the DPS again in the opposite direction. Back inside the centre of the WGTS they scatter
off residual gas particles, resulting in a diffuse reflection. Thus, all ions pass the DPS
many times, so that the amount of ions inside the DPS will increase over time. While
the FT-ICR Penning trap allows to analyse the different kinds of ions (qualitatively and
quantitatively), they do not eliminate them.

For this purpose an additional electric dipole system will be installed inside the central
three beam tube sections of the DPS. Figure 3.8 gives an impression of the design set-
up. Each dipole consists of one pair of electrodes. Each part of that pair contains a half
cylindrical tube (562 mm in length) in its centre and a half-cone each at both ends (simple
length: 140 mm). They are made of stainless steel. During standard KATRIN operation,
only one part of a pair will be set to negative voltage, creating an electric dipole field.

This perpendicular electric dipole field is superimposed on the DPS magnetic field, along
the z-axis. Ions passing through the electric field will thus be shifted to an outer part of the
magnetic flux tube by the $\vec{E} \times \vec{B}$-drift. After several passes through the additional electric
field, ions exit via gaps of the dipole elements and are then neutralised. Subsequently,
they react like common neutral gas, and are pumped via the turbo molecular pumps or

trapped by the cryogenic pumping section.

The ion suppression is based on simple physical assumptions. All charged particles, passing through the DPS beam tube, experience a Lorentz force:

$$\vec{F}_{\mathrm{L}} = q \left(\vec{E} + \vec{v} \times \vec{B} \right) \quad . \tag{3.13}$$

The three equations of motion, derived from equation 3.13, can be solved with the following three motions, assuming a homogeneous magnetic field in z-direction and a stationary electric dipole field [109]:

$$
\begin{aligned}
x(t) &= r_{\mathrm{c}} \cdot \sin \left(\omega_{\mathrm{c}} \cdot t \right) + v_{\mathrm{Drift},x} \cdot t + x_0 \\
y(t) &= r_{\mathrm{c}} \cdot \cos \left(\omega_{\mathrm{c}} \cdot t \right) - v_{\mathrm{Drift},y} \cdot t + y_0 \\
z(t) &= \frac{qE_z}{2m} t^2 + v_z t + z_0 \quad ,
\end{aligned}
\tag{3.14}
$$

with the cyclotron radius r_{c} and the cyclotron frequency ω_{c}. Next to the cyclotron motion, an additional $\vec{E} \times \vec{B}$-drift in the $x - y$ plane can be observed. It can be written as:

$$\vec{v}_{\mathrm{Drift}} = \frac{\vec{E} \times \vec{B}}{|\vec{B}|^2} \quad . \tag{3.15}$$

The particles are dislocated as a function of geometrical dimension, and the electrical layout. The degree of dislocation is given by [110]:

$$R = v_{\mathrm{Drift}} \cdot \tau_{\mathrm{D}} = v_{\mathrm{Drift}} \cdot L_{\mathrm{D}} \sqrt{\frac{m_{\mathrm{ion}}}{qU_{\mathrm{D}}}} \quad , \tag{3.16}$$

where τ_{D} is the sojourn-time of an ion in the electric dipole field for an electrode of length L_{D}.

The ion suppression has been investigated via simulations for the precursor of the DPS, the DPS2-F cryostat (in operation until 2012), in [54], [109], [110], and [111]. The result was that T_5^+ cluster ions have to pass about four times through the dipole field to be eliminated, T^+ ions therefore need eight dipole transits. Both calculations assumed a dipole field of $-100\,\mathrm{V}$. Since the current DPS dipole design does not differ significantly from the old design, the ion life time is expected will be of the same order of magnitude. The current dipole electrodes, with a half-cone on each side will be roughly 10% longer than the old design, therefore the inner diameter will be 23% larger. The ion suppression characteristics in the new design is simulated within the framework of an ongoing master thesis [112].

The electrode design features the distinct advantage to operate each pair of electrodes in a monopole mode. In this case β-decay electrons of decaying neutral tritium inside a monopole region will start at a different potential than β-decay electrons from the grounded WGTS beam tube. This leads to a significant shift of the β-decay spectrum, which can be detected in the scanning procedure of the main spectrometer. By subsequently switching on and off the monopole mode of the three dipole pairs, the gas reduction factor between modules two, three, and four can be measured directly by monitoring the β-decay spectrum with the spectrometer section. A maximum monopole voltage of $\pm 500\,\mathrm{V}$ will be possible.

3.3. Cryogenic Pumping Section

The CPS cryostat is one of the most complex components of the KATRIN experiment. It is the final tritium retention unit of the transport section, and therefore the conclusion of the beam line in the radiation controlled tritium laboratory. The performance
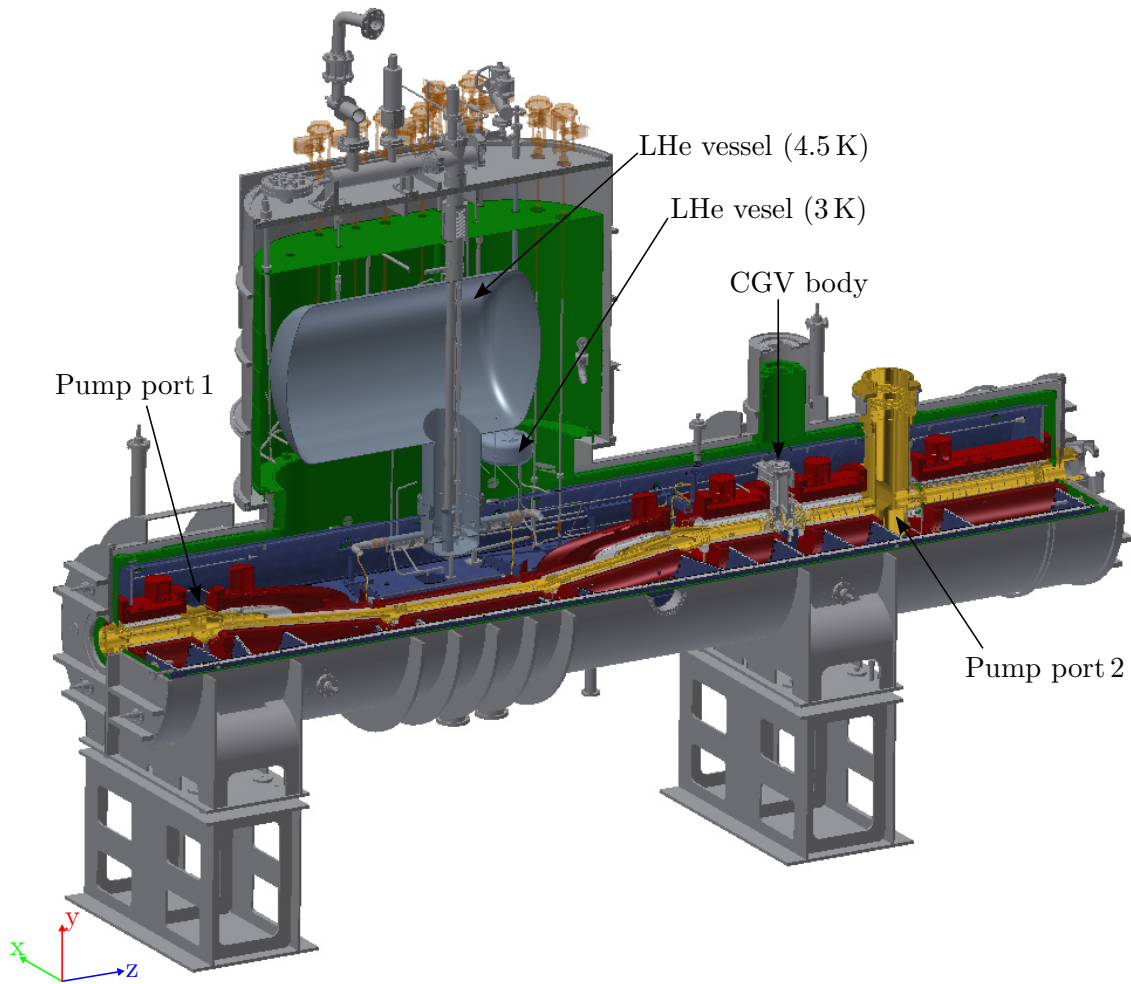
Figure 3.9.: Schematic of the CPS assembly. The DPS will be on the left side, the pre-spectrometer on the right side. Between pump port 1 and 2, the argon frost layer will be prepared and kept at 3 K. Green: 77 K cooling shield. Light blue: LHe vessels. Purple: 4.5 K cooling shield, called cold mass. Red: Solenoids. Gold: Beam tube and pump port assembly. The cold gate valve (CGV) is a safety valve operated inside the CPS at a temperature of 4.5 K.

of this component is of utmost importance for the KATRIN neutrino mass measurement to guarantee a negligible tritium flow into the spectrometer. Legal aspects are much less stringent than the more challenging requirement on a flow rate below 10^{-14} mbar ℓ/s which is required to ensure the nominal KATRIN sensitivity on the neutrino mass. As outlined previously, the CPS is designed to reduce the tritium flow from the WGTS and DPS to the pre-spectrometer by more than seven orders of magnitude, down to an absolute value less than 10^{-14} mbar ℓ/s. The tritium partial pressure at the outlet side has thus to be less than 10^{-20} mbar. The CPS will operate as a cryosorption pump, where the incoming gas will be adsorbed on an argon frost layer. According to the design specifications, the CPS will operate until an activity of 1 Ci has been accumulated. According to the source reference design, this should happen after about 60 days of nominal KATRIN operation. More details on sorption processes with solid argon and on the CPS vacuum performance are given in chapters 5 and 6. The CPS thus has to operate over a huge temperature range from bake-out temperatures of up to 620 K down to cryogenic standby temperatures of 3 K. At present it is in the final stage of assembly at the industrial partner ASG [113] in Genoa (Italy). Figure 3.9 gives an overview of its assembly. The CPS consists of:
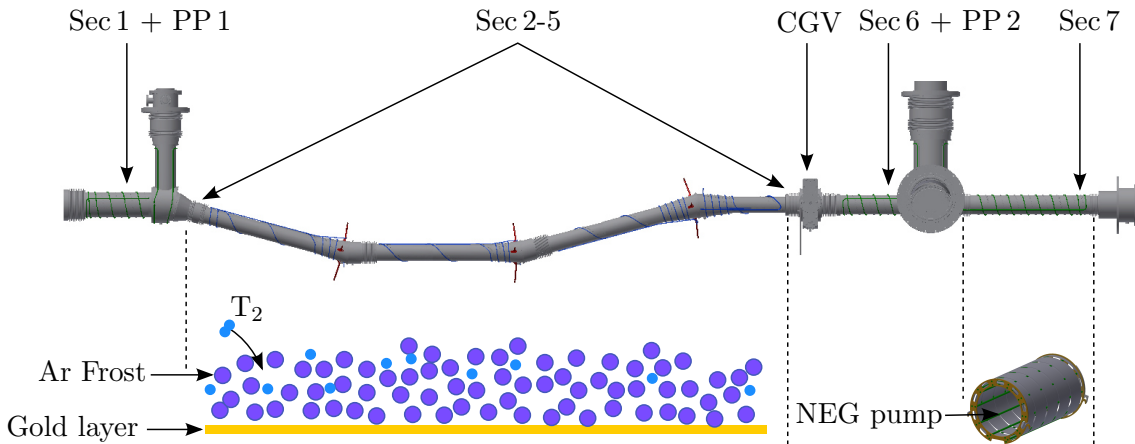
Figure 3.10.: CPS vacuum system with its pumping principles. All parts are gold plated on the inner surface for less tritium adsorption on the beam tube walls. In green, wound around sections (Sec) 1, 6, 7, and pump ports (PP) 1, and 2, are shown the LN$_2$ cooling pipes. In blue the LHe cooling system, around section 2-5. The hooks in red are feedthroughs for the argon frost preparation.

- a 6.5 m long vacuum system, being built out of seven beam tube sections. In sections 3, 4, and 5 the argon frost layer will be prepared.

- a magnet system, consisting of seven superconducting coils with nominal fields up to 5.6 T.

- a 3 K pumping station (see section 3.3.3) to decrease the beam tube temperature below the 4.5 K value, achieved when operating LHe at ambient pressure.

- the beam tube instrumentation, consisting of a FBM (Forward Beam Monitor, see section 3.3.5) for real-time β-decay activity monitoring of the source, and a condensed krypton source for regular calibration procedures of the spectrometer (section 3.3.6).

- a complex system of radiation shieldings, isolation vacua, and in particular cryogenic liquid circuits to ensure beam tube operation between 3 K and 600 K.

3.3.1. The beam tube and vacuum system

The vacuum system is a 6.5 m long arrangement of beam tube elements, subdivided into seven sections and two pump ports. Each beam tube component is made out a stainless steel tube gold-plated at the inner surface. The gold-plating of the inner surface will on the one hand suppress diffusion of the hydrogen isotopes into the stainless steel. On the other hand, it smoothens the temperature distribution along the beam tube axis and provide a clean surface for argon frost crystallisation. Three sections (elements two, three, and four) of the CPS are tilted by 15° to avoid gas beaming effects of tritiated molecules entering from the DPS. These elements will also contain the frozen argon layers. Figure 3.10 shows the vacuum system of the CPS together with the pump ports and the cold gate valve (CGV). The temperatures of each section are given in section 3.3.4 and in appendix D, where the operation modes are detailed.

- **Section 1:** The first section (about 647 mm long at LN$_2$ temperature) of the CPS includes the DN 200 entrance flange to the DPS, a bellow, and a beam tube segment with an inner diameter of 148.4 mm. Inside the tube an in-vacuum copper shield ($d_{min} = 96.3$ mm) will reduce the conductance at the entrance of the CPS as well as the radiative heat load onto the argon frost section coming from the 300 K warm DPS. During operation it will be kept at 77 K via liquid nitrogen cooling.

- **Section 2-4:** These elements form a chicane covered by argon frost. All three elements consist of tubes of 720 mm length and 95.3 mm diameter each. A total of about 90 circular fins per section, with an inner diameter of 75.2 mm, are welded in equidistant distances to the inner surface of the tubes. The inner diameter of the fins increases in a cone-like manner at both ends of the tube. This shape is adapted to the magnetic flux tube (see next section 3.3.2). If tritiated molecules pass through the beam tube elements, they will hit the argon frost layer, i.e. they are "pumped" with a sticking probability of 70% [59]. For preparation of the argon frost layers, three capillaries are fed through into each section from the outside of the CPS cryostat. These capillaries contain 23 holes with diameters of 0.2 mm each. First, the argon frost layer will be prepared at an optimised beam tube temperature of 6 K. The details of the entire argon layer preparation and regeneration steps will be given in chapter 5. The beam tube sections 2 to 4 are interconnected via cones and bellows to ensure that the magnetic flux tube does not collide with the beam tube walls.

- **Section 5:** Section 5 (3-6 K) shows an identical circular shape, however with a smaller number of fins. The minimal inner diameter amounts to 75.2 mm while the length of the fin-covered tube is 346.1 mm. Diffuse scattered argon, from the argon preparation process, will condensate on the inner side of this beam tube. Beside that, there will be no active argon preparation in order to avoid pumping of tritiated molecules in the vicinity of the cold gate valve. If tritium would indeed diffuse to the cold gate valve, it might be pushed into the valve body/head when the valve is opened for standard operation. In this way the gate valve would accumulate an intrinsic activity, which has to be avoided.
  Including the connecting cone to section 4, section 5 features an overall (warm) length of almost 570 mm.

- **Cold Gate Valve:** Section 5 is followed by an all-metal cold gate valve. It is a specially designed valve by VAT [114], which is able to operate at cryogenic temperatures (4.5 K). For thermal decoupling it is connected to the neighbouring sections 5 and 6 via two gold-plated bellows. The valve body itself is made of pure stainless steel. The overall length, including the two bellows, is 428.8 mm. In opened position state it provides an inner diameter of 112 mm. On the upstream side which faces section 5, a helium capillary is installed which is accessible from the outside of the CPS. After the CPS has accumulated a radioactive inventory of 1 Ci, the argon frost layer has to be removed. For this purpose the system is heated up to a level of 100 K and subsequently it is purged in a laminar flow with gaseous helium. It is important to achieve a well-defined gas stream towards pump port 1, where the argon and tritiated molecules are transferred back to the tritium infrastructure of TLK.

- **Section 6:** Section 6 includes a cylindrical tube, 112 mm in diameter and 352.4 mm in length. There is a circular element with a diameter of 82 mm, at the cold gate valve side, which was originally foreseen as a means to mount an additional getter pump. This section is cooled with liquid nitrogen down to 77 K.

- **Section 7:** The last section of the CPS includes an additional getter pump (see chapter 7). The length of the 112 mm wide tube is 700.2 mm. As in section 6, a circular narrowing element with an inner diameter of 82 mm is placed at the end to avoid a potential moving of the getter pump towards the pre-spectrometer. Section 7 ends with a DN 200 flange.

- **Pump Port 1:** Pump port 1 is positioned horizontally between sections 1 and 2. It reaches sideways up to the outside of the CPS cryostat. Dedicated vacuum monitoring equipment, such as residual gas analysers, pressure gauges and pumps, will be
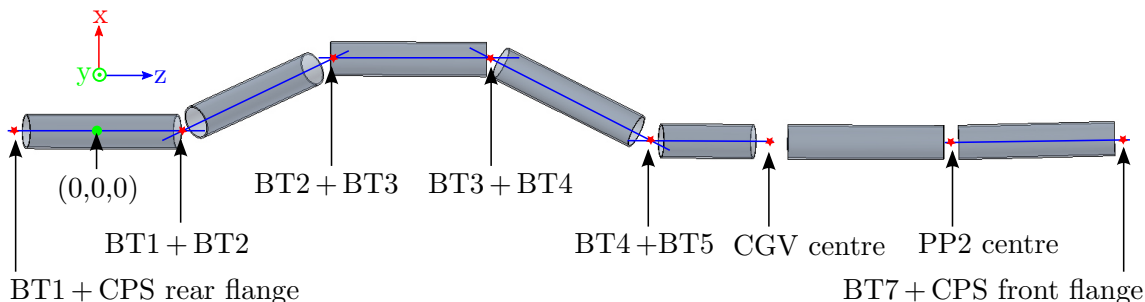
Figure 3.11.: Scheme of the CPS beam tube alignment measurements. The intersections between the axis of each part have been determined by experiment [117]. The deviations from the design values are listed in table 3.6. (BT = Beam Tube, CGV = Cold Gate Valve, PP = Pump Port).

placed there. The beam tube will be evacuated during bake-out and argon regeneration through this port, and tritiated molecules can be fed back to the inventory of tritium laboratory.

- **Pump Port 2:** Pump port 2 provides both a vertical and a horizontal port which can be accessed from the outside of the CPS. They lead to a 255.7 mm wide circular chamber, which connects beam tube sections 6 and 7. Again, specific vacuum gauges, a residual gas analyser and a TMP will be mounted at the horizontal part, as well as an electron flux monitoring system, the forward beam monitor (FBM) [115]. To do so, a solid-state detector system can be pushed forward into the inner parts of the pump port to scan the transported flux tube (see section 3.3.5).
  In addition to the FBM, a calibration system will be installed at the vertical part. To do so, a cold finger with condensed krypton, will be driven into the inner of the pump port to perform regular calibrations of the spectrometer [116], more information on this device is given in section 3.3.6. Both instrumentation devices can be detached via all-metal VAT valves at each branch of the pump port.

Alignment of the beam tube system

During the manufacturing process and at specific assembly steps careful and detailed alignment measurements of the beam tube and the magnet system were performed by the industrial partner ASG. All metrology data given here were measured and calculated by the manufacturer [117]. The origin of the coordinate system defined here resides inside the centre of the first CPS solenoid. The z-direction points to section 7, the y-direction in vertical to the top, and the horizontal x-direction is defined according to a right-handed system. Figure 3.11 shows a scheme of the measurement and the coordinate system.

The specifications require transport of the 191 Tcm^2 magnetic flux tube without collision with the beam tube elements. This requires coaxiality of the beam tube elements and magnet modules according to DIN ISO 1101. Table 3.6 shows the actual deviations of the intersection points between two beam tube axes from the design values. The difference in temperature between room temperature position measurements and the later CPS operation is however 290 K. Accordingly, the inner components of the CPS cryostat will thermally contract between three fixed points, namely the CPS rear flange (connected to the DPS), the CPS front flange (connected to the pre-spectrometer beam tube), and the inner CPS contraction centre, which is at a location of 3451 mm in z-direction from the rear flange (design value). The contraction is expected by ASG to be 3 μm/mm between room temperature down to 4.5 K, equivalent to a scaling factor of 0.997 [117]. The coordinates in cold conditions in table 3.6 were calculated from the measured values at warm conditions making use of this scaling factor. The total uncertainty of the measured data

Table 3.6.: Alignment of the CPS beam tubes. Given are the deviations between the as-built and the design position. The data are based on [58] and [117]. (BT = Beam Tube, CGV = Cold Gate Valve, PP = Pump Port).

Intersection point	Warm conditions (mm)			Cold conditions (mm)		
	Δx	Δy	Δz	Δx	Δy	Δz
CPS rear flange + BT 1	0.5	-0.6	0.0	0.5	-0.6	0.0
BT 1 + BT 2	0.0	0.2	2.3	0.0	0.2	1.7
BT 2 + BT 3	0.0	-0.1	-0.5	0.0	-0.1	-1.1
BT 3 + BT 4	0.1	0.0	2.5	0.1	0.0	1.9
BT 4 + BT 5	-0.2	0.2	3.6	-0.2	0.2	3.0
CGV centre	0.0	0.4	0.4	0.0	0.4	-0.1
PP 2 centre	0.7	0.1	0.5	0.7	0.1	0.0
BT 7 + CPS front flange	0.3	0.7	0.8	0.3	0.7	0.8

is ± 0.25 mm [117].

One can thus expect that beam tube elements 2 to 5 are shifted by up to 3 mm in the z-direction. The centre of pump port 2 is expected to undergo the largest movement in x-direction. The rather strong deviation at room temperature are only rudimentary being compensated by the thermal contraction at cold conditions. The deviations in x- and y- direction point to a tilt of almost every beam tube. From the vacuum point of view, these misalignments in the lower millimetre and sub-millimetre range have no influence at all on the pumping performance of the CPS. However, from the electromagnetic point of view, such deviations, including the ones of the magnet modules, may cause problems with respect to the distance between the magnetic flux tube and the beam tube walls. One possible countermeasure proposed here would be to lower the magnetic field in the WGTS to obtain a larger clearance of the flux tube with respect to the beam tube dimensions. More details about that are given in the following section 3.3.2.

3.3.2. Set-up of the magnet system

The magnet system consists of seven magnet modules, connected in series. Figure 3.12 shows the alignment of the solenoids inside the cold mass. Each solenoid surrounds one beam tube section to transport the signal electrons through the CPS vacuum system. To avoid significant heat exchange between the magnets and the beam tubes, inner radiation shields made of copper, which were gold-plated are placed between each of them, except at sections 1 and 6. Furthermore, there is active liquid nitrogen cooling for the radiation shield of section 7.

The superconducting coils are based on Cu/NbTi multi-filamentary round wires. The bare wire diameter is 1.27 mm, while each filament has a diameter of 80 μm. Altogether more than 100 km of wiring was used to build the magnet modules. The maximal field in the centre is designed to be 5.7 T with a nominal current of 200 A (118.6 A/mm^2 in average per magnet) [58]. The pressure inside the liquid helium supply vessel of the magnets will be about 1200 mbar. This results in an operating temperature of 4.5 K, following the vapour pressure curve of liquid helium (see appendix E). Operating the magnets at this specific temperature leads to a safety margin of the superconductors of almost 70 A in current and roughly 2.5 T in the magnetic flux density [58].

The as-built positioning of the magnet modules shows, similar to the case of the beam tube elements, non-negligible deviations from the design values, as measured by ASG during
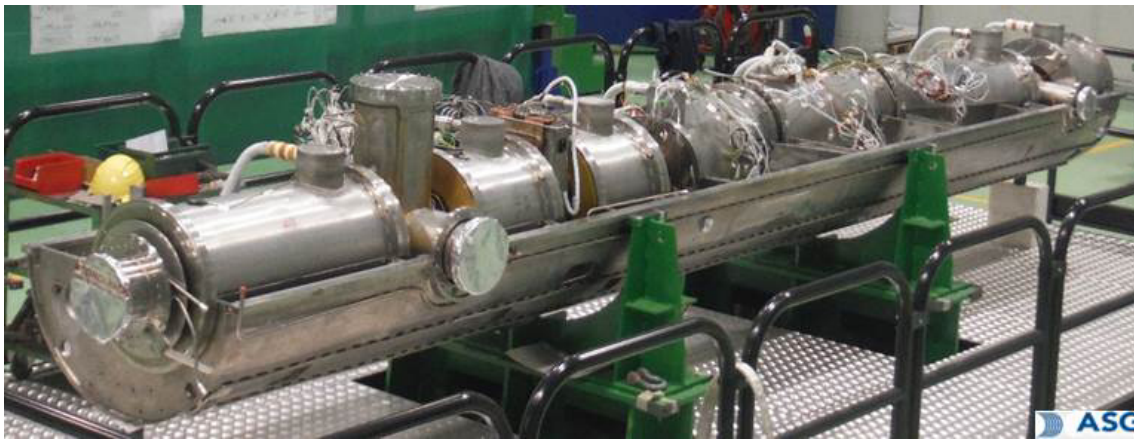
Figure 3.12.: Assembly of the CPS magnet system inside the cold mass. From left to right is section 7 to section 1. Parts of the beam tube and pump ports can be seen as well.

Table 3.7.: Alignment of the CPS magnet modules. Given are the deviations between as-built and design position. The cold conditions have been calculated with an estimated thermal contraction of $3\,\mu m/mm$. The deviations are given in the KATRIN coordinate system. The data base on [117].

Magnet module	Warm conditions (mm)			Cold conditions (mm)		
	Δx	Δy	Δz	Δx	Δy	Δz
Coil 1	0.5	0.2	-0.46	0.5	0.2	-0.66
Coil 2	-0.54	1.3	1.69	-0.7	1.3	2.05
Coil 3	-0.17	0.2	-1.3	-0.15	0.2	-1.74
Coil 4	-0.04	0.8	1.03	-0.1	0.8	0.7
Coil 5	0.3	0.2	1.2	0.3	0.2	1.37
Coil 6	0.2	0.0	1.56	0.2	0.0	1.82
Coil 7	0.0	-0.6	0.95	0.0	-0.6	1.57

assembly [117]. Table 3.7 lists the deviations of the magnet modules. The coordinate system is the same as in figure 3.11. Listed here are the differences between the coil centre points of the as-built and the design positions for both room temperature and cold conditions (at $4.2\,K$). The scaling factor between warm and cold conditions, as well as the overall uncertainty is identical to the calculations for the beam tube system.

The y-direction is perpendicular to the horizontal plane, as defined by the chicane (x-z-plane). For example, the centre of magnet module 2 deviates more than a millimetre from its designed position. Therefore it pushes the magnetic flux tube upwards into the y-direction, which can be seen in figure 3.13b. This misalignment cannot be corrected with the other CPS coils. Since the as-built dimensions, especially in y-direction, do not exactly fit the specified design requirements, it has to be ensured that the flux tube of $191\,Tcm^2$ still fits into the beam tube system.
The KATRIN analysis and simulation software package Kasper was used to perform a distance test between magnetic field lines and beam tube walls. Kasper consists of a bundle of modules and libraries, primarily programmed in C++, for solving various electromagnetic problems, including particle tracking. The algorithms for the distance testing for a given geometry are implemented in the Kassiopeia module, which is used for the particle
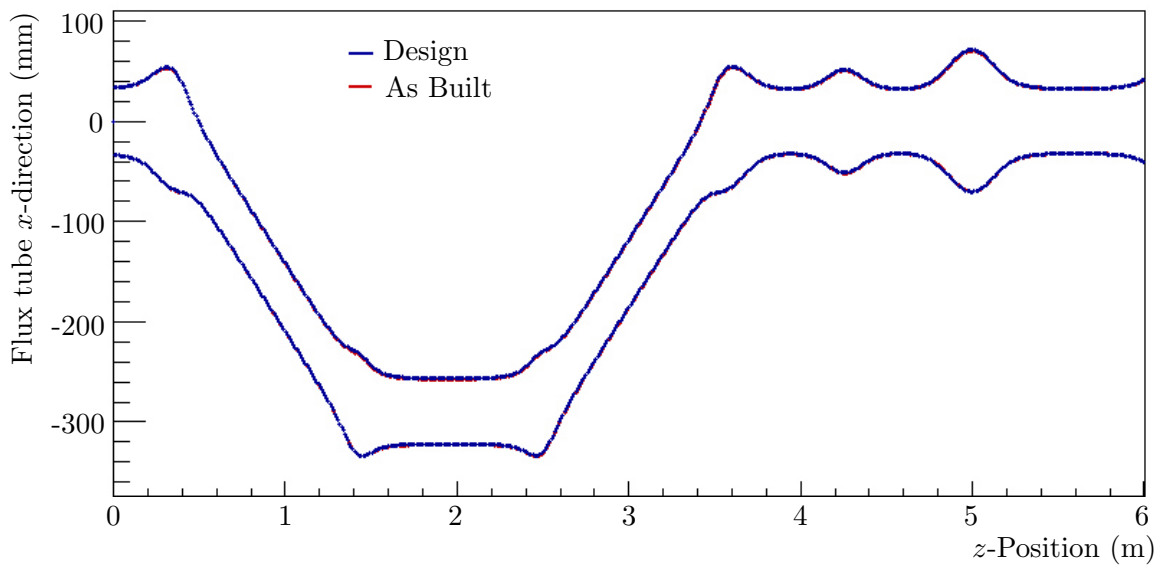
(a) Flux tube in x-direction.
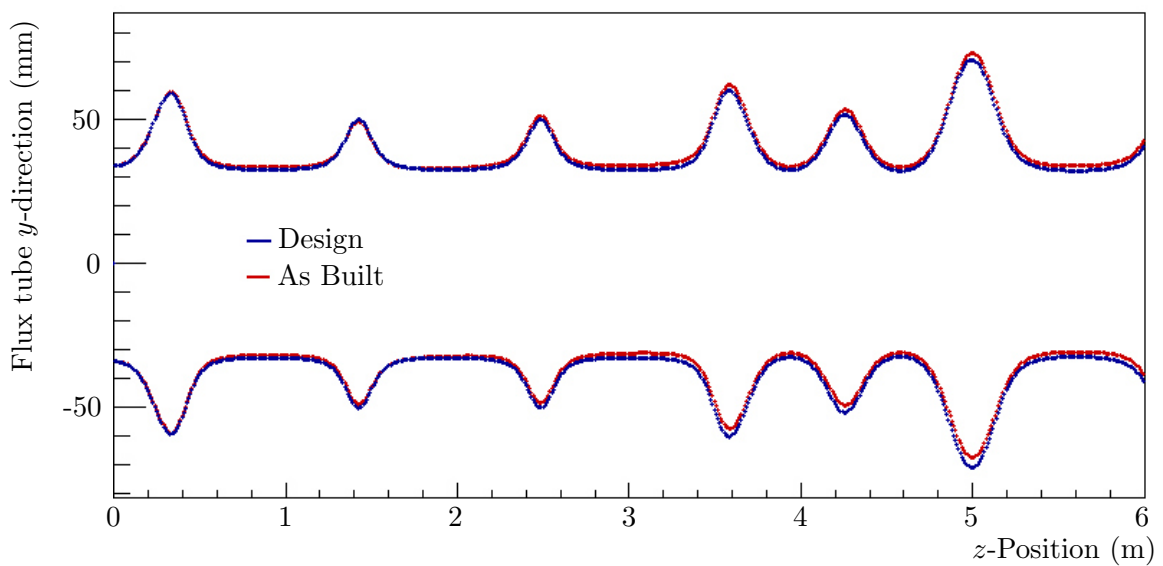
(b) Flux tube in y-direction.
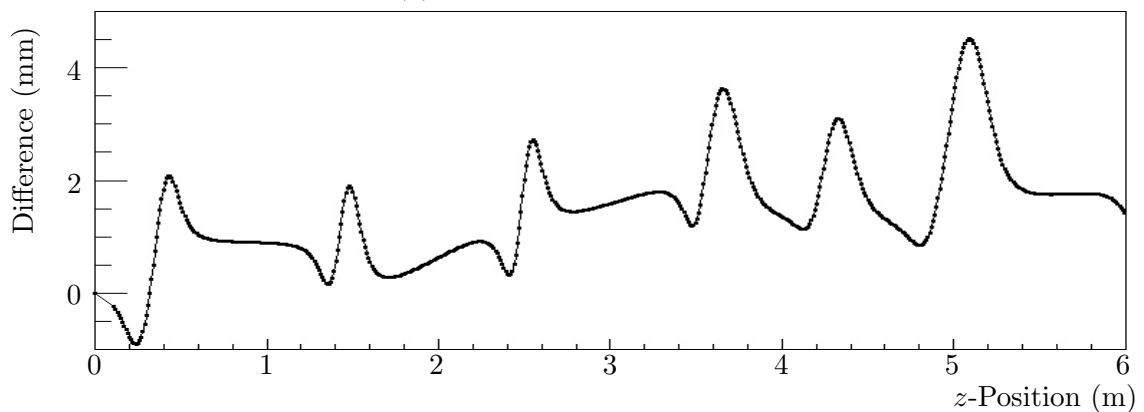
(c) Deviations as-built minus design flux tube in y-direction.

Figure 3.13.: Comparison of the as-built and the design flux tube in x- and y-direction. The flux tube is shifted in the y-direction (vertical). The shift results in a deviation of about $2\,\mathrm{mm}$ at the end of the CPS. Deviations in the x-z plane are negligible.
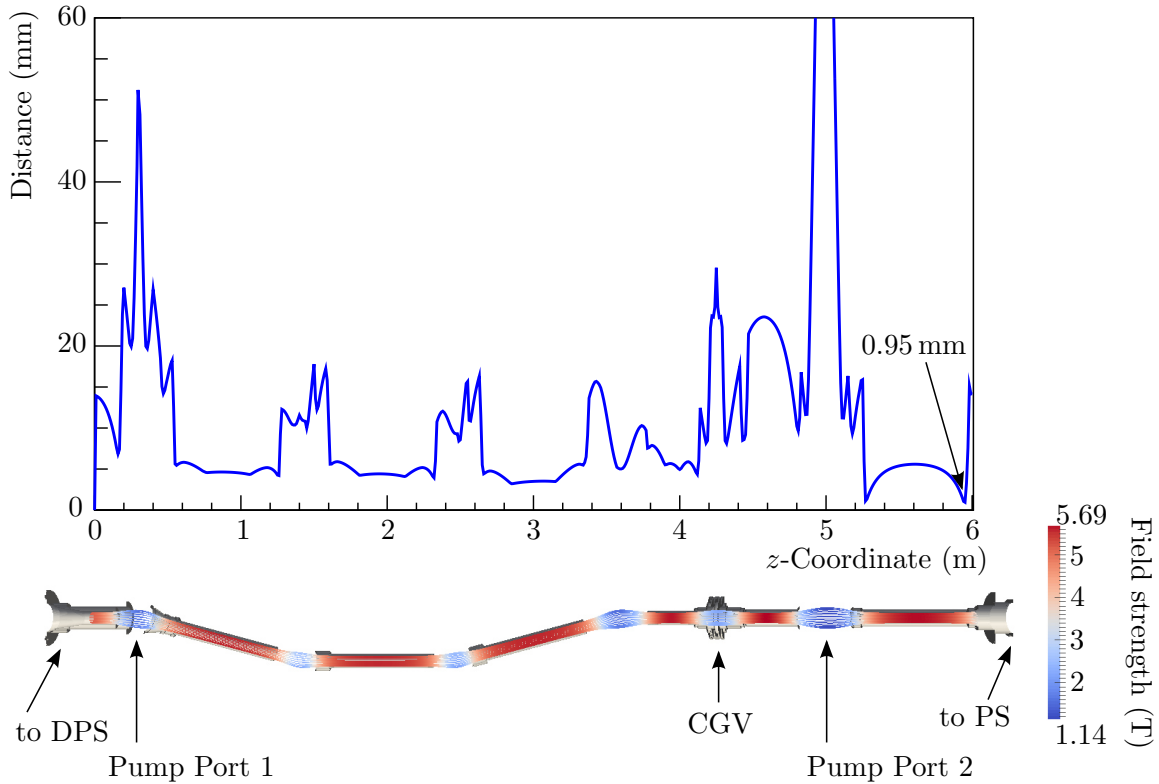
Figure 3.14.: CPS distance check between flux tube ($191\,\mathrm{Tcm^2}$) and the as-built vacuum system with installed NEG pump in section 7. Except section 7, a minimum leeway of $3\,\mathrm{mm}$ exists (top). CGV = Cold Gate Valve, PS = Pre-Spectrometer.

tracking. It uses the KGeoBag and the KEMField libraries, to calculate the distance between magnetic position vectors and geometric edges. All objects, such as the CPS related modules, are composited of a few simple geometries, such as tubes, cones, cut-cones, etc., all collected in KGeoBag. The algorithms for electro- and magneto-static field calculations are implemented in the KEMField library. The distance check has been performed in the framework of an ongoing master thesis [112]. There it is assumed that the flux tube enters the CPS without prior deviation, which would be caused by possible misalignments inside the WGTS or DPS units. Cold conditions taking the geometries of the as-built magnet system and the as-built beam tube assembly are used for these calculations. Figure 3.14 shows the distance of the $191\,\mathrm{Tcm^2}$ flux tube to the vacuum system walls with a precision of $\pm0.1\,\mathrm{mm}$. A distance between the ($191\,\mathrm{Tcm^2}$) flux tube and the whole beam tube system of more than $3\,\mathrm{mm}$ is given, except in section 7, where the non-evaporable getter pump (NEG) will be positioned. The NEG pump will be mounted by KIT after the CPS acceptance tests. It consists of four single cartridges, each $169\,\mathrm{mm}$ long, with an inner diameter of $76\,\mathrm{mm}$. More details about the NEG pump and its influence on the vacuum performance are given in chapter 7. The minimum distance between the flux tube and the getter pump, with its overall length of $676\,\mathrm{mm}$, is $0.95\,\mathrm{mm}$. The distance check assumes a perfect alignment of the NEG pump inside the CPS. A detailed view of the flux tube in section 7 is given in figure 3.15. Figure 3.15a shows the distance between the $191\,\mathrm{Tcm^2}$ flux tube and the bare beam tube system (without NEG installed). The minimum distance at the beam tube narrowing (end of section 7) is $2.82\,\mathrm{mm}$. In figure 3.15b, the distance calculation for a 5% longer NEG pump is presented to analyse the axial leeway, when mounting the pump. As can be seen clearly, the flux tube intersects the NEG pump at a z-position of $5.273\,\mathrm{m}$. The $191\,\mathrm{Tcm^2}$ flux tube fits into a tube with $76\,\mathrm{mm}$ in diameter, over a length

(a) Without NEG pump

(b) With extended NEG pump
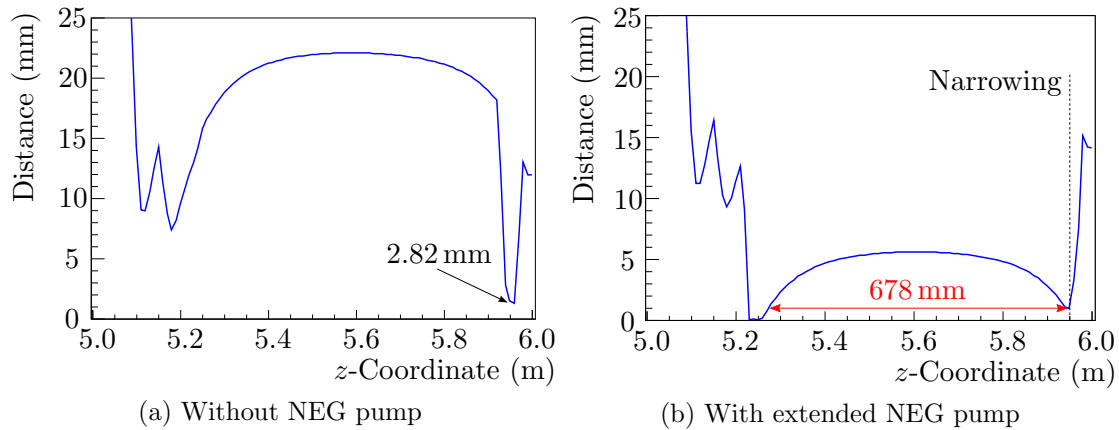
Figure 3.15.: CPS distance check between the flux tube $(191\,\mathrm{Tcm}^2)$ and the beam tube of section 7. A leeway of at least $2.82\,\mathrm{mm}$ is given in section 7 at the narrowing in front of the outlet flange without the NEG pump (figure 3.15a). The flux tube crosses a NEG pump with an assumed length of $678\,\mathrm{m}$ (figure 3.15b). The axial leeway when mounting the NEG pump is $2\,\mathrm{mm}$.

of $678\,\mathrm{mm}$, when assuming a safety margin of $1\,\mathrm{mm}$. Hence, the axial tolerance of the design concept is only $2\,\mathrm{mm}$. Again, an adjustment of the WGTS field is proposed to relax the rather tight margins.

Summary

The CPS magnet system, as well as the beam tube system, are aligned with a precision which does not fulfil the specifications, based on laser tracker measurements performed during assembly. Starting with the measured coordinates at room temperature the coordinates in cold conditions were calculated to characterise the beam tube and magnet modules. From the vacuum point of view these deviations, tilts, and shifts between design and as-built values are negligible, however, they critically endanger the full transport of the nominal $191\,\mathrm{Tcm}^2$ flux tube.
Magnet module 2 in particular pushes the magnetic flux tube into the y-direction (in KATRIN coordinates this is from bottom to top). The deviations between the outer flux tube lines $(191\,\mathrm{Tcm}^2)$ of the design and the as-built flux tube can be taken from figure 3.13. The shift in section 2 cannot be corrected inside the CPS, so that the flux tube will pass through the CPS with a shift of about $2\,\mathrm{mm}$ in vertical direction.
Although the magnet system has been aligned not within the limits of the specifications, the $191\,\mathrm{Tcm}^2$ flux tube still passes through the CPS vacuum system with a distance of at least $2.82\,\mathrm{mm}$ (compare figure 3.14 and 3.15a), however, without the additional NEG pump. For a getter pump geometry optimised to the CPS reference design, it will pass through section 7 with a distance less than one millimetre. The analysis presented in figure 3.15 showed that the leeway in axial direction is $2\,\mathrm{mm}$, in radial direction $0.95\,\mathrm{mm}$. It is therefore recommended to redesign the getter pump, by widening the inner radius by a value of at least $2\,\mathrm{mm}$, and by shortening each of the four cartridges by $1\,\mathrm{mm}$. This would lead to a leeway of $4\,\mathrm{mm}$ in axial and $2\,\mathrm{mm}$ in radial direction.

3.3.3. Cryogenic Cooling Circuits

The CPS is designed to operate over a very large temperature range from $3\,\mathrm{K}$ up to $620\,\mathrm{K}$. It is build in a shell-like structure as can bee seen in figures 3.9 and 3.16. From the outside to the inside the cryogenic components are build as follows: The outer part is formed by
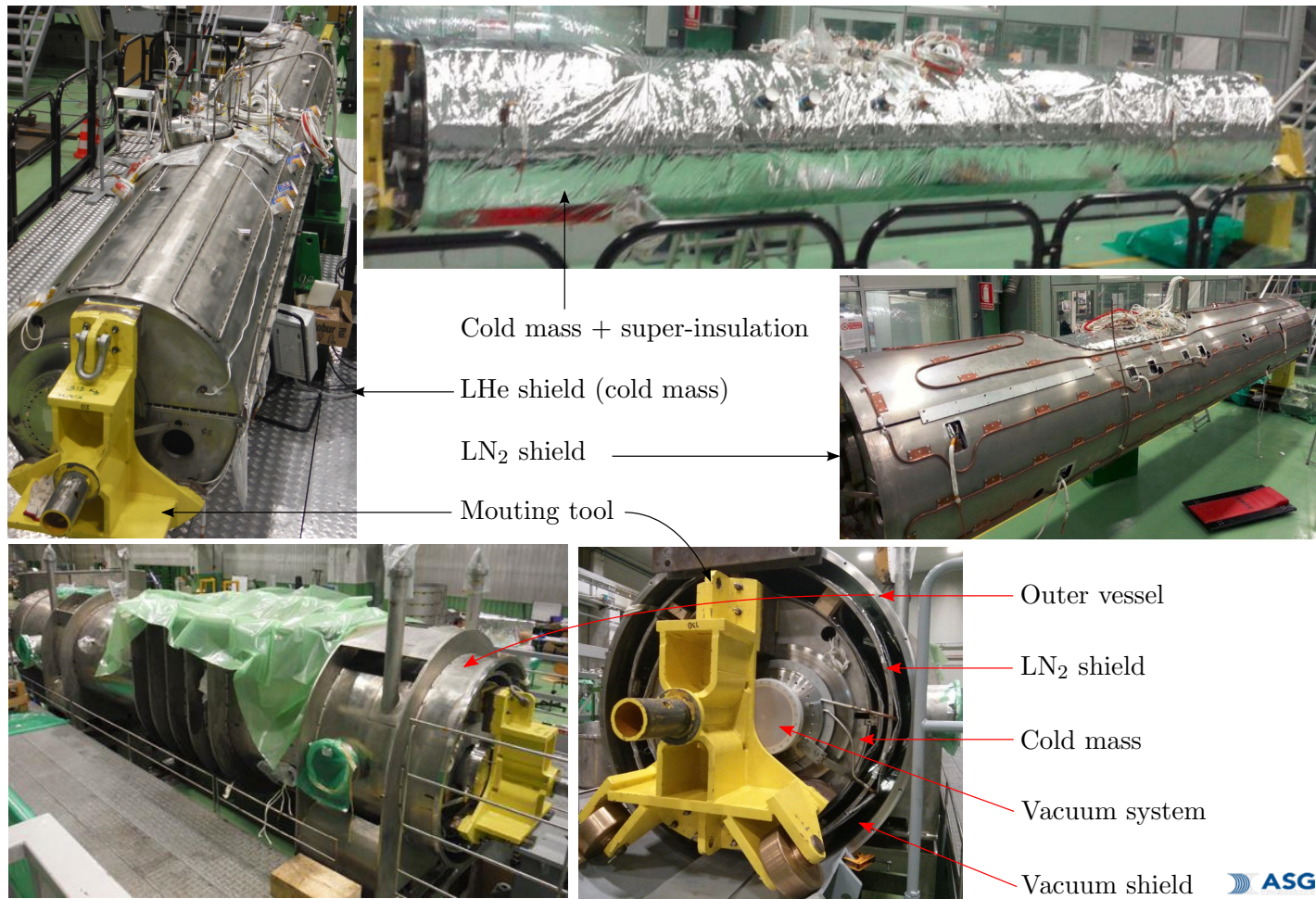
Figure 3.16.: CPS shell structure. Top left: Liquid helium cooling system, called cold mass. Top right: Cold mass with super-insulation. Middle right: Cold mass + super-insulation inside liquid nitrogen cooling shield. Bottom left: CPS outer vessel. Bottom right: View into the outer shell, with assembled cold mass and nitrogen cooling shield. Pictures are provided by courtesy of ASG.

the CPS cryostat vessel operated at room temperature, which is followed by an actively cooled liquid nitrogen shield. Inside the shield there resides the so called cold mass. This rather massive cryo-element is cooled with a liquid helium bath down towards 4.5 K. The cold mass is the supporting structure for the magnets with the vacuum system inside the magnet bores. Additional radiation shields are mounted in between the solenoids and beam tubes. The space between each shell, except for the inside of the magnets, is wrapped with super-insulation. It will be evacuated via an additional pumping station, consisting of a scroll- and a turbo molecular pump, to serve as an insulation vacuum.

To achieve a reliable operation of the CPS, well-defined temperatures for each component and shells are an absolute necessity. Therefore, three major cryogenic cooling circuits are implemented. For the supply with liquid gases, tritium laboratory hosts a cryogenic transfer line providing helium gas at 5 K and 5 bar.

LN$_2$-Circuit (77 K)

The CPS is supported by a supply of liquid nitrogen from the transfer line. Inside the CPS cryostat, an 11 ℓ vessel is installed to buffer liquid nitrogen. The outer radiation shield, beam tube elements 1, 6, and 7, the pump ports 1 and 2, and the radiation shield around section 7 can be cooled down to 77 K. Liquid nitrogen is provided to each part in a controlled manner by means of cryogenic valves, except in case of the radiation shield. The liquid nitrogen, after flowing through these parts, enters the buffer vessel. As soon as a liquid inventory has accumulated inside the vessel, the liquid will flow by gravity through the radiation shield of section 7. A relief valve ensures safe operation.

LHe-Circuit (4.5 K)

The cold mass is an actively cooled (4.5 K) support structure inside the 77 K radiation shield. The magnets and beam tubes are mounted inside this shell. Beside the cold mass, the solenoids and the cold gate valve will be cooled down towards 4.5 K with liquid helium. The cold mass and the cold gate valve body will be provided with liquid helium from the transfer line (5 K at 5 bar). During CPS operation, except during the cool down phase, both magnets and the cold gate valve head will be cooled from a 1300 ℓ helium reservoir inside the CPS turret. This vessel can be filled directly from the transfer line with liquid helium.

The current leads of the magnets are guided through the liquid helium vessel. They feature a handful of capillary holes, where liquid helium evaporates. This evaporating helium cools the current leads, and is then guided out of the vessel, through a heated water bath, back into the chiller.

LHe-Circuit (3 K)

Very low temperatures beyond the standard LHe regime are preferred for the cryogenic pumping elements, since the mean sojourn time of tritiated molecules on the argon frost layer will increase with decreasing temperature. More details are given in chapter 6. The beam tube sections 2 to 5 are specifically designed to be cooled down with liquid helium to the final temperature of 3 K. A vacuum pumping station is thus necessary to lower the temperature, following the vapour pressure curve in appendix E. This extensive 3 K pumping station will be connected to the CPS as an external component. Besides the big 4.5 K reservoir, a smaller vessel with a volume of 10.6 ℓ, is mounted inside the CPS turret to provide the 3 K liquid helium and to act as a heat exchanger. A cooling pipe is guided through the 3 K vessel, and in the extension it is wound around beam tubes 5, 4, 3, and 2, in this order, before entering back the 4.5 K helium reservoir. Liquid helium (4.5 K) will be led through this pipe from the transfer line. By passing through the smaller 3 K vessel
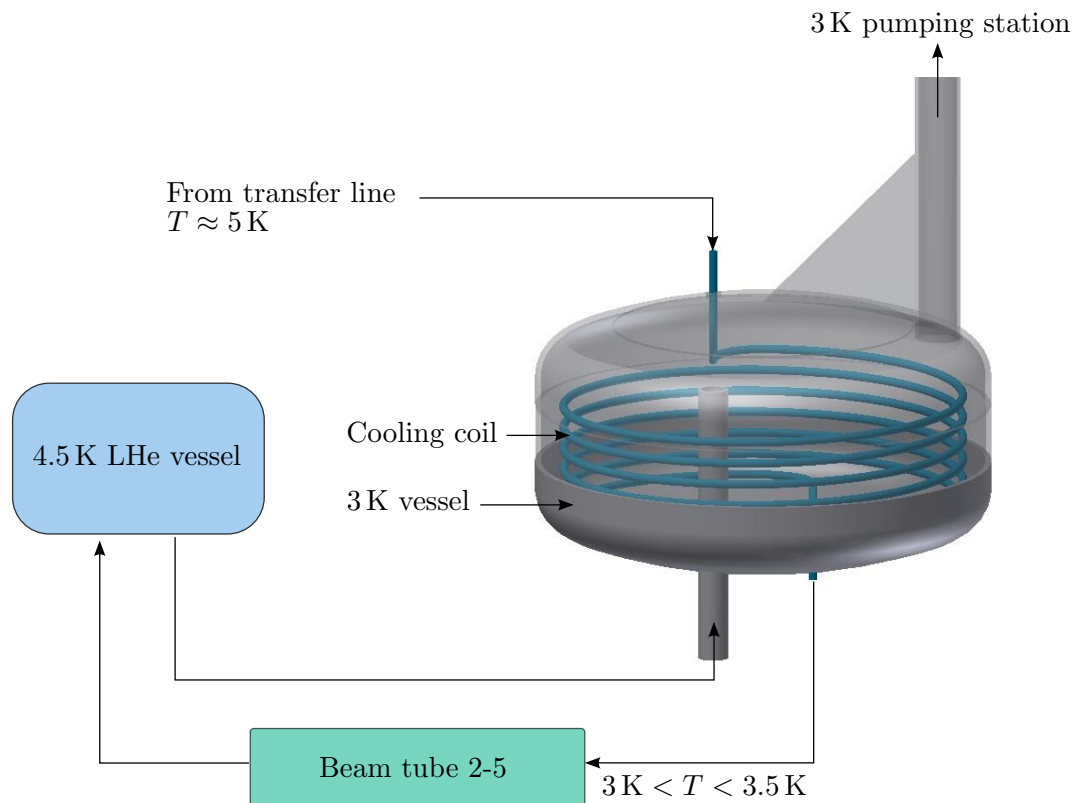
Figure 3.17.: The 3 K cooling principle. The 3 K vessel is filled with liquid helium from the 4.5 K vessel. The temperature is reached by lowering the pressure via the external 3 K pumping station. Helium from the transfer line is flowing through a cooling coil through this vessel, acting as a heat exchanger, into the cooling pipes of beam tubes 2-5.

Heat exchanger

Return pipe to chiller

From CPS 3 K vessel

Emergency valve

By-pass pipe + valve
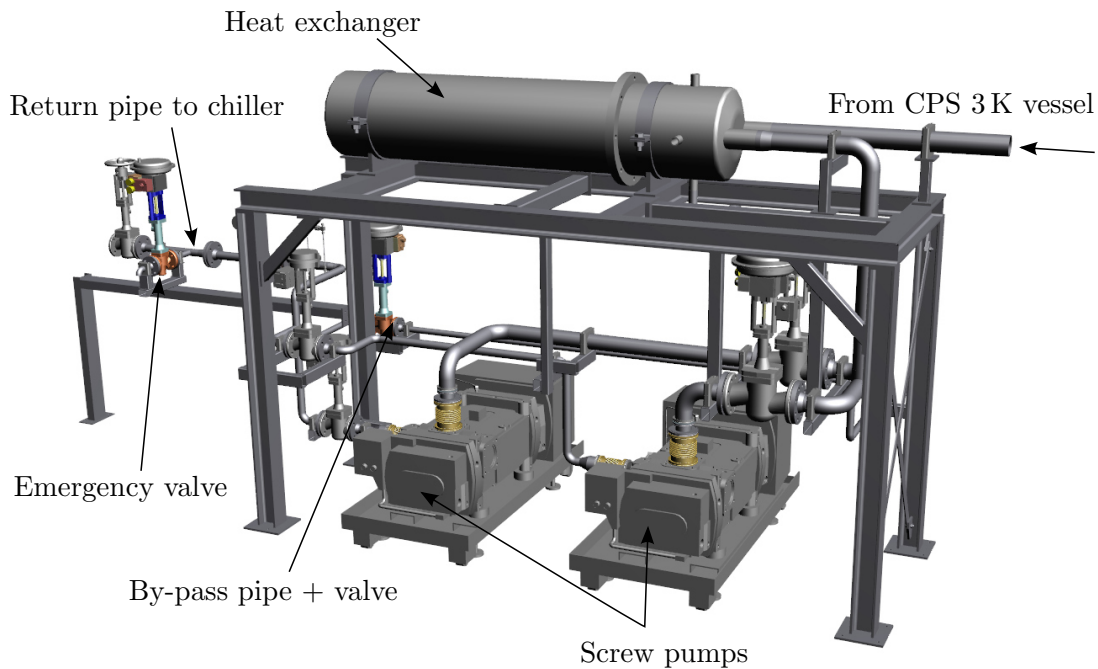
Screw pumps

Figure 3.18.: 3 K pumping station. Two screw pumps ($650\,\mathrm{m^3/h}$ each) will keep the 3 K vessel inside the CPS at an absolute pressure of about 240 mbar. The helium is heated before entering the pumps. For safety reasons a by-pass pipe and an emergency valve are installed. The pumping station will be positioned in a container outside the KATRIN transport hall.

it will be cooled down towards the required temperature. Figure 3.17 shows a drawing of the 3 K cooling principle inside the CPS.

The external 3 K pumping station consists of an electric heat exchanger, two dry compressing screw pumps, of the type Dryvac DV 650 from Leybold providing a pumping speed of $650\,\mathrm{m^3/h}$ each, and a couple of valves. Figure 3.18 illustrates the assembly. The pumping station is housed outside the KATRIN transport hall 457 and designed to pump a maximum amount of 2.5 g/s of liquid helium. It is connected via a flexible pipe designed for cryogenic purposes to the CPS. The two pumps can be separated via two valves each in case of maintenance work. Together, they will keep the absolute pressure inside the CPS 3 K vessel at about 240 K. The pumping speed is regulated via the frequency of the pumps. An electric heat exchanger, with 4.8 kW maximum power, which is monitored and controlled via three temperature sensors, will warm up the cold helium before entering the screw pumps. The extracted gas will then be led back into the chiller. The maximum pressure at the outlet of the pumps, and of the return pipe to the chiller, must not exceed 1.2 bar absolute, otherwise the vacuum pumps would operate out of their specifications. In case of overpressure, a by-pass pipe and an emergency valve will bring the system back to a well-defined and safe condition.

3.3.4. Modes of operation

During the long-term KATRIN operation, the complex CPS cryostat has to be driven in various modes. These include the bake-out procedure to minimise outgassing effects of the vacuum chambers, the cool down towards the required temperature of 3 K, the preparation mode, where the argon frost layer can be prepared, the phase of argon frost purging, and, finally, a calibration mode for the KATRIN spectrometer and detector. All modes are summarised from [118], and listed in the following paragraphs. The corresponding temperature regimes are given in appendix D. The CPS will thus be driven in cycles of

Bake-Out and NEG activation

Cool-Down

Argon-Preparation

Regeneration   Standby   CKrS Calibration

Standard Operation

(Accumulation of $1\,\mathrm{Ci}\ T_2$)

Warm-Up

Bake-Out and NEG activation
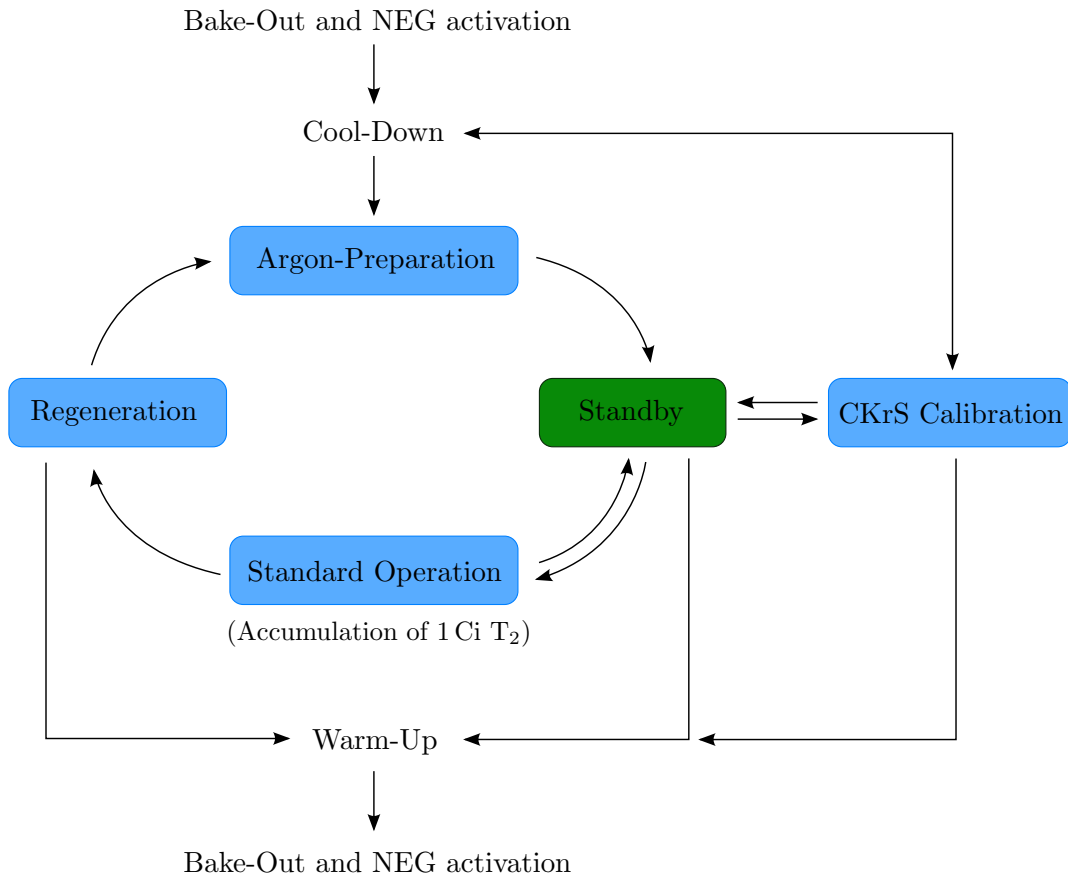
Figure 3.19.: CPS Operation cycles. Starting from the Bake-Out and NEG Activation, the CPS will be cooled down to $6\,\mathrm{K}$ inside beam tube elements 2-5. The CPS will run a cycle of argon preparation, standby, standard operation and regeneration. The standby mode is the initial state from which every other mode can be reached inside the circle, including the CKrS calibration phase. The warm up can be started from the standby mode, or, if the CPS has been exposed to tritium, after the regeneration phase.

Argon-Preparation $\rightarrow$ Standard Operation, including neutrino mass measurement, $\rightarrow$ and Regeneration, as illustrated in figure 3.19. During this cycle, and in the CKrS Calibration mode the magnets will remain running. The cold gate valve (V3) will be open only in the Standard Operation mode, otherwise it will remain closed.

Bake-Out and NEG Activation

The vacuum system has to be baked out before operation. This is achieved by heating the beam tube sections 1-5, including pump port 1, up to a temperature range of $500\,\mathrm{K}$. Likewise, the beam tube sections 6-7 as well as pump port 2 will be heated up to $620\,\mathrm{K}$, so that the inner surface is cleaned. When stainless steel is exposed to normal air, it stores small quantities of hydrogen, water, carbon dioxide, etc. These compounds are emitted from the metal surface under vacuum conditions, resulting in the so called outgassing process. By increasing the temperature, this process will run significantly faster. In doing so, the heating gradient must not exceed $30\,\mathrm{K/h}$, however, according to the specifications. During bake-out, at least one turbo molecular pump at pump ports 1 and 2 must run, since otherwise the pressure inside the beam tube would increase. Sections 6 and 7 will be baked out at higher temperatures. Within this process, also the getter pump in section 7 (see chapter 7 for more details) will be activated indirectly via thermal radiation. It is planned to hold a maximum temperature of $620\,\mathrm{K}$ for no longer than 24 hours. During the thermal

cleaning of the vacuum system and the simultaneous getter activation, the magnets have to be protected, in order to avoid non-reversible thermal damages. Therefore they will be purged with cold helium gas to a level below room temperature.

Cool-Down

It is planned to run the CPS with its beam tube elements 2-5 at a nominal temperature of 3 K. Before filling the different circuits with liquid gases, all corresponding elements have to be purged with gaseous helium, and nitrogen respectively, to avoid freezing of air pockets contained inside the system. A handful of valves at the top of the CPS turret allows to control all gas flow circuits. The nitrogen shield will be kept at 77 K, the cold mass including the magnets at 4.5 K. All solenoids will be filled with liquid at the same time. Beam tube sections 1 and 6, as well as pump ports 1 and 2 will be cooled down to 77 K with liquid nitrogen. Sections 2 to 5 are targeted to reach 3 K with the help of the external pumping station, see previous section 3.3.3. Section 7, including the getter pump, will be operated at 300 K. A special cooled radiation shield (77 K) will protect the solenoid 7 from radiative heating by beam tube 7. According to the specifications, the temperature gradient along the beam tubes and the cold mass must not exceed 30 K.

Argon-Preparation

The crucial pumping performance of the CPS is reached via a thin argon frost layer with a thickness between $1 - 3\,\mu m$. During the argon frost preparation at 6 K, nine capillaries in sections 2-4 will allow to inject gaseous argon into the vacuum system. The capillaries will be heated to a level of more than 40 K to avoid freezing inside. The argon will thus condense and form porous frost layers only on the cold inner side of beam tube elements 2-5. More details on the preparation procedure and the pumping properties are given in chapters 5 and 6. The sections 1 and 6, pump ports 1 and 2 will be at 77 K during the argon preparation mode, while section 7 will be at 300 K. After the argon injection is finished, sections 2-5 will be further cooled down to 3 K.

Standby

Most of the time the CPS will be operated in the Standby or the Standard Operation mode. The Standby mode is the final state after argon preparation. It represents a ready-to-operate condition of the whole component. The outer radiation shield will have a temperature of 77 K, the solenoids and the magnets will be at 4.5 K. The 4.5 K helium vessel and the 3 K helium vessel will be filled up to 90% each. The 3 K pumping station will be running and the desired temperature will be achieved inside the reservoir vessel. Section 1 and pump port 1 will be at 77 K, while sections 2-5 will be kept at 3 K with a prepared argon frost layer. Section 6 and pump port 2 will be at 77 K, as well as the radiation shield of section 7, which will be at 300 K. The cold gate valve (V3) between section 5 and 6, will be operated at 4.5 K, and will be closed as well as valve V2 at the entrance flange. This mode is the starting point for all further operation actions. Even during maintenance intervals at the KATRIN experiment, this mode will be held.

Standard Operation

This mode represents the same temperature values as the Standby mode, however, it includes active data acquisition as it will proceed during commissioning, various test runs, and the neutrino mass measurement. Correspondingly the cold gate valve has to be opened as well as all other beam tube valves. During regular tritium runs, the CPS argon layer will adsorb all migrating tritiated molecules from the DPS up to an accumulated activity of 1 Ci on the adsorption surface. According to design values this limit will be reached after a time period of 60 days. Afterwards, a complete cycle of Regeneration, Argon-Preparation, and Standby has to be executed.

CKrS Calibration

Condensed krypton ^{83m}Kr, with its well-known characteristic emitted conversion electron energies at 17.8 keV, will be used to calibrate the tandem spectrometer (see section 3.3.6). To do so, a cold finger with the substrate on its surface will be moved to a well-known position into the magnetic flux tube via the vertical branch of pump port 2. By cooling beam tube 7 to 77 K, the heat load onto the specimen will be reduced. All other cryostat temperatures will remain identical to the Standby mode. The cold gate valve between section 5 and 6 will be closed during calibration measurements to suppress β-decay electrons from the actual tritium content of WGTS and DPS.

Regeneration

After the argon frost layer has accumulated an activity of 1 Ci, it has to be renewed. First, the cold gate valve (V3) and the valve between DPS and CPS (V2) will be closed. The beam tube elements 1-5 and pump port 1 will be heated up to 100 K, including the valve V3, to evaporate the condensed and tritiated argon frost layer. All other temperatures will remain identical to the Standby mode. With a purging rate of 2 ℓ/s, warm helium gas will be injected via a special tube at the gold gate valve. The tritium-argon-helium mixture will be pumped out at pump port 1 via redundant roots pumps [119]. When the purging process is finished, the CPS will be cooled down towards the temperatures required for the Argon-Preparation mode. A new, clean, active argon frost layer can then be prepared and the CPS will be set to Standby mode again.

Warm-Up

Warming up the CPS cryostat may be forced in case of extended maintenance intervals, leakage in the system, or in case of insufficient getter operation. Depending on the actual working process, the argon frost has to be purged before warm up, if exposed to tritiated molecules. Then, the liquid helium vessels, the solenoids, the cold mass, and the beam tube, including V3, have to be warmed up in a controlled way up to a first holding point at 77 K. Then the complete CPS can be heated up to 300 K. The heating rate should not exceed a value of 30 K/h. Once the entire system is at 77 K, the overall temperature gradient during warm-up should not exceed 30 K.

3.3.5. Forward Beam Monitor

A significant part of the overall systematic uncertainty budget in the neutrino mass analysis can arise from instabilities of the tritium source. This includes fluctuations in temperature, column density (gas injection pressure), and the resulting source activity. One way to detect potential instabilities is by monitoring the intensity of the β-decay electrons. A non-zero change in intensity over time is a hint for a variation of the scattering processes inside the tritium source. On the one hand this could indicate a non-stable column density, and hence non-stable injection conditions for tritium, or, on the other hand, it could point to a change in the isotope composition, or be a hint for impurities of the injected gas.

The aim of the Forward Beam Monitor (FBM) is the permanent monitoring of the β-decay electron flux with a precision of 0.1% in an outer region of the magnetic flux tube. The FBM will be located inside the pump port 2 of the CPS. Figure 3.20 shows the extensions of the horizontal CPS pump port and the mounting position of the FBM. The FBM is based on a doped silicon detector, bonded on an Al_2O_3 board and fixed on a manipulator. Via cogwheels the FBM can be moved in radial direction along the x-y-plane. The manipulator and detector will be mounted on a 2.4 m long stainless steel tube, connected at one end to a second manipulator at the outer horizontal part of pump port 2. This tube (outer
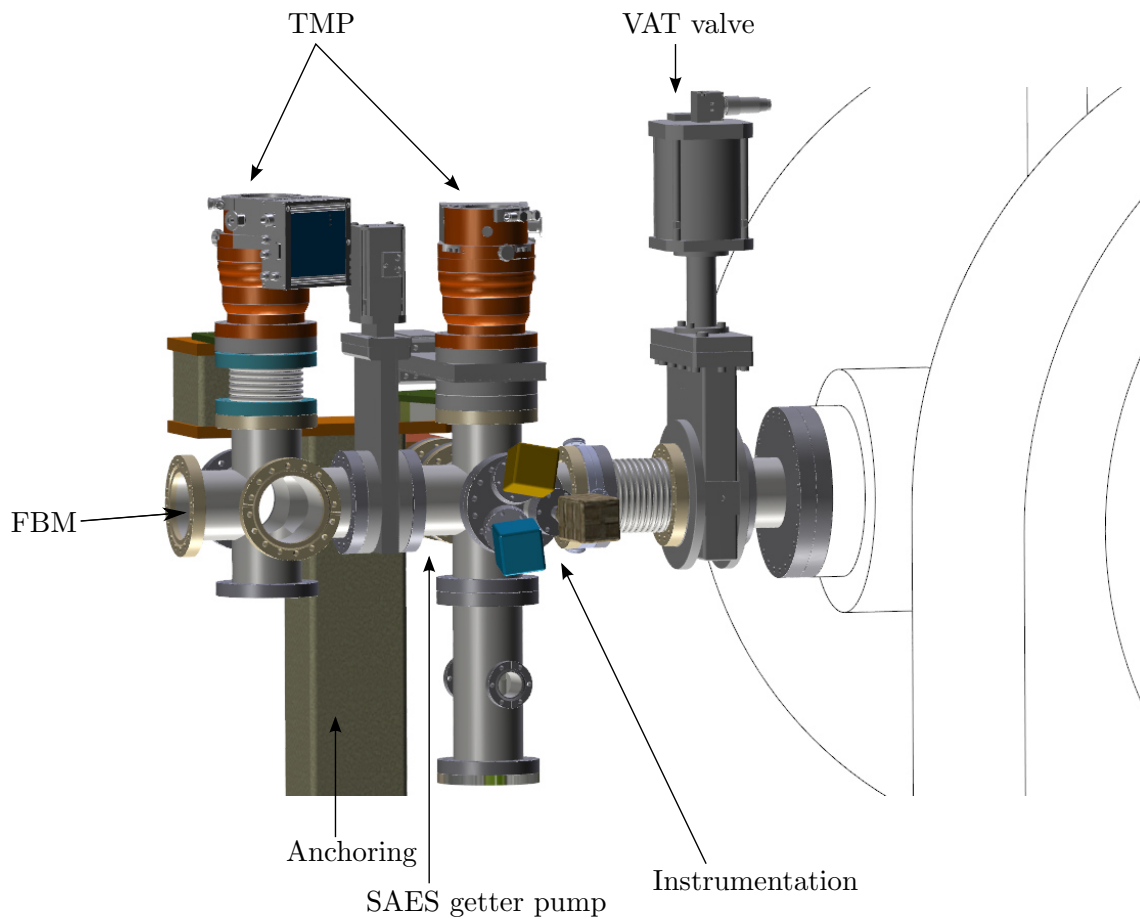
Figure 3.20.: Mounting port for the forward beam monitor (FBM). The FBM is pushed all the way through the vacuum extension into pump port 2. The vacuum instrumentation comprised several pressure gauges which cover a pressure range from atmospheric pressure down to UHV, and a residual gas analyser (RGA).

diameter: 54 mm, wall thickness: 4 mm) can be driven in the x-direction into the centre of the pump port. The mounting position defines the z-position of the FBM.

The most challenging issues, when considering to construct an adequate monitoring system, are:

- **The detector dead layer thickness:** Electrons in the keV-range exhibit very low mean free paths in matter due to their frequent inelastic scattering. For example, the mean free path of a 5 keV electron in silicon is only about 90 nm [120]. The dead layer should therefore be extremely thin, so as not to lose a significant fraction of signal electrons.

- **Size of the detector and its housing:** The detector is to be positioned in an outer part of the magnetic flux tube larger than 191 Tcm². Crossing the nominal flux tube must be avoided, so that no interference with signal electrons occurs. At the design position of the FBM, an electron flux of approximately $10^6 (\mathrm{mm}^2 \cdot \mathrm{s})^{-1}$ is expected [121]. The active area of the detector can thus be small (of the order of 0.1 mm² [121]), allowing to reduce noise and obtain good energy resolution.

- **Signal to noise ratio:** As in all detector systems, the ratio of signal to noise, as well as the energy resolution, are the most prominent properties. Noise can be created by fluctuations in temperature, and by the read-out and control electronics. All effects have to be well known when monitoring the KATRIN tritium source activity.

The forward beam monitor is currently under development by the Wuppertal group of the KATRIN collaboration. The basics of the system are given in [115] [121] [122]. It will be constructed and commissioned in the framework of the ongoing thesis of E. Ellinger.

Thermal impact of the FBM on the argon frost layer

The commercial software COMSOL Multiphysics allows to investigate the impact of different forward beam monitor temperatures on the cold stage. This is achieved by the COMSOL heat transfer (ht) module, as described in chapter 5. The detector board, including the electronics of the FBM will deposit thermal energy onto the argon frost layer via thermal radiation. This process has been calculated by defining a set of FBM operating temperatures between $-20°C$ and $+60°C$ with the unit being positioned in the centre of pump port 2. The rectangular board surface is assumed to point towards the cold stage and to consist of Al_2O_3 (ceramic). It will be approximately 50 mm wide and 30 mm high, with a 1 mm thickness. For the simulation, the temperature was defined at a position equivalent to the board surface, on the opposite side of the CPS cold stage. At room temperature, Al_2O_3 exhibits an emissivity of $\epsilon = 0.9$ [123], which does not significantly change as a function of temperature in the considered interval.

In a first simulation step, the irradiation properties without forward beam monitor were determined. Figure 3.21 shows the simulated radiation flux of the cold gate valve, section 6, pump port 2, and section 7, during standby operation, as modelled with COMSOL Multiphysics. To optimise the computation time, all bellows were approximated by simple tubes, with adequate thermal conductivity. (Appendix A contains an analysis on this simplification in describing bellows in thermal simulations.) The temperatures of each component in the model were set according to the modes of CPS operation (see section 3.3.4). The emissivity of the gold-plated parts was defined to 0.02, and that of the bare stainless steel components to 0.2. A generic temperature independence of the coefficients was assumed in the particular temperature regimes. This 'blank case' simulation (without FBM) leads to a standard value of 0.152 W for the radiative power which enters the cold stage. Except for positions at the edges, the incoming radiation is distributed almost homogeneously.
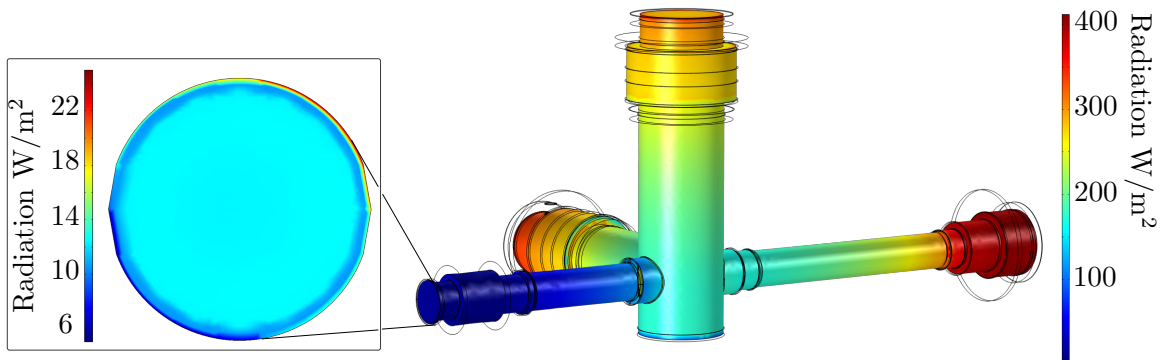
Figure 3.21.: Incoming radiation onto the Ar frost layer. The irradiation is homogeneously distributed, except in the vicinity of the edges. Without any instrumentation the cold stage has to deal with 152 mW radiative heat load.
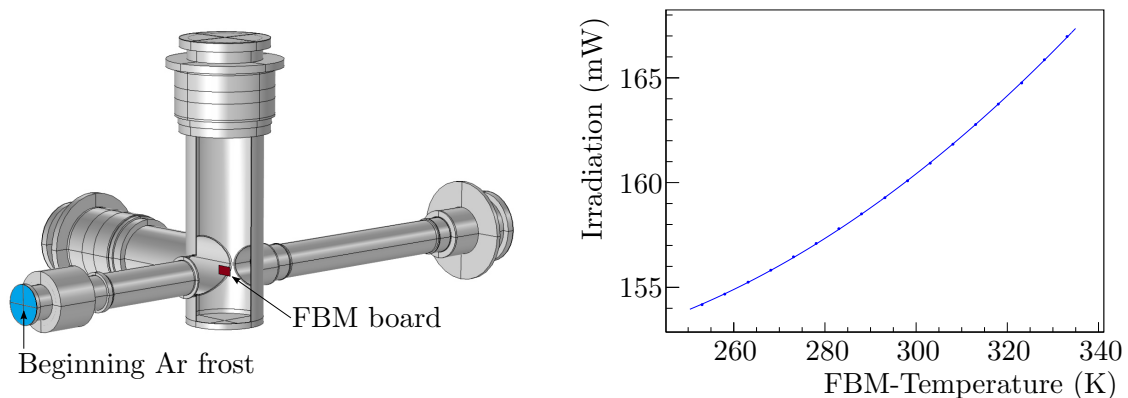
Figure 3.22.: Thermal impact of different FBM temperatures onto the argon frost layer. Left: Geometry of the COMSOL model (without the NEG pump), the FBM board is positioned in the centre of pump port 2. Right: Irradiation in mW onto the Ar frost layer in dependency of the FBM board temperature in K.

In a second simulation the FBM was positioned in the centre of pump port 2. While increasing the temperature of the forward beam monitor successively from $-20°C$ to $+60°C$, the corresponding increase of irradiation onto the argon frost layer was simulated. Figure 3.22 presents the thermal, irradiative impact of different FBM temperatures onto the crucial argon frost layer. This parameter can be approximated by a second order polynomial in the given temperature interval between $-20°C$ and $+60°C$:

$$P_{\mathrm{irrad}} = a_0 + a_1 \cdot T_{\mathrm{FBM}} + a_2 \cdot T_{\mathrm{FBM}}^2 \quad , \tag{3.17}$$

with the coefficients listed in table 3.8. For conditions where the forward beam monitor is temperature-stabilised (for reliably operation) at 293.15 K, the irradiation onto the argon frost layer will increase by a factor of 4.6% in total only, which should not impact its pumping properties. Of course, the FBM can be operated at lower temperatures than

Table 3.8.: Fit parameters according to equation 3.17.

Parameter	Value	Uncertainty	Unit
a_0	181.82	0.97	mW
a_1	$-3.12 \cdot 10^{-1}$	$0.07 \cdot 10^{-1}$	mW/K
a_2	$8.05 \cdot 10^{-4}$	$0.11 \cdot 10^{-4}$	mW/K^2

293.15 K, thus reducing the irradiation onto the argon frost layer.

3.3.6. Condensed Krypton Source (CKrS)

When measuring the neutrino mass with a sensitivity of $0.2 \, \text{eV}/c^2$, the tandem spectrometer section needs to be calibrated frequently. An ideal source to do so is given by K-shell conversion electrons of ^{83m}Kr. These mono-energetic conversion electrons possess a very well-known energy of $(17824.3 \pm 0.5) \, \text{eV}$ [74], and a line width of only 2.7 eV [116]. These K-shell electrons are predestined for spectrometer calibration purposes, since their energy is very close to the end-point energy of the tritium β-decay spectrum.

A so-called quench Condensed Krypton Source (CKrS) from the University of Münster will be installed at the vertical pump port 2 at the end of the CPS. The calibration source is an external device separated from the CPS via an all-metal gate valve. During the calibration mode, this gate valve is opened and the condensed ^{83m}Kr source will be moved into the flux tube of pump port 2. There it will be shifted stepwise in the x-y-plane to cover the entire flux tube. This means to cover a circular area of roughly 140 mm in diameter, so that each pixel of the focal plane detector can be calibrated individually. After a calibration run has been finished, the ^{83m}Kr source will be refracted so that the gate valve at pump port 2 can be closed again.

The CKrS set-up itself consists of a gas preparation system, which provides the ^{83m}Kr via the electron capture (EC) process of ^{83}Rb, a slow control system for controlling purposes, an ellipsometry set-up to monitor the cleanliness, a laser ablation unit to clean the substrate surface, a cold finger with the condensed ^{83m}Kr on the substrate, and a variety of vacuum components, such as bellows to decouple vibrations, pressure gauges, and different kinds of pumps.

A key part of the CKrS is the HOPG (Highly Oriented Pyrolytic Graphite) substrate, which is placed on a sample holder (cold finger) at the second stage of a two-stage cryocooler. The working temperature will be about 25 K, which is monitored by a Si-diode temperature sensor [124]. Gaseous ^{83m}Kr will be frozen onto the electrically conductive substrate. To avoid accumulation of external residual gases during measurements, an additional baffle around the source has been implemented, which is thermally dumped at the cold finger. A highly clean krypton layer is essential for calibration purposes, as in case of increasing amount of impurities, the energy line of the decay electrons will shift. With ellipsometry the contaminations on the substrate can be monitored, not the krypton layer thickness itself [124]. Therefore a HeNe laser is installed in the set-up. To clean the surface of the substrate before the krypton layer is condensed, an ablation laser combined with a substrate heater is used. For more information see [81] [116] [124].

4. The CPS Magnet Safety System

After technical problems with the initial design of the DPS2-F magnet safety system, an improved safety concept was developed for both the CPS and the WGTS cryostats in the KATRIN transport section. The DPS2-F cryostat was in operation until mid-2012, when a protection diode was damaged during a quench of a superconducting magnet coil. In case of a quench, superconductivity is lost on a rather short timescale during magnet operation. As a result, the diode experienced a short circuit due to overheating. As the unit was not accessible without major repair work on the entire cryostat, the DPS2-F had to be replaced by a new system [125]. In order to avoid such an incident at the CPS and the WGTS cryostats, their magnet safety systems were redesigned. The main focus was targeted to improve the reliability and accessibility of the protection diodes.

The adiabatic guiding of the signal electrons through the CPS requires strong magnetic fields between $5.1\,\mathrm{T}$ and $5.7\,\mathrm{T}$ with negligible fluctuations in time to guarantee adiabatic transport conditions [58]. The seven superconducting magnets will all be operated with the same nominal current of $I_\mathrm{nom} = 200\,\mathrm{A}$. With a total inductance of $177\,\mathrm{H}$, this current leads to a stored energy of $3.5\,\mathrm{MJ}$ in the whole system. The magnets will be driven in series, so that the magnet system can only be operated as one coherent unit, i.e. single magnet modules cannot be driven independently. Accordingly, if one single magnet of the assembly would fail as a result of a quench, the complete system has to be shut down. This implies discharging of seven solenoids at once, or in other words safely dumping the stored energy within a few seconds. To do so, silicon diodes and an external dump resistor are installed in parallel to the magnet coils. The diodes serve as an electric switch, guiding the current around the quenched coil. In view of the high currents and the amount of stored energy, no commercial diode system was found to be applicable. Thus, the resulting magnet safety system was redesigned by taking into account long-term experience from other coupled superconducting beam line magnets, in particular from the LHC [126] [127]. The optimum solution for our case is given by a stack of diodes, type SKN 240/04 from SEMIKRON. A massive array of gold-plated copper heat sinks prevents the diodes from overheating ($T_\mathrm{max} = 450\,\mathrm{K}$). Table 4.1 summarises the specifications and hardware requirements for the CPS by-pass diode stacks, the implemented test set-up, and the CPS assembly. In order to verify the performance of this special concept, a series of test measurements at cryogenic conditions has been carried out for each diode stack. The experimental set-up is described in section 4.2, while the results of the tests and their impact on the CPS are discussed as well in section 4.2 and 4.3.

Table 4.1.: Specification for the CPS by-pass diode stacks and the hardware, as used for the testing procedures of this thesis.

Diodes and by-pass diode stacks	
Forward-Current	$I = 200\,\text{A},\ \Delta I = 1\,\text{A}$
Forward-Voltage U_f at $200\,\text{A}$	$(0.93 \pm 0.01)\,\text{V}$ at $293\,\text{K}$
	$(1.25 \pm 0.01)\,\text{V}$ at $77\,\text{K}$
	$> 3.5\,\text{V}$ at $4.5\,\text{K}$
Reverse-Current I_r	$< 1\,\mu\text{A}$ at $300\,\text{V}$ reverse-voltage
	at $293\,\text{K}$ after each cycling at $77\,\text{K}$ and $4.5\,\text{K}$
Maximum Temperature	$T_\text{max} < 450\,\text{K}$ during each test cycle
	$(200\,\text{A}$ for $253\,\text{s})$
Number of test cycles at $4.5\,\text{K}$	> 5 cycles
Stack assembly	Reliable and controlled contact pressure
	between diode and heat sink
Deviation in diode thickness	$\leq 0.2\,\text{mm}$
Test set-up	
Pulse duration during characterisation	$t < 200\,\mu\text{s}$
Required temperatures for stress tests	$4.5\,\text{K}$ (cryostat)
	$77\,\text{K}$ (Styrofoam box)
Data acquisition	Diode voltages $(U = \pm 10\,\text{V},\ \Delta U = 1\,\text{mV})$
	Heat sink temperatures
	$(T = 4.5 - 550\,\text{K},\ \Delta T = 1\,\text{K})$
	Reverse-Voltage $(U = \pm 2200\,\text{V},\ \Delta U = 1\,\text{mV})$
	Reverse-Current $(I = 0 - 10\,\text{mA},\ \Delta I = 1\,\mu\text{A})$
Sampling rate during test cycles	$> 1000\,\text{Hz}$
CPS cryostat assembly	
Diode stacks must be accessible / exchangeable without cutting the CPS cryostat structure.	
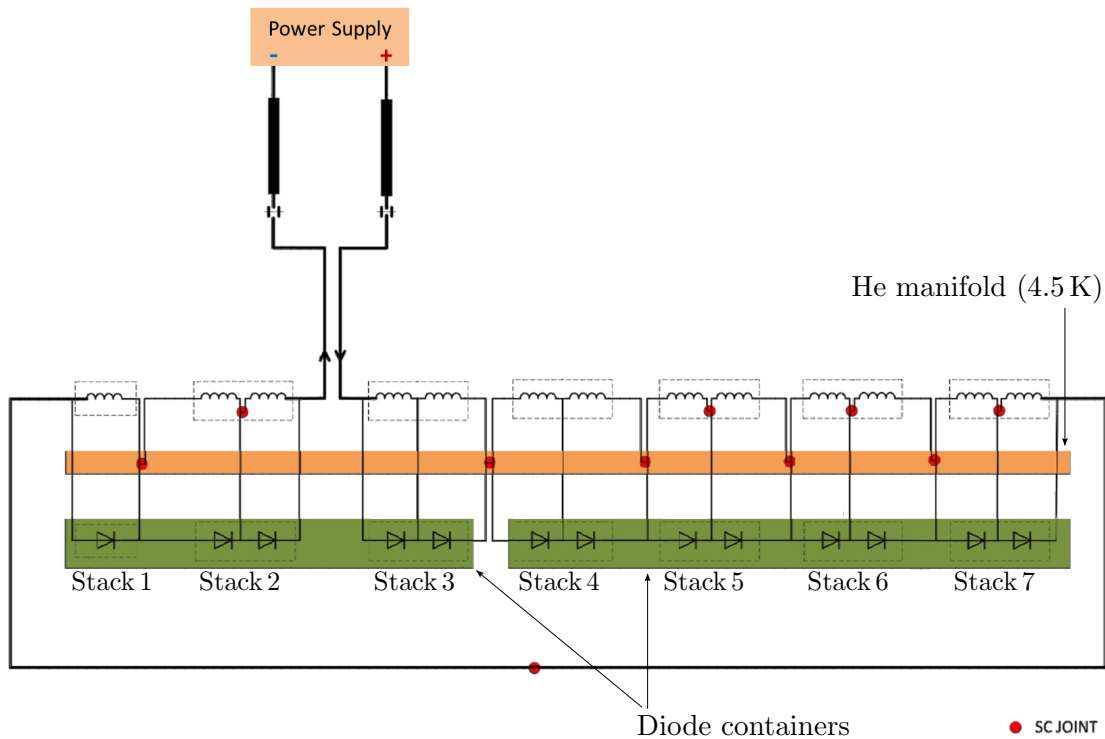
Figure 4.1.: Scheme of the electric circuit inside the CPS. There are two diode-housing containers (see also section 4.3), with one including three and the other one four diode stacks. Both are connected to one single helium manifold, which allows to cool down the diodes to liquid helium temperature. Electrically, the diodes are installed in parallel to the solenoid coils, allowing the CPS to be operated in only one magnetic field direction.

4.1. Dimensions of the quench protection system

A sketch of the electrical circuit of the CPS magnets, including its magnet protection diodes, is given in figure 4.1. The CPS consists of seven solenoids, six of them (number 2 to 7) are subdivided into two sections each. Each section is protected by its own diode, which is mounted in parallel to the coil. Thus the magnet safety system consists of a total of 13 diodes, which are grouped in pairs of so called diode stacks. This results in six stacks with two diodes each and one stack with a single diode. The CPS magnets can thus be operated with one current direction only, since there are no anti-parallel oriented diodes. In the KATRIN assembly the specific magnetic field direction, which corresponds to the current direction, points due south, from the KATRIN detector to the tritium source.

Figure 4.2 illustrates the electrical scheme of a diode in protecting a quenching coil. A quench of L_2 is symbolised by a resistor R_q in series to L_2, reflecting the instantly increasing ohmic resistance of the coil during a quench. Accordingly the turn-on voltage of the by-pass diode D_2 is exceeded, which is strongly temperature-dependent. In contrast to normal-conducting metals, the resistance of semiconductors increases with decreasing temperature. Once the voltage drop across the coil exceeds the turn-on voltage, the diode serves as an electric switch, guiding the current around the quenched coil, and thus avoiding overheating of the magnet wiring. All magnets in the system are discharged via this specific diode and an external dump resistor.
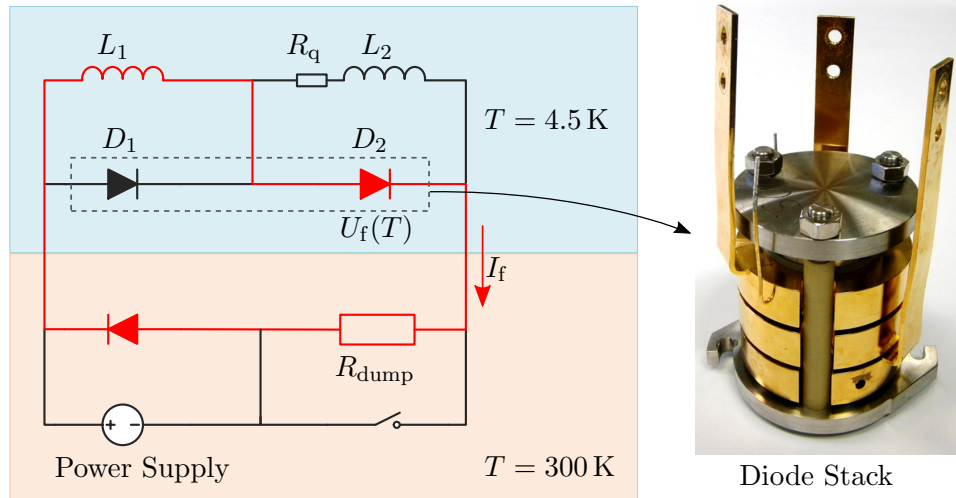
Figure 4.2.: Simplified electric circuit of the magnet protection system. In red indicated is shown the way of the current during a quench of coil L_2 with a resistance R_q in series. Components in the blue coloured area are at $4.5\,\mathrm{K}$, components in the orange box are at room temperature. The two diodes in the cold regime are grouped together in a diode stack.

Quantitatively the CPS will be operated with a nominal current density in the range between $118.58\,\mathrm{A/mm^2}$ and $118.63\,\mathrm{A/mm^2}$. The solenoids will store $3.5\,\mathrm{MJ}$ inside their magnetic field. This amount of magnetic energy is converted into electric energy, according to Lenz's law, and subsequently into thermal energy via the by-pass diode and the dump resistor. A critical temperature of $450\,\mathrm{K}$ must not be exceeded, as in this case the silicon wafer of the diode would be damaged permanently [128]. The diodes are thus sandwiched between very massive copper blocks. The copper mass acts as heat sink to prevent over-heating. The dimensioning of the heat sinks and the dump resistors has been performed in collaboration with by A. Hervé [127] and D. Hagedorn [126] from CERN and W. Gil from KIT [129] [130] [131]. There adiabatic conditions during a quench are assumed, as the most conservative approach. By limiting the maximum temperature to $450\,\mathrm{K}$, according to the specifications of the diode, one calculates a required heat sink mass m for one diode based on the following power balance:

$$m \cdot C_{\mathrm{pCu}}(T) \cdot \frac{dT(t)}{dt} = I(t) \cdot U_{\mathrm{f}}(T(t)) \tag{4.1}$$

$$\Rightarrow \frac{dT}{dt} = \frac{I(t) \cdot U_{\mathrm{f}}(T(t))}{m \cdot C_{\mathrm{pCu}}(T)} \quad , \tag{4.2}$$

with the thermal capacity of copper C_{pCu}, and the temperature dependent forward-voltage across the diode $U_{\mathrm{f}}(T(t))$. With Kirchhoff's second law one obtains

$$L\frac{dI(t)}{dt} + U_{\mathrm{f}}(T(t)) \cdot N_{\mathrm{diodes}} + R_{\mathrm{dump}} \cdot I(t) = 0 \quad , \tag{4.3}$$

with the number of diodes N_{diodes}. From this a heat sink mass for one diode was calculated to $m = 500\,\mathrm{g}$. The dump resistance was chosen to $R_{\mathrm{dump}} = 0.46\,\Omega$. According to equation 4.3, an exponentially decreasing current during a quench is expected. Since no exactly matching current could be applied to the diodes during test measurements (as described in section 4.2), a constant current of $200\,\mathrm{A}$ was applied, which corresponds to the nominal CPS current. In order to transfer a quench-equivalent electric energy into thermal energy, the current to be applied to the diodes had to last for at least $195\,\mathrm{s}$. During the actual test measurements this duration was extended to $253\,\mathrm{s}$, to provide a safety factor of 30%
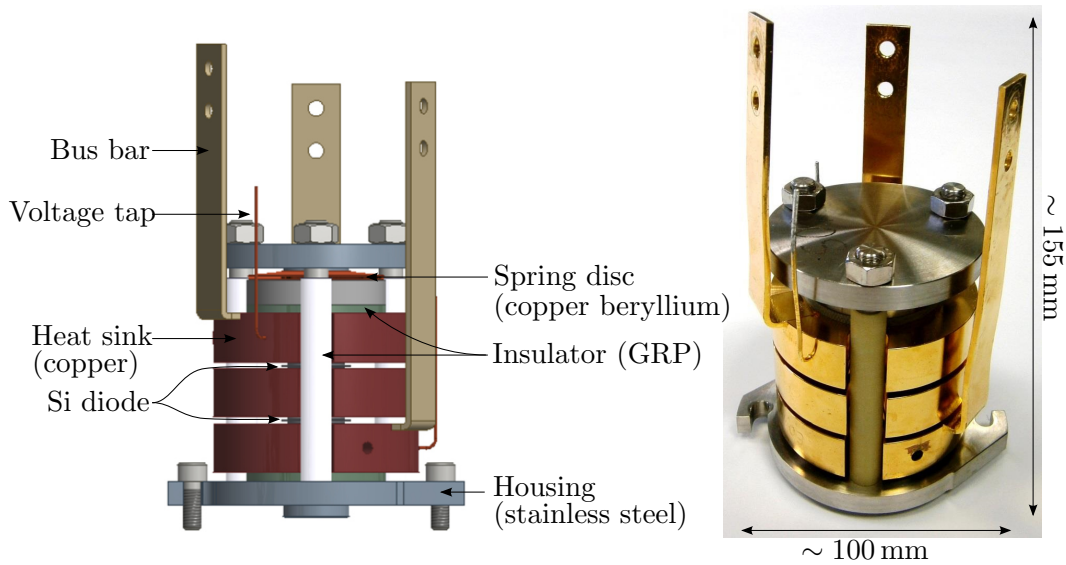
Figure 4.3.: Diode stack assembly for the CPS with two by-pass diodes (GRP = glass-fibre reinforced plastic).

for the later use.

The final design of the by-pass diode stack is shown in figure 4.3. Each stack has a total heat sink mass of 1350 g, which is 35% more than the proposed value. The heat sinks are gold-plated copper discs of 16 mm hight with a diameter of 68 mm. A notch on one side is used for concentric positioning of the diodes during mounting. In azimuthal direction, with 120° spacing, a twelve millimetre wide groove holds an insulator tube for the through-going bolts, which hold together the whole assembly. Each heat sink has been gold plated for well defined thermal and electrical contact to the diode. In order to monitor the voltage across the diodes during both the actual test experiments and the later CPS operation, voltage taps, in the form of thin copper wires with a diameter of 1 mm, have been brazed to each heat sink. The heat sinks also feature small holes, 4 mm in diameter and 22 mm in length, which house PT 500 sensors. Their task is to monitor the temperature during the test experiments, as discussed in the following section. The connection of the diode stacks with the solenoids is implemented as oxygen-free copper bus bars, with a length of 132 mm and a cross section of 32 mm^2. The bus bars are brazed to each copper disc. The upper ends of the bus bars are connected to the CPS bus bar system (see section 4.3). The angle between the three bus bars is 120°, in the assembled stack.

The silicon diodes are power rectifier diodes of the type SKN 240/04 from SEMIKRON. Normally this type is supplied in a housing. However, in this application only the bare diodes without the housing were used. The composition and the cross section is shown in figure 4.4. The bare diodes are about 2.3 mm thick and consist of the silicon wafer and a thin tin/silver contact disc soldered to each side. The contact discs are not exactly parallel, with thickness variations of ±0.31 mm. The surface area of a disc typically corresponds to 2.84 cm^2 with a diameter of 19 mm. Hence the overall contact surface for cooling is approximately 5.7 cm^2. To establish a well-defined thermal contact, a thin indium foil was placed on the top and at the bottom of each diode before mounting. The edge of the silicon wafers are covered by insulating plastics.

The copper discs and diodes are fixed in a stainless steel housing, which is electrically insulated via GRP (glass-fibre reinforced plastic) based plates and tubes. The two caps at bottom and top are connected with three rods. At the bottom end the rods have been spot-welded to the cap. On the top end they feature a gold-plated screw thread for fixation.
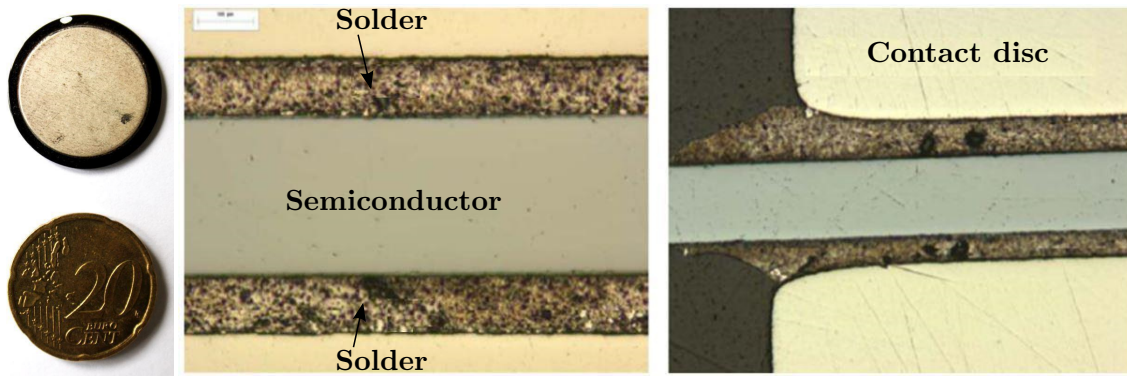
Figure 4.4.: Composition of a diode. Left: The bare diode in comparison to a 20 Euro cent coin. The black frame is insulating plastic. Right: Cross section of the diode (taken from [132] and [133]). In the middle is the silicon wafer, on top and on bottom a thin tin/silver disc is soldered to provide the electrical and thermal contact.

The gold plating serves as grease for the nuts. The mounted assembly is finally pressed together with a force of 2 kN to guarantee optimal thermal and electrical contact [134]. A spring disc, made of copper beryllium, is placed between the top cap of the housing and the insulator, in order to maintain the pressure over long time periods with many thermal cycles. In doing so, the spring disc compensates thermal expansions during temperature cycling.

4.2. Experimental set-up for diode tests

Previously, silicon diodes equipped with massive copper heat sinks as quench protection have been thoroughly investigated at the LHC-Division of CERN [135] [136] [137]. Based on these encouraging results, endurance tests at cryogenic temperatures were carried out for the KATRIN diode stacks. Before mounting a diode into the stack assembly, it had to pass several specifications and acceptance tests. These included geometrical properties, such as parallelism of the two contact faces, mechanical properties, such as structural stability after shock cycling in liquid nitrogen, and electric properties, such as blocking of reverse-voltages of up to 300 V. The acceptance conditions are described in particular in more detail in section 4.2.1. After assembly, each diode was characterised individually, with regard to its temperature-dependent electrical characteristics. This was achieved by applying short current pulses of up to 250 A and by monitoring the voltage drop as a function of current. This procedure was performed at two different temperatures, 77 K and 293 K. The aim there was to employ the diodes themselves as highly sensitive temperature sensors for the endurance tests for a nominal current of 200 A at cryogenic temperatures (see figure 4.8 and section 4.2.2). More details on the set-up of the experiment are given in section 4.2.3. The results of the current endurance tests for the final assembly of the diode stacks at 77 K under non-adiabatic conditions are given in section 4.2.4, the corresponding results at 4.5 K under adiabatic conditions are summarised in section 4.2.5. With this final test campaign at liquid helium temperature, the dimensioning of the diode stacks has been verified. In addition, the turn-on voltage at 4.5 K, an important parameter for the design of the magnet safety control system, was determined for each diode in the final assembly.

4.2.1. Selection tests for CPS diodes

The geometric surface parallelism of the bare diodes (type SKN 240/04 from SEMIKRON) was tested with an outside micrometre. The thickness of each diode was measured at four

Cool down
$295\,\mathrm{K} \to 77\,\mathrm{K}$
$\Delta t \approx 1\,\mathrm{min}$

Room temperature
Forward-voltage at $5\,\mathrm{A}$
$\to U \approx 0.75\,\mathrm{V}$
Current at $U_\mathrm{r} = 300\,\mathrm{V}$
$\to I < 1\,\mathrm{\mu A}$

Liquid nitrogen temperature
Forward-voltage at $5\,\mathrm{A}$
$\to U \approx 1.1\,\mathrm{V}$
Current at $U_\mathrm{r} = 300\,\mathrm{V}$
$\to I < 1\,\mathrm{\mu A}$

Warm up
$77\,\mathrm{K} \to 295\,\mathrm{K}$
$\Delta t \approx 10\,\mathrm{min}$
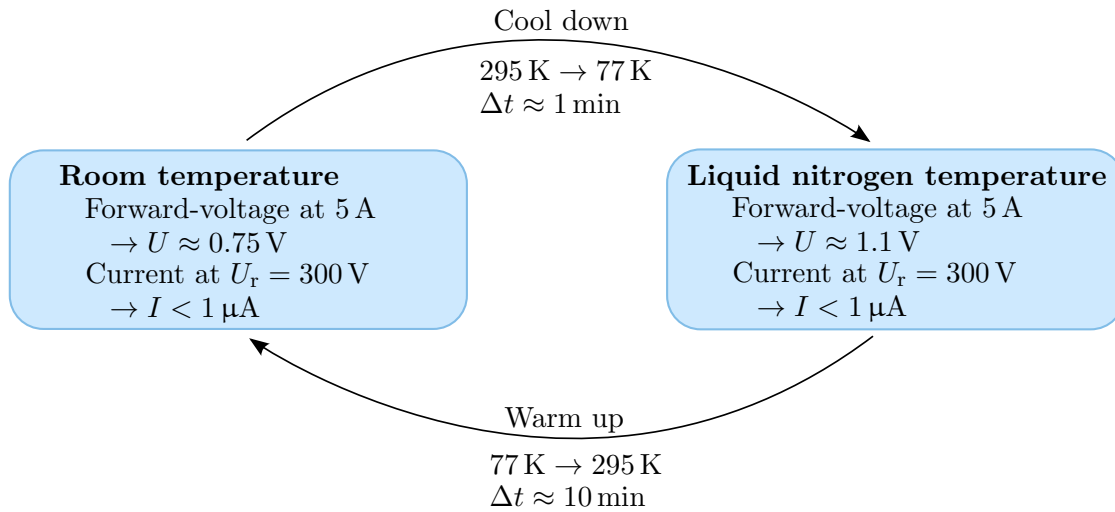
Figure 4.5.: Temperature cycle of the pre-selection tests for the CPS diodes. The test stack with the diodes was shock cooled by dipping it into a dewar filled with liquid nitrogen. The tests involved measuring the forward-voltage at $5\,\mathrm{A}$ and verification of the blocking property at a reverse-voltage of $U_\mathrm{r} = 300\,\mathrm{V}$.

different points, at angles of 90 degree relative to each other. Only diodes with a coplanar surface with a thickness difference of $0.20\,\mathrm{mm}$ or less were used in the final stack assembly. In total a fraction 152 out of 187 diodes fulfilled the required coplanarity of the contact surfaces.

To characterise the initial mechanical and electrical diode properties a test stack was built. It consisted of two thin copper heat sinks ($5\,\mathrm{mm}$ in thickness each) held together by a hand-screwed stainless steel housing, similar to the housing of the original stacks. A single diode could thus be positioned between the heat sinks. The test stack was equipped with copper cables, with two cables being screwed into each heat sink, thus connecting it to a power supply and a multimeter. With this generic test stack the polarity of coplanar diodes was determined. The positive pin was marked with a white dot. In order to check the blocking behaviour at reverse-voltage, a voltage of $300\,\mathrm{V}$ was applied across the diode. In addition the current was monitored with a sensitivity below the micro ampere range. In particular, it was required that no current above $1\,\mathrm{\mu A}$ was detected, while the reverse-voltage was applied. This crucial test was carried out in a cycle at two different temperature regimes, as shown in figure 4.5. A fraction of about 11% of the diodes failed this further test. The current limit of $1\,\mathrm{\mu A}$ was reached at a reverse-voltage of $2400\,\mathrm{V}$ at room temperature, and at $1800\,\mathrm{V}$ at liquid nitrogen temperature. If the reverse-currents were low enough to avoid thermal destruction, the blocking behaviour returned when lowering the reverse-voltage again. The $300\,\mathrm{V}$ reverse-voltage which is required for standard operation, falls well within the maximum range of $2400\,\mathrm{V}$ at $293\,\mathrm{K}$, and of $1800\,\mathrm{V}$ at $77\,\mathrm{K}$, respectively.

Only diodes which conform to these geometrical, mechanical, and electrical requirements were used for installation in one of the seven CPS by-pass diodes stacks. Table 4.2 lists the numbering of the stacks with the built-in diodes. All stacks show a proper isolation resistance between the heat sinks (including the diodes) and the housing of more than $20\,\mathrm{G\Omega}$.

4.2.2. Characterisation of the diodes

Each by-pass diode has also been characterised individually in the assembled state. For this purpose each diode was exposed to short semi-sinusoidal current pulses with a length of less than $200\,\mathrm{\mu s}$ from a custom made pulse generator at two different temperatures ($300\,\mathrm{K}$ and $77\,\mathrm{K}$). For pulse durations of less than $200\,\mathrm{\mu s}$, the self-heating, and hence

Table 4.2.: Numbering of the CPS by-pass diode stacks. All names have been assigned conveniently.

Stack name	Number of diodes	Comment
S01	2	Backup stack, commissioning of cryostat
S02	2	Backup stack, quench protection during quench tests of single magnets at ASG (seven tests)
S03	2	Protection for magnet module 2
S04	2	Protection for magnet module 3
S05	2	Protection for magnet module 4
S06	2	Protection for magnet module 5
S07	2	Protection for magnet module 6
S08	2	Protection for magnet module 7
S09	1	Protection for magnet module 1

Table 4.3.: Fit parameters for the I-U-characteristics of the built-in by-pass diodes according to figure 4.7. A parametrisation $I_f = c_0 + c_1 \cdot U_f + c_2 \cdot U_f^2$ was used, with the forward-current I_f and the forward-voltage U_f.

Temperature	c_0 (A)	c_1 (A/V)	c_2 (A/V^2)
293 K	$(4.405 \pm 0.010) \cdot 10^3$	$(-1.140 \pm 0.002) \cdot 10^4$	$(7.399 \pm 0.013) \cdot 10^3$
77 K	$(1.10 \pm 0.02) \cdot 10^3$	$(-2.92 \pm 0.03) \cdot 10^3$	$(1.76 \pm 0.01) \cdot 10^3$

shifts of the turn-on voltage, can be neglected. Two capacitors in series ($100\,\mu F$ and $600\,\mu F$), both charged by a common power supply, a thyristor, and the diode to be tested formed an electric circuit (see the circuit diagram in appendix F). The capacitors could be discharged via the thyristor. The emerging short current peak was monitored with an oscilloscope with a precision of $\pm 1\,A$. The current was varied between $50\,A$ and $250\,A$. The resulting forward-voltage was measured with a four-point-measurement for each diode with an uncertainty of $\pm 5\,mV$. Figure 4.6 shows the data of a single exemplary pulse of $200\,A$ at liquid nitrogen temperature. The forward-voltage was taken when the current pulse reached its maximum. This ensures that no inductive voltage contributions are taken into account. The energies deposited in the diode with a $200\,A$ current pulse are about $8\,mJ$ at $290\,K$ and $12\,mJ$ at $77\,K$, respectively. The self heating of the diode during the fast current increase ($dI/dt > 0$) is less than $0.1\,K$, and therefore negligible [134].

It is important to note that almost identical characteristics were observed for all 13 diodes, as well as for the 4 spare diodes, as shown in figure 4.7. During this characterisation 12% of the diodes already mounted in a stack did fail. When applying a reverse-voltage, these diodes did not block the voltage, and thus had to be exchanged. After doing so, each diode in that particular stack had to be characterised again. The I-U-characteristic for both temperatures was parametrised with a polynomial of second order. The corresponding fit parameters are listed in table 4.3. At nominal CPS operating current of $200\,A$, a mean turn-on voltage of $(0.928 \pm 0.009)\,V$ at $293\,K$ was observed, and of $(1.253 \pm 0.035)\,V$ at $77\,K$, respectively. The dependency between forward-voltage and temperature was obtained by parametrising the two data points with a linear function (compare figure 4.8):

$$U_f = a_0 + a_1 \cdot T \quad , \tag{4.4}$$
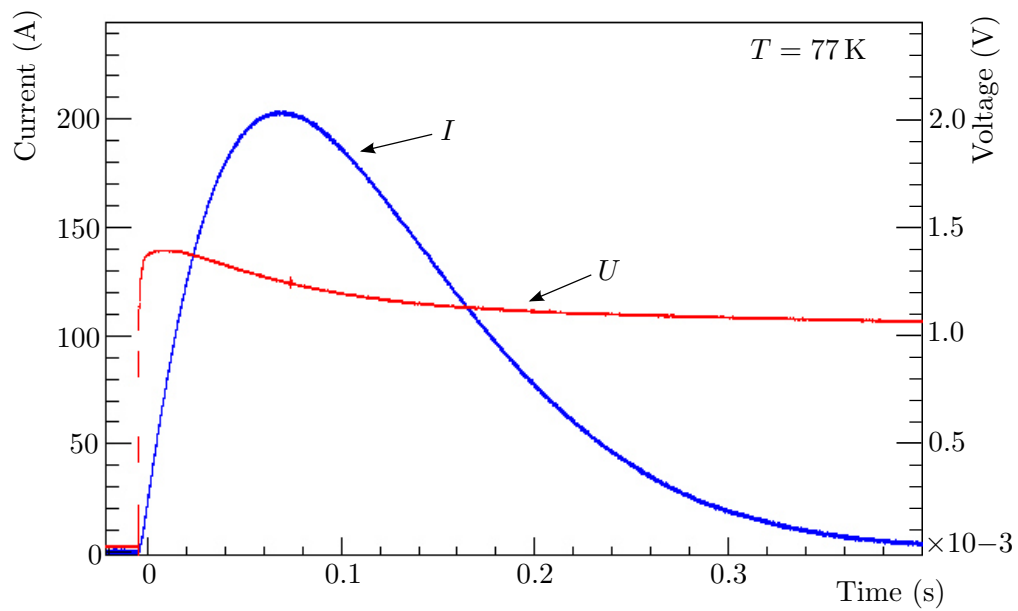
Figure 4.6.: Characterisation pulse of a CPS diode. Current (blue) and voltage (red) over time for one single current pulse during the characterisation measurements at liquid nitrogen temperature.
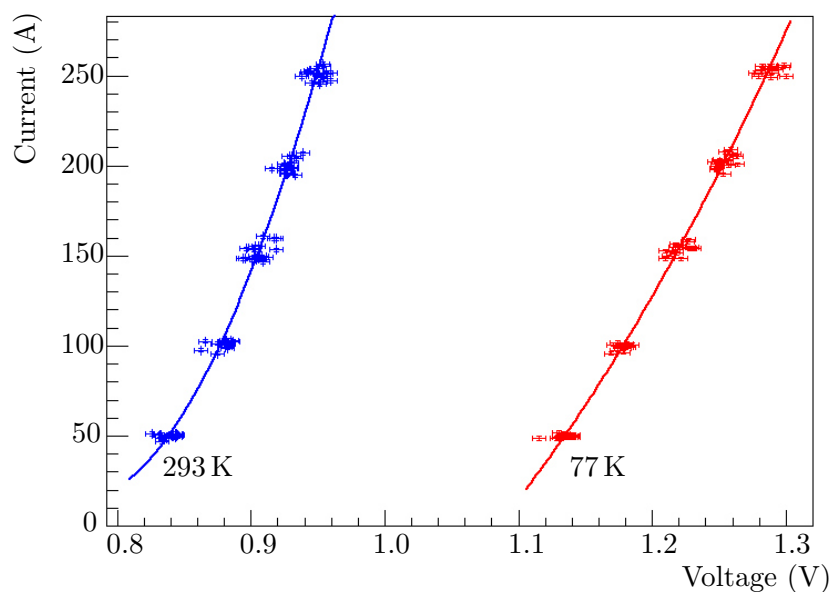
Figure 4.7.: Diode characteristics at temperatures of $293\,\mathrm{K}$ (blue) and $77\,\mathrm{K}$ (red). Both curves were measured by applying short current pulses to the diode. Each data point consists of 17 single pairs of values, one for each tested diode. The data were parametrised with a polynomial of second order with parameters given in table 4.3.
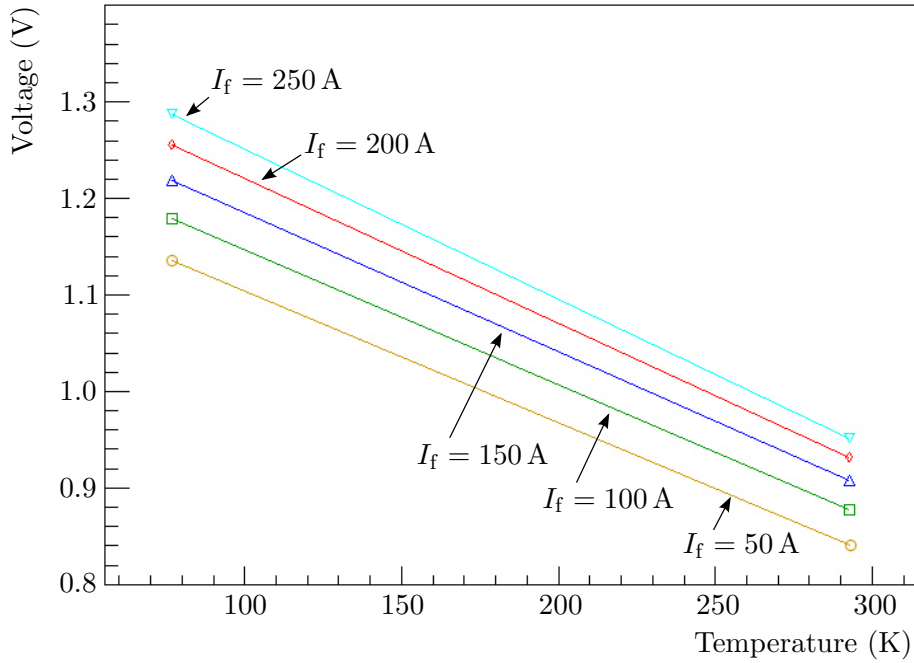
Figure 4.8.: Forward-voltage of the diodes as a function of the working temperature at constant forward-current (I_f). Analysis based on measured values displayed in figure 4.7.

with $a_0 = 1.4\,\text{V}$ and $a_1 = -1.5 \cdot 10^{-3}\,\text{V/K}$ for $I_f = 200\,\text{A}$. Equation 4.4 is valid over the entire temperature range between $77\,\text{K}$ and $300\,\text{K}$, with a precision of $\pm 10\,\text{K}$. By measuring the forward-voltage, the diodes can therefore serve as their own temperature sensor during the current endurance tests and also during long-term operation in the CPS. For monitoring purposes, i.e. to check the integrity of the diodes during long-term operation, a precision of $\pm 10\,\text{K}$ is sufficient. A more precise description between forward-voltage and temperature is given in [137]. Compared to the data given there, equation 4.4 yields slightly higher temperatures. For safety aspects, as required here, this deviation is beneficial.

4.2.3. Experimental set-up for current endurance tests at cryogenic temperatures

Each diode stack has been stress-tested at the nominal current ($200\,\text{A}$) for a time period of $253\,\text{s}$ at cryogenic temperatures ($4.5\,\text{K}$ and $77\,\text{K}$). This allowed to verify experimentally the dimensioning of the heat sinks, the layout of the thermal and electrical connections between each component in the stack and thus to ensure the reliability of all diodes. For these tests a cryostat with appropriate instrumentation, control system, and suitable data acquisition system were set up. The endurance tests at $77\,\text{K}$ were used as pre-selection tests under non-adiabatic conditions, specifically for checking the correct assembly and cabling of the hardware. The later quasi-adiabatic tests at $4.5\,\text{K}$ were performed inside the cryostat, where the conditions were as close as possible to the long-term operating conditions inside the CPS. Quasi-adiabaticity here means that all heat loads on the diode stack, except for Joule's heating are negligible. Under these conditions, the dimensioning of the heat sinks as well as the stack assembly geometry can be verified. The performance requirement was to archive a maximum diode temperature of less than $450\,\text{K}$ during the current endurance tests.

The hardware was designed to test three diode stacks at the same time. Table 4.4 gives an overview of the installed hardware and the monitored parameters. Figure 4.9 shows

Table 4.4.: Installed hardware and monitored parameters at the CPS by-pass diode stack test stand.

Indicator	Sensor	Quantity	Control unit	Monitoring
Temperature	PT100	2	Keithley 2701 + 6221	Temperature of the current feedthroughs
Temperature	PT500	9	Keithley 2701 + 6221	Heat sink
Temperature	PT500	4	Keithley 2701 + 6221	Current lead
Temperature	TVO	1	Keithley 2701 + 6221	Temperature inside cryostat vessel
Voltage	Wire (Teflon insulated)	6 pairs	Knick buffer stage + NI USB-9205	Voltage over the diodes
Voltage	Wire (Teflon insulated)	6 pairs	Knick buffer stage + NI USB-9205	Voltage over different parts of the current leads
Voltage	Standard wire	2 pairs	Knick buffer stage + NI USB-9205	Voltage over current feedthroughs
Voltage	Standard wire	1 pairs	Knick buffer stage + NI USB-9205	Overall voltage of the power supply
Voltage	Wire (Teflon insulated)	6 pairs	Knick high voltage buffer stage + NI USB-9205	Reverse-voltage
Current	Standard wire	1 pair	Knick buffer stage + NI USB-9205	Reverse-current
Current	Standard wire	1 pair	TopCon TC.P.20.52.400.S + NI USB-9205	Applied forward-current [138]
Level	American Magnetics Inc. Liquid Helium Level Meter Model KE 101A	1	NI USB-9205	Liquid helium level inside cryostat
Pressure	PHILIPS Transmitter P20	1	NI USB-9205	Pressure inside cryostat vessel

a schematic drawing of the wide-neck cryostat. The head of the cryostat (5) includes six instrumentation feedthroughs (32-pole sockets on a KF 40 flange each) (4) to monitor temperatures and voltages inside the cryostat. For current endurance tests, two feedthroughs (1) were mounted. In order to fill the cryostat with liquid helium, a transfer tube was installed (3). With a pressure gauge (2), the pressure inside the cryostat was monitored. The cryostat head permanently features a LHe quench gas tube (20), where evaporating helium is guided into a liquefaction facility. For safety reasons, an overpressure valve (0.5 bar) is usually installed.

On the inner side of the cryostat head flange a holding structure for the diodes (9) was attached. This inset provided a platform for diode positioning, which was fixed with three threaded rods in a distance of roughly 1.5 m below the flange. There the diode stacks (11) were mounted. The diodes were connected by bus bars (16) to the current feedthroughs, and via voltage taps to the instrumentation feedthroughs. On the platform a TVO sensor (12) for temperature-monitoring was mounted. In order to warm up the cryostat, four electric heaters (14) were mounted on the platform as well.

The head was tightened to the cryostat body (6) via eight screws and an O-ring seal, before every test at LHe temperature. In order to reduce liquid helium consumption, copper radiation shields (8) were installed on the holding structure. Inside the 180 litre helium chamber (17), Styrofoam rings (10) were placed as volume reduction elements. The cryostat featured a thermal shielding system, consisting of an isolation vacuum (13), and a 45 litre liquid nitrogen shield (15) with its own overpressure valve (19). Each chamber was monitored by an analogue pressure gauge (7) for safety reasons.

As mentioned above, liquid helium was filled through the flange (3) into the helium chamber. The evaporated helium was exhausted through the quench gas tube (20) on top, or through a second helium return flange (18) at the cryostat body. Gas exhausting through flange (18) was guided through a water bath before reaching the liquefaction facility. The bigger flange (20) was only used once the pressure inside the cryostat reached a level of 1.5 bar absolute, to avoid opening of the safety valve.

A LabView-based data acquisition software was used to monitor all processes inside the cryostat during the extended test procedures. The software code was programmed by *itk Engineering* [139], more information on the software interface and its features can be found in [140].

Current endurance test procedure at 77 K

Testing of individual diodes at liquid helium temperature is rather time consuming and also quite expensive, as it takes about one week per test cycle at 4.5 K, compared to half a day for a test at 77 K. Therefore a current endurance test at 77 K was introduced as an initial test for pre-selecting diodes. Only diodes passing the 77 K test were further tested at liquid helium temperature. Each pre-selection test cycle included forward- and reverse-voltage checks at room temperature and at 77 K and a current endurance test with the nominal current of 200 A for $\Delta t = 253$ s. For these tests only the cryostat head with the holding structure was used. It was suspended from a support frame, built of aluminium profiles, with the diode platform hanging in a Styrofoam box which was filled with liquid nitrogen. As a result, the stacks were covered with liquid nitrogen at all times during the test cycles. The measuring plan at 77 K was subdivided into the following steps:

1. **Installation of the diode stacks:** Up to three stacks could be mounted for testing at the same time. The voltage taps and the bus bars were insulated with shrinkable tubing. All unused voltage taps were short-circuited to avoid inductive voltage contributions.

2. **Check of proper electrical installation:** The insulation resistance between diodes
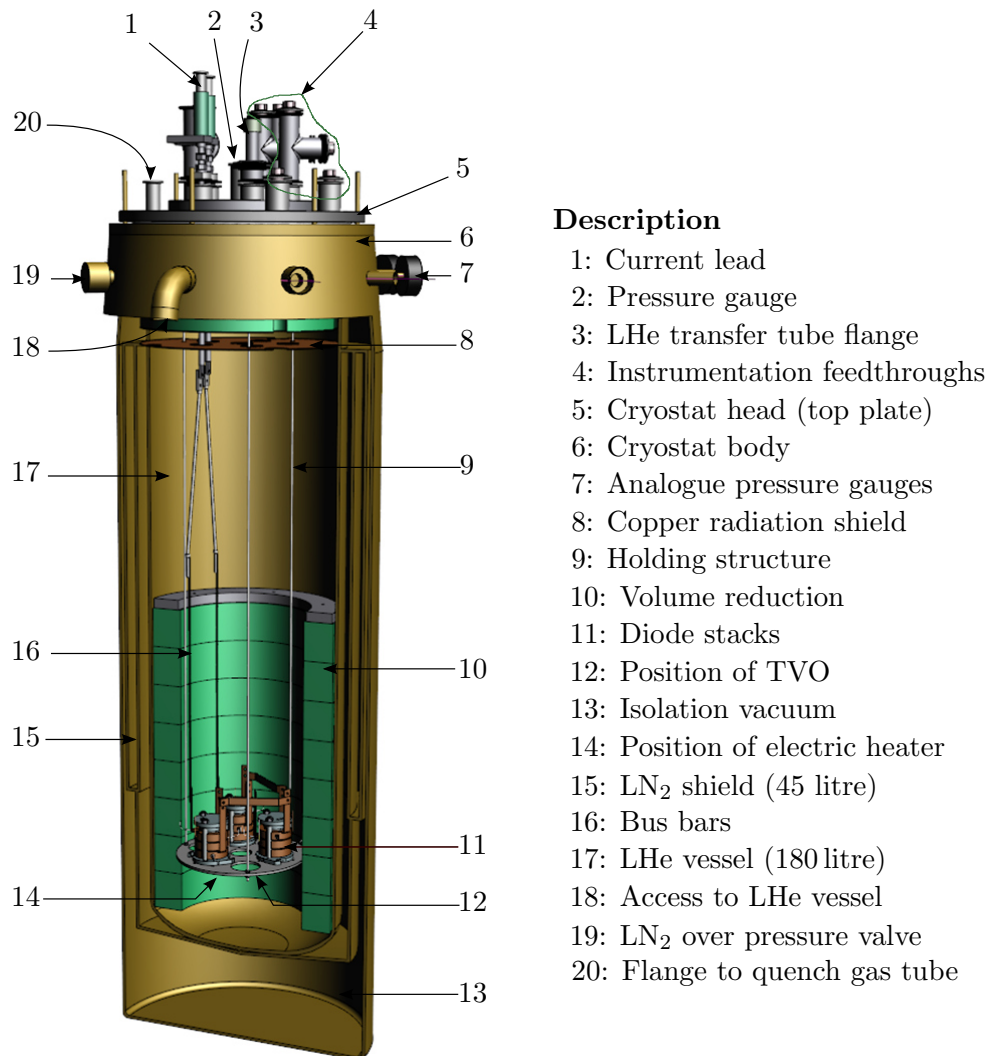
Description

1: Current lead
2: Pressure gauge
3: LHe transfer tube flange
4: Instrumentation feedthroughs
5: Cryostat head (top plate)
6: Cryostat body
7: Analogue pressure gauges
8: Copper radiation shield
9: Holding structure
10: Volume reduction
11: Diode stacks
12: Position of TVO
13: Isolation vacuum
14: Position of electric heater
15: LN_2 shield (45 litre)
16: Bus bars
17: LHe vessel (180 litre)
18: Access to LHe vessel
19: LN_2 over pressure valve
20: Flange to quench gas tube

Figure 4.9.: Schematic drawing of the wide-neck cryostat, featuring three diode stacks. The test instrumentation was connected at the cryostat head via 32-pole sockets (4). Vaporized helium was guided through the flanges (18) and (20) to a liquefaction facility. Not visible are the access flanges to the LN_2 shield and to the isolation vacuum. The part of the cryostat head (radiation shield, holding structure, diode stacks, etc.) which dips into the cryostat body is called the cryostat inlet.

(heat sinks respectively) and the cryostat head was verified to be larger than $1\,\mathrm{G\Omega}$. During this test, both ends of each diode were short-circuited for safety reasons. Routinely negligible leak currents were observed, due to the connected measurement and control unit.

3. **Measurements at room temperature:** Validation of the correct forward-voltages with a multimeter ($U_\mathrm{f} \approx 0.4\,\mathrm{V}$), and checking of the expected blocking property at reverse-voltage ($U_\mathrm{r} = 300\,\mathrm{V}$).

4. **Check of the data acquisition:** All data were monitored and stored for later in-depth analysis when applying a small feed current of $5\,\mathrm{A}$ through the diode system. A slight increase in heat sink temperatures and a decrease in diode voltages was expected in the data to prove that the data acquisition system worked correctly.

5. **Cooling down to $\mathrm{LN_2}$ temperature:** The diode stacks were finally cooled down in a temperature shock by filling the Styrofoam box with liquid nitrogen from a standard $\mathrm{LN_2}$ can. When the diode stacks were completely covered with liquid, the temperature (PT 500 and TVO) reached the $\mathrm{LN_2}$-equivalent value of about $77\,\mathrm{K}$.

6. **Check filling level:** The $\mathrm{LN_2}$ level was checked visually, ensuring the diode stacks to be covered completely with liquid nitrogen during the measurements.

7. **Current endurance test at $77\,\mathrm{K}$:** The nominal CPS operation current of $200\,\mathrm{A}$ was then applied to the diode system for 253 seconds. During this time interval, the diode voltages, all temperatures of the heat sinks, bus bars, and current leads, and the output of the power supply were recorded.

8. **Check blocking at reverse-voltage at $77\,\mathrm{K}$:** The reverse-current was measured with a reverse-voltage of $300\,\mathrm{V}$, with one diode being checked at a time.

9. **Warming up the diode stack:** After finishing all measurements under cold conditions, the Styrofoam box was removed and the diode stacks were slowly heated up with a hot air gun.

10. **Performance test:** After warm up of the diodes, the measurements at room temperature in (3) were repeated to check the intrinsic diode functionality.

A subset of the seven original plus two spare diode stacks were tested in groups of three. S01, S02, and S06 were measured alone, while S03 + S04 + S05 and S07 + S08 + S09 were tested in a group of three. The grouped diode stacks were connected in series during these measurements. For each set of stacks five test cycles were performed, with each test cycle including items (5) to (8). All stacks passed the test.
The same mounting configuration was then used for the more challenging $4.5\,\mathrm{K}$ test campaign.

Current endurance test procedure at $4.5\,\mathrm{K}$

For the current endurance tests at $4.5\,\mathrm{K}$ the complete cryostat assembly was used. The diode stacks (maximal three at once) were mounted on the holding structure platform before closing of the cryostat. After evacuation of the helium chamber by a Leybold Scrollvac SC 15 D pump and its purging with gaseous helium, the liquid nitrogen shield was filled. Once a temperature below $200\,\mathrm{K}$ was reached inside the cryostat body the cool-down was continued with liquid helium until the TVO sensor displayed a reading of $4.5\,\mathrm{K}$. At that temperature five cycles of current endurance tests (applying $200\,\mathrm{A}$ for $253\,\mathrm{s}$) were performed in a row for each set. When including the warm-up of the cryostat and the dismounting of the diode stacks, one complete run took about one week. The measuring plan at $4.5\,\mathrm{K}$ was similar to the one at $77\,\mathrm{K}$ presented above. In detail it was subdivided into the following steps:

1. **Installation of the diode stacks:** Same procedure as for the 77 K tests.

2. **Installation of the cryostat head in the cryostat body:** After closing of the cryostat and inspection of the electrical installation with a multimeter and the data acquisition software, the insulation resistance between diodes (heat sinks respectively) and the cryostat body had to be larger than $1\,\mathrm{G\Omega}$. During this test the diodes were short-circuited. Usually, negligible leak currents were observed due to the connected measurement and control unit.

3. **Leak tests of cryostat and connection tubes:** After each time that a flange at the cryostat had been opened or changed, the leak-tightness of the entire system had to be proven. To do so, each flange was wrapped in a plastic bag. Then, helium gas was filled into the cryostat chamber up to a pressure of $p_{\mathrm{abs}} = 1.4\,\mathrm{bar}$. The leak rate was measured with a sniffer inside each plastic bag. The tightness of each flange connection was determined to be of the order of $10^{-5}\,\mathrm{mbar}\,\ell/\mathrm{s}$.

4. **Measurements at room temperature:** Same procedure as for the 77 K tests.

5. **Check operational capability of the data acquisition:** Same procedure as for the 77 K tests.

6. **Filling the LN$_2$ shield:** The helium chamber was separated with a ball valve from the tubing to the liquefaction facility. Subsequently it was evacuated with a scroll pump and filled with gaseous helium, to avoid freezing of remaining ambient air inside during cool-down. The LN$_2$ shield was then filled with a standard LN$_2$-can. The filling limit was reached after approximately 25 minutes. Because of the high nitrogen vaporization rate, the shield had to be refilled the day after, minimum 100 to 150 litres being required. The minimum temperature inside the cryostat chamber was reached after two days, corresponding to about 190 K.

7. **Cooling down to 4.5 K:** The filling of liquid helium into the helium chamber was performed with a standard LHe-can to a level above the diode stacks, so as to immerse the stacks into LHe. The filling was stopped once the PT 500 sensors (heat sinks) and the TVO (holding structure platform) reached their minimum temperatures of $T_{\mathrm{PT\,500}} = 32\,\mathrm{K}$ and $T_{\mathrm{TVO}} = 4.5\,\mathrm{K}$. Once reaching the desired operating temperatures, it took a short time period until the LHe level was below the diode stacks, to reach quasi-adiabatic conditions.

8. **Checking fill level:** Since level metres are too imprecise, the LHe level was checked by applying a current of 1 A through the diode system. By depositioning a heat load of about 4 W into liquid helium ($P = 1\,\mathrm{A} \cdot 4\,\mathrm{V}$, for an estimated voltage of 4 V at 4.5 K), the helium will be evaporated, resulting in a gas flow of 0.2 g/s (with an evaporation energy of 20.75 J/g [141]). In view of the large volume expansion of factor 700, this would have resulted in a large increase in pressure inside the helium chamber, in case the diodes would still have been covered with liquid helium.

9. **Current endurance test at 4.5 K:** Same procedure as for the 77 K tests.

10. **Check blocking at reverse-voltage at 4.5 K:** Same procedure as for the 77 K tests.

11. **Warming up the cryostat:** With four electric resistors the helium chamber was heated. The LN$_2$ shield was purged with gaseous nitrogen, requiring one bottle with 50 litre at 200 bar. The subsequent warm up took four days.

12. **Performance test:** After warming up the diodes, the measurements at room temperature in (4) were repeated to check the complete diode functionality.

The diodes were tested in the same order and grouping as for the 77 K tests. Again five measurement cycles (items (7) to (9)) were performed for each set.
After the campaign the stacks were shipped to ASG for installation into the CPS cryostat.

4.2.4. Results for current endurance tests at 77 K

During reverse-current measurements, at temperatures equivalent to room temperature (≈ 300 K) as well as at 77 K, a small leakage current was observed, with readings between $40\,\mu$A and $60\,\mu$A. At 77 K the leakage current was slightly higher. The leakage-currents are assumed to arise from the instrumentation and control units themselves, being a result of their different internal resistances. Correspondingly a change in leakage-current was observed when dismounting parts of the instrumentation, such as the PT 500 sensors.
The same effect occurred during the insulation measurements between diode stacks and the cryostat head. It resulted in an insulation resistance (tested with 250 V) of about 1 GΩ between diode stack and cryostat inset (= ground). As a reminder, we mentioned that the insulation resistance between the heat sinks and the diode stack housing (outside the cryostat inset) was larger than 20 GΩ. The lower resistance is thus caused by leakage-currents of the connected data acquisition system, which had no impact on the current endurance tests.
Figure 4.10 shows the result of the endurance tests (200 A for 253 s) for one exemplary run performed with the set of diode stacks S03, S04, and S05 mounted in series. In the figure, the applied current and the resulting voltages over each diode are plotted. The observed turn-on voltages are about 1.24 V. They drop quickly, due to the heating of the silicon wafer, and remain constant at a level of (1.20 ± 0.01) V. This indicates thermal equilibrium between heat sinks, diodes and the ambient liquid nitrogen. All six diodes show an identical behaviour when applying high currents, although small deviations in the range of ± 10 mV in the voltage drop across the diodes can be observed. The temperatures of the silicon wafers have been calculated with the measured voltages and equation 4.4. The results are given in figure 4.10d. Instead of using the fit parameter given for equation 4.4, they are calculated for each diode individually, with a characteristic fit for each single diode. By applying a current of 200 A through the diode stacks, the heat sink temperatures increased about 5 K, however they remained below 80 K. Figure 4.10c shows the temperature increase over the time period of the endurance test. Since the PT 500 sensors were plugged rather loosely into the 4 mm heat sinks holes, the temperature varies somewhat on average. The diode temperatures increased by about 40 K, and remained constant at (116 ± 5) K. The differences, even in one stack, can be traced to be a result of the different thermal contacts between diode and heat sink, which are caused by the slightly curved contact disc surfaces of the diodes. The calculated temperature in equation 4.4 is very sensitive to voltage variations, with 10 mV corresponding to 15 K. Therefore it is more likely that the deviations in diode temperature of one stack are an artefact caused by different resistances in the soldering points between voltage tap and supply line.

The endurance test for the set of the diode stacks S07, S08, and S09 yields similar results, which are illustrated in figure 4.11. The turn-on voltages are close to 1.24 V and converge to a value of (1.19 ± 0.01) V when reaching thermal equilibrium. The temperatures of the heat sinks and the diode stacks of this particular run are given in figure 4.11c and figure 4.11d. The temperatures vary in a narrow range between 75 K and 78.3 K (heat sinks), and between 114 K and 118 K (diodes of stack S07 and S08). The stack S09 shows a slightly different behaviour in the diode temperature. It includes one diode only (compare table 4.2). Since the ratio between heat sink mass and number of diodes is higher for this particular stack, one can expect a better cooling and higher diode resistance. This leads to a higher voltage over the diode and hence a lower wafer temperature. This characteristic

(a)

(b)

(c)

(d)
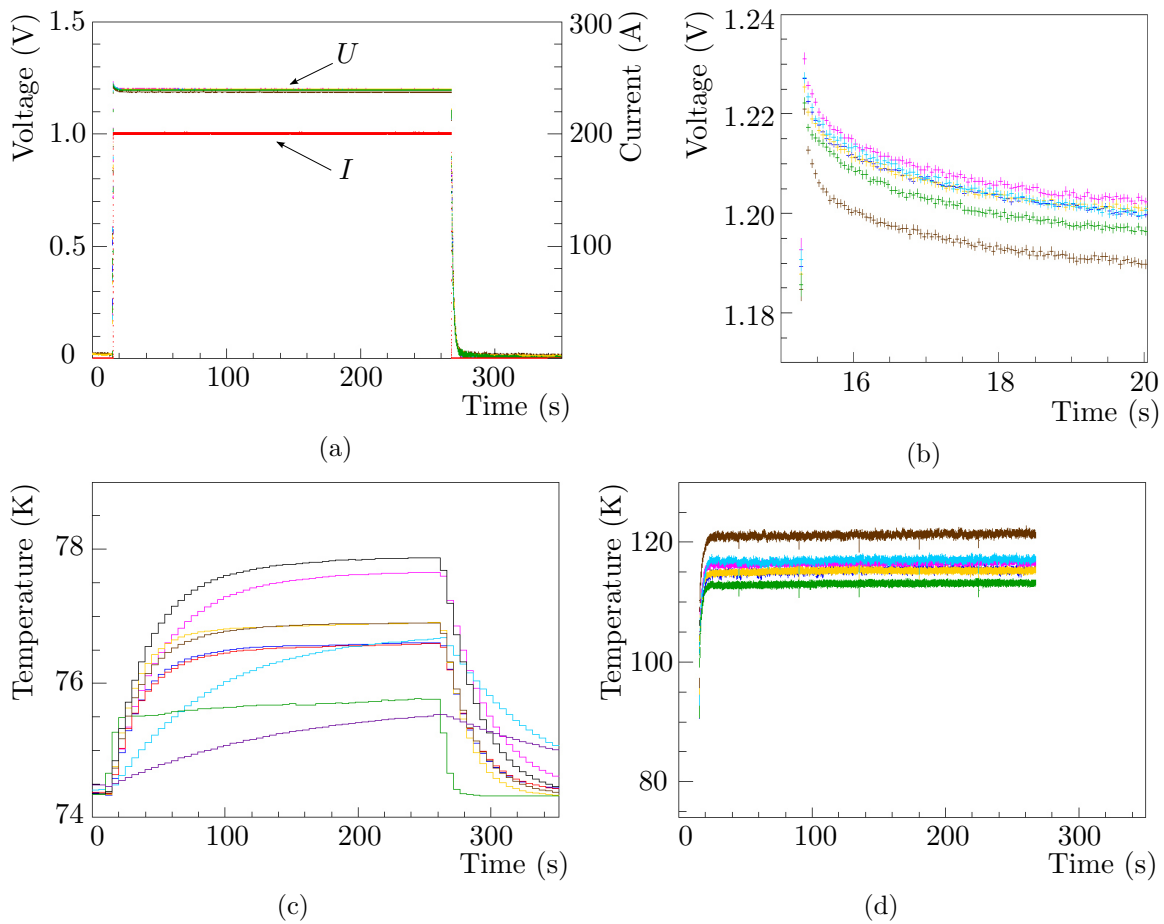
Figure 4.10.: Endurance test at 77 K initial temperature with the three diode stacks S03, S04, and S05 being tested at the same time (six diodes in series). Shown is one specific run out of a total of five runs being performed. Plot 4.10a shows the voltage and the current of one complete run, plot 4.10b a detailed view of the turn-on moment. Plot 4.10c shows the heat sink temperatures, and plot 4.10d the diode temperatures calculated with the measured voltages.

(a)

(b)

(c)

(d)
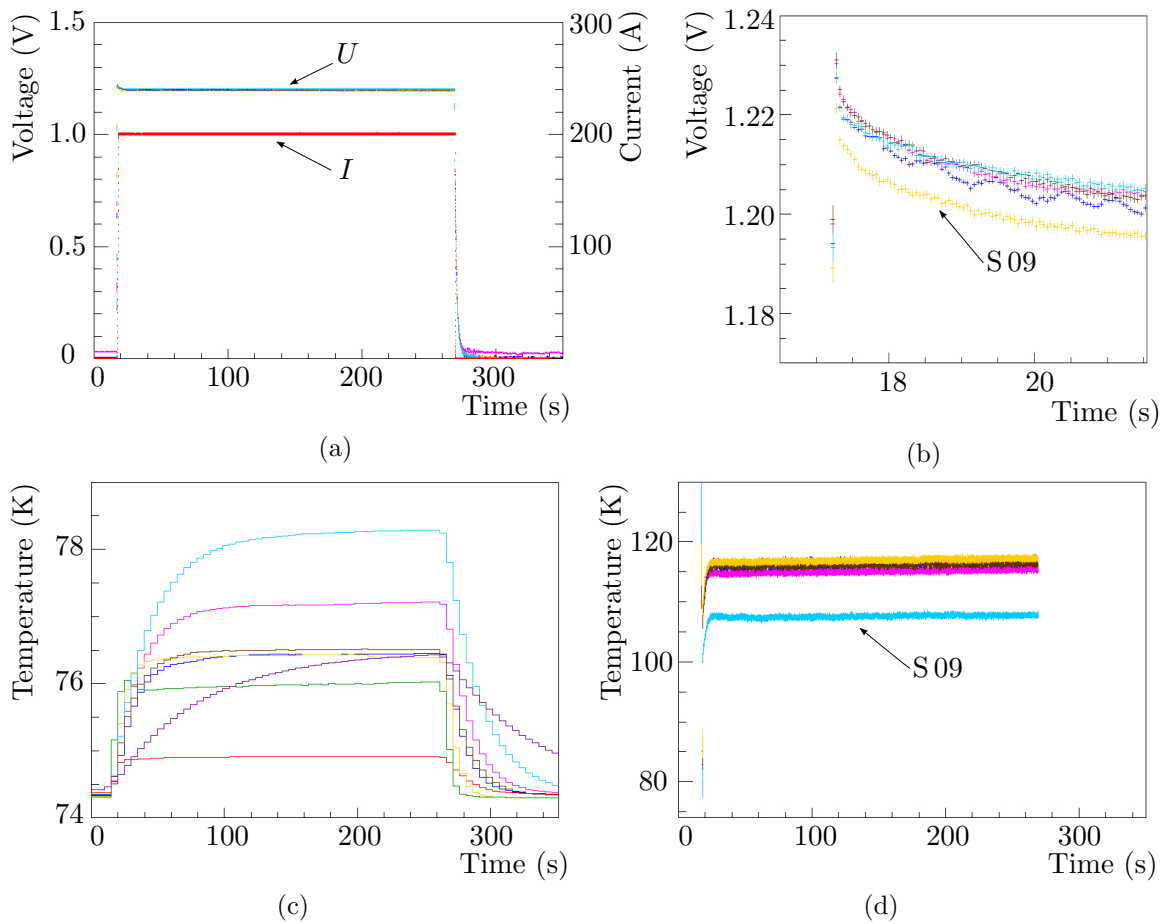
Figure 4.11.: Endurance test at 77 K initial temperature with the three diode stacks S07,
            S08, and S09 at the same time (five diodes in series). Shown is one specific
            run out of five. Part 4.11a shows the voltage and the current of the complete
            run, part 4.11b a detailed view of the turn-on moment. Plot 4.11c shows the
            heat sink temperatures, and plot 4.11d the diode temperatures calculated
            with the measured voltages.
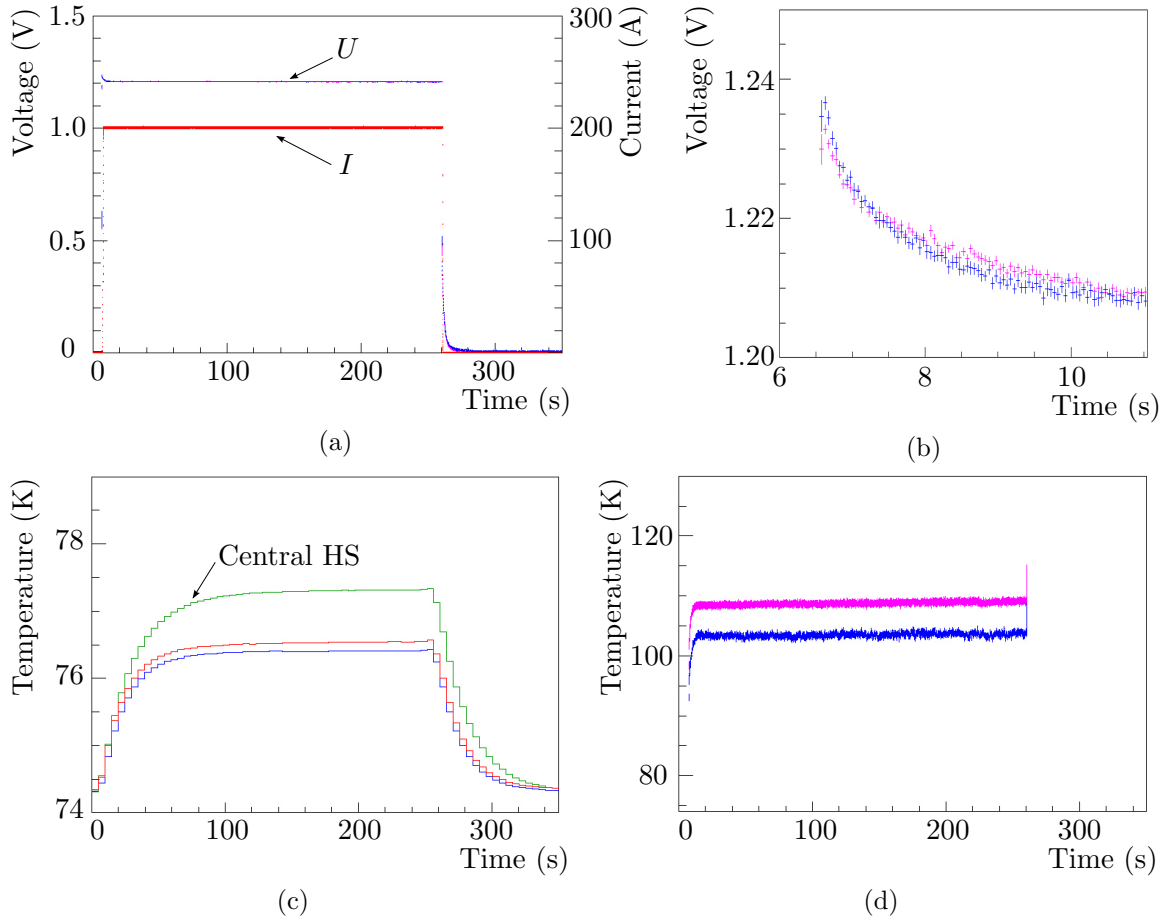
Figure 4.12.: Endurance test at $77\,\mathrm{K}$ initial temperature with one diode stack S06. Shown is one specific run out of five. Part 4.12a shows the complete run, part 4.12b a detailed view of the turn-on moment. The turn-on voltage is close to a value of $1.25\,\mathrm{V}$. Plot 4.12c shows the heat sink (HS) temperatures, and plot 4.12d again the diode temperatures calculated with the measured voltages.

behaviour was observed for each of the five test runs performed with each diode stack. The diode temperature in thermal equilibrium was about $90\,\mathrm{K}$.

The diode stack S06 was tested alone in liquid nitrogen. Figure 4.12 shows the corresponding data. The turn-on behaviour and the evolution of the diode resistance is similar to the characteristics of the other diode stacks, presented above. The temperature evolution clearly shows the different positions of the heat sinks and the diodes in the stack. The central heat sink in figure 4.12c is noticeably warmer ($T_{\max} = 77.3\,\mathrm{K}$) than the other two, located at the top and bottom ($T_{\max} \approx 76.5\,\mathrm{K}$), because it is heated by the diodes from both sides. The upper diode shows a higher temperature ($T_{\max} \approx 110\,\mathrm{K}$) (compare figure 4.12d) than the lower one ($\Delta T \approx 6\,\mathrm{K}$). This effect may be caused by a difference in the voltage tap resistances, as mentioned above. During the endurance test, the liquid nitrogen evaporated around the hot spots of the diode stack. This led to a rise of bubbles, hence the upper part of the diode stack experienced cooling by the solid-gas transition, and the lower part by a solid-liquid transition, which is beneficial in transferring thermal energy. These effects can explain the observed temperature differences.

For each set of diode stacks, almost identical values in voltage and diode temperatures were observed during each of the five cycles. Also, the reverse-voltage measurements at the end of a run series turned out successfully. No mechanical and electrical damage was observed
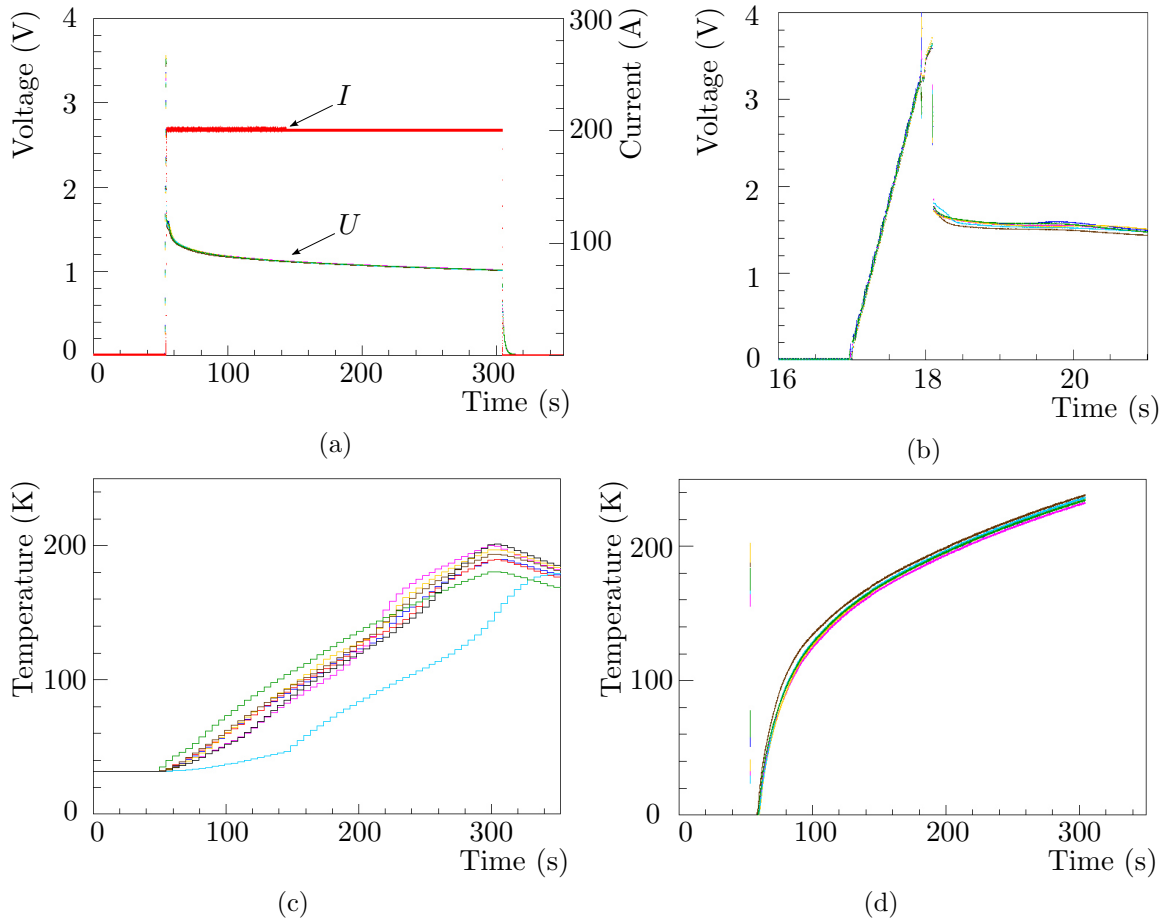
Figure 4.13.: Endurance test at 4.5 K initial temperature with the three diode stacks S03, S04, and S05 at the same time (six diodes in series). Shown is one specific run out of a total of five. Part 4.13a shows the voltage and current of the complete run, part 4.13b a detailed view of the turn-on moment. Part 4.13c shows the heat sink temperatures, part 4.13d the diode temperatures.

for any diode and diode stack, respectively, after the endurance and reverse-voltage tests in liquid nitrogen. Each diode passing the acceptance tests (see section 4.2.1 and 4.2.2), also passed the current endurance tests in liquid nitrogen.

4.2.5. Results for current endurance tests at 4.5 K

Following the measurement plan at 4.5 K, a total of five current endurance tests were performed at quasi-adiabatic conditions for each set of diode stacks. In case of the S03, S04, and S05 set, no equilibrium temperature inside the cryostat was found, as can be seen in figures 4.13. The lower limit of the measurements with PT 500 sensors was 32 K, hence only the increase in temperature above 32 K could be recorded. By monitoring the TVO sensor at the bottom of the holding structure plate (4.5 K), the initial temperatures of the heat sinks, and the diodes respectively, are estimated to be between 4.5 K and 10 K. When applying 200 A to the diodes, the temperature of the silicon wafers increased significantly, and almost instantaneously in the order of milliseconds. Depending on the sampling rate of the data acquisition system, different turn-on voltages were thus observed. With the actual sampling rate of 1000 Hz a turn-on voltage of about 3.6 V was measured for all six diodes in the set of S03, S04, and S05. The temperatures of the diodes (figure 4.13d), calculated with the measured voltages, show a similar evolution in time. After a steep rise, which is caused by the T^3-dependency of the specific heat at low temperatures, the
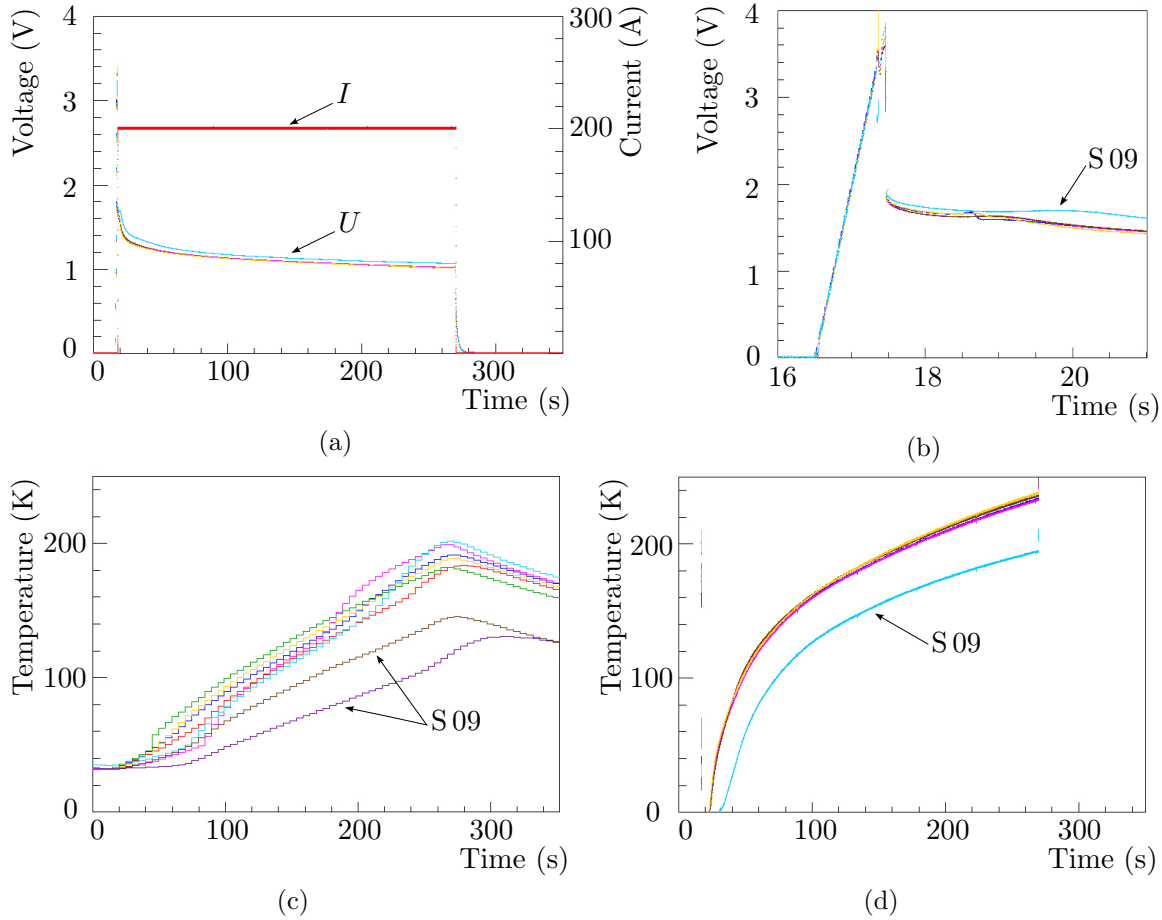
Figure 4.14.: Endurance test at $4.5\,\text{K}$ initial temperature with the three diode stacks S07, S08, and S09 (five diodes in series). Shown is one specific run out of five. Part 4.14a shows the voltage and the current of the complete run, part 4.14b a detailed view of the turn-on moment. Part 4.14c shows the heat sink temperatures, part 4.14d the diode temperatures.

wafer temperature increased approximately linearly to its maximum value of $(230 \pm 5)\,\text{K}$. Significant deviations were observed in heat sink temperatures, which displayed rather large spreads between $120\,\text{K}$ and $200\,\text{K}$ (see figure 4.13c). Some of the PT 500 sensors reacted with a specific delay in time, which was observed in all runs and was caused by a non-optimal contact between sensor and heat sink.

Identical results were observed for the diode stack set S07, S08, and S09. Figure 4.14 shows the corresponding data. The observed turn-on voltages were about $3.7\,\text{V}$. The diode in stack S09 showed a slightly higher value, indicating a lower temperature of the silicon wafer and the heat sink. The same effect already occurred during the measurements at $77\,\text{K}$ and was caused by the higher ratio between heat sink mass and the number of diodes of this particular stack. The temperature evolution can be seen in figure 4.14c and figure 4.14d. The behaviour in temperature was identical to the S03-S04-S05-set, with the exception of S09. The maximum average heat sink temperature of S07 and S08 was about $190\,\text{K}$, while the calculated diode temperatures were about $240\,\text{K}$. Since the central diode in stack S09 was cooled by two heat sinks, the maximum temperature of this diode as well as the corresponding heat sink temperatures did not increase as much as those of stacks S07 and S08. The S09 heat sink thus reached a maximum temperature of approximately $140\,\text{K}$, while the diode itself was heated up to $190\,\text{K}$.
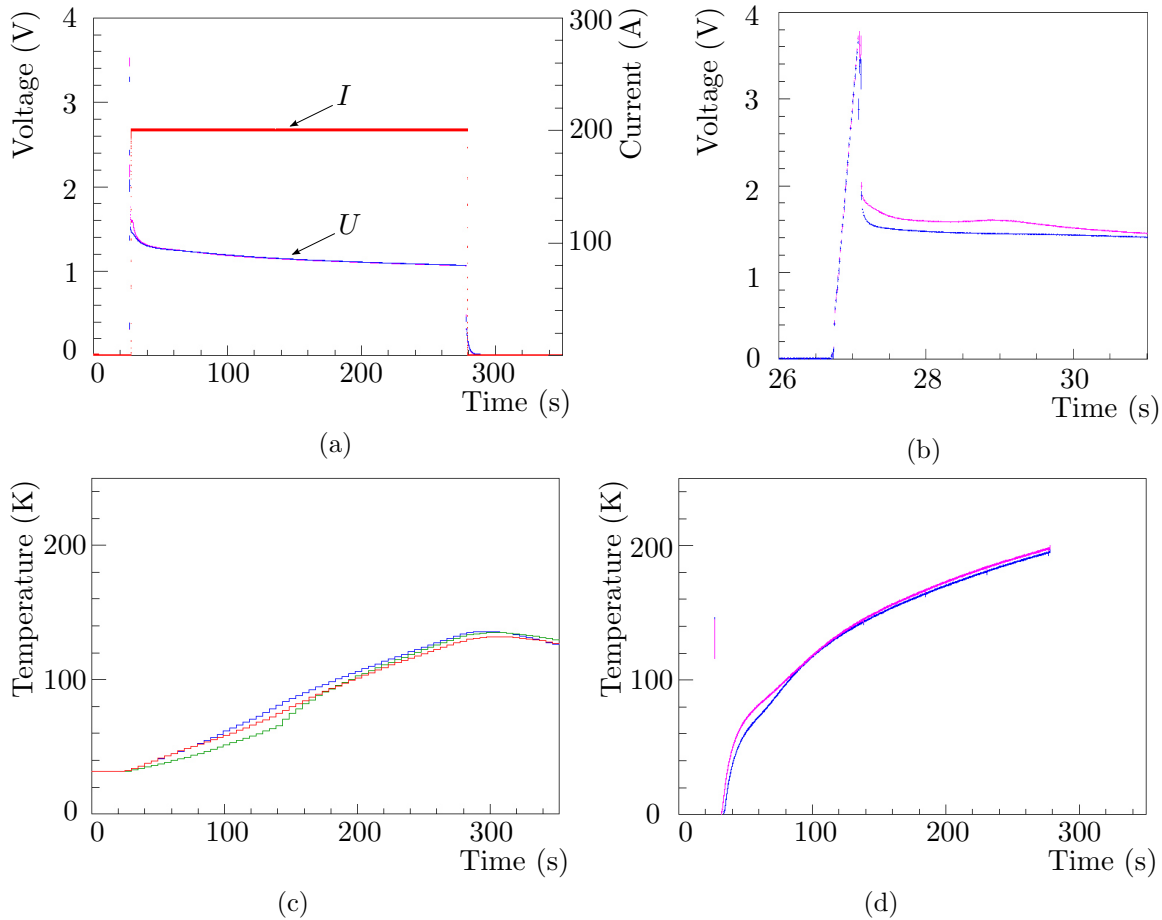
Figure 4.15.: Endurance test at 4.5 K initial temperature with one diode stacks S06 (two diodes in series). Shown is one specific run out of five. Part 4.15a shows the voltage and current of the complete run, part 4.15b a detailed view of the turn-on moment. Part 4.15c shows the heat sink temperatures, part 4.15d the diode temperatures.

Stack S06 was tested alone at 4.5 K initial temperature. With a 3.6 V turn-on voltage, it showed the same characteristics as all other diodes (figure 4.15). Unlike the measurements in liquid nitrogen, no significant difference in the heat sink temperatures could be observed (figure 4.15c). The average maximum heat sink temperature was 135 K. This was significantly lower than the temperatures observed in the measurements with three stacks (190 K). The calculated maximum temperature of the diodes, with the measured voltage over the diodes, was about 190 K (figure 4.15d). At the end of each endurance test run, the silicon wafers reached a temperature of about 190 K.

The reverse-voltage measurements went well for all diodes. All diodes blocked an applied voltage of 300 V at liquid helium temperature and again at room temperature after warming up. The visual inspection at the end of the test series showed no changes or damages in the mechanical structure.

4.2.6. Summary of diode tests

In a measuring campaign, all seven by-pass diode stacks for the CPS magnet safety system and in addition two spare systems were tested successfully. The campaign was subdivided
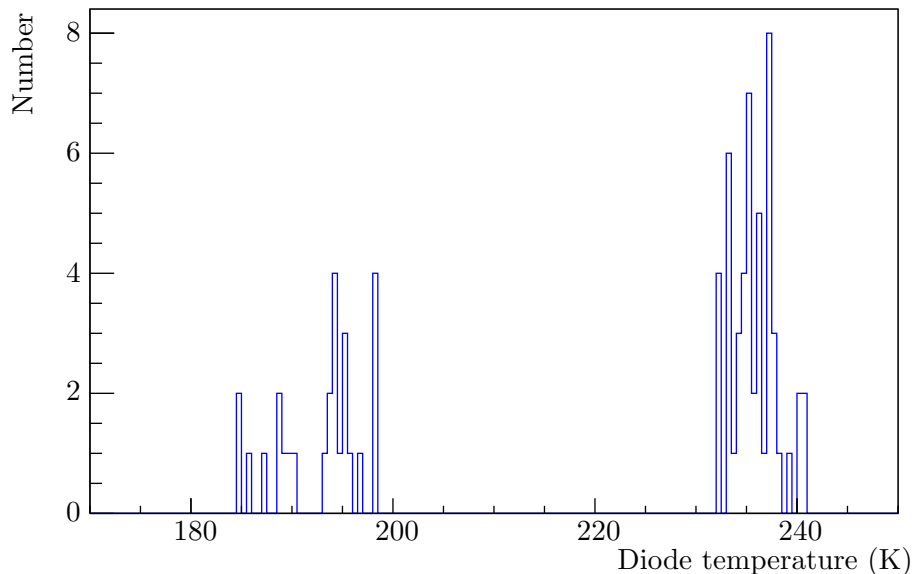
Figure 4.16.: Maximum temperature distribution of the CPS diode stacks after endurance
tests with 200 A for 253 s at 4.5 K initial temperature. Two distinct temper-
ature regimes are observed: The higher temperatures occur for arrangements
where three stacks were tested at the same time. The lower temperature
group belongs to tests with single diode stacks and to the stack with only
one diode installed (S09).

into the following steps:

1. **Selection tests:** Selection of diodes, which had to fulfil geometrical, mechanical,
   and electrical specifications, at 293 K and 77 K. Out of 187 bare diodes, a total of
   only 132 fulfilled the geometrical specifications. There of, a number of 75 were used
   for the electric tests. Within these tests a small number of 8 diodes failed.

2. **Diode characterisation:** The I-U-characteristic was determined by applying short
   current pules to each selected diode, and by measuring the voltage across the diode.
   During this characterisation step a total of 8 diodes failed and had to be replaced.

3. **Current endurance tests at 77 K:** Each diode stack was tested under non-
   adiabatic conditions in liquid nitrogen. A current of 200 A was applied for 253 s
   to the diodes. Every diode stack passed this crucial test.

4. **Current endurance test at 4.5 K:** The quasi-adiabatic tests at 4.5 K initial tem-
   perature were performed with identical procedures as during the measurements at
   77 K. Again each diode stack passed the test.

During the final quasi-adiabatic current endurance tests at 4.5 K the nominal operation
current of 200 A was applied for 253 s to each diode stack, which corresponds to the same
amount of energy released during a quench of the CPS magnets through the diodes plus
30% safety. The temperature of the silicon wafers increased well within the specifications
($T < 450$ K). When testing three stacks at the same time (six diodes in series) in a
wide-neck cryostat, the maximum temperature reached was 240 K. When testing a single
stack (two diodes in series) a temperature of only 190 K was observed. An overview of
the observed maximum temperatures is given in figure 4.16. The two distinct temperature
regimes show that the cooling by helium gas inside the cryostat is not negligible, in contra-
diction to the adiabatic assumption, but it reproduces the operation conditions inside the
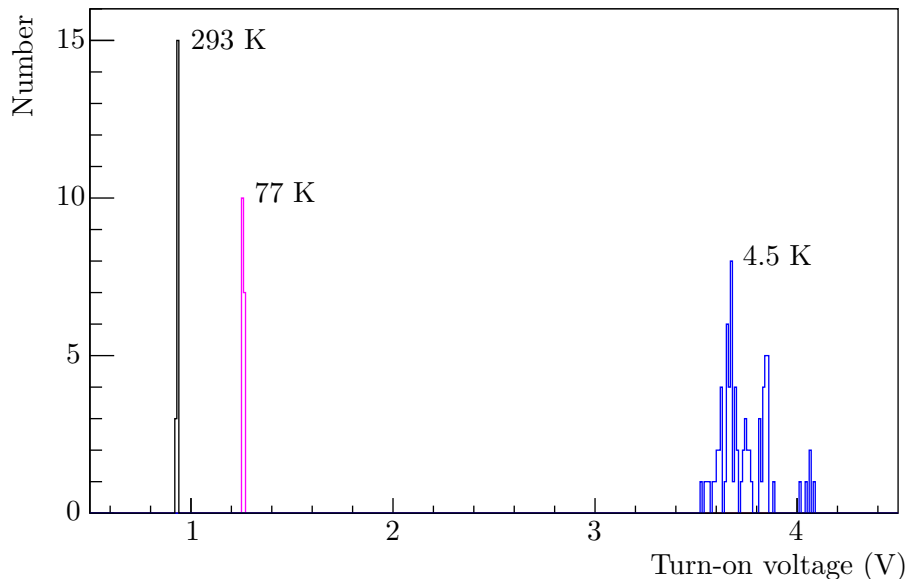
Figure 4.17.: Distribution of the turn-on voltages of the CPS by-pass diodes at 200 A. The voltages at 293 K and 77 K have been derived from the characterisation measurements, the 4.5 K data come from the current endurance tests.

CPS very well. In the CPS the seven stacks will be mounted inside two diode vessels, filled with liquid helium (see section 4.3). The heat sink temperatures reached their maximum at 200 K (for three diode stacks), and 140 K for one diode stack. Even if the silicon wafer temperatures will increase more during CPS operation than in the cryostat tests presented here, there will still be enough cooling power from the heat sinks to prevent the diodes from exceeding their critical temperature of 450 K.

Figure 4.17 shows the observed turn-on voltages at 293 K, 77 K and 4.5 K for the CPS diodes at the nominal current of 200 A. The data at 293 K and 77 K were taken from the characterisation measurements, the turn-on voltages at 4.5 K accordingly from the current endurance tests. The apparent width of the voltage distribution at 4.5 K suggest that the initial temperature at each current endurance test campaign was not identical for different runs. This is likely caused by the imprecise temperature measurement in this low temperature regime. Since the rise time of voltages after turn-on was of the order of milliseconds, a higher sampling rate than the one during the tests ($f = 1\,\text{kHz}$), would have resulted in a better resolution and hence a smaller spread of the 4.5 K turn-on voltages.

4.3. Mounting the by-pass diode stacks inside the CPS

In this section, the mounting of the CPS by-pass diode stacks is described in detail. The generic properties and dimensions of the components are based on [142].

The previous manufacturer-proposed mounting position of protection diodes was located inside the helium vessel of the superconducting magnet. In case of a diode failure, the magnet housing and all other parts, covering the magnet, had to be opened by welding to get access to the diodes. Since the accessibility of sensitive parts is of utmost importance for the KATRIN experiment, the initial diode concept of ASG was abandoned and a new design was developed by KIT together with CERN experts for the CPS. A major motivation for these works is the fact that once KATRIN is running with tritium, a repair of tritium-bearing components, such as the CPS, outside of the radiation-monitored area at TLK will be almost impossible. Thus, placing the sensitive by-pass diode stacks behind
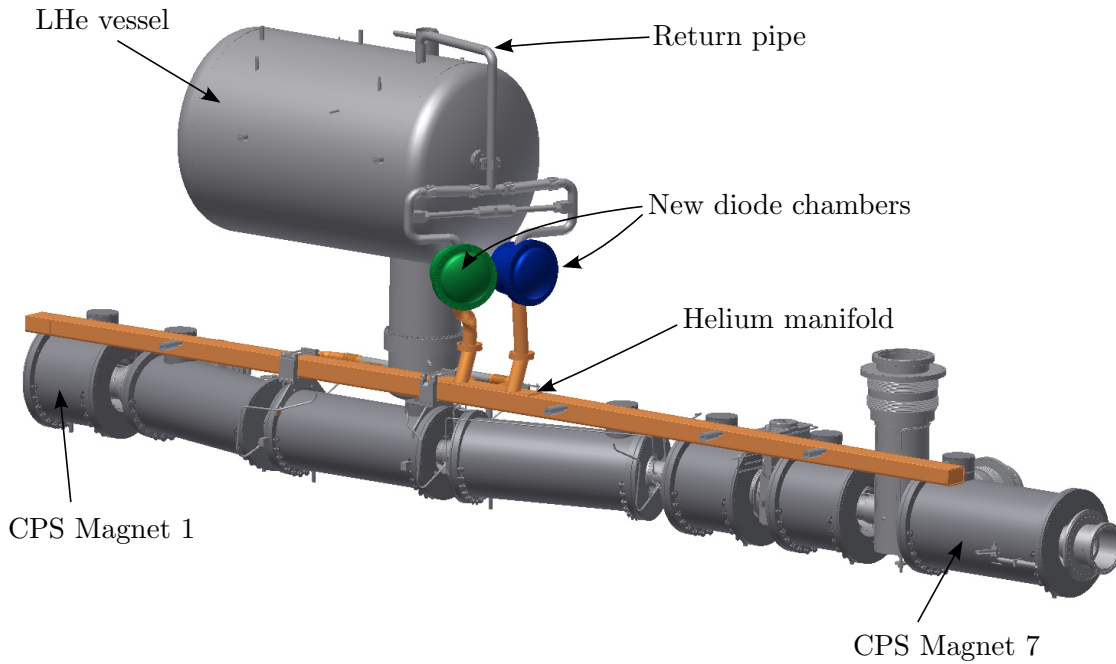
Figure 4.18.: New design of the by-pass diode stack vessels (green and blue). They are cooled with liquid helium from the manifold (orange), which is returned into the helium vessel via the return pipe. In case of a superconducting magnet quench, evaporated helium will flow through the pipe system of the two diode vessels, providing additional cooling for the diodes.

flanges for easy access ensures a more reliable operation of the whole KATRIN experiment. The diode stacks were therefore placed in two extra diode chambers, next to the helium vessel, inside the turret of the CPS cryostat (figure 4.18). All magnets, the 4.5 K-vessel, and the two new diode containers are interconnected by a manifold for filling with liquid helium. The new cabling between diodes and magnets has been placed inside that manifold. For this purpose, a set of new oxygen-free copper (OFHC) bus bars, connection bars, and flexible copper braids was installed. Figure 4.19 illustrates the assembly. The new bus bars, with a cross section of $21 \, \text{mm}^2$, were brazed to the existing bus bars from each magnet, using special connection bars with a cross section of $45 \, \text{mm}^2$. For optimal thermal, electrical, and mechanical contact these joints have been screwed (as fixation for assembly reasons) as well as brazed. In order to reach the by-pass diode stacks, a flexible copper braid with a cross section of $25 \, \text{mm}^2$ was chosen. These braids have been soldered into fittings, which were then brazed to one end of the new bus bars and soldered on the other end to the heat sinks. At the heat sinks two M5 screws have been used in addition as a mechanical fixation. Figure 4.20 shows schematically the joint at one diode stack, between copper braid and heat sink. The large cross sections, as well as the combination of different soldering, screwing and brazing techniques guarantee an optimal thermal and electrical connection between solenoids and protection diodes. Brazing and soldering causes an increase in temperature of the by-pass diode stacks during mounting inside the CPS. The temperature evolution of the heat sinks, and thus of the diodes, during that process has been investigated with a mock-up by ASG. By making use of SnPb as solder together with deoxidizer paste on the surfaces, and in particular due to after-cooling with compressed air, the temperature of the heat sinks will be less than $46°\text{C}$ during soldering. More details are found in [142].

The diode chambers are accessible from the outside of the CPS via a flange at the turret
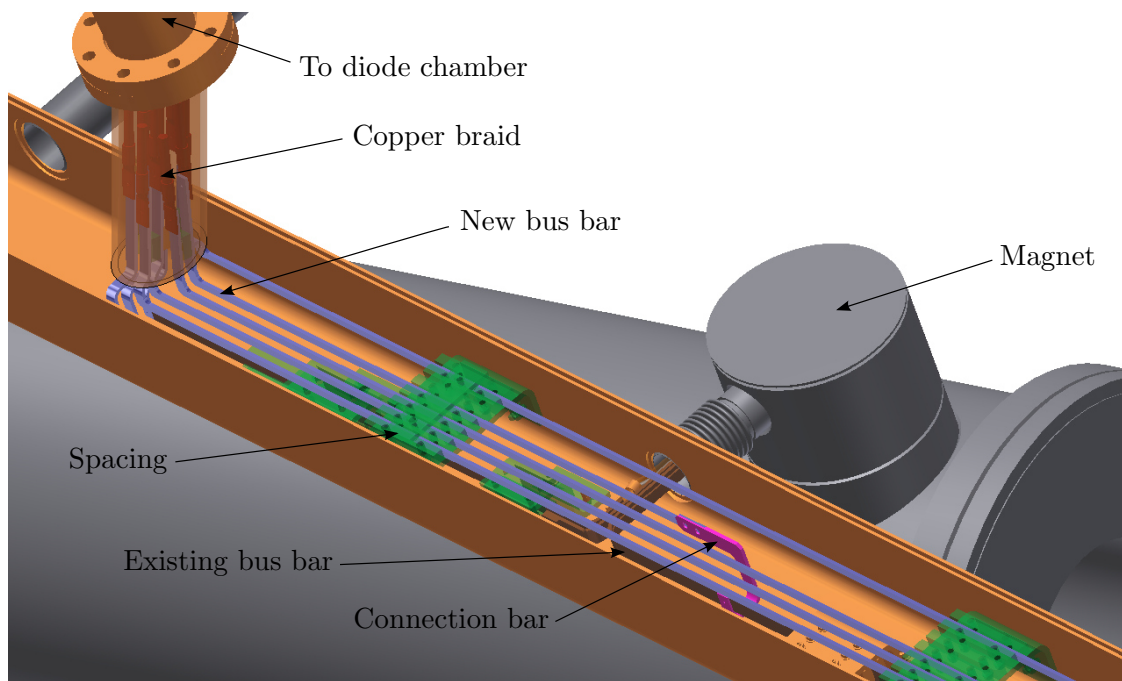
Figure 4.19.: New connection system inside the helium manifold. Red: Connection between the new bus bars and the copper braids to the diode stacks. Light blue: New bus bars. Green: Spacings (GRP) between the new bus bars and support (steel) fixed in the manifold. Pink: Connection bus bar. Brown: Existing bus bars, coming from the magnets.
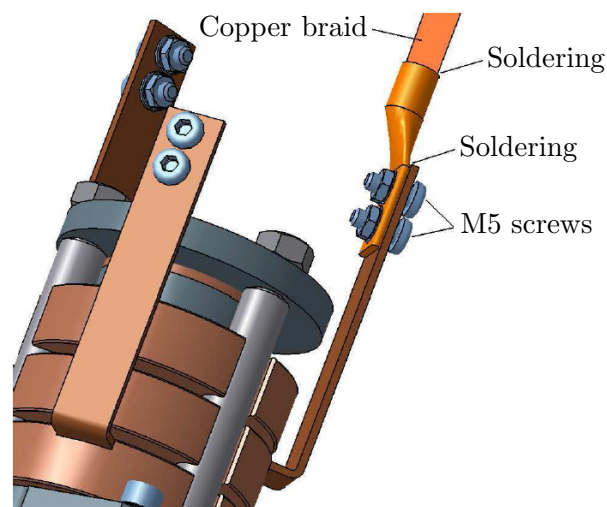
Figure 4.20.: Schematics of the connection between by-pass diode stack and copper braids. The copper braids are screwed and soldered to the bus bars of the diode stacks. Taken from [142].

(a)   (b)
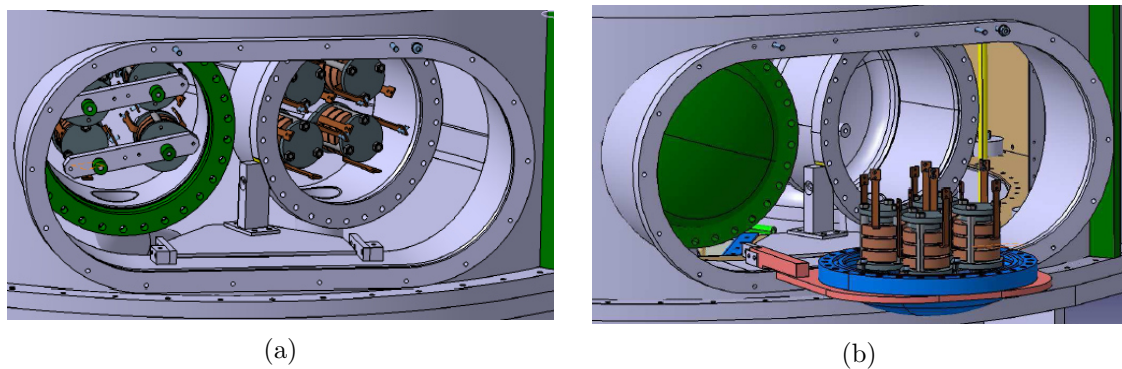
Figure 4.21.: Mounting of by-pass diode stacks inside the CPS turret. In 4.21a the grouping (three and four stacks each) can be seen. The connections to the magnets point inwards. In 4.21b one group has been dismounted and placed on an extra support frame for maintenance. The figures are taken from [142].

and hence the diode stacks are exchangeable, as required. They were grouped into three and four stacks. Each group is mounted in one chamber. The connections to the magnets lead into the turret. The mounting can be seen in figure 4.21a. For maintenance reasons an additional support frame, shown in figure 4.21b (blue), can be placed in front of the two vessels.

During CPS operation, the manifold will be filled with liquid helium, thus providing a LHe environment inside the two diode chambers. If a quench occurs, a part of the evaporating helium will flow through the return pipe and hence through the diode stacks into the helium vessel. The stream of cold helium gas will further cool the by-pass diode stacks. Together with the extensive pre-selection and quality tests, the careful redesign of the diode stack chamber and the flow pipes, the new system represents a reliable, stable, flexible, and manageable quench protection for the CPS cryostat.

5. Argon frost preparation in the Cryogenic Pumping Section

The functionality of the CPS, in providing ultra-low levels of tritiated molecules at the entry of the spectrometer sections, strongly depends on the preparation procedure and techniques for the argon frost. Determination of the argon injection parameters requires a deep understanding of the gas flow characteristics and the heat flux through the capillaries. Therefore the conductance of a capillary has been determined both theoretically (section 5.1.1) and experimentally (section 5.1.3), at well known conditions. These results were transferred to temperature-dependent gas simulations of the argon capillaries inside the CPS, as given in sections 5.2 and 5.3. These specific input data were then used to suggest a proposal for the argon injection procedure, given in section 5.4.

The importance and principles of the functionality of the cryogenic pumping section (CPS) have been outlined in chapter 3.3. Its central requirement is to provide a further tritium retention factor of at least seven orders of magnitude. Therefore an argon frost layer is prepared inside the beam tube of sections 2, 3, 4, and 5. These sections, except number 5, contain three stainless steel capillaries each, which are aligned at an angle of 120 degrees relative to each other inside the particular beam tube section. Each capillary has an inner diameter of 3.5 mm and an outer diameter of 4 mm. The length is about 1030 mm. A total of 23 orifices, with distances of 32 mm relative to each other and a diameter of 0.2 mm, were placed in each capillary. To obtain a homogeneous temperature distribution, all capillaries are gold plated. They are fixed at the vacuum system of the beam tube via a so called capillary holding tube. This element is made out of stainless steel, which is welded on a feedthrough on the beam tube. At the opposite side a wire, fixed at the beam tube via screws, is wound loosely around the capillary. Figure 5.1 shows schematically the arrangement of the argon injection system, whereas figure 5.2 gives a visual impression of the assembly at ASG Superconductors. According to the modes of operation, presented in chapter 3.3, the beam tube temperature will be kept at 6 K during the initial stages of the argon preparation. To avoid freezing of argon inside the capillaries these crucial elements will be heated via one electric heater each up to a temperature of at least 40 K. A second heater is mounted and used as redundancy. Both elements are fixed with a clamp to obtain high reliability.
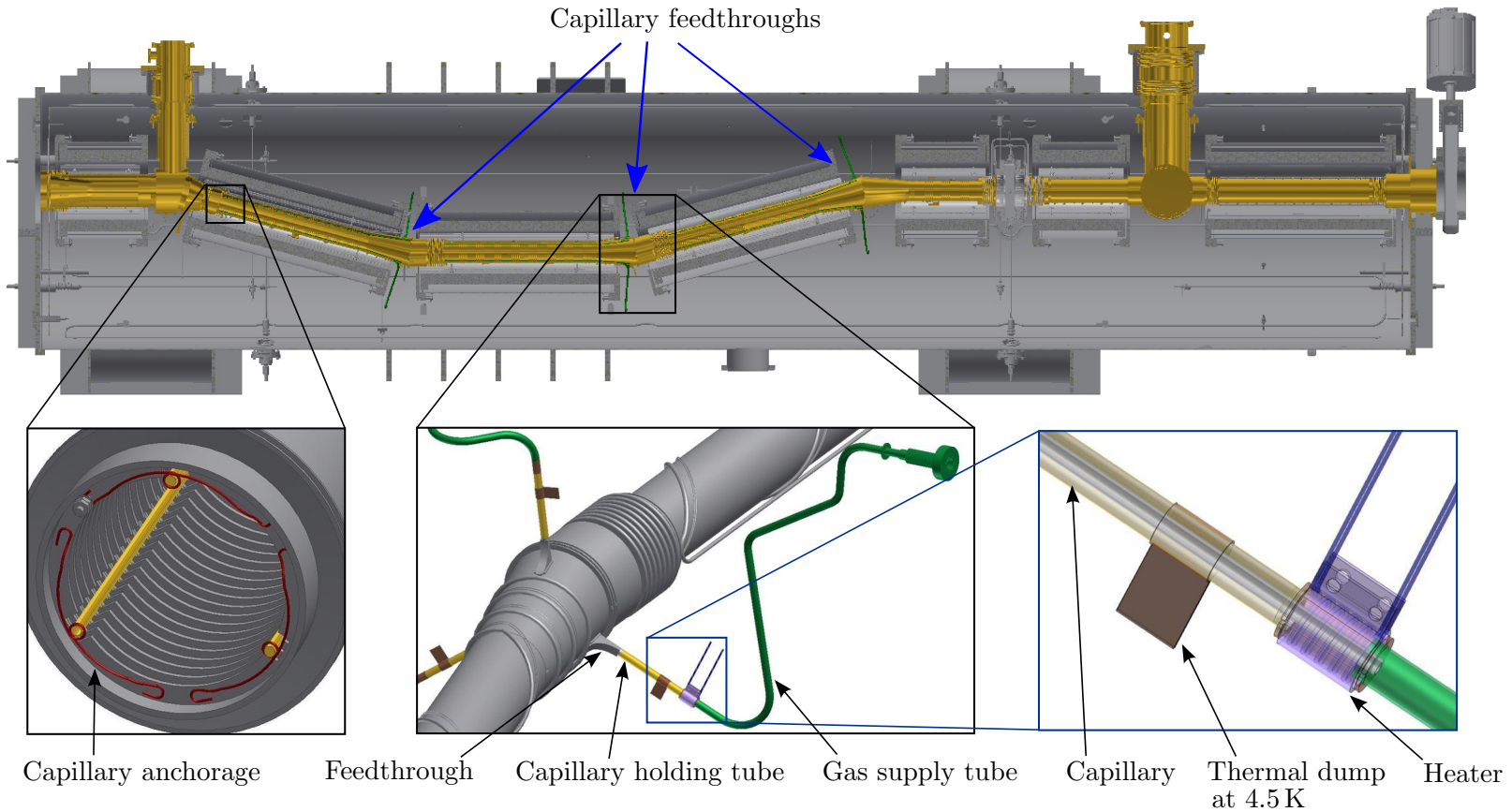
Figure 5.1.: Arrangement of argon injection components. On top: CPS vacuum system, the capillaries and their feedthroughs are coloured green. Bottom left: Capillary anchorage. Bottom middle: Beam tube (grey) with the argon gas supply tubes (green), which are thermally dumped at 77 K, 230 mm in front of the connection with the capillary holding tube (yellow). The capillary holding tube is thermally dumped at 4.5 K, 20 mm below the welding point between capillary and capillary holding tube. Bottom right: At that point two identical electric heaters (blue) are wrapped around that welded joint and fixed with a clamp (purple). There is no contact between capillary and beam tube beside the anchorage and feedthrough.
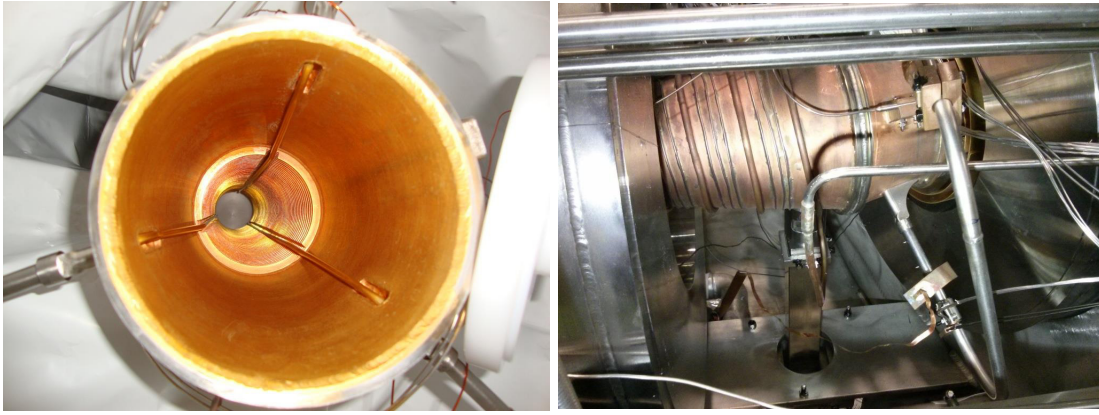
Figure 5.2.: Left: View inside a beam tube element with three capillaries, during the mounting preparations as ASG. Right: Connection of beam tube elements 4 and 5 during assembly, with the capillary feedthrough, the dumping at 4.5 K, and the capillary electric heater. Photos by ASG and KIT.

5.1. Conductance of the argon capillaries

In order to detail the complex argon preparation procedure, the conductance of each part of the argon inlet system has to be known. The injection system consists of an apposition of tubes, valves, and the capillary itself with its 23 gas orifices. In fact in vacuum design, the conductance of straight tubes with well-defined bendings can be calculated by making use of well-known formulas given in the technical literature [82] [83] [84]. However, in this case, the capillary cannot be calculated analytically, since its geometry is too complex. In addition the capillary experiences a temperature transition from room temperature to approximately 40 K. Accordingly one important task of this thesis was to perform a detailed simulation of the CPS conductance in the molecular flow regime (compare section 5.1.1), which is the relevant case here, as will be shown. The simulation result was then validated by an experimental determination of the conductance. For the validation of the simulation a capillary was replicated and flow tests were performed in an appropriate UHV chamber (sections 5.1.2 and 5.1.3).

5.1.1. Simulation of the molecular conductance

The conductance of the argon capillary system has been simulated in the molecular flow regime. Since the experimental measurement of the conductance was carried out under isothermal conditions (see experimental section 5.1.2 below), the simulation was simplified by tracking particles through an adequate geometry, without taking account of temperature dependencies. The most suitable software for this problem is MolFlow+, a code which is based on the single particle Monte Carlo method. The free software tool, developed at CERN [95], has been introduced in section 3.1.

Figure 5.3 shows a screen shot of a typical capillary simulation. Only the vacuum part is being considered here, which is equal to the inverse of the capillary. The facet at the beginning of the capillary (#0 in figure 5.3) was defined as gas inlet with a sticking probability of 1. Since the conductance of the gas inlet system, which is not shown here, is much larger than the one of the capillary itself, a cosine-like desorption characteristic was chosen. The sticking coefficients of the 23 outlets were set to unity (#1-#23 in figure 5.3). Hence, each particle hitting such a facet is adsorbed (pumped), and removed form the simulation.

The simulation was stopped if the number of hits on all desorptive facets was larger than 10^4. This results in a statistical uncertainty less of than 1% for each outlet. The ratio of
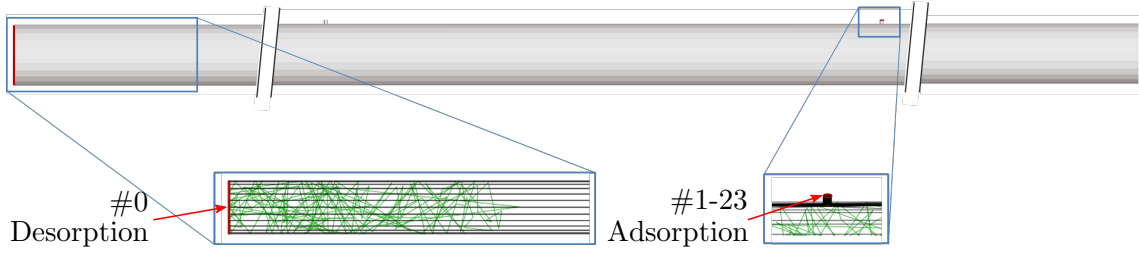
Figure 5.3.: Capillary model in MolFlow+. From facet #0 particles are desorbed into the capillary with a cosine-like angular distribution. With a sticking probability of 1, these particles are adsorbed at facet #1 to #23 (the 23 outlets). Particles, which are reflected backwards onto the desorbing facet are adsorbed as well. In green: Examples of particle trajectories.

adsorbed and desorbed particles then defines the transmission probability:

$$
\begin{aligned}
P &= \frac{\text{Number of adsorbed particles}}{\text{Number of desorbed particles}} \\
&= \frac{\sum_{i=1}^{i=23} \text{adsorption}_{\#i}}{\text{desorption}_{\#0}} \\
&= \frac{1.584 \cdot 10^6}{2.089 \cdot 10^8} = 7.580 \cdot 10^{-3} \quad .
\end{aligned}
\tag{5.1}
$$

With Gaussian error propagation, this yields a transmission probability through the capillary of $P = (7.580 \pm 0.006) \cdot 10^{-3}$.

The conductance is related to the transmission probability via [83]:

$$
C = C_\text{B} \cdot P = \frac{\bar{c}}{4} \cdot A \cdot P \quad ,
\tag{5.2}
$$

with C_B denoting the conductance of the inlet aperture and $\bar{c} = \sqrt{\frac{8 k_\text{B} T}{\pi m_\text{T}}}$ the Maxwell-Boltzmann mean velocity of a particle with mass m_T. For the obtained transmission probability P, the conductance $C_\text{theo.}$ for the molecular flow regime is expected to be:

$$
\begin{aligned}
C_\text{theo.} &= (7.265 \pm 0.006) \cdot 10^{-3}\, \ell/\text{s} \qquad \text{for argon at } 300\,\text{K} \\
C_\text{theo.} &= (2.297 \pm 0.002) \cdot 10^{-2}\, \ell/\text{s} \qquad \text{for helium at } 300\,\text{K} \quad .
\end{aligned}
\tag{5.3}
$$

In the following sections 5.1.2 and 5.1.3, the conductance of a replicated capillary was determined for both argon and helium at room temperature ($T = 300\,\text{K}$).

5.1.2. Test stand to determine the isothermal conductance

To validate the simulation results described in section 5.1.1, the conductance of the capillary was determined experimentally. To do so, equation 5.4 is used:

$$
C = V \cdot \frac{dp_V}{dt} \cdot \frac{1}{\Delta p} \quad .
\tag{5.4}
$$

In this case, the conductance can be obtained by evacuating a specific buffer vessel (volume V) through the capillary and by recording the pressure drop inside that buffer vessel ($\frac{dp_V}{dt}$), as wells as of the difference in pressure (Δp) around the capillary. This measurement was performed in a dedicated UHV test stand. Figure 5.4 shows the flow chart of the set-up. The two major parts are the UHV chamber and the gas inlet system, both being connected by one capillary.
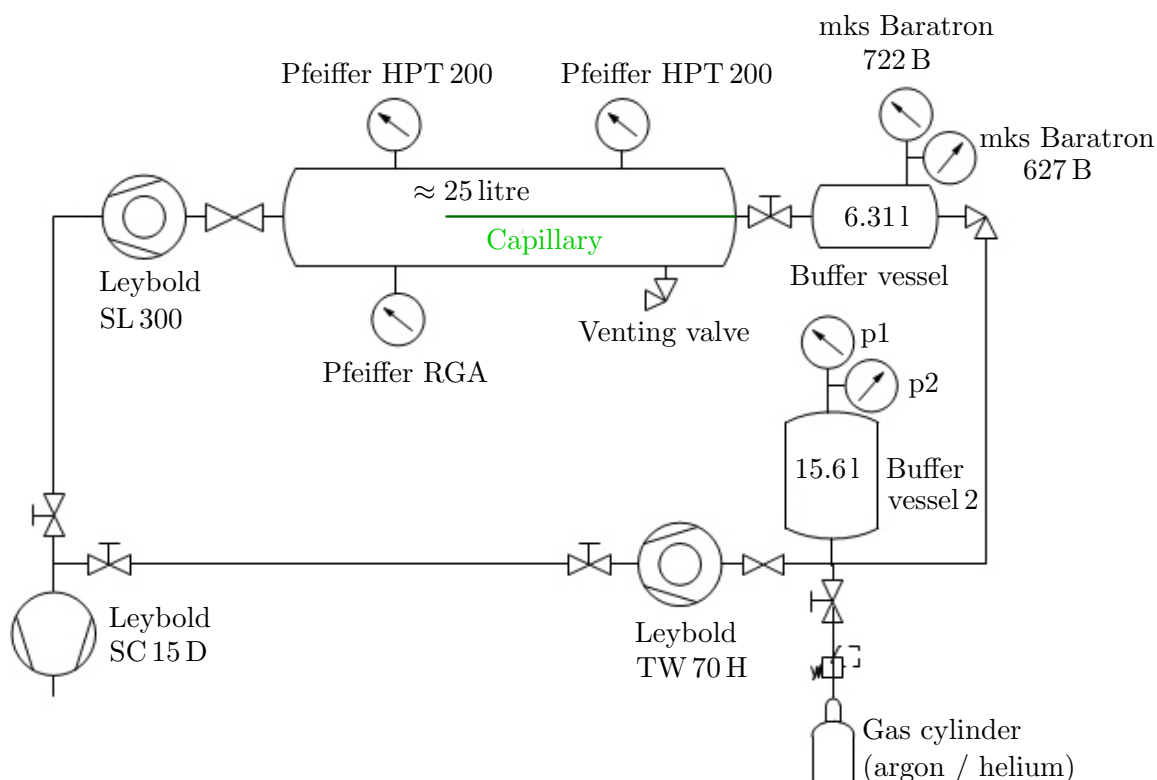
Figure 5.4.: Flow chart of the test stand to determine the conductance of a capillary. The indicators p1 and p2 denote additional pressure gauges at an extra buffer vessel 2. The noble gas was filled into the buffer vessel 2, from which the second buffer vessel was filled. The valve V1 separates the capillary from the buffer vessel.
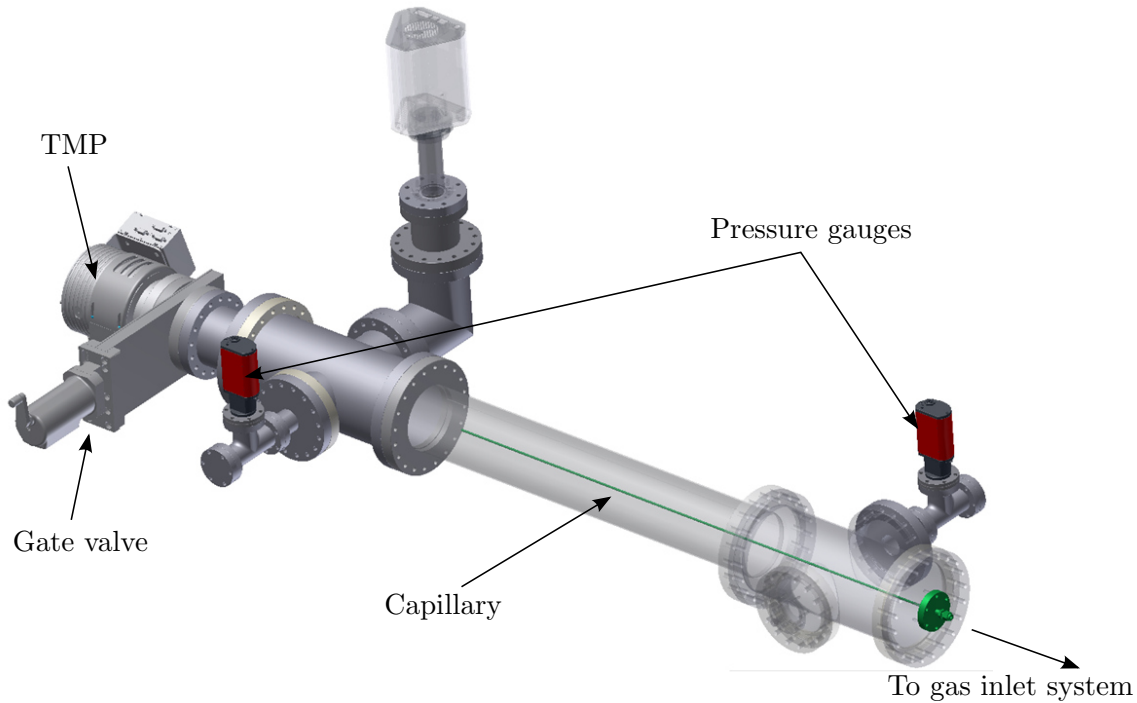
Figure 5.5.: UHV chamber of the test stand to determine the conductance of an argon capillary. In red the two pressure gauges (Pfeiffer HPT 200) are shown, in green the capillary with its 23 orifices on the left end. The gas inlet system is attached to the right. The RGA (rest gas analyser) is shown in transparent, as it was not used during measurements.

UHV chamber

The UHV chamber consists of two four-way cross pieces (DN CF 160) with a 754 mm long tube in between. Figure 5.5 shows a scheme of the test stand. The overall length is about 1500 mm, the minimal inner diameter is 112 mm. At one end a gate valve and a turbo molecular pump (type Leybold SL 300) are mounted. A scroll pump (type Leybold SC 15D) was used as a backing-pump. At the other end the capillary was plugged into the cross-tube assembly and tightened via a CF 40 flange. Due to the large inner diameter of the tube and the corresponding huge conductance, the pressure inside the UHV chamber and thus the pressure around the capillary outlets can be expected to be homogeneous. This assumption was confirmed during measurements. The UHV chamber was equipped with two wide range pressure gauges (type Pfeiffer HPT 200), one at each cross. The Pfeiffer HPT 200 are gas-dependent pressure gauges with uncertainties of the order of $\pm 10\%$ for pressure regimes form $1 \cdot 10^{-8}\,\mathrm{mbar} < p_\mathrm{HV} < 1\,\mathrm{mbar}$ and $\pm 30\%$ for $20\,\mathrm{mbar} < p_\mathrm{HV} < 1000\,\mathrm{mbar}$ [143]. They were used to monitor the pressure of the vacuum end of the capillary. The technical data of the indicators used are given in appendix B. The same system was used to investigate the NEG pumping properties in the last beam tube section of the CPS. A detailed description of the vacuum chamber is therefore given in chapter 7.

The purpose of the UHV chamber is to provide a vacuum which is negligible compared to the pressure of the gas inlet system. This reduces the systematic error of the term $\Delta p = p_\mathrm{HV} - p$ in equation 5.4. By being able to neglect the UHV pressure, the conductance becomes a function of only the capillary inlet pressure.

Gas inlet system

The gas inlet system consists of a buffer vessel with a specific volume of $V = (6.31 \pm 0.05)\,\ell$. Two capacitive vacuum gauges were attached to measure the pressure drop inside the buffer

(a) Capillary feedthrough.

(b) End of the capillary.
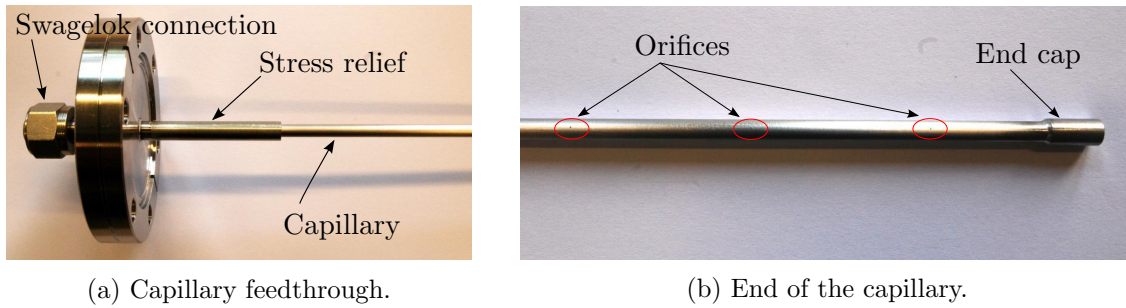
Figure 5.6.: Left: Capillary soldered in a DN CF 40 flange, with a Swagelok connection to the gas inlet system and a stress relief on the UHV site. Right: End of capillary with the last three orifices and a soldered end cap.

volume with high precision over the relevant pressure range. One mks Baratron 722B with a full scale range of 1332 mbar and one mks Baratron 627B with a full scale range of 0.1 mbar were used. These two capacitive gauges guaranteed a gas-independent pressure measurement in the buffer vessel. For evacuation purposes an additional turbo molecular pump (type Leybold TW 70H) was connected to the buffer vessel. The scroll pump of the UHV chamber served as backing-pump here as well. For gas-dependent conductance measurements two different gas species such as the noble gases argon or helium could be filled into the volume by a standard KF 25 valve. The capillary was separated from the inlet system by a Swagelok valve, with an inner diameter of 8 mm. Compared to the capillary, the conductances of each part of the inlet system were large. The pressure drop during measurements was therefore dominated by the capillary itself.

Design of the capillary

The examined capillary was a replication of the original ones, which were already assembled in the CPS. The capillary was based on the technical drawing by ASG (see appendix C). The capillary was roughly 1030 mm long with 23 orifices (ID = 0.2 mm), which were drilled into the stainless steel tube (4×0.25) with a distance of 32 mm each. The tube was closed at one end and soldered on the other side into a feedthrough, which was welded into a DN CF 40 flange. Via a Swagelok adapter this arrangement was connecting the gas inlet and the UHV system. Figure 5.6 shows the significant characteristics of the replicated capillary.

In the CPS all capillaries are bent at the position where they immerse into the beam tube. Because the bending radius is much bigger than the inner diameter ($\frac{r}{d} \gg 1$), this fact has no influence on the gas flow properties within the molecular flow regime [83]. The rebuilt, straight capillary is therefore a very good approximation to the original ones.

5.1.3. Experimental determination of the conductance

Previous investigations in the literature (compare [83]) suggest a constant conductance which is independent of the inlet pressure within the molecular flow regime, due to the non-interacting nature of gas particles in this regime. In the higher viscous region a blocked flow may be observed. The upper / lower limits in pressure for the molecular / viscous regime can be calculated via the Knudsen number and the equation for the mean free path (see equations 3.1 and 3.2). For the molecular flow regime (Kn > 0.5) one obtains:

$$
\begin{aligned}
p &< \frac{k_{\mathrm{B}}T}{\sqrt{2} \cdot \pi \cdot d^2} \cdot \frac{1}{\bar{l}} \\
&< 3.5 \cdot 10^{-2} \, \text{mbar} \qquad \text{(Argon)} \\
&< 6.3 \cdot 10^{-2} \, \text{mbar} \qquad \text{(Helium)} \quad .
\end{aligned}
\tag{5.5}
$$
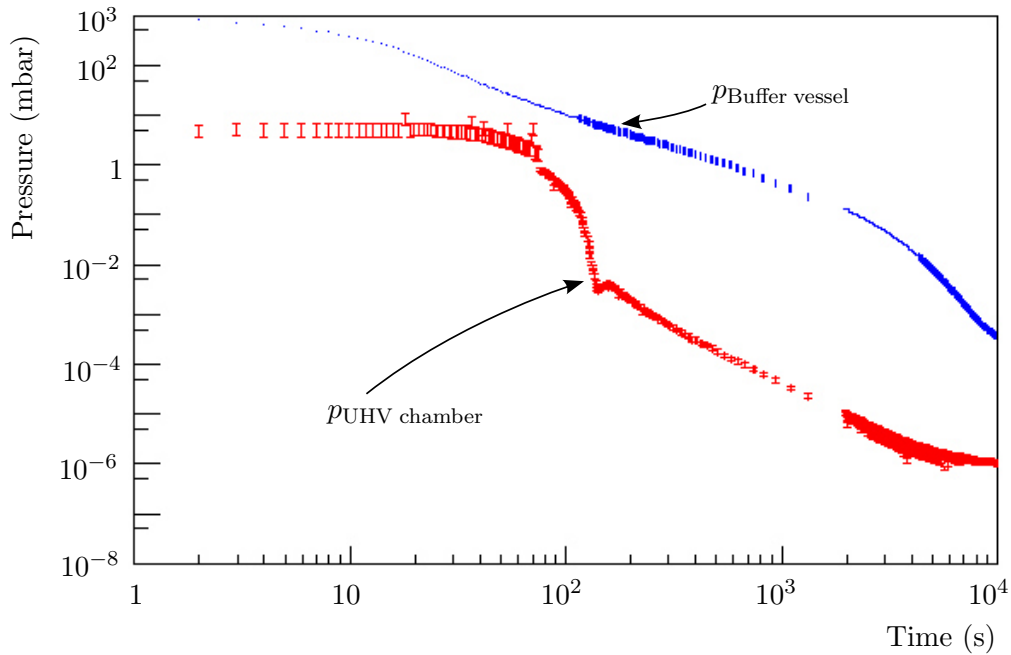
Figure 5.7.: Raw data of one conductance measurement run with argon. The parameter
p_{HV} is the pressure inside the UHV chamber, and has been calculated with
the arithmetic mean of both gauges. After 30 s the TMP was switched on.
The gap between 1000 s and 2000 s in the pressure of the buffer vessel is due
to a measurement gap in the range of both capacitive gauges.

For the viscous flow regime, (Kn < 0.01) respectively, one obtains:

$$
\begin{aligned}
p &> 1.75 \,\text{mbar} \qquad \text{(Argon)} \\
p &> 3.15 \,\text{mbar} \qquad \text{(Helium)} \quad .
\end{aligned}
\tag{5.6}
$$

Here the mean free path was calculated with Van-der-Waals radii of argon $r = d/2 =$
188 pm and helium $r = 140$ pm, respectively, and an ambient temperature of $T = 300$ K.

After commissioning of the test stand, the conductance of one capillary was determined by
evacuation of the buffer vessel with the scroll and the turbo molecular pump through the
capillary. The measurement was performed at room temperature ($T = 300$ K). In detail,
the measurement was performed in the following steps:

1. Filling of the vessel with argon (helium) up to $p = 1$ bar.

2. Evacuation of the UHV chamber with the scroll pump down to $p_{HV} \approx 10^{-3}$ mbar.

3. Opening of the valve V1 between the capillary feedthrough and the buffer vessel (see
   figure 5.4).

4. Switching on of the turbo molecular pump at about $p_{HV} \approx 250$ mbar.

Ahead of each run the capacitive gauges were set to zero. During the measurement phase
the pressure drop over time in the buffer vessel was recorded, as well as the pressure rise
inside the UHV chamber. Figure 5.7 shows the pressure over time for the complete system
during one measurement. After 30 s the TMP was switched on, which can clearly be seen
in the sudden pressure drop in the UHV chamber. The kink after 100 s occurs due to
internal switching of the HPT 200 gauges from the Pirani sensor to the Bayard-Alpert
sensor. Apart from the time interval between 20 s and 100 s, the parameter p_{HV} is at least
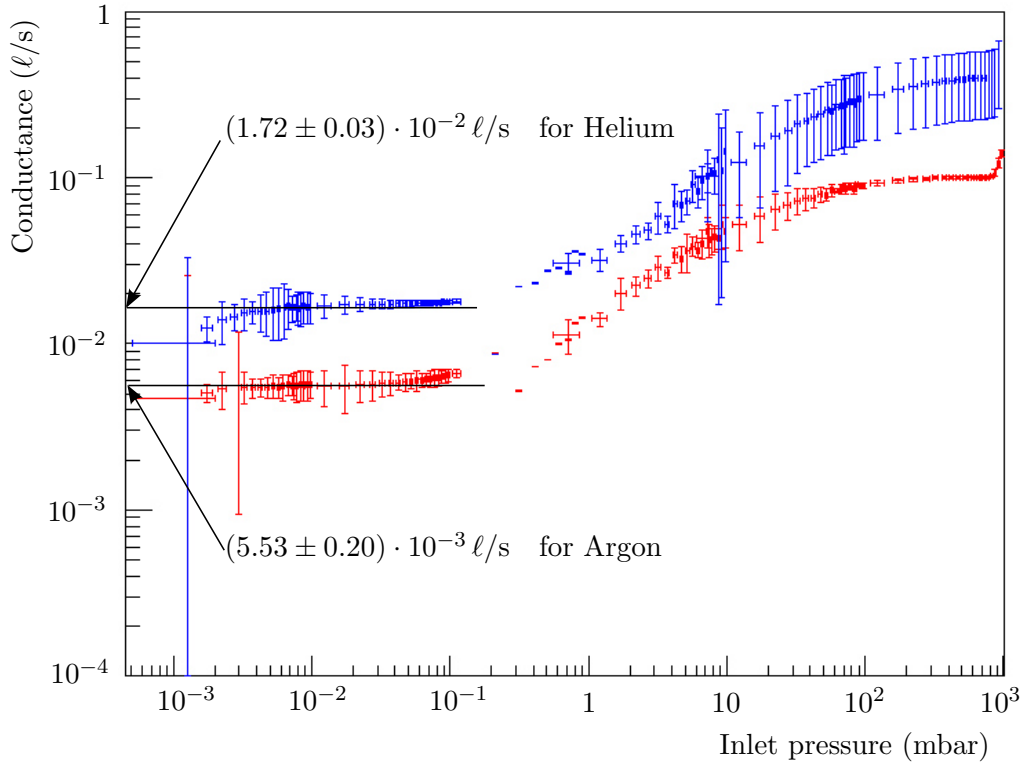
Figure 5.8.: Measured conductance of a capillary for two different noble gases at room temperature. The kink on the right end (at high pressure) is due to the opening of valve V1. Clearly visible is the molecular regime below a pressure of 10^{-1} mbar.

two orders of magnitude lower than the pressure in the buffer vessel.

The conductance can thus be calculated stepwise by using equation 5.4:

$$C = V \cdot \left| \frac{p_V(t_1) - p_V(t_2)}{(t_1 - t_2) \cdot (p_V(\bar{t}) - p_{\mathrm{HV}})} \right| \quad . \tag{5.7}$$

Here, the parameter p_{HV} describes the pressure inside the UHV chamber while $p_V(\bar{t})$ is the average pressure in the buffer vessel between two time steps. Figure 5.8 shows the measured conductance for argon and for helium. A constant conductance for both gases well below their specific pressure limit for the molecular flow region confirms the theoretical expectation in equation 5.5. In the low pressure range, the conductance can be fitted by a constant. This yields to:

$$\begin{aligned} C_{\mathrm{exp.}} &= (5.53 \pm 0.20) \cdot 10^{-3} \, \ell/\mathrm{s} & \text{for argon at } 300\,\mathrm{K} \\ C_{\mathrm{exp.}} &= (1.72 \pm 0.03) \cdot 10^{-2} \, \ell/\mathrm{s} & \text{for helium at } 300\,\mathrm{K} \quad . \end{aligned} \tag{5.8}$$

This agrees to better than 30% with the simulated values given in equation 5.3, which is considered to be good agreement in vacuum physics in view of the complex calibration issues when dealing with pressure gauges.

With increasing inlet pressure the conductance increases as well. In the viscous flow regime a blocked flow is observed for argon at about $p > 100\,\mathrm{mbar}$.

Additional tests were performed to verify that the conductance is dominated by the first section of the capillary (straight tube between the gas inlet and the first orifice). The capillary was first cut at the end, transforming into an open-ended tube, and secondly it was cut before the first orifice, reconfiguring it to a normal tube. The results of measurements
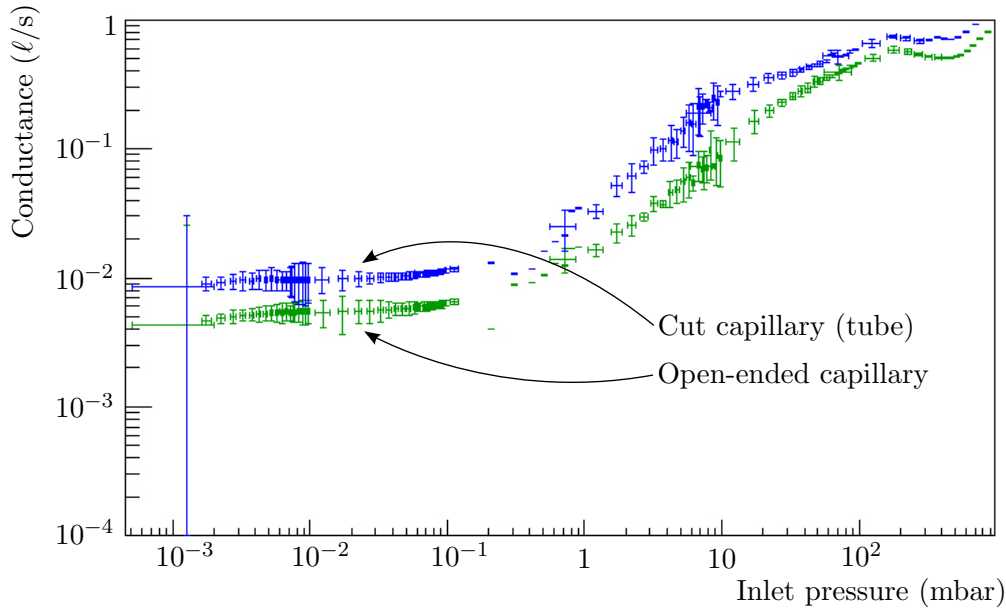
Figure 5.9.: Conductance of an open-ended capillary and a tube (cut capillary, ID: 3.5 mm, L = 310 mm) with the same inner diameter as the capillary. The conductances have been determined with argon gas.

with both configurations are presented in figure 5.9. For the cut capillary the conductance is about 40 % higher than for the uncut one. This conductance change is in good agreement with numerical calculations for tubes of arbitrary length [83]:

$$C = C_{\mathrm{B}} \cdot P = C_{\mathrm{B}} \cdot \frac{14 + 4\frac{l}{d}}{14 + 18\frac{l}{d} + 3\left(\frac{l}{d}\right)^2} \tag{5.9}$$
$$= 1.44 \cdot 10^{-2}\,\ell/\mathrm{s} \qquad \text{for argon at } 300\,\mathrm{K},$$

where $C_{\mathrm{B}} = \bar{c}A/4 \propto \sqrt{T}$ denotes the orifice conductance and P the transmission probability. For later purposes the flow rate through the capillary within the molecular flow regime will be important (compare section 5.3). Therefore the throughput for argon gas has been determined from the measured data. Here, the pV flow rate is defined as [82]:

$$q_{pV} = \frac{p \cdot V}{t} \quad . \tag{5.10}$$

In the specific case of the measurement presented here, this results in:

$$q_{pV} = V \cdot \left| \frac{p_V(t_1) - p_V(t_2)}{(t_1 - t_2)} \right| \quad . \tag{5.11}$$

Figure 5.10 gives the flow rate through the capillary within the molecular flow regime. A linear correlation between the inlet pressure and the flow rate is observed, as expected. This correlation has been fitted by a polynomial of first degree:

$$q_{pV} = a_0 + a_1 \cdot p_V \quad , \tag{5.12}$$

with fit parameters given in table 5.1. The experiments thus have determined both the conductance and the throughput, so that the argon injection procedure can be defined, as described in section 5.4.
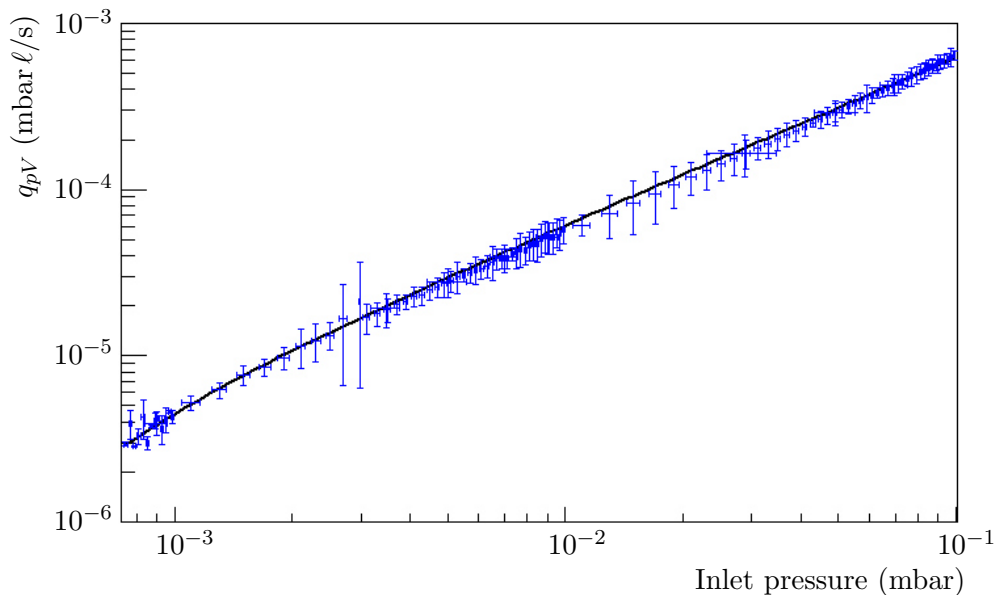
Figure 5.10.: Molecular flow rate through the capillary at room temperature for argon. The linear fit parameters are given in table 5.1

Table 5.1.: Parameters for the fit in figure 5.10 according to equation 5.12.

Parameter	Value	Uncertainty
a_0	$-1.777 \cdot 10^{-6}\,\mathrm{mbar} \cdot \ell/\mathrm{s}$	$7.8 \cdot 10^{-8}\,\mathrm{mbar} \cdot \ell/\mathrm{s}$
a_1	$6.165 \cdot 10^{-3}\,\ell/\mathrm{s}$	$8.4 \cdot 10^{-5}\,\ell/\mathrm{s}$

5.2. Simulation of the temperature distribution for one capillary

The argon injection procedure strongly depends on the temperature distribution of the capillaries, since the maximum throughput is determined by the vapour pressure of argon. A freezing of argon inside the capillaries must be avoided in all cases. During argon injection, the capillary is therefore heated (max. 125 mW) at the connection to the gas supply tube.

This process is of major importance for the tritium pumping functionality of the CPS and thus has been simulated with COMSOL Multiphysics. The simulation framework of COMSOL allows to consider the thermal constraints, given by the CPS design, and the molecular gas flow through the capillary including conductive heat transfer. More details on the gas flow are given in section 5.3.

The modelling of thermal problems in the COMSOL Multiphysics suite requires an adequate, simplified geometry. Based on technical drawings (see appendix C), a geometry has been implemented, as shown in figure 5.11. This geometry includes the capillary, the capillary holding tube, the gas supply tube, the feedthrough shoe between capillary and beam tube, both thermal dumps at liquid nitrogen and liquid helium temperature, and finally the capillary heater. A closer look at the part where the capillary is connected to the gas supply tube is given in figure 5.12a and for the end-piece of the capillary in figure 5.12b. The gold-plated capillary is welded to the holding tube at its upper end. There is a mechanical and thermal contact between capillary and holding tube over a length of 23.5 mm, which allows thermal heat transfer from the holding tube onto the capillary. At that point a copper plate is mounted around the welded part. On top of the copper support, two redundant electric heaters are mounted. The capillary has no contact to the
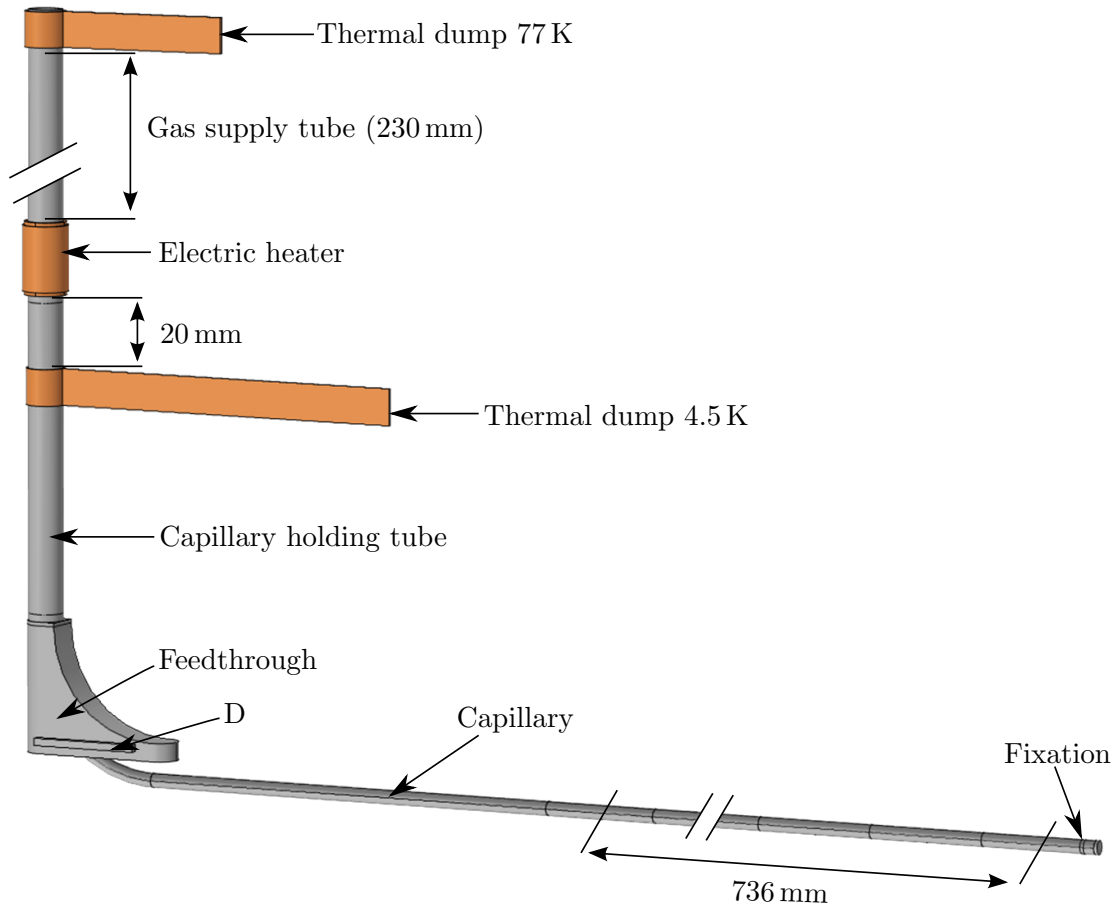
Figure 5.11.: Implemented model of the argon capillary in COMSOL Multiphysics. Implemented are the thermal dump at 77 K (copper), gas supply tube (OD: 9.53 mm, wall thickness: 0.51 mm), electric heater (max. 125 mW), thermal dump at 4.5 K (copper), capillary holding tube (OD: 9.53 mm, wall thickness: 0.2 mm), feedthrough shoe (D) welded onto beam tube (6 K during argon preparation), gold plated capillary (OD: 4 mm, wall thickness: 0.25 mm) with 23 orifices at intervals of 32 mm, and the fixation of the capillary.

(a) Capillary fixation.

(b) End-piece of capillary.
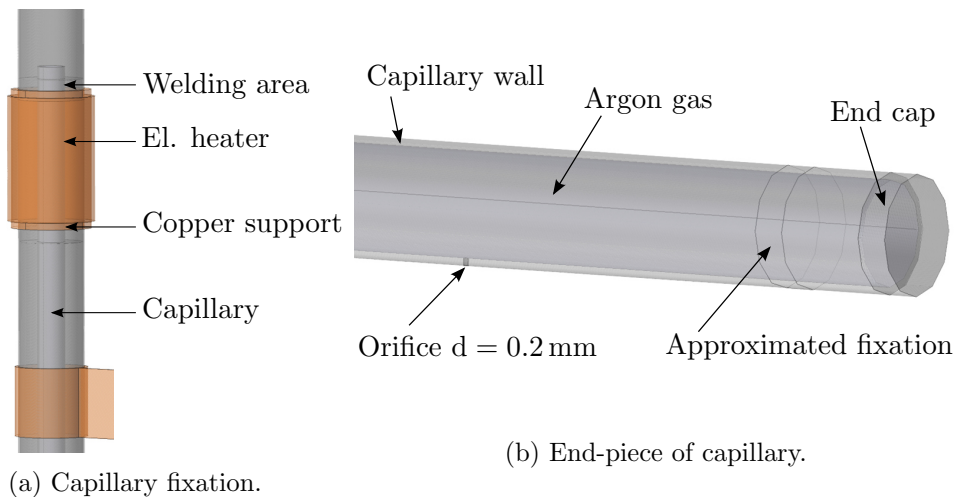
Figure 5.12.: Detailed view of the fixation at the inlet of the capillary 5.12a and the closed end-piece with the approximated fixation at the end of the capillary 5.12b.

beam tube, beside the welding area and a loose connection at its end. There the capillary is fixed with a wire, loosely wrapped around the tube and clamped against the beam tube (compare figure 5.1). The contact area is a straight line, since both objects (tube and wire) feature round geometries. By applying a finite mesh in COMSOL Multiphysics, the heat load through this contact is negligible. This particular difficulty has been solved by specifying the heat load directly. Therefore a ring surface has been created (figure 5.12b "Approximated fixation") instead of the wire holding.

After modelling the geometry, the physical properties were defined. The thermal dumps were fixed to 77 K and 4.5 K, respectively. The gas supply tube, the capillary holding tube, and the feedthrough shoe radiate in equilibrium with the ambient. The ambient temperature was set to 4.5 K. At point D in figure 5.11 the feedthrough was fixed to 6 K. That point represents the connection to the beam tube. Inside the capillary holding tube, a surface to surface radiation was defined between the capillary and the holding tube. Most parts of the capillary radiate in equilibrium with the beam tube. The beam tube temperature was set to the optimal temperature for argon preparation at 6 K.

The heat load at the anchorage (figure 5.11 "Fixation") was specified directly, as mentioned above. The heat load is then given by the pressed contact between capillary and wire, with almost no force. By calculating the weight of the capillary (≈ 24 g) it can be assumed that the connecting force at the holding wire is approximately the gravitational force, with half weight (≈ 0.1 N). Heat conduction across pressed contacts depend on force and are independent of the contact area. Also the thermal conductance increases approximately linearly with pressure [141].

Assuming a contact temperature of 40 K (as specified), the thermal conductivity k (in W/K) between capillary and anchorage (wire) can be estimated, using appendix G, and the linear scaling in pressure:

$$k_{\text{Au-Au: 100 N}} \approx 7 \cdot 10^{-1}\,\text{W/K} \quad \text{at} \quad 10\,\text{kg force [141]}$$
$$\Rightarrow \quad k_{\text{Au-Au: 0.1 N}} \approx 7 \cdot 10^{-4}\,\text{W/K} \quad \text{at} \quad 12\,\text{g force} \quad . \tag{5.13}$$

This value is two orders of magnitude below a typical soldered contact, i.e. Pb solder, with a contact area of only $1\,\text{mm}^2$ ($k_{\text{Pb solder, 1 mm}^2} \approx 3 \cdot 10^{-1}\,\text{W/K}$ [141]). In general, solid contacts have a higher thermal conductivity than soldered joints, and pressed contacts [141]:

$$k_{\text{pressed}} < k_{\text{solder, varnish, grease}} < k_{\text{solid body}} \quad , \tag{5.14}$$

thus the thermal conductance of a pressed contact is at least two orders of magnitude below the thermal conductivity of a solid. The maximum heat transfer across the anchorage can be assumed with the following approach, since there is no tabulated data available for pressed gold/gold contacts in the temperature region below 100 K:

1. Calculating the maximum heat load on the capillary by assuming a perfect solid/solid contact (one body) to the fixation.

2. From equation 5.13 it is known that the thermal conductivity of a pressed contact is at least two orders of magnitude below a solid/solid interface. Thus the maximum heat load can be multiplied by a factor of 0.01 to obtain a new upper heat load limit.

3. Definition of a parametric sweep in COMSOL, where the heat load is varied between the worst case (full heat transfer) and the best case (no heat transfer).

From figure 5.1 it can be seen that the capillary anchorage is fixed at two ends to the 6 K cold beam tube. The length between fixation of the anchorage and the capillary is 30 mm each. The diameter of the wire is 1 mm. This results in a maximum heat load on the capillary of:

$$q = k(T) \cdot \frac{A}{l} \cdot \Delta T \cdot c = k \cdot 5.24 \cdot 10^{-5}\,m \cdot \Delta T \cdot c \quad , \tag{5.15}$$

Table 5.2.: Settings for the 'heat transfer (ht) module' in COMSOL for the thermal heating of one argon capillary during argon injection.

COMSOL property	Parameter	Value	Description
Heat flux 1	q_{tot}	125 mW	Electric heater
Heat flux 2	q	$5.24 \cdot 10^{-5}\,m \cdot \\ \cdot k(T) \cdot \Delta T \cdot c$	Heat load through capillary anchorage with the thermal conductivity $k(T)$.
	c	0, 0.001, 0.01, 0.1, 1	Parametric sweep of heat flux 2
Temperature 1	T_0	6 K	Temperature of connection parts to the beam tube.
Temperature 2	T_0	4.5 K	Thermal dump of holding tube at 4.5 K.
Temperature 3	T_0	77 K	Thermal dump of gas supporting tube at 77 K.
Surface to ambient radiation 1	ϵ T_{amb}	0.04 6 K	Radiation between capillary and beam tube.
Surface to ambient radiation 2	ϵ T_{amb}	0.2 4.5 K	Radiation between gas holding/supply tube and cold mass.
Surface to surface radiation	ϵ	0.02	Radiation between capillary and capillary holding tube.

with the material-dependent thermal conductivity k and a dimensionless scaling factor $c = 1$. By sweeping the parameter c from 1 to 0, the impact on temperature caused by different heat loads can be simulated.

All simulation parameters are given in table 5.2. The basic time-independent equations for the heat transfer problems described here and which have been implemented in COMSOL, are equations 5.16 to 5.19 [96]. Table 5.3 specifies the descriptions of the variables and constants used in the simulation.

With this set of variables and constants, one obtains four equations, with the basic equation for heat transfer in solids given by:

$$\rho C_p \vec{u} \cdot \nabla T = \nabla \cdot (k\nabla T) + Q \quad , \tag{5.16}$$

the temperature gradient caused by a given heat flux q_{tot}:

$$-\vec{n} \cdot (-k\nabla T) = \frac{q_{\text{tot}}}{A} \quad , \tag{5.17}$$

the temperature gradient caused by radiative heat exchange with the ambient:

$$-\vec{n} \cdot (-k\nabla T) = \epsilon\sigma(T_{\text{amb}}^4 - T^4) \quad , \tag{5.18}$$

and, finally, the temperature gradient caused by radiative heat exchange between different surfaces:

$$-\vec{n} \cdot (-k\nabla T) = \epsilon(G - e_b(T)) \quad . \tag{5.19}$$

Table 5.3.: Description of used variables in the COMSOL 'heat transfer module'. Based on [96].

Variable	Description
T	Absolute temperature
T_{amb}	Ambient temperature such as the temperature of a surrounding body.
ρ	Density
C_p	Specific heat capacity at constant pressure
$\vec{u}$	Velocity vector
k	Thermal conductivity
q_{tot}	Total heat power (positive or negative)
A	Surface area
ϵ	Emission coefficient
σ	Stefan-Boltzmann constant
$e_b(T)$	Emission power
G	Irradiation power (subdivided into several aspects of irradiation)
Q	Heat sources other than viscous heating

By solving this set of equations with the finite element method, the temperature distribution along a capillary is obtained. In principle it is possible to add a convective heat transfer term to consider the heat transfer by the molecular gas flow inside the capillary (compare section 5.3). When comparing the anticipated conductive and radiative heat loads, this term can be neglected, as done in this simulation. Figure 5.13 shows the result without convective heat transfer. The temperature over the capillary length is plotted in figure 5.14 for different heat loads at the anchorage (c = 0, 0.001, 0.01, 0.1, 1). The maximum temperature reached during argon preparation is 76.1 K with a heating power of 125 mW. It turned out that the maximum temperature only weakly depends on the heat transfer at the anchorage, but that it strongly depends on the 4.5 K thermal dump. If the dumping distance is far enough, more than 100 K can be reached.

The minimum temperature at the end of the capillary is between 17 K (maximum heat load at the anchorage) and 69 K (no heat load at the anchorage). Assuming a thermal conductivity of the pressed contact, i.e. two orders of magnitude below the maximum heat load (see approach above), a temperature of 62 K is reached at the anchorage.

5.3. Temperature-dependent gas flow simulation through the capillaries

To avoid freezing of argon inside the capillary, the argon pressure must be less than the vapour pressure at the corresponding temperature along the capillary shown in figure 5.15 and appendix E. The pressure gradient along the capillary has thus been simulated with COMSOL Multiphysics in the molecular flow regime, taking into account the temperature distribution of section 5.2. For the simulation, the same model as described in section 5.2 was used. In the 'free molecular flow (fmf)' module the options "reservoir" and "total vacuum" were set. The pressure at the border of each orifice was defined to be zero, which corresponds to "total vacuum". The inlet of the capillary was fixed at constant pressure ("reservoir"). During argon preparation this implies a constant inlet pressure and hence a constant gas flow. This inlet pressure was calculated (equation 5.5) with the maximum
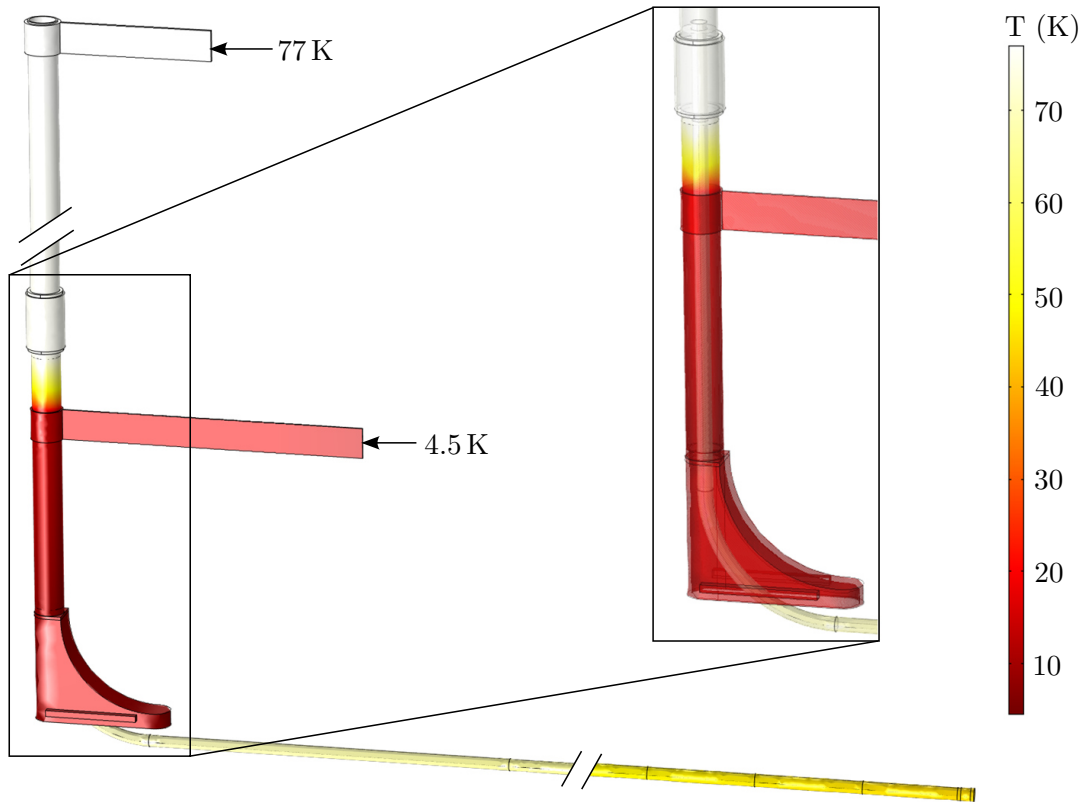
Figure 5.13.: Temperature along the argon capillary during argon preparation. A bright colour represents higher temperatures. The maximum temperature of the capillary is reached at 76.1 K. Note, that the capillary is surrounded by the beam tube (T = 6 K), which is not shown in the picture.
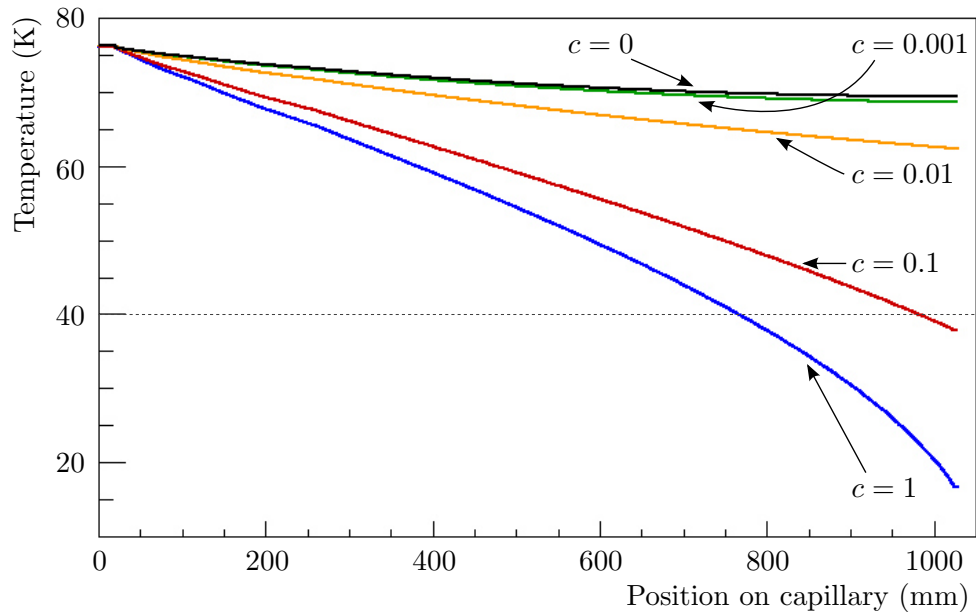
Figure 5.14.: Temperature gradient along the capillary. The beginning of the capillary inside the feedthrough lies at $x = 0$ mm. The maximum temperature is about 76.1 K. The minimum temperature depends on the thermal conductivity at the anchorage (fixation at the end of the capillary) and will be between 17 K and 69 K. The dashed line shows the specified 40 K temperature regime.
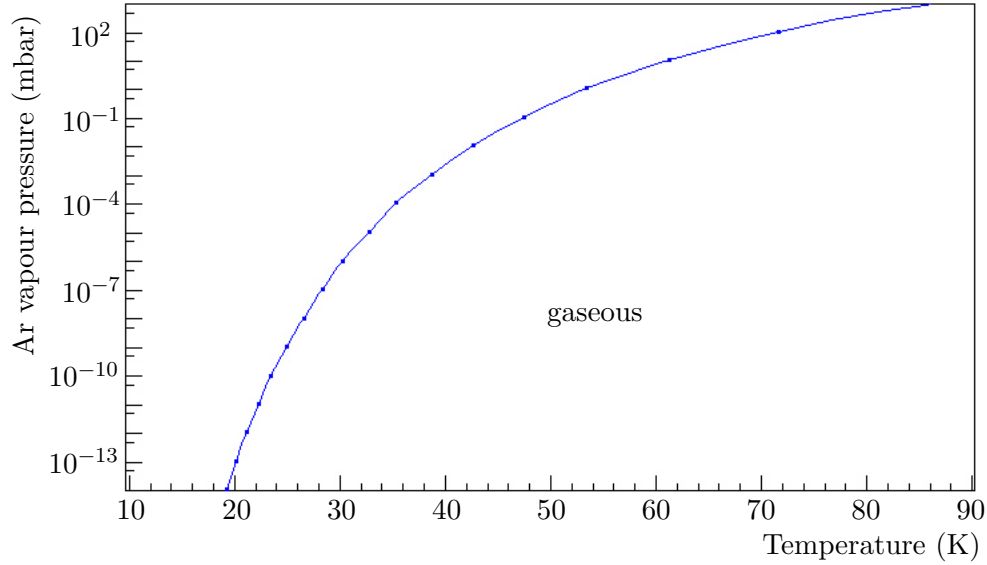
Figure 5.15.: Argon vapour pressure curve. Data are taken from [59], based on [144]. Below the line is the gaseous regime, above argon starts to freeze.

temperature at this point of 76.1 K for the molecular flow:

$$p_{\text{in}} = 9.6 \cdot 10^{-3}\,\text{mbar} \approx 10^{-2}\,\text{mbar} \quad . \tag{5.20}$$

In COMSOL, problems corresponding to the free molecular flow are solved by the angular coefficient method. The problem (geometry) has to be discretized by a mesh. The molecular flow is then calculated by summarizing over the incoming flux on a mesh element from all other surfaces in its line-of-sight [96]. By solving the set of equations 5.21 the pressure, the number density, and the incident molecular flux are determined.

$$\text{Incident molecular flux:} \quad G = -\int_S \frac{J'(\vec{n} \cdot r)(\vec{n'} \cdot r)}{\pi r^4} dS$$

$$\text{Number density:} \quad n = -\int_{S'} \frac{J'(\vec{n'} \cdot r)}{\pi r^3} \left\langle \frac{1}{c'} \right\rangle dS' + 2J \left\langle \frac{1}{c'} \right\rangle \tag{5.21}$$

$$\text{Pressure :} \quad p = \int_{S'} \frac{J'(\vec{n} \cdot \vec{r})^2 (\vec{n'} \cdot \vec{r})}{\pi r^5} m \left\langle c' \right\rangle dS' + \frac{2}{3} Jm \left\langle c \right\rangle \quad .$$

Explanations to the variables and constants used here are given in table 5.4. By employing the mean velocity in the number density and the pressure, the temperature dependency is included.

Figure 5.16 shows the pressure gradient along the capillary and the expected argon vapour pressure according to the temperature simulations shown in figure 5.14. Here, only the worst case with maximum heat load at the capillary anchorage ($c = 1$), the best case with no heat transfer at the anchorage ($c = 0$), and one value in between are plotted. The different temperature distributions only have negligible influence on the pressure distribution inside the capillary. The pressure drops from the predefined inlet pressure of $\approx 10^{-2}\,\text{mbar}$ down to approximately $(1 \pm 0.2) \cdot 10^{-4}\,\text{mbar}$ at the position of the last orifice. A linear decrease is observed between 0 mm at the beginning of the capillary (welded part), and at 290 mm, as expected for simple tubes, with no orifice. The following 23 orifices are placed at distances between 290 mm and 1027 mm with a distance of 32 mm to each other.
In the worst but rather unrealistic case of maximum cooling at the end, argon will freeze

Table 5.4.: Description of the variables used in the COMSOL 'free molecular flow (fmf) module'. Based on [96].

Variable	Description
S	Surfaces in the line of sight of the surface x that should be calculated.
J	Outgoing flux from the surface x.
$\vec{n}$	Surface normal of x.
$\vec{n}'$	Surface normal of the surfaces in the line of sight of x.
r	Distance between x and surrounding surfaces.
$\langle c \rangle$	Mean velocity $\sqrt{\frac{9\pi k_\mathrm{B} T}{8m}}$.
$\langle \frac{1}{c} \rangle$	Mean inverse velocity.
m	Particle mass.

inside the capillary. If the thermal conductance is only 10% of the worst case, argon freezing is not expected. In this case, there is even a safety factor of 10 between the expected pressure inside the capillary and the argon vapour pressure.

The mean total molecular net flux J_tot (= emitted molecular flux minus incident molecular flux = $J - G$) at the inlet was calculated to be $3.32 \cdot 10^{20}\,(\mathrm{m}^2\mathrm{s})^{-1}$. This means a total flux of $3.20 \cdot 10^{15}\,\mathrm{s}^{-1}$ for the capillary over a cross-section area of $9.62 \cdot 10^{-6}\,\mathrm{m}^2$. The simulated flow rate at $76.1\,\mathrm{K}$ can be derived from equation 5.10:

$$
\begin{aligned}
q_{pV\,\mathrm{sim.}} &= \frac{p \cdot V}{t} = \frac{n \cdot k_\mathrm{B} \cdot T}{t} \\
&= J_\mathrm{tot} \cdot k_\mathrm{B} \cdot T \\
&= 3.35 \cdot 10^{-5}\,\frac{\mathrm{mbar} \cdot \mathrm{l}}{\mathrm{s}} \quad .
\end{aligned}
\tag{5.22}
$$

This can be compared with the experimental value of the measured flow rate (equations 5.12 and 5.20). Since the throughput is directly proportional to the temperature, the flow rate at any temperature can easily be determined to be:

$$
q_{pV}(T') = q_{pV}(T) \cdot \frac{T'}{T} \quad .
\tag{5.23}
$$

$$
\begin{aligned}
\Rightarrow q_{pV,\mathrm{exp.}}(76.1\,\mathrm{K}) &= q_{pV,\mathrm{exp.}}(300\,\mathrm{K}) \cdot \frac{76.1\,\mathrm{K}}{300\,\mathrm{K}} \\
&\stackrel{\mathrm{eqn.\,5.12}}{=} (a_0 + a_1 \cdot p_\mathrm{in}) \cdot 0.25 \\
&= 1.39 \cdot 10^{-5}\,\frac{\mathrm{mbar} \cdot \mathrm{l}}{\mathrm{s}} \quad .
\end{aligned}
\tag{5.24}
$$

The temperature-corrected measured and the simulated molecular flow rates during argon injection differ by a factor of 2.44. The experimentally measured flow rate has been scaled down towards a lower temperature, assuming a constant temperature along the capillary. The simulation with COMSOL Multiphysics therefore considers a temperature gradient. By considering all approaches, both the measurement and the simulation lead approximately to the same molecular flow rate through the capillary.
With the simulation, the ratio between the flow rate of each outlet can be determined. The transmission probability for each orifice is the same, since the geometrical dimensions are identical. By taking the pressure of the first orifice (normalised to one) as reference, the
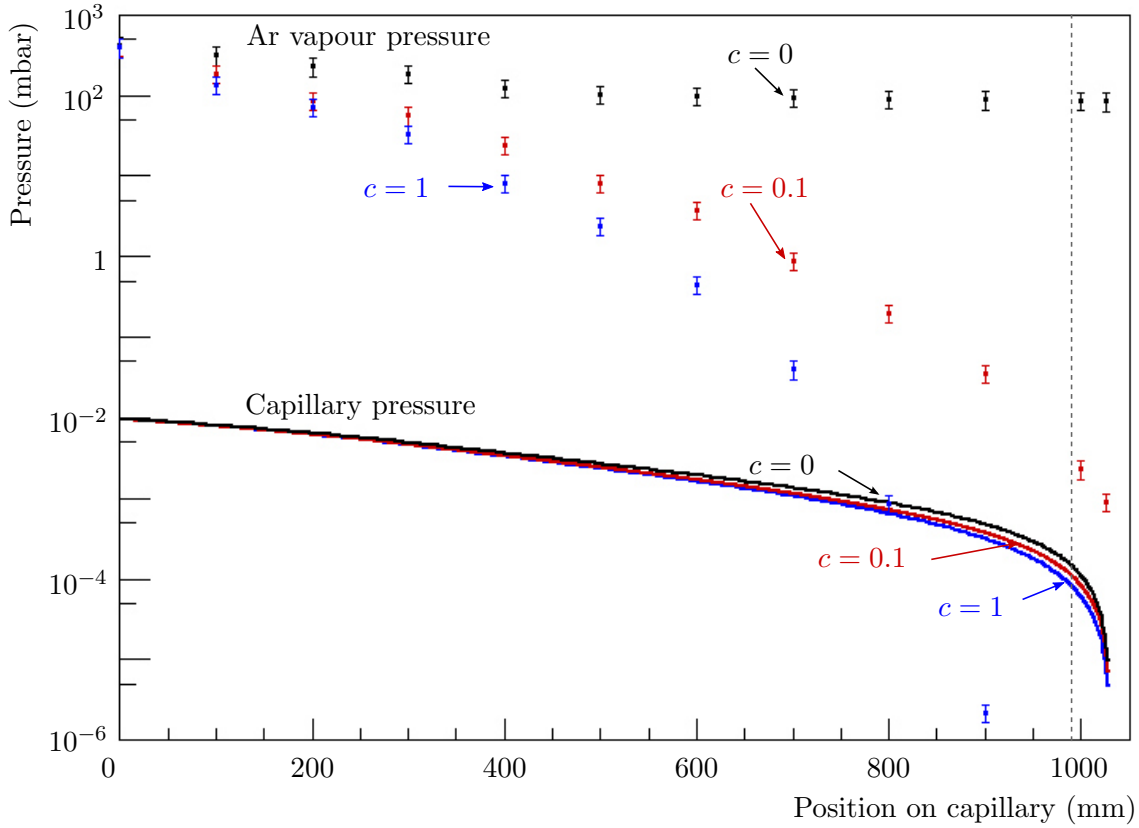
Figure 5.16.: Pressure distribution along the argon capillary. The position $x = 0\,\text{mm}$ marks the beginning of the capillary inside the feedthrough. Curves on top: Argon vapour pressure according to the temperature distribution shown in figure 5.14. The error bars are caused by uncertainties in figure 5.15. Curves on bottom: Simulated pressure inside the capillary. The parameter c is the scaling factor of the thermal conductance at the capillary anchorage, according to equation 5.15. The grey dashed line is the position of the last orifice.

Table 5.5.: Flow rate ratio between the 23 orifice of the capillary. The flow of the first orifice was set to one and serves as the reference. The units are chosen arbitrarily to be 10^{-2}.

# Orifice	Flow rate	# Orifice	Flow rate	# Orifice	Flow rate
1	100.0	9	42.6	17	14.4
2	90.3	10	38.0	18	11.8
3	81.6	11	33.9	19	9.2
4	73.9	12	29.8	20	6.9
5	66.3	13	26.4	21	5.0
6	59.5	14	22.9	22	3.0
7	53.4	15	19.8	23	1.1
8	48.0	16	15.9		

ratios in the flow through each orifice can be determined ($q \propto p$). Table 5.5 summarises the corresponding ratio values. The gas flow between the first and the last orifice differs by a factor of about 100 and is the prime reason that the argon frost layer will not be distributed homogeneously in its thickness, in contradiction to the expectations during the design of the CPS.

5.4. Specification of the argon injection procedure

After having determined the conductance of the argon capillary (section 5.1) and the mass flow rate at the operation temperature during argon preparation (section 5.3), the argon injection procedure can now be fully defined. The injection system consists of two parts: the external gas injection control system outside of the CPS cryostat, and the inner capillaries with their gas supply tubes, which have been described in the previous sections. The outer system was drafted by O. Kazachenko [145] and built by M. Sturm (TLK, KIT), based on experiences at the previous TRAP experiment at TLK [146] [147] [148]. Aim of the TRAP (Tritium Argon frost Pump) experiment was to determine the tritium pumping properties with layers of argon frost. The main component of the experiment was a 20° bent beam tube featuring a cryo-surface area of 1/15 of the CPS size. The results of the tritium retention measurements have been used to design the argon injection system for the CPS. A flow chart of the outer injection system is shown in figure 5.17. It consists of a 3 litre buffer vessel, which is connected to a manifold. In between a flow meter (type mks Flow Meter 179A), an automatic valve, and a regulation valve are mounted to fill the manifold. The manifold itself includes 18 valves, two successively for each capillary. Pressure sensors of the type mks Baratron 750 C and mks Baratron 627 D are mounted at the buffer vessel and the manifold. A turbo molecular pump allows to evacuate the buffer vessel and the manifold separately. Compensation tubes have to be installed between the nine valves at the manifold and the nine automatic valves. These are directly located at the CPS cryostat, in order to connect the external gas injection control system with the inner argon capillaries. Their length will be between three and four metres. They will compensate the difference in length between the gas supply tubes inside the CPS providing equal conductance for each argon channel. The design of the compensation tubes has to be defined during commissioning measurements (see below).

During argon injection the pressure at the beginning of each capillary should be constant, at $p = 10^{-2}$ mbar (equation 5.20). Therefore the pressure inside the manifold of the outer gas injection system must be constant in time as well. For the commissioning, the initial parameter has to be estimated. For this estimation the following assumptions have been set:

- An average length of the gas supply tubes (inner diameter = 8.51 mm) inside the CPS of 0.5 m.

- An average length of the compensation tubes (inner diameter = 8.51 mm) between the injection system and the CPS capillary flanges of 3.5 m.

- A temperature of the gas supply tubes of 77 K.

- The compensation tubes are at room temperature (293.15 K).

Inside the compensation and the gas supply tubes, the gas flow falls in the molecular and the transitional flow regime. The conductance in this part can be approximated to be $C = C_{\mathrm{mol}} + C_{\mathrm{lam}}$. Here, C_{lam} is the conductance in the laminar flow regime, yielding [83]:

$$
\begin{aligned}
C &\approx C_{\mathrm{mol}} + C_{\mathrm{lam}} \\
&= \frac{A \cdot \bar{c} \cdot d}{3 \cdot l} + \frac{\pi \cdot d^4}{256 \cdot \eta \cdot l} \cdot (p_{\mathrm{in}} - p_{\mathrm{out}}) \quad ,
\end{aligned}
\tag{5.25}
$$
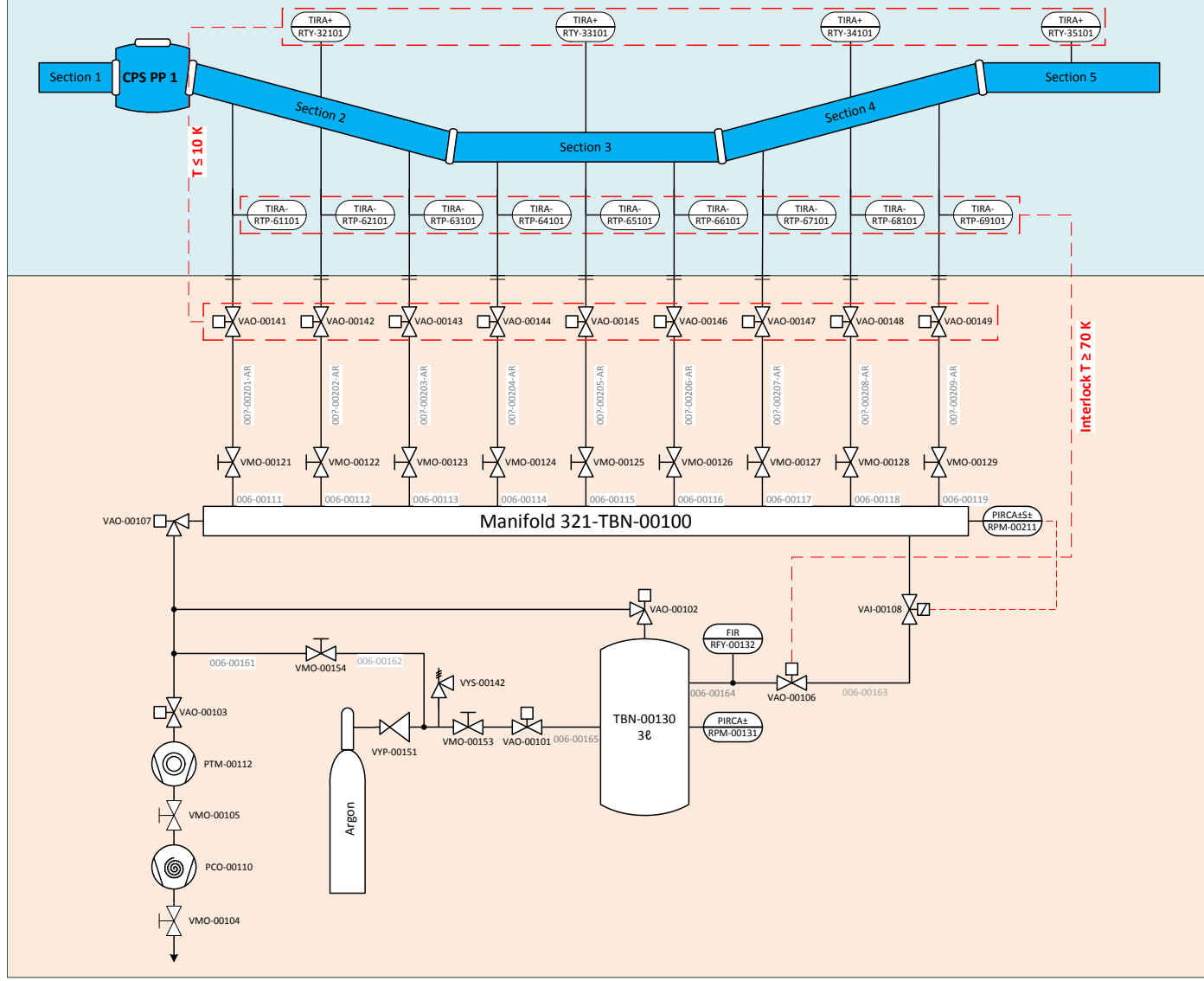
Figure 5.17.: Flow chart of the argon injection system. Components against the light blue background are inside the CPS cryostat. Components against the light orange background belong to the external argon injection control system. Based on the flow chart from M. Sturm (TLK, KIT).

where A defines the cross-section area, $\bar{c}$ the mean velocity (depending on temperature), d the inner diameter of the tube, ℓ the length of the tube, η the dynamic viscosity, and finally $(p_{\text{in}} - p_{\text{out}})$ the difference between inlet and outlet pressure.

Because of the different temperatures between the compensation and the gas supply tube, the conductance can not be calculated in one step. First the inlet pressure of the gas supply tube must be calculated. This inlet pressure can then be used as the outlet pressure of the compensation tube:

$$\Delta p = p_{\text{in}} - p_{\text{out}} = \frac{q_{pV}}{C}$$
$$p_{\text{in}} = \frac{q_{pV}}{C_{\text{mol}} + C_{\text{lam}}} + p_{\text{out}} \quad . \tag{5.26}$$

By doing so, the inlet pressure of a gas supply tube is determined to be $p_{\text{in}} \approx 0.01\,\text{mbar}$. Accordingly, the inlet pressure of one compensation tube should be $p_{\text{in}} = 0.0112\,\text{mbar}$. Hence the initial pressure inside the manifold must be of the same order of magnitude. The flow rate from the buffer vessel into the manifold must be set to:

$$q_{pV/\text{tot}} = N_{\text{capillaries}} \cdot 3.35 \cdot 10^{-5}\,\frac{\text{mbar} \cdot \ell}{\text{s}} \cdot \frac{293.15\,\text{K}}{76.1\,\text{K}}$$
$$= 1.16 \cdot 10^{-3}\,\frac{\text{mbar} \cdot \ell}{\text{s}} \quad , \tag{5.27}$$

with the number of capillaries $N_{\text{capillaries}} = 9$.

Determination of the required amount of argon

The amount of argon needed to form the frost layer can be calculated in a straight forward manner. The surface to be covered by the argon frost consists of the sections 2, 3, 4, and 5 inside the CPS. They offer an area of $A = 2.57\,\text{m}^2$ with the bellows being approximated by a tube in this calculation. The beam tube temperature during preparation will be 6 K. The density of solid argon decreases with increasing temperature and reaches a value of $\rho_0 \approx 1.77\,\frac{\text{g}}{\text{cm}^3}$ at 6 K [149] [150]. As shown in detail in chapter 6, not more than 3000 monolayers should be prepared. The value of 3000 monolayers corresponds approximately to a thickness of about $\delta = 3\,\mu\text{m}$. When preparing an argon frost layer at 6 K, the argon will freeze to a porous structure, with a porosity Φ of 15% [151]. The porosity is defined as:

$$\Phi = 1 - \frac{\rho}{\rho_0} \quad . \tag{5.28}$$

Hence, the necessary amount for preparation is $m = (1 - \Phi \cdot)\,\rho_0 \cdot A \cdot \delta = 11.6\,\text{g}$. With the molar mass of $39.948\,\text{g}\,\text{mol}^{-1}$ and the ideal gas law at room temperature, this leads to an maximum amount of argon of:

$$pV = \frac{m \cdot N_A \cdot k_B \cdot T}{M_{\text{Ar}}} = 7.07 \cdot 10^3\,\text{mbar} \cdot \ell \quad . \tag{5.29}$$

Designing the compensation tubes between argon injection system and CPS

During commissioning the compensation tubes have to be adjusted in length in order to achieve the same mass flow for each capillary to ensure a homogeneous argon distribution inside the beam tube. The aim here is to compensate the difference in length of the gas supply tubes within the CPS cryostat, which is up to more than half a metre. A conductance measurement is thus necessary to compensate these differences. Within the molecular flow regime, the conductance does not depend on pressure, only on the geometrical dimension. It is therefore recommended to carry out the measurement in the molecular flow regime. Equivalently, the buffer vessel in figure 5.17 (TBN-00130) should

be filled with argon up to 10 mbar. The pressure inside the manifold (321-TBN-00100) should then be kept at about $1.5 \cdot 10^{-2}$ mbar. The beam tube of the CPS should be pumped out continuously, via a turbo molecular pump, at pump port 1. The argon is then injected through one capillary. The flow rate, and the pressure drop inside the buffer vessel respectively, should be monitored. This yields the conductance of one capillary plus gas supply tube plus compensation tube. The measurement has thus to be repeated for each of the nine capillaries, with the same initial set of parameters. Finally, from the difference in conductance obtained, the difference in lengths can be obtained. It should be noted that room temperature is recommended for these measurements.

Summary

In this section it could be shown, that no freezing of argon inside the capillaries can be expected during the argon preparation process with respect to the molecular flow regime. As described in the next section, at least 1000 monolayers of argon should be prepared in order to reach the specified gas reduction ($> 10^7$) and the specified capacity. The CPS must be able to handle at least 1 Ci within 60 days of nominal KATRIN operation, without regeneration of the argon frost layer. With the experimentally and theoretically determined argon throughput of 10^{-3} mbar ℓ/s (molecular flow regime), through all 9 capillaries, it will take about 3-4 weeks to prepare the argon frost layers. In order to shorten this time period the inlet pressure and thus the flow rate must be increased beyond the molecular flow regime. Since non-isothermal calculations in the transitional flow regime are only estimates, an exact calculation on the argon preparation cannot be performed in this particular flow regime. The detailed argon preparation procedure, with respect to the injection time, has to be determined during commissioning of the CPS cryostat.

6. Cryogenic pumping in the CPS

The cryogenic pumping section (CPS) is designed to accomplish a tritium reduction factor of more than seven orders of magnitude. The tritium partial pressure at the end of the CPS has to be less than 10^{-20} mbar in order to avoid non-negligible background effects inside the spectrometers during neutrino mass measurements due to β-decays of tritiated molecules [63].

In general, ultra high vacuum (UHV) conditions below 10^{-10} mbar can be reached with cryogenic- or getter-pumping. The mechanisms of getter-pumping are described in detail in chapter 7. Cryogenic pumps can even lead to very clean XHV (extra high vacuum) conditions below the UHV range. Typically, one can reach levels partially below the measurable pressure limits of 10^{-13} mbar. This specific kind of pumping technique is mainly used to remove residual gas species in the UHV range, namely hydrogen. Cryopumping can be subdivided into four processes (based on [59]):

1. **Cryocondensation:** The cryocondensation takes place between identical gas particles based on van-der-Waals forces which bind together atoms or molecules at very low temperatures. The minimal pressure in the gaseous phase is limited only by the finite vapour pressure. For hydrogen, a temperature regime below 2.78 K (deuterium: 4.03 K) is needed to reach the 10^{-11} mbar range. Since the binding forces are rather weak between the particles, the cryocondensation process is very sensitive to the temperature variations due to thermal radiation, or due to heat load from neighbouring systems. An adequate shielding for condensation of hydrogen and its isotopes is thus absolutely necessary.

2. **Cryosorption:** For cryosorption a special surface (adsorbent) is needed. For example, charcoal or a gas condensate like frozen argon can be used, as it will be in the CPS. The cryosorption process is based on pure physisorption via van-der-Waals forces between the adsorbate (gas that should be pumped) and the adsorbent. It enables light gas species such as hydrogen to be pumped above their condensation temperatures since their binding energies between the adsorbent and the gas particles are much larger than the binding energy between the gas particles themselves. Hydrogen can thus be pumped at temperatures of about 20 K. The final equilibrium pressure is given by the adsorption isotherm:

$$\log p = \Delta H/(2.303\,RT) + B \quad , \tag{6.1}$$

with the isosteric adsorption energy ΔH, the vapour pressure constant B [152], the universal gas constant R, and the temperature T.

3. **Cryotrapping:** Here, a process gas with condensation temperatures above the temperature of the vacuum chamber surface, is injected into a vacuum system. There it mixes with the residual gas species, commonly with much lower condensation points. At the cold surfaces, the mixture will condensate (physisorption). A huge part of the residual gas is thus incorporated into the condensed layer. When making use of this principle, a very low equilibrium pressure of the residual gas can be reached. A commonly used process gas is argon.

4. **Cryogettering:** Cryogettering is based on chemisorption, where chemically active gases are bound on a special, technical surface, such as titan. Again, very low temperatures are beneficial for a large sticking probability. After dissociation of the molecules at the surface, they diffuse into the pumping material, so that multilayer adsorption is possible.

In order to pump hydrogen (as well as deuterium, and tritium respectively) very low temperatures are necessary for the process of cryocondensation, as well as a comprehensive thermal shielding. At least a temperature of $2.31\,\mathrm{K}$ ($3.39\,\mathrm{K}$) is required in order to reach a H_2 (D_2) partial pressure of 10^{-14} mbar, which is still six orders of magnitude above the specifications [59]. Since KATRIN requires an undisturbed guiding of the $191\,\mathrm{Tcm}^2$ magnetic flux tube from the source to the detector, a comprehensive thermal shielding for even lower temperatures is almost impossible, and hence the cryocondensation process is not applicable inside the transport section. The cryotrapping process would require the use of a process gas, which would increase the total pressure inside the CPS, thus increasing the energy loss of signal electrons through scattering processes. A continuous pumping would not be possible, which is essential to maximise the gas reduction factor.

An attractive solution is thus the cryogettering process which provides a high pumping speed for hydrogen. With multilayer adsorption and comparatively high working temperatures, this pumping type is of major interest for KATRIN. Since the main processes are based on chemisorption, this type of pump can however not be reactivated in an easy way. Hence it will lead to a huge accumulation of radioactive tritium inside the CPS during KATRIN operation. The favoured process in the CPS is therefore the cryosorption with frozen argon as adsorbent.

The tritium flux into the pre-spectrometer has to be limited to a maximum flow rate of $10^{-14}\,\mathrm{mbar}\cdot\ell\cdot\mathrm{s}^{-1}$ by means of an argon frost layer. The argon frost layer will be prepared via nine capillaries on the inner surface of beam tube elements 2, 3, and 4 at an initial temperature of $6\,\mathrm{K}$. Subsequently, the beam tube is cooled down to $3\,\mathrm{K}$. The argon preparation procedure has been presented in detail in chapter 5. The efficiency of the argon frost depends strongly on two parameters: the preparation temperature and the layer thickness. The sorption capacity and the pumping probability both depend on the operation temperature, which is chosen to be in the interval from $3-3.5\,\mathrm{K}$. In section 6.1 the physics of argon condensation and the properties of the argon frost layer are given. The implications for the KATRIN experiment, i.e. to the reduction factor of the CPS, are given in section 6.2.

6.1. Sorption properties of frozen argon layers

The most properties of frozen noble gases were determined during the 1960's, 1970's, and 1980's. Since neutral noble gases have a closed valence electron shell, their atomic structure is rather simple. Solid-state properties based on quantum effects can therefore be investigated more easily compared to other elements, which readily form molecules with a huge number of degrees of freedom. The heavier noble gases like argon, krypton, and xenon play a special role here, since their melting points are comparatively high. They

remain in the solid state in a large temperature range, and they can be condensed with the help of liquid gases. A wide range of temperatures and phases of heavy noble gases are thus accessible through a combination of liquid nitrogen and liquid helium.

The main matters of interest with respect to the pumping performance of an argon-based pump are: the morphology formed during the condensation process, the size of the pores, the porosity, the adsorption properties, like the adsorption energy, and the capacity in dependency on the preparation and operation temperature. These effects are summarised within the following subsections.

6.1.1. Monolayer capacity of frozen argon and its morphology

Argon crystallizes in a (close-packed) face-centred cubic (fcc) lattice [153]. The binding between two inert gas atoms can be described by quantum theory with the van-der-Waals (induced dipole-dipole) potential. For spherical atoms, such as noble gases, a central force law can be assumed. This simplifies the description of the binding forces to the well-known Mie-Lennard-Jones potential with two characteristic constants A and B [153]:

$$\Phi(r) = \frac{A}{r^{12}} - \frac{B}{r^6} \quad . \tag{6.2}$$

If the interaction between the first next neighbours in the crystal is dominant, octahedral (111) and cubic (100) growth faces will occur [59] [154].

Argon layers formed at temperatures below ~ 0.3 times the argon triple point will exhibit a large sorption capacity for hydrogen [155] [156]. This corresponds to a temperature below $27\,\mathrm{K}$ (the triple point is at $83.81\,\mathrm{K}$). This increase in adsorption capacity can be explained by taking into account the structure of the frozen gas. The density of solid argon for a preparation temperature of $6\,\mathrm{K}$ is only about 80% of the density when preparation will take place at $83\,\mathrm{K}$ [152]. In [151] the porosity is given as 15%, thus the argon frost density is 85% at a preparation temperature of $6\,\mathrm{K}$, compared to its nominal density. From this one can conclude that a large number of pores is formed by freezing argon at lower temperatures.

The monolayer adsorption capacity of hydrogen on different noble gases has been investigated by H. Abe and W. Schulze [152]. They found the capacity to strongly depend on the preparation temperature of the adsorbing layer. Argon shows a maximum monolayer adsorption capacity of $60\,\mathrm{mMol_{H_2}/Mol_{Sorbent}}$ at a preparation temperature of $5.5\,\mathrm{K}$. At $11\,\mathrm{K}$, the capacity is already only 60% of the maximum value. The maximum at $5.5\,\mathrm{K}$ can be explained by the resulting layer density, which decreases in a non-linear way with temperature. The argon density starts to decrease at a gas characteristic temperature of 0.25 times the triple point. A lower density means a higher porosity, as well as an increase of the adsorbing area, corresponding to a higher monolayer capacity. [152]

From atomic force microscopy (AFM) of the surfaces of frozen argon crystals, S.A. Nepjika, I. Rabin, and W. Schulze concluded that the morphology of argon layers is nearly independent on layer thicknesses exceeding $150\,\mathrm{nm}$ at condensation temperatures of $5\,\mathrm{K}$ [151]. A significant formation of pores was observed at the surface of the layer. For low condensation temperatures, more pores with a larger size will occur. At $5\,\mathrm{K}$ a maximum average size of almost $65\,\mathrm{nm}$ is reached [151]. The distribution of pore sizes as function of the preparation temperature can be taken from [151]. The non-smooth structures influence the sorption properties in a positive way, as the effective surface A_0 will increase with the formation of pores. It can thus be assumed that all the pores are accessible to the sorbate gas [152].

The mean crystal size δ is correlated with the effective surface. Assuming a condensate of

normal cubics with an edge length δ, the relation between effective surface A_0 and crystal size is given by [59]:

$$\delta = \frac{6}{A_0 \rho} \quad , \tag{6.3}$$

with the temperature dependent density of the cryodeposit ρ. The monolayer capacity a_0 of a cryodeposit is correlated to its specific surface A_0 [m^{2}kg^{-1}] [59]:

$$A_0 = a_0 \cdot F \cdot \frac{N_A}{M_A} \quad , \tag{6.4}$$

where F describes the required space for one adsorbed particle, N_A the number of adsorbed particles and M_A the molar mass. For hydrogen molecules, the parameter F is $12.25 \cdot 10^{-20}\,\mathrm{m}^2$, when a close-packed configuration is assumed [59]. If argon is condensed at $6\,\mathrm{K}$, as is specified for the CPS, the specific surface (A_0) and the monolayer capacity (a_0) are [59]:

$$
\begin{aligned}
A_0 &= 1.38 \cdot 10^5\,\mathrm{m}^2/\mathrm{kg} \\
a_0 &= 58\,\mathrm{mmol}_{H_2}/\mathrm{mol}_{Ar} \quad .
\end{aligned}
\tag{6.5}
$$

The calculated surface of the CPS sections 2-4 is about $2.33\,\mathrm{m}^2$. With a molar mass of $M_{Ar} = 39.948\,\mathrm{g/mol}$, a density at $6\,\mathrm{K}$ of $\rho = 1.77\,\mathrm{g/cm}^3$ [149] [150], and a porosity of 15%, the required amount of argon can be calculated as function of the desired layer thickness inside the CPS. An argon frost with a thickness of $1\,\mu\mathrm{m}$ ($\approx 0.1\,\mathrm{mol}_{Ar}$) will feature a total capacity of $5.61\,\mathrm{mmol}_{H_2}$ or $5.61 \cdot 10^{20}\,\mathrm{H}_2$ molecules. This corresponds to an inventory of $60\,\mathrm{Ci}$ assuming identical sorption properties for T_2 and H_2.

During nominal KATRIN operation, a rate of about $10^{19}\,T_2/\mathrm{s}$ is injected into the WGTS. Assuming a gas flow reduction of the DPS1-F and DPS units by seven orders of magnitude, a total of 10^{12} tritium molecules per second will reach the CPS. With an argon frost layer of $1\,\mu\mathrm{m}$ it will take about 10^3 days until free adsorption spots are no longer available. Here it has been assumed that equation 6.5 is valid for T_2 molecules and that no desorption occurs. According to specifications, the CPS will be purged after having accumulated an inventory of $1\,\mathrm{Ci}$ of tritium. With these assumptions a safety factor of 60 in sorption capacity is achieved.

6.1.2. Adsorption energy of H_2 and D_2 on frozen argon

Since the adsorbate (hydrogen) exhibits a smaller diameter ($0.293\,\mathrm{nm}$ [157]) than the distance between next neighbours of the argon crystal ($0.37\,\mathrm{nm}$ [158]), it can be assumed that the adsorption will take place at free lattice spots of the frozen argon crystals. Depending on the adsorption face, the adsorbed particles will have either 5 or 9 next neighbours for a (111) face, or 5 or 8 next neighbours for a (100) face. Depending on the number of next neighbours, the binding energy for hydrogen on frozen argon will vary. With the sublimation enthalpy ΔH of the adsorbate (H_2) and the adsorbent (Ar), the binding energy ϕ per particle pair can be calculated [154]:

$$\phi \cdot N_A = \frac{1}{6} \left(\Delta H_{\mathrm{adsorbat}} \cdot \Delta H_{\mathrm{adsorbent}} \right)^{\frac{1}{2}} \quad , \tag{6.6}$$

with the Avogadro constant N_A. This yields a binding energy of $440\,\mathrm{J/mol}$ between one hydrogen molecule and one argon particle [159]. The potential energy for hydrogen molecules on argon crystals can thus be calculated for the case of the (111) face configuration with nine next neighbours ($3.96\,\mathrm{kJ/mol}$), and for a configuration with eight next neighbours ($3.52\,\mathrm{kJ/mol}$), i.e. a (100) face. During the test experiment TRAP, see subsection 6.1.3 below, a binding energy of $1.4\,\mathrm{kJ/mol}$ was found for the isotope D_2 on argon [147].

The adsorption energy of hydrogen molecules will depend on the concentration of already adsorbed particles. One expects the following relation: the higher the concentration, the smaller the adsorption energy. For a clean argon frost surface formed at 5.6 K, an adsorption energy of about 2.55 kJ/mol [152] is expected. H. Abe and W. Schulze showed that the adsorption energy is independent on the speed of layer growth and on the layer thickness for hydrogen on xenon at low temperatures (less than 13.9 K). The same relation has been observed for argon as adsorbent at comparable temperatures [152].

The value of the binding energies given above are of the same order of magnitude, but they show considerable variations depending on the number of next neighbours, the concentration of adsorbed particles, and on the argon frost preparation temperature. Calculations and design parameters for a cryopump operating with argon frost can therefore only be seen as a rough estimate.

6.1.3. Dynamics of pumping hydrogen with frozen argon

The pumping based on cryo-condensates is a highly dynamic process. It consists of adsorption and desorption as function of the adsorbent and adsorbate temperatures. For non-radioactive gases one has to consider:

- **Adsorption:** Particles entering the cryopump will randomly hit the cryo-surface. Each time when a particle will hit the surface, it will be adsorbed with a temperature-dependent sticking probability α. This probability will increase in case of a decreasing temperature. A sticking probability of $\alpha = 0.7$ was found in [59] for H_2 on Ar at 4.2 K. The rate of adsorption can be expressed by [110]:

$$j_{\text{ad}} = \frac{1}{\sqrt{2\pi k_{\text{B}}}} \cdot \frac{\alpha \cdot p}{\sqrt{T_{\text{gas}} M}} \quad , \tag{6.7}$$

  with the gas temperature T_{gas}, the molecular mass M of the gas, and the partial pressure p.

- **Desorption:** The adsorbed particles vibrate in thermal equilibrium at the cryo-surface with frequencies comparable to solid-state vibration frequencies of about $\nu_0 \approx 10^{13}$ Hz. This leads to a desorption rate of [110] [146]:

$$j_{\text{des}} = \frac{n_{\text{ad}}}{A} \cdot \nu_0 \cdot e^{-E_{\text{B}}/(RT_{\text{C}})} \quad , \tag{6.8}$$

  with the number of adsorbed particles n_{ad}, the cryo-surface A with temperature T_{C}, the binding energy E_{B}, and the universal gas constant R. Equation 6.8 includes the so called mean sojourn time τ of particles being physisorbed at a surface [83]:

$$\tau = \frac{1}{\nu_0} \cdot e^{E_{\text{B}}/(RT)} \tag{6.9}$$

  The calculation of the mean sojourn time for deuterium and hydrogen on frozen argon based on the known binding energies given in section 6.1.2 at 3 K leads to values of:

$$\tau_{\text{D}_2} = 2.38 \cdot 10^{11}\,\text{s}$$
$$2.03 \cdot 10^{25}\,\text{s} < \tau_{\text{H}_2} < 8.96 \cdot 10^{55}\,\text{s} \quad . \tag{6.10}$$

In equilibrium between adsorption and desorption ($j_{\text{ad}} = j_{\text{des}}$), a final pressure p_{end} will occur inside the cryo-pump:

$$p_{\text{end}} = \frac{n_{\text{ad}}\sqrt{T_{\text{gas}} M}}{\alpha A} \cdot \sqrt{2\pi k_{\text{B}}} \cdot \nu_0 \cdot e^{-E_{\text{B}}/(RT_{\text{C}})} \quad . \tag{6.11}$$

The final pressure also will depend on the cryo-surface coverage a. The maximum operation time of a cryo-pump ($t_{\max}$) can be calculated via [146]:

$$t_{\max} = \frac{n_{\mathrm{ad}} \cdot a_{\max}}{j_{\mathrm{ad}}} \quad , \tag{6.12}$$

with the number of adsorbed particles n_{ad}, and the maximum covarage $a_{\max}$, which has either to be estimated, or determined by experiment. Here, the desorption rate has been neglected in equation 6.12.

Since the geometry of the CPS vacuum system is rather complex, analytical calculations of the reduction factor are not possible. In general, the reduction will depend on the binding energies between hydrogen isotope molecules and the argon frost, the surface coverage, the adsorption rate, the desorption rate, and finally the process of re-adsorption. For a radioactive isotope T_2, the decay electron induced diffusion has to be taken into account as well. Moreover, each parameter will depend on the position inside the CPS beam tubes, and will also be a function of the time since preparation. Therefore, specialised simulations are required to assess the adsorption and desorption rates. Furthermore, to demonstrate the general feasibility of the concept with argon frost in advance, the test experiment TRAP was performed, which is described briefly below.

Summary of the TRAP experiment

The Tritium Argon Frost Pump experiment (TRAP) was built to investigate the pumping properties of hydrogen isotopes on a 4.2 K argon frost surface. It consisted of two tubes with almost the same conductance as the CPS beam tubes which were welded together with a bend of 20°. The inner surface was 1571 cm^2, which is about 1/15 of the CPS surface. Inside the tube an argon capillary was installed with orifices of 0.2 mm in diameter. The assembly was positioned in a cryostat filled with liquid helium. An external flow system was used to inject hydrogen isotopes into the vacuum system with its layers of argon frost. At the opposite end, a detector system was mounted to monitor the residual gas which passed through the cold stage. With this configuration, a deuterium and tritium flow suppression rate $R = \frac{Q_{\mathrm{in}}}{Q_{\mathrm{out}}}$ of

$$\begin{aligned} R_{\mathrm{D}_2} &> 2 \cdot 10^8 \\ R_{\mathrm{DT}} &> (6.9 \pm 0.5 \pm 3.1) \cdot 10^6 \end{aligned} \tag{6.13}$$

was determined [146], resulting in a transmission probability ($P = 1/R$) for this particular cryo-pump of:

$$\begin{aligned} P_{\mathrm{D}_2} &< 5 \cdot 10^{-9} \\ P_{\mathrm{DT}} &< (1.5 \pm 0.7 \pm 4.5) \cdot 10^{-7} \quad . \end{aligned} \tag{6.14}$$

Unfortunately, the gas flow suppression has not been investigated for pure tritium molecules. A maximum argon layer thickness of less than 5 μm was specified to keep the surface temperature low [146]. In addition the operation temperature was recommended to be between 3 K and 4.5 K in order to lower the vapour pressure of the residual gases like HT. The complete test experiment is described in detail in [146] and summarised in [147] and [148].

6.2. Simulation of the argon frost reduction factor

Based on the existing technical drawings of the CPS beam tubes and its pump ports, the geometry of the vacuum system has been set up, with Autodesk Inventor. In doing so, several simplifications with respect to the geometry had to be implemented. These include ignoring gaps of welding connections, cavities, regions where two parts overlap, or any
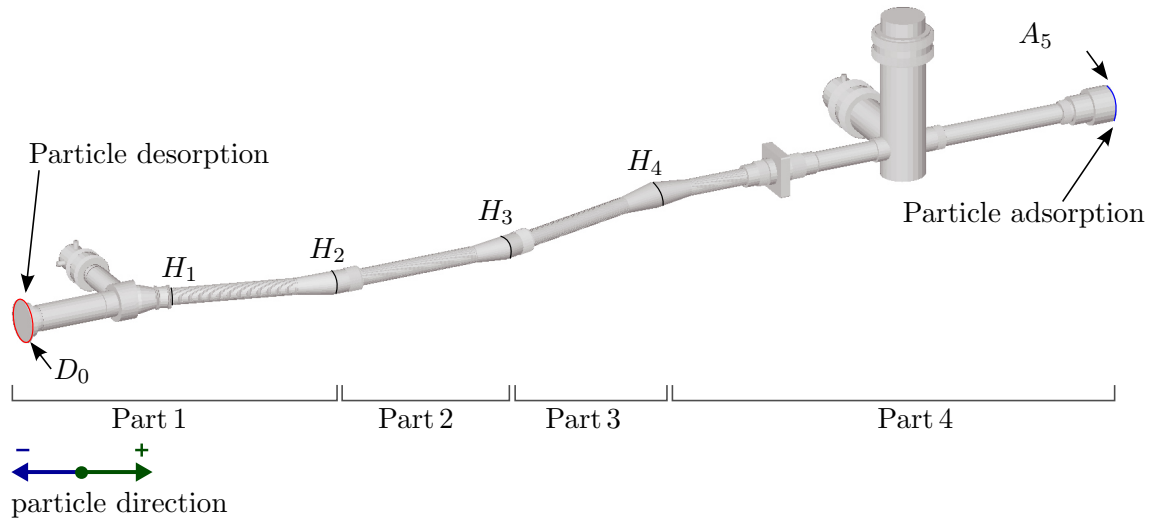
Figure 6.1.: MolFlow+ model of the CPS vacuum system. The simulation targeted onto the overall gas reduction factor of the CPS. It was subdivided into four parts, limited by five facets, as presented here.

kind of holes, hooks, and non-descript small-scale geometries, which have no impact on the vacuum performance or the molecular gas flow. According to the ongoing works of J. Wolf and M. Krause at KIT it is proved that built-in bellows will have a significant impact on the conductance of a vacuum system [160]. Hence, each bellow has been implemented into the model. This model was then been imported into MolFlow+. Figure 6.1 shows a screenshot of the implemented vacuum system. The simulation was targeted to obtain the flow reduction factor, i.e. the suppression rate for tritiated molecules, of the CPS, which corresponds to the conductance. Here the stand-alone conductance has been simulated, as defined in see section 3.1. This means that the surfaces D_0 and A_5, or facets as called in MolFlow+, were defined with a sticking probability of unity. The central sections of the vacuum system (sections 2-5), being covered with the argon frost layer, were assigned a sticking coefficient of 0.7 [59]. In the simulation described here each particle hitting the argon frost layer was assumed to see a free spot on the crystal lattice. The desorption processes, resulting in a mean sojourn time (equation 6.9), were neglected.

Due to the rather large sticking probability, almost none of the particles are expected to reach facet A_5 at the pre-spectrometer side, when starting on facet D_0. With a specified reduction factor of at least 10^7 [1], a number of 10^9 initial particles have to be desorbed to reach a statistical uncertainty of 10% within the simulations. Evidently, tracking of this huge number of particles through a complex system such as the CPS requires enormous computation time. In order to optimise the simulation time, the CPS was simulated in sections. This implies to determine transmission probabilities of predefined sections inside the CPS vacuum system. The vacuum system was therefore subdivided into four parts listed in table 6.1. The particles passing through the inlet and outlet facets of each part were counted. Here the count rates in + and - direction were distinguished (for the definition see figure 6.1). The transmission probability of one part can then be calculated with:

$$P_i = \frac{\text{Particles through outlet facet (+ direction)}}{\text{Particles through inlet facet (+ direction)}} \quad . \tag{6.15}$$

Again, the overall transmission probability can be calculated, by making use of the following identity:

$$P = \prod_i P_i = \frac{H_{2+}}{D_0} \cdot \frac{H_{3+}}{H_{2+}} \cdot \frac{H_{4+}}{H_{3+}} \cdot \frac{A_5}{H_{4+}} \quad . \tag{6.16}$$

Table 6.1.: Settings for the CPS reduction factor simulation. For the definitions of the single facets see figure 6.1. Between facet H_1 and H_4 a sticking coefficient of 0.7 was set, representing the argon frost layer. In the general settings of MolFlow+ a mass of $6\,\mathrm{g/mol}$ was chosen.

Part	Section of interest		Desorption	Adsorption
	Inlet facet	Outlet facet	(cosine)	($\alpha = 1$)
1	D_0	H_2	D_0	D_0, A_5
2	H_2	H_3	H_1	H_1, A_5
3	H_3	H_4	H_2	H_2, A_5
4	H_4	A_5	H_3	H_3, A_5

Table 6.2.: Simulation results for the CPS transmission probabilities. The four parts have been defined in table 6.1. The hits on the different facets in + direction are listed as "Counts through".

Part	Counts through		Leaks	Ratio P	Uncertainty	
	Inlet	Oulet		(outlet/inlet)	σ_P	Δ_P
1	$1.29 \cdot 10^7$	2100	288	$1.55 \cdot 10^{-4}$	$0.03 \cdot 10^{-4}$	$0.22 \cdot 10^{-4}$
2	$4.99 \cdot 10^6$	138	15	$2.77 \cdot 10^{-5}$	$0.24 \cdot 10^{-5}$	$0.30 \cdot 10^{-5}$
3*	-	-	-	$2.77 \cdot 10^{-5}$	$0.24 \cdot 10^{-5}$	-
4	$4.56 \cdot 10^5$	260	9	$5.70 \cdot 10^{-4}$	$0.35 \cdot 10^{-4}$	$0.20 \cdot 10^{-4}$

* Since parts 2 and 3 are geometrically identical their transmission probabilities have been assumed to be equal.

Theoretically, during the high statistics simulation, small leaks showed up, where particles reach the outside of the CPS vacuum system due to tiny clearances between neighbouring facets. When particles indeed hit such a non-descript area, they are removed from the simulation and counted as a leak. If these particles are registered to be lost within the section of interest, they are treated as sources of systematic uncertainties. The simulation yields the following single built-in transmission probabilities listed in table 6.2. The simulation of part 2 took more than a week on a dedicated PC. The resulting statistical uncertainty corresponds to the above listed target of $\sim 10\%$. Since parts 2 and 3 are geometrically identical, it was assumed that their transmission probabilities should be identical as well. With equation 6.16 the overall stand-alone transmission probability is calculated to:

$$P = \prod_i P_i = (6.78 \pm 0.94_\mathrm{stat} \pm 1.93_\mathrm{sys}) \cdot 10^{-17} \quad . \tag{6.17}$$

This leads to a stand-alone conductance of:

$$C = C_\mathrm{B} \cdot P = (5.42 \pm 0.8_\mathrm{stat} \pm 1.55_\mathrm{sys}) \cdot 10^{-13}\,\ell/\mathrm{s} \tag{6.18}$$

with the aperture conductance of the entrance flange $C_\mathrm{B} = \frac{\bar{c}}{4} \cdot A = 7988\,\ell/\mathrm{s}$ for incoming particles starting at $20°\mathrm{C}$.

Discussion of the vacuum simulation

In the vacuum simulation described above the cryo-surface was assumed to be a continuous pumping unit with no surface coverage and no desorption of pumped particles. This results

in an ideal transmission probability which is almost ten orders of magnitude higher than specified. Since it would require structural changes of the available simulation programs (COMSOL and Molflow+) in order to take into account the desorption and the surface coverage, the real transmission probability has to be determined by experiment during the CPS commissioning.

In the meantime, a more realistic approach can be followed by making use of the TRAP experimental results. As summarised in section 6.1.3, TRAP measured a total gas reduction factor of $R > 10^7$ for its specific geometry. This corresponds to a transmission probability for incoming particles to reach the detector system of roughly $P_{\text{TRAP, tot}} < 1/R \approx 10^{-7}$. This includes the pumping performance of the cryo-surface and the conductance between cryo-trap and detector system. This transmission probability (cryo-trap to detector system) was estimated from drawings in [146] and is expected to be $\sim 6 \cdot 10^{-2}$. Hence the transmission probability of the cryo-trap is about $P_{\text{TRAP, cryo}} \approx 2 \cdot 10^{-6}$. Transferring now these data to the CPS geometry will lead to:

$$P_{\text{CPS}} < P_{\text{CPS Sec.1}} \cdot P^*_{\text{TRAP, cryo}} \cdot P_{\text{CPS Sec.6}-7} \quad . \tag{6.19}$$

with the transmission probability of section 1 ($P_{\text{CPS Sec.1}}$), and sections 6-7 ($P_{\text{CPS Sec.6}-7}$), and with the adjusted transmission probability $P^*_{\text{TRAP, cryo}}$ from the TRAP experiment onto the CPS cold stage (sections 2-5). The CPS cold stage is roughly 25% larger in diameter and it is about 50% longer than the cold stage of the TRAP experiment. It features a cold surface which is approximately 15 times larger. Within the assumptions made here it can be assumed that the transmission probability $P^*_{\text{TRAP, cryo}}$ is at least one order of magnitude smaller in comparison to the transmission probability inside the TRAP experiment ($P^*_{\text{TRAP, cryo}} \leq 0.1 \cdot P_{\text{TRAP, cryo}}$).
The transmission probabilities of the CPS entrance section 1 and the exit sections 6 and 7 were simulated using the model shown in figure 6.1:

$$\begin{aligned} P_{\text{CPS Sec.1}} &= (3.07 \pm 0.03) \cdot 10^{-2} \\ P_{\text{CPS Sec.6}-7} &= (6.50 \pm 0.06) \cdot 10^{-2} \quad . \end{aligned} \tag{6.20}$$

Using equation 6.19 one obtains a rough transmission probability for particles (hydrogen isotopes) entering the CPS of:

$$P_{\text{CPS}} < P_{\text{CPS Sec.1}} \cdot P^*_{\text{TRAP, cryo}} \cdot P_{\text{CPS Sec.6}-7} \approx 4 \cdot 10^{-10} \quad . \tag{6.21}$$

Comparing equation 6.21 with equation 6.17 shows a significant deviation by a factor 10^7. However, when comparing the mean sojourn time, e.g. for deuterium at $4.2\,\text{K}$ (TRAP conditions) and at $3\,\text{K}$ (CPS conditions), the same factor of almost 10^7 occurs.

To sum up it can be concluded that the CPS is expected to reach a reduction factor ($R = 1/P$) from $2.5 \cdot 10^9$ up to $1.5 \cdot 10^{16}$. In this regime it would be several orders of magnitude better than specified, giving ample safety factors in case of inevitable temperature fluctuations. Also, the radioactive nature of large-scale tritium adsorption will influence this reduction factor over the measuring interval of $60\,\text{days}$.

7. NEG-Pumping in the CPS

A non-evaporable getter (NEG) pump will be the final pumping stage of the transport section. It will be installed in beam tube 7 inside the CPS (see figure 7.6). Its main purpose is to serve as a safety barrier in the case of an unplanned release of tritiated molecules in the beam tube. To do so, it has to be thermally activated during the commissioning of the CPS. Since activation temperatures inside the CPS are in general quite low $(250 - 350 \,^\circ\text{C})$, the getter material ST707 from the SAES group was chosen. NEG pumping can be compared to a sponge, where gas molecules are absorbed with a specific, gas dependent sticking probability until the bulk material is saturated. The basic physics of NEG pumps is described in section 7.1.

In case that an unsafe condition would occur during CPS operation the cold gate valve between section 5 and 6 will be closed. This will take about 15 s, until a safe state is reached, sealing off the spectrometer section from the tritiated molecules propagating in the source and transport section. During a potential faulty operation mode, some of these molecules may pass this valve. The downstream getter pump in beam tube section 7 is expected to reduce significantly the harmful flow of tritiated molecules to the spectrometer until safe conditions are reached. The NEG pump will thus be mounted prior to CPS commissioning. During five years of KATRIN operation, this pump should be activated only once during CPS commissioning. The activation will be done via thermal radiation during CPS bakeout. The maximum temperatures with respect to the modes of operation, are described in section 7.2. To investigate in detail the NEG activation behaviour as a function of activation time and temperature (see section 7.3), a dedicated test facility has been built and operated as part of this thesis. For the designed getter pump, the sticking probability was determined by this set-up for two different activation temperatures, as described in section 7.4. The impact of the NEG pump on the CPS vacuum performance is finally discussed in section 7.5.

7.1. Basic physics of NEG-pumping

Getter pumps cover a huge spectrum of applications. They are used to create UHV conditions below 10^{-10} mbar and to maintain this vacuum in a closed system. Depending on the kind of gas to be pumped, different getter pumps are in use. These can be subdivided into two groups: ion-getter pumps (this includes orbitron pumps and sputter ion pumps) and non-ionising getter pumps (NEG-pumps and sublimation pumps). The main task of all getter pumps is to lower the hydrogen and the hydrocarbon partial pressures inside

the vacuum chamber. The focus here is on non-evaporable getter (NEG) pumps. Further information on the above mentioned other types are given in [83] [84].

Active gas particles hitting the surface of a getter pump are chemisorbed. The material and gas-specific probability for a particle to be adsorbed on the getter surface when hitting it once is called sticking coefficient α. Particles stick to the surface via covalent bound between the adsorbent (= surface of the getter material) and the adsorbate (= gas particles). Molecules, like hydrogen, need an activation (dissociation) energy and two times the adsorption (= desorption / binding) energy to be bound to the surface. The bonding strength of chemisorbed particles is about $80 \, \text{kJ/mol}$ to $800 \, \text{kJ/mol}$ which is about ten times stronger than the physisorption, the main process occurring in cryogenic pumps [83]. The adsorption is followed by diffusion into the bulk, which is described by Fick's law:

$$
\begin{aligned}
\text{Fick's first law}: \quad & j_{\text{diff}} = -D \frac{\delta n_{\text{L}}}{\delta x} \\
\text{Fick's second law}: \quad & \frac{\delta n_{\text{L}}}{\delta t} = D \frac{\delta^2 n_{\text{L}}}{\delta x^2} \quad .
\end{aligned}
\tag{7.1}
$$

With the coefficient for diffusion:

$$
D = D_0 \cdot \exp\left(-\frac{E_{\text{diff}}}{RT}\right) \quad .
\tag{7.2}
$$

E_{diff} is the energy needed to jump from one free spot to another, and R the universal gas constant. The concentration gradient is described by the derivative of n_{L}. Diffusion processes occur faster in case of higher temperatures, since equation 7.2 is strongly temperature-dependent. If the diffusion exceeds the rate of adsorbed particles, the pumping speed of the getter pump becomes maximal. The adsorption depends on the temperature of the adsorbent and the adsorbate, as well as on the degree of surface coverage $f(\theta)$, where θ described the fraction of surface coverage by the gas particles. Assuming the sticking coefficient (= adsorption probability) to be independent of temperature, it can be written as:

$$
\alpha = \alpha_0 f(\theta) \quad ,
\tag{7.3}
$$

with the temperature-independent sticking coefficient α_0 for an empty surface. The most basic approach to describe the coverage dependency of α is given by Langmuir, with $f(\theta) = 1 - \theta$ [83]. The rate of adsorption is then given by multiplying equation 7.3 with the rate of impinging particles $j = n \cdot \bar{c}/4$ [83]:

$$
j_{\text{ad}} = \alpha_0 (1 - \theta) \frac{n \cdot \bar{c}}{4} \quad .
\tag{7.4}
$$

For an increased number of bound particles, the adsorption rate and hence the pumping speed decreases. Particles that have been adsorbed on the getter surface can desorb again, if their kinetic energy exceeds the desorption (= adsorption) energy. The basic equation has already been given in chapter 5:

$$
j_{\text{des}} = -\nu_0 \cdot \exp\left(-\frac{E_{\text{des}}}{RT}\right) \quad .
\tag{7.5}
$$

At room temperature the adsorption rate is dominant. Since the diffusion rate is quite slow, the pumping speed is limited by the speed of diffusion. The getter temperature can be increased in order to improve the pumping performance.

The diffusion strongly depends on the type of adsorbed gas. Hydrogen, for example, readily diffuses into the getter bulk over a wide range of temperatures, even for conditions below room temperature [161], whereas the diffusion of gases such as oxygen into the bulk is inhibited at room temperature. These gas types form a passive layer on the getter surface,

which results in a high surface coverage. Before using a getter pump, this passive layer has to be removed by heating the getter. Depending on the type of NEG alloy temperatures of up to $800°C$ are required [84]. Most surface compounds diffuse into the bulk material, thereby leaving the surface. This process is called getter activation. Hydrogen plays a special role here, as it desorbs from the getter bulk during activation. Figure 7.1 illustrates the sorption processes.

Non-evaporable getter ST707

Inside the CPS non-evaporable getter of type ST707 from SAES Group [162] will be used. All information and data sheets on the properties of ST707 getter material given here are based on [163].

Getter material of type ST707 is an alloy, consisting of 70% zirconium, 24.6% vanadium, and 5.4% iron. Figure 7.2 shows a scanning-electron-microscopy (SEM) analysis of the material, obtained in the framework of a bachelor thesis [164]. The alloy can be purchased as pressed pills or washers, or fixed onto a thin metal strip. For the CPS, ST707 which is pressed on a constantan strip is used. Constantan is an amagnetic alloy made of 55% copper and 45% nickel. On both sides of the constantan strip ($\sim 160\,\mu m$ in thickness), a layer of $70\,\mu m$ of getter powder alloy is fixed. Although the geometrical surface is rather small, the effective surface is huge, owing to the porosity of the powder, providing an active area of about $1500\,cm^2/g$. The porosity can be seen in figure 7.3, where two pictures of the SEM analysis are shown for different resolutions ($100\,\mu m$ and $1\,\mu m$).

Under vacuum conditions the getter can be exposed to a maximum temperature of $700°C$. Temperatures exceeding $200°C$ [163], as well as sparks during further processing of the strips under atmospheric pressure (air) can lead to metal burning of the strips. For safety reasons, they should be handled under inert atmosphere, like an argon bath.

The ST707 is characterised by a low operation temperature in the range between $20°C$ and $100°C$. Its pumping properties have been verified under cryogenic temperatures by [161] [163]. The getter can be fully activated by heating to comparatively low temperatures of $450°C$ for a period of at least 10 minutes. During this time, the passive surface layer will diffuse into the getter bulk and incorporated hydrogen will diffuse out to the surface where it is emitted (outgassing). At lower heating temperatures, only a partial activation is reached, as shown in figure 7.4. Low-temperature getters offer the opportunity to activate the getter material during baking of a vacuum systems, in particular via indirect heating by radiation or thermal contact with the vacuum chamber. In this case separate electrical heating is not necessary to reach the desired temperature.

Once activated, the getter material will chemisorb active gases like H_2, H_2O, CO, CO_2, and N_2. Non-polar gases, like methane and the inert gases, are not pumped. A bulk temperature of about $200°C$ provides a faster diffusion of the adsorbed particles into the getter material and hence avoids the forming of passive layers on the surface. The only exceptions are the hydrocarbons, for which the pumping speed is decreasing for increasing temperatures. The particles mentioned above, except hydrogen, will remain in the getter material once they are chemisorbed. They form strong chemical bounds and diffuse deeper into the getter bulk at higher temperatures. Since the binding energy is strong, they will not desorb again, even at high temperatures ($T > 450°C$). This limits the lifetime and the capacity of a ST707 pump. Once the bulk is saturated with active gases, the pumping speed will decrease quickly.

Unlike other pumped gas species, hydrogen shows a special behaviour. It diffuses more quickly into the getter material than all other gases, even at low temperatures. The gradient in hydrogen concentration is small and hence the distribution is almost uniform.

(a) Adsorption

(b) Diffusion at low temperatures

(c) Diffusion and desorption at high temperatures
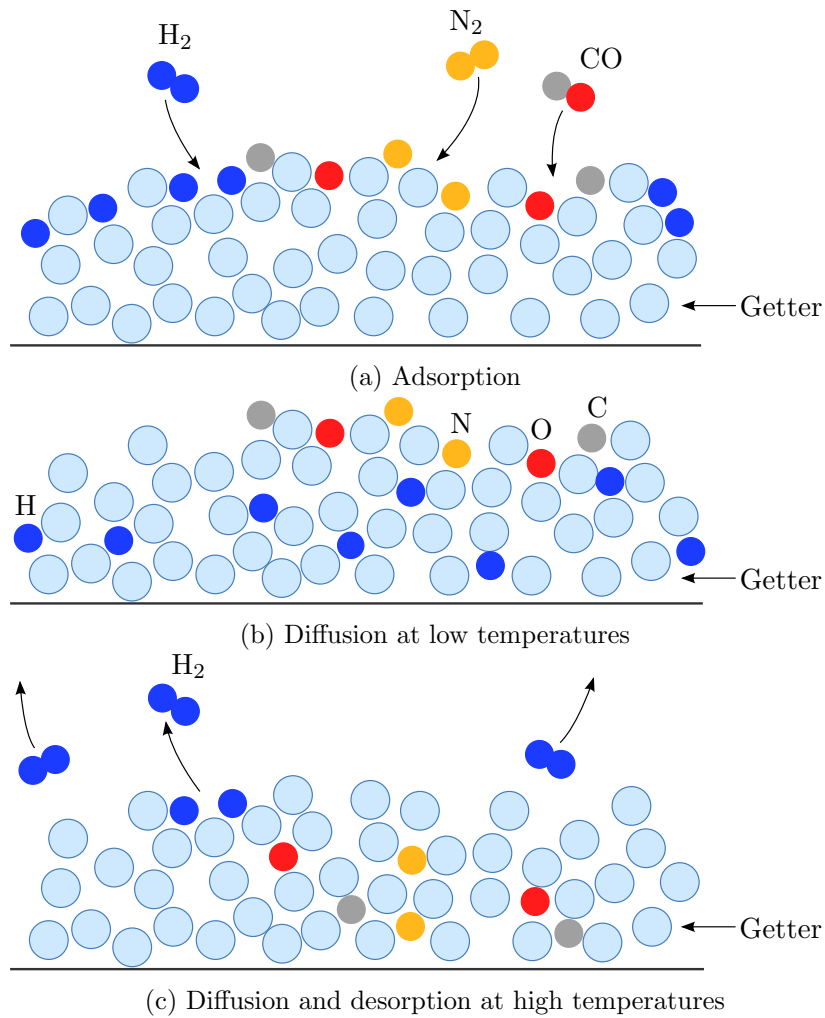
Figure 7.1.: Illustration of sorption processes on the surface and in the bulk of a getter. Adsorption of active gases (7.1a): Gas molecules hit the surface, dissociate, and are bound covalently to the surface. Diffusion into the getter bulk occurs at low temperatures (7.1b): Hydrogen atoms diffuse into the getter material, whereas all other gases remain as a passive layer at the surface. Diffusion and outgassing occur at higher temperatures (7.1c): At high temperatures most bound atoms diffuse deeper into the getter material, except hydrogen, which forms molecules at the surface and desorbs again.
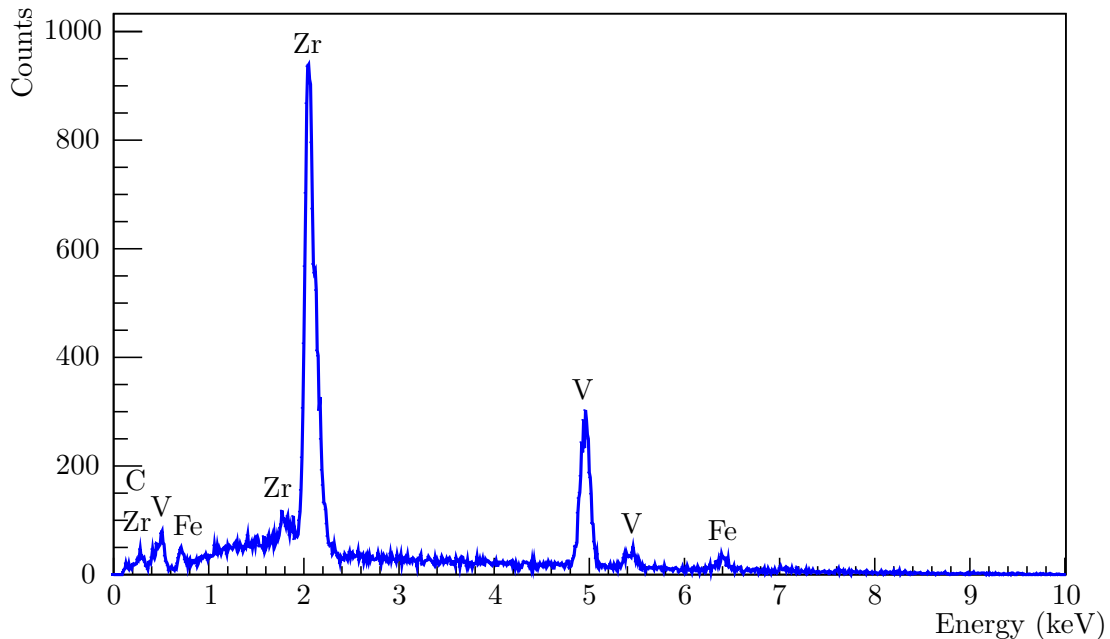
Figure 7.2.: Scanning-electron-microscopy (SEM) analysis of the ST707 getter material. As expected only zirconium (70%), vanadium (24.6%), and iron (5.4%) have been observed [164].

Since the binding energy is weak, in comparison to other gases, hydrogen starts to desorb from the getter when heating to higher temperatures. The sorption process is therefore reversible. In [163], the equilibrium pressure for hydrogen on ST707 was found out to follow Sieverts' law:

$$\log p = 4.8 + 2 \cdot \log Q - \frac{6116}{T} \quad , \tag{7.6}$$

with the pressure p (in torr), the concentration Q of hydrogen in the getter (in torr ℓ/g), and the temperature T (in Kelvin). The two heavy hydrogen isotopes, D_2 and T_2, which are of specific importance for the KATRIN operation, show the same sorption behaviour as H_2, albeit with slightly different equilibrium pressures [163]. The maximum recommended amount of absorbed gas should not exceed a value of 20 torr ℓ/g, since embrittlement will occur for higher concentrations.

A parameter, especially important for vacuum simulations of getter strips, is the sticking coefficient α. It is correlated with the pumping speed S via [83]:

$$S = \frac{A}{4} \cdot \bar{c} \cdot \alpha \quad , \tag{7.7}$$

where $\bar{c}$ is the mean thermal velocity given by a Maxwellian distribution and A the geometrical surface. In [166] the maximum sticking coefficient of a ST707 getter strip has been determined to be 0.0290(4). There, the getter was baked out at 350°C for 24 hours. These conditions are adapted to the operating conditions of KATRIN. After activation the sticking probability was determined for hydrogen. In the original set-up, two vacuum chambers were connected via an orifice. Both chambers featured pressure gauges, and one chamber included the getter sample. Then, a test gas was injected into the system. By monitoring the pressure of both chambers the pumping speed of the getter strip was determined. The resulting maximum adsorption probability was calculated to be 2.9%, as mentioned above.

After bake-out at 400°C for one hour, or at 350°C for one day, a fully activated ST707 getter strip (30 mm wide) provides a pumping speed per strip length of about $1000 \, \ell/(\text{s} \cdot \text{m})$ for H_2, $2000 \, \ell/(\text{s} \cdot \text{m})$ for CO, and $450 \, \ell/(\text{s} \cdot \text{m})$ for N_2 (taken from [167]). The pumping
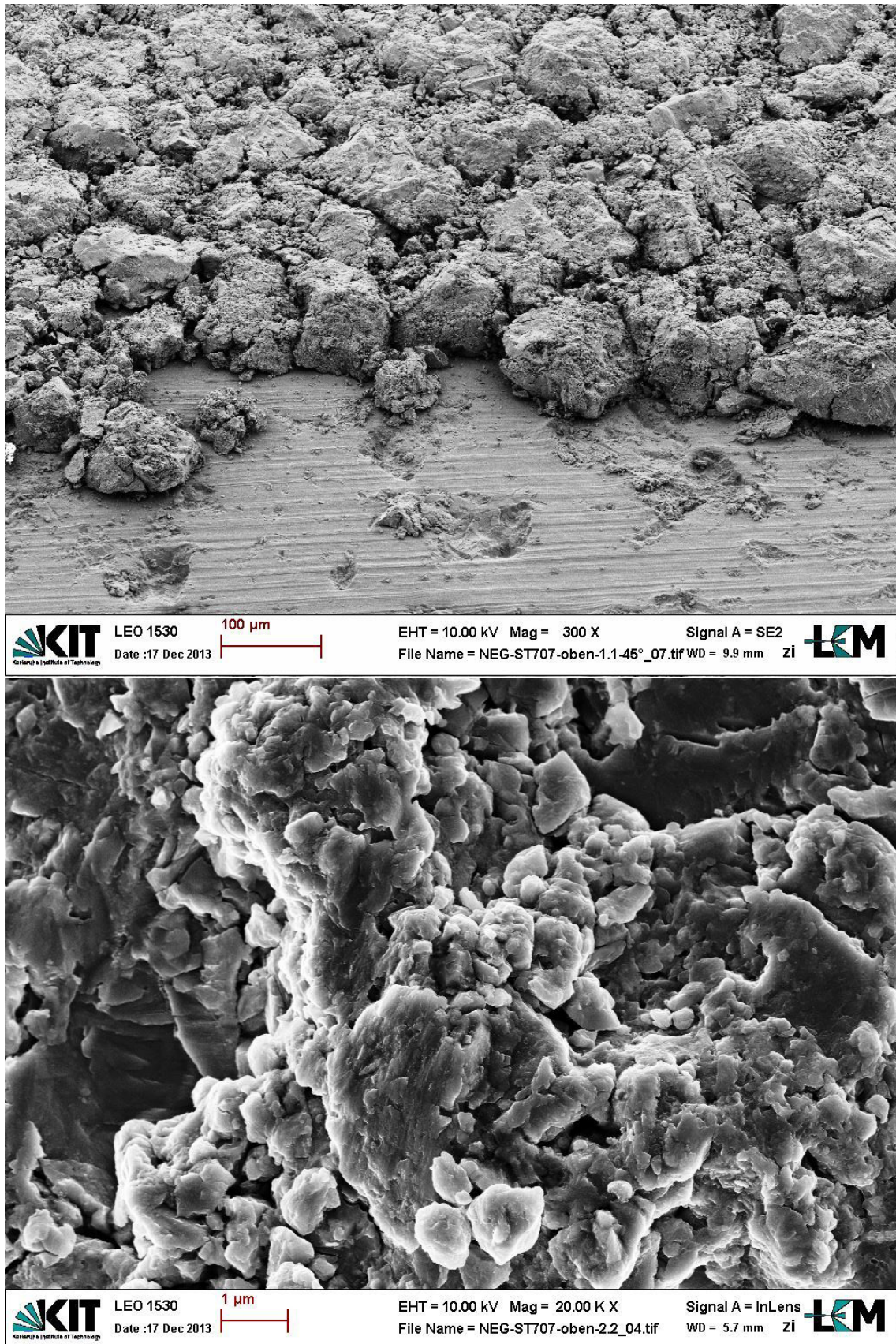
Figure 7.3.: Scanning-electron-microscopy (SEM) of the ST707 getter material. The porosity can clearly be seen in two different resolutions. Top (scale: 100 μm): The getter powder alloy is pressed on a constantan strip (smooth area in the front). Bottom (scale: 1 μm): Arbitrary chosen spot of the powder alloy. Thanks to [165] for the support with the SEM analysis.
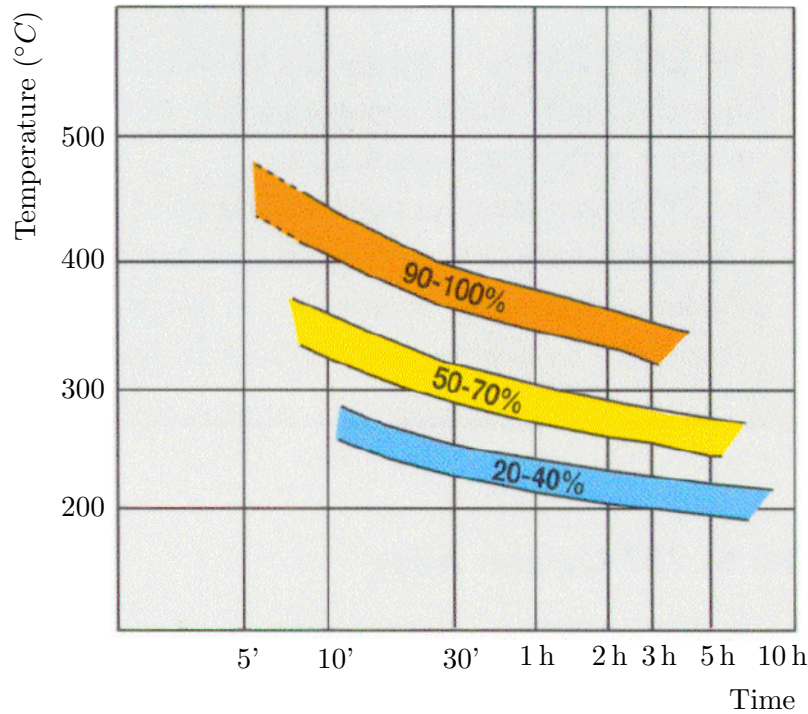
Figure 7.4.: Activation properties of ST707 getter material. Different degrees of activation are reached as function of temperature and activation time. Taken from [163].

speed for CO is twice as high as for hydrogen, but it will drop more quickly with the amount of adsorbed gas [167], since CO does not diffuse into the getter material. The pumping speed of H_2 is lower when CO is pumped at the same time.

7.2. Design of the CPS NEG pump

The getter pump has initially been designed under the supervision of J. Kleinfeller (KIT) in 2009. It will be located in the last section of the CPS, where it will serve as the final stage for tritium retention in the transport section. It also acts as a safety barrier for tritium desorbing from the cold gate valve behind the argon section. The design for mounting a NEG pump inside the CPS, as well as the pump itself, are described in section 7.2.1. The operation and activation conditions are then given in section 7.2.2.

7.2.1. Design and mounting procedure of the CPS NEG pump

The getter pump will be mounted inside section 7 after successful completion of the acceptance tests of the CPS cryostat. There are several boundary conditions for the NEG pump:

- It has to fit into the beam tube element 7 with its maximum diameter of 112 mm and maximum length of 700 mm.

- The 191 Tcm^2 magnetic flux tube must fit through the pump.

- It must not exceed a maximum weight of 1.5 kg.

- It has to be mounted via pump port 2.

- It must be activated via thermal radiation only.

With these specifications in mind, the pump was designed as an array of four cylindrical cartridges. A CAD drawing is shown in figure 7.5. Two rings (face caps) are connected via hollow tubes to a cage. The tubes are welded to these rings, which feature holes to reduce weight. The whole cage is made of stainless steel. Small hooks are placed on both sides to hold two cartridges together. More details are given below. One cartridge has a length of 169 mm, an inner diameter of 76 mm, and an outer diameter of 98 mm (without hooks). The hollow connection tubes form an inner and an outer cylinder. The getter strips (30 mm wide) are wound around both cylinders. One cartridge provides four getter strips with together 27 mm × 2.1 m active getter material. The active area is therefore 1134 cm^2, the weight of one single cartridge is (273.6 ± 0.2) g.

Section 7 provides space for a total of four cartridges. All cartridges will be mounted on a rail, which has to be inserted into the CPS in advance. The rail can be folded up to fit through the CPS flange at the pre-spectrometer side. Inside section 7 it has to be unfolded again. The four NEG cages are fixed together via hooks at each cartridge. A narrowing (inner diameter: 82 mm) at the end of beam tube 7 prohibits to move the rail and the NEG pump to the spectrometer. Figure 7.6 shows a cross section of the last part of the CPS together with the installed rail and one single cartridge. The bottom of the vertical pump port 2 features a place holder for a cartridge mounting rail. The four cartridges will be placed successively on the mounting rail through the vertical pump port 2 and subsequently pushed on the rail inside section 7. During mounting it has to be ensured that the hooks of two touching cartridges interlock. For the mounting and dismounting procedure special rods have been manufactured. After installing all four NEG cages in section 7, the mounting rail will be removed again.

7.2.2. Operation conditions inside section 7

There are two important operation modes which define the performance of the getter pump: the activation and the standard operation mode. The NEG pump has to be activated indirectly via radiation heat load only, during the bake-out period of the CPS. Sections 6 and 7 as well as pump port 2 are therefore designed to withstand higher temperatures than other parts of the CPS. During bake-out (see section 3.3), these parts will be heated up to a range of 620 K for a maximum time period of 24 h. The standard operation temperatures are foreseen to be 300 K (section 7) and 77 K (section 6 and pump port 2). Since beam tube 7, including the NEG cartridges, is not cooled or heated during standard operation, a temperature gradient between room temperature and 77 K will occur.

To investigate this gradient, the temperature of the getter pump has been simulated with COMSOL Multiphysics in both operation modes. The geometry shown in figure 7.7 has been used with different temperature boundaries to determine the activation and operation conditions of the NEG pump. The cooling and heating tubes, respectively, have been neglected. The temperature values for the simulation were defined directly on the surface of the respective component. To minimise computation time, the NEG cartridges were simplified. Only the NEG strips have been implemented, with no mechanical, and hence no thermal contact to each other. One cartridge consists of eight single strips each, forming a cylinder. Four cylinders build the outer part, whereas the other four strips shape the inner part of the double layer system. The thermal simulation then provides the temperature of each getter strip.

The temperatures during bake-out and during standard operation of the CPS were simulated by using equations 5.16 - 5.19. Table 7.1 lists the configuration for standard operation, and table 7.2 for the bake-out mode. Figure 7.8 shows the simulated temperature distribution of the CPS section 6, pump port 2, and section 7, including the NEG cartridges. Since section 7 is not explicitly temperature-stabilized, a gradient will occur. Along beam tube 7 and the bellows on each end, the temperature drops from room temperature down to liquid nitrogen temperature. The highest decrease occurs around the bellow which

(a)

(b)

(c)
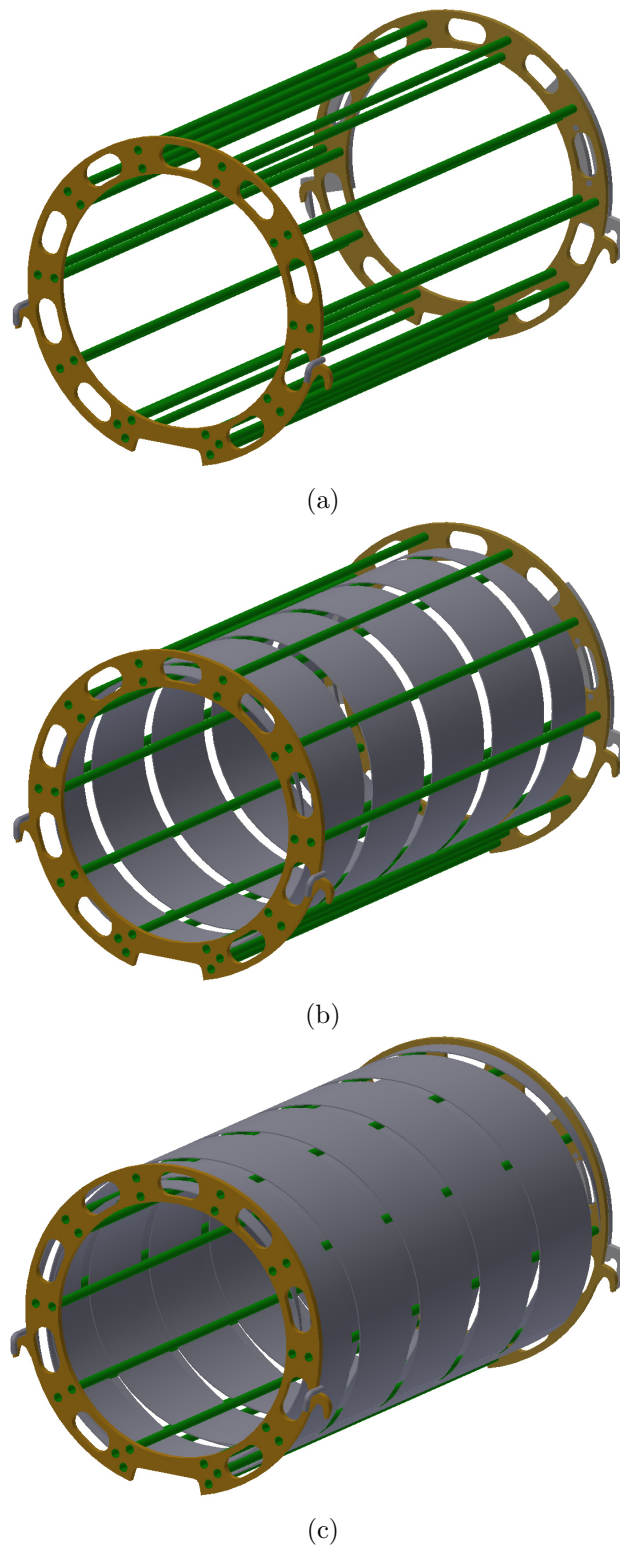
Figure 7.5.: Design of a NEG cartridge. Green: hollow stainless steel tubes. Ochre: face caps with recesses to lower the weight. Gray: ST707 getter strips. In 7.5a the cage is shown with the two layers of hollow tubes. In 7.5b the inner getter layer has been mounted and in 7.5c both layers of getter were wound on the cage. The two face caps feature small hooks for fixation.
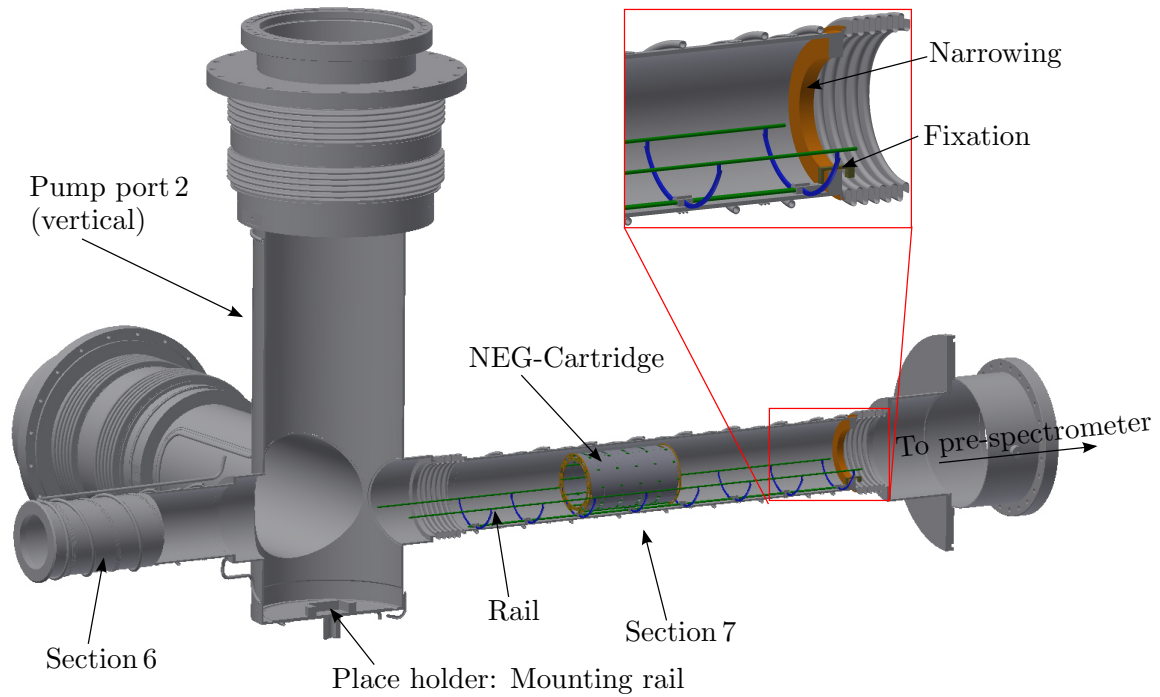
Figure 7.6.: NEG cartridges inside the CPS. The rail is pushed into section 7 in the folded
state through the pre-spectrometer flange. Inside the CPS it is unfolded and
clamped on the narrowing. The NEG cartridges are pushed on the rail through
the vertical pump port 2.
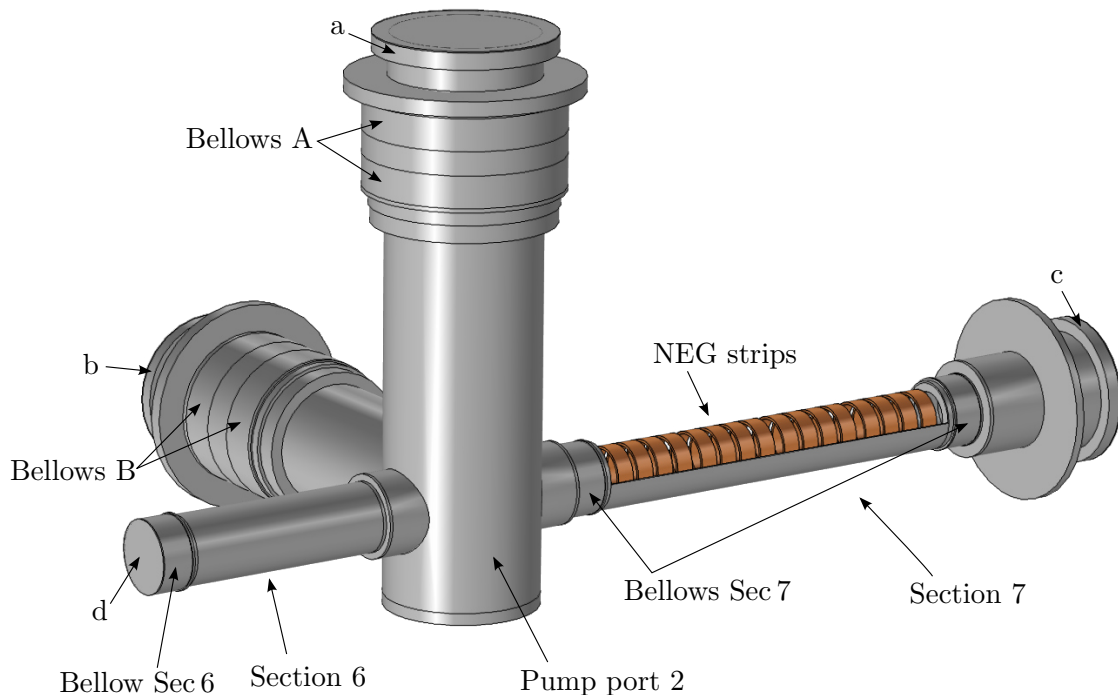
Figure 7.7.: Simulation model in COMSOL Multiphysics to investigate the activation and
operation conditions of the NEG pump of the CPS. Beam tube 7 has been cut
to make the NEG cartridges visible. The meaning of the indexing is given in
table 7.1 and 7.2.

Table 7.1.: Settings for the thermal simulation of the NEG pump of the CPS during standard operation. All defined temperatures have been taken from appendix D. A description of the parameters can be taken from table 5.3.

COMSOL property	Parameter	Value	Description
Temperature 1	T_0	4.5 K	Cold gate valve body
Temperature 2	T_0	77 K	Pump port 2
Temperature 3	T_0	300 K	Surfaces at a, b, c (outer part of the CPS)
Surface to surface radiation 1	ϵ	0.02	Pump port 2, section 6 and 7 are gold plated.
Surface to surface radiation 2	ϵ	0.20	The surfaces of the outer flanges (a,b,c) and the cold gate valve body (d) are stainless steel.
Surface to surface radiation 3	ϵ	0.65	Emission coefficient of the NEG strips. According to simulations and experiments in previous theses [45] [168].
Bellows A: thermal conductivity	k	$0.0142 \cdot k(T)$	Implemented thermal conductivity multiplied with a correction factor according to equation 8.4, appendix A.
Bellows B: thermal conductivity	k	$0.0119 \cdot k(T)$	
Bellow Sec 6: thermal conductivity	k	$0.0343 \cdot k(T)$	
Bellows Sec 7: thermal conductivity	k	$0.0343 \cdot k(T)$	

Table 7.2.: Settings for thermal simulation of the CPS NEG pump during bake-out. All defined temperatures have been taken from appendix D. A description of the parameters can be taken from table 5.3.

COMSOL property	Parameter	Value	Description
Temperature 1	T_0	500 K	Cold gate valve body
Temperature 2	T_0	620 K	Pump port 2
Temperature 3	T_0	573.15 K	Surfaces at a, b, c (outer part of the CPS). The valves there are heatable up to 573.15 K.
Surface to surface radiation 1	ϵ	0.02	Pump port 2, section 6 and 7 are gold plated.
Surface to surface radiation 2	ϵ	0.20	The surfaces of the outer flanges (a,b,c) and the cold gate valve body (d) are stainless steel.
Surface to surface radiation 3	ϵ	0.65	Emission coefficient of the NEG strips. According to simulations and experiments in previous theses [45] [168].
Bellows A: thermal conductivity	k	$0.0142 \cdot k(T)$	Implemented thermal conductivity multiplied with a correction factor according to equation 8.4, appendix A.
Bellows B: thermal conductivity	k	$0.0119 \cdot k(T)$	
Bellow Sec 6: thermal conductivity	k	$0.0343 \cdot k(T)$	
Bellows Sec 7: thermal conductivity	k	$0.0343 \cdot k(T)$	

Figure 7.8.: Temperature profile of the NEG pump of the CPS during standard operation, simulated with COMSOL. Since the final section is not explicitly temperature stabilized, a gradient between 226 K and 275 K along the NEG strips occurs.

connects beam tube 7 with pump port 2. The four NEG cartridges show a continuous temperature gradient between 226 K and 275 K, in thermal equilibrium. The plot in figure 7.9 shows the average temperature of the 4×4 getter strips. As illustrated in figure 7.5, all strips of one single cartridge are thermally connected to each other. The cartridges again are loosely connected via hooks. These conditions will lead to a lower temperature gradient along the NEG pump, in thermal equilibrium. Nevertheless, the simulation gives a lower and an upper limit for the NEG pump temperature that can be expected during standard operation.

With the settings given in table 7.2, the maximum getter temperature has been calculated for the bake-out mode. During bake-out, the two VAT Series 48 gate valves at pump port 2, and one between CPS and the pre-spectrometer, will be closed and heated separately up to a value of 573.15 K (application condition of the gate valves are given in [169]). The cold gate valve will be closed as well and kept at 500 K. Figure 7.10 shows the thermal equilibrium temperature of the NEG pump during bake-out. In figure 7.11 the temperature of the getter strips is plotted. Within the series of cartridges, an upper limit in temperature of 607.5 K is reached. The lower limit will be at 595.2 K. The CPS is specified to ramp up the temperature with a maximum rate of 30 K/h [58]. With an average temperature of (604.4 ± 0.9) K, the expected time to reach 100% activation, according to figure 7.4, will be less than 5 hours. According to the modes of operation (appendix D), a temperature value of 620 K can be kept for 24 hours [118]. This implies a safety factor of almost five, with respect to the five hours activation time.

In order to investigate the activation behaviour inside the CPS, a test set-up has been
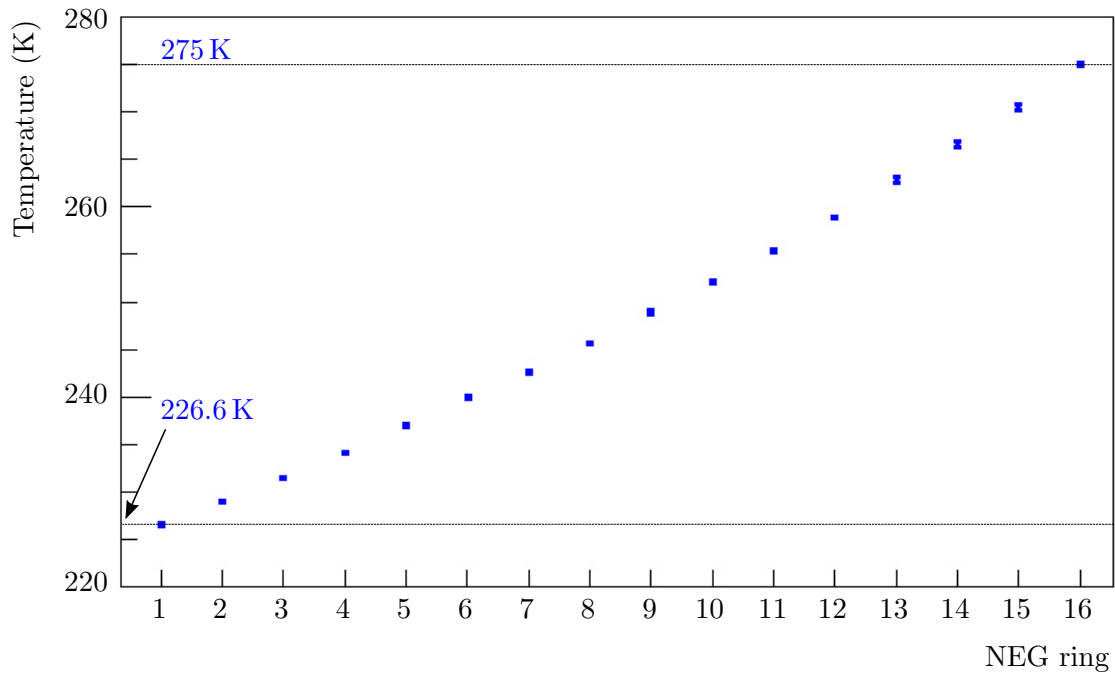
Figure 7.9.: Simulated temperature distribution of the NEG strips in the CPS during standard operation. The temperature has been averaged for each pair of inner and outer NEG ring. Since the cartridges are connected mechanically, an almost linear temperature profile between the simulated minimum ($\sim 226\,$K) and maximum ($\sim 275\,$K) occurs.
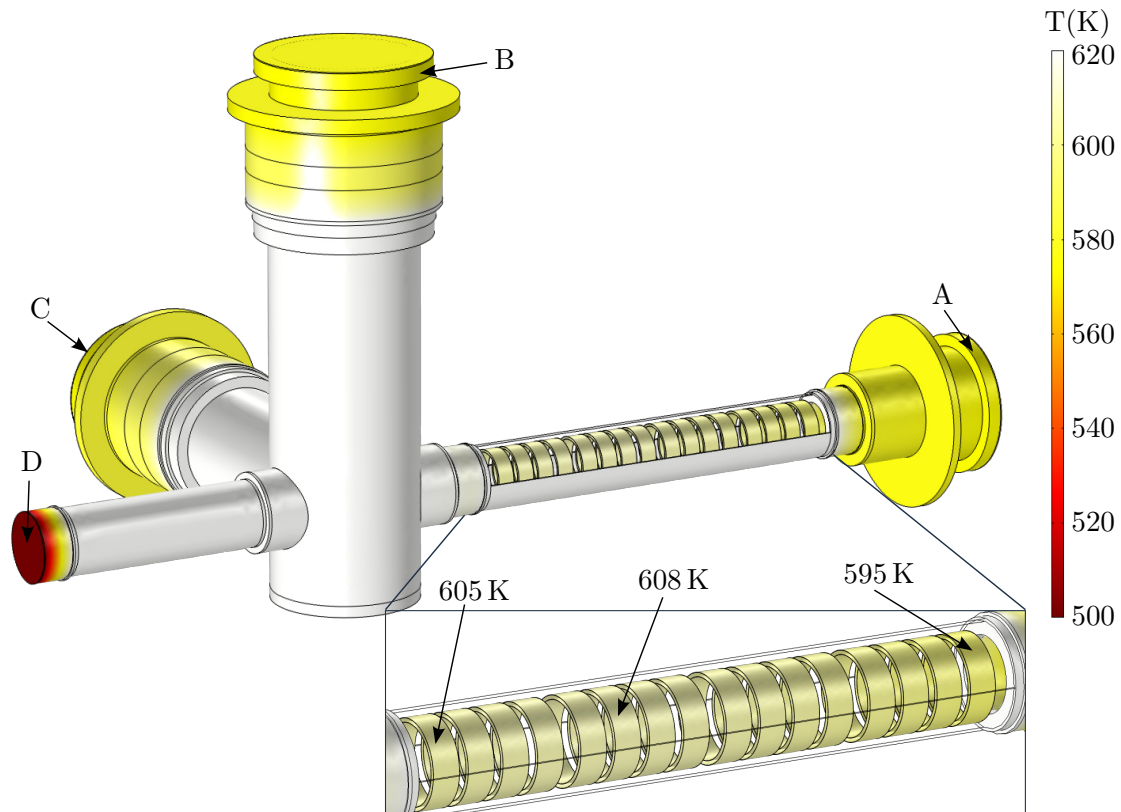
Figure 7.10.: Temperature profile of the CPS NEG pump during bake-out, simulated with COMSOL. Three VAT gate valves are mounted at positions A, B, and C. They are bakeable up to 300°C. The surface D represents the closed cold gate valve. The simulation settings are listed in table 7.2.
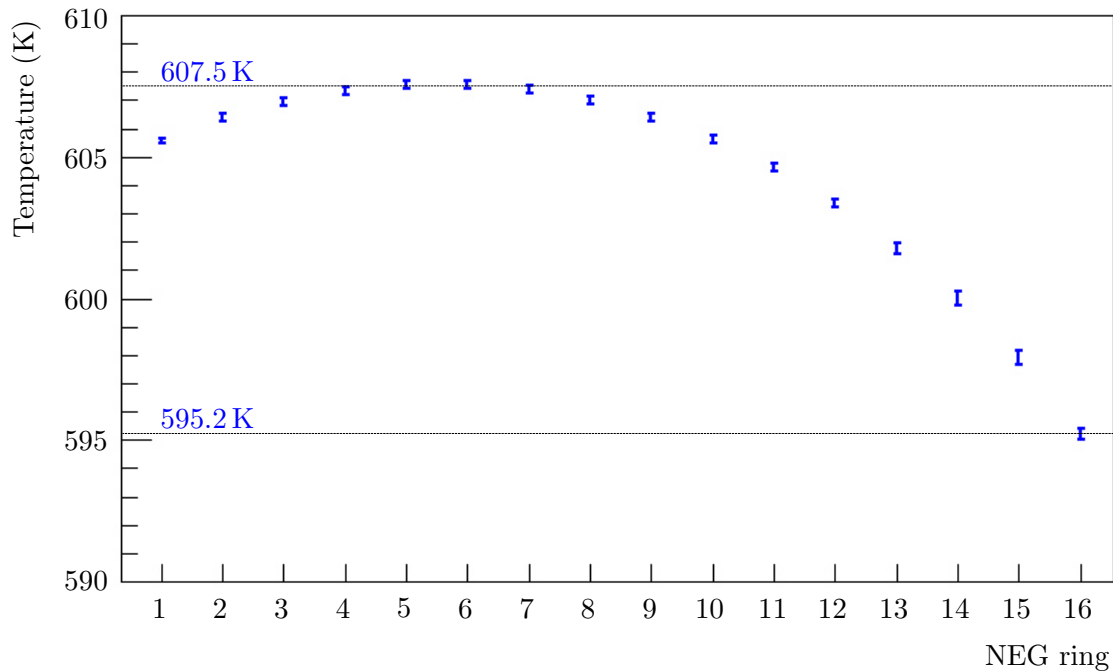
Figure 7.11.: Simulated temperature profile of the CPS NEG pump during bake-out. The temperature has been averaged for each pair of inner and outer NEG rings. Since they are connected mechanically, a specific temperature profile between the simulated minimum ($\sim 595\,\mathrm{K}$) and maximum ($\sim 608\,\mathrm{K}$) will occur.

used to verify the activation method and to determine the sticking probability, which is proportional to the pumping speed of the getter pump.

7.3. Experimental test stand for the CPS NEG-pump

To investigate the activation behaviour of the NEG pump, a specific test facility has been build by [170]. First measurements were performed in [164] and [171]. The specific aim of the set-up was to determine the sticking coefficient of the ST707 getter material in a CPS-like environment. The sticking probability can be used to evaluate its impact on the CPS vacuum system in the KATRIN assembly (see section 7.5). The test stand closely models the section 7 of the CPS and consists of three major parts: the UHV chamber, the gas inlet system, and the NEG pump.

Ultra-High-Vacuum (UHV) chamber

The UHV chamber (illustrated in figure 7.12) has already been introduced in section 5.1.2. A flow chart of the vacuum system, with the position of the temperature sensors, is given in figure 7.13. It is a simplified replication of the CPS beam tube section 7. Its main part is a 730 mm long gold-plated tube, with an inner diameter of 112 mm. Inside the tube, the rail and the getter cartridges can be placed to investigate the activation behaviour. At both ends of the gold-plated tube, two vacuum crosses are mounted. They provide spots for suitable instrumentation:

- **Residual Gas Analyser (RGA):** The RGA is implemented as a Pfeiffer Vacuum Prisma QMS 200 M (A and B in figure 7.12). If features a mass range between 1 and 100 amu. The scanning velocity is between 200 ms and 60 s per mass unit. Depending on the analysing mode, the resolution is of the order of $10^{-14}\,\mathrm{mbar}$ (Channeltron) or $5 \cdot 10^{-12}\,\mathrm{mbar}$ (Faraday). The temperature range during operation in the Faraday
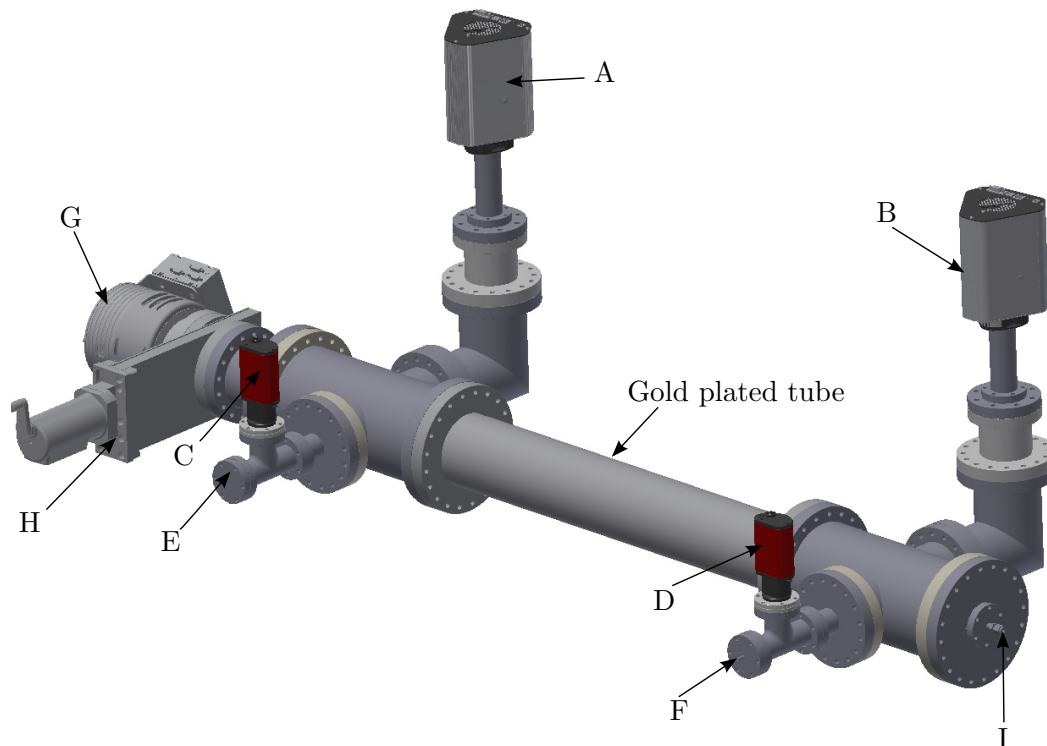
Figure 7.12.: UHV chamber test set-up to investigate the properties of the NEG pump of the CPS. A, B: Residual gas analyser type Pfeiffer Prisma QMS 200 M. C, D: Wide-range pressure gauge type Pfeiffer HPT 200. E: Extractor gauge type Leybold Ionivac IE 514. F: Feedthrough with two thermocouple type K sensors. G: TMP type Leybold Turbovac TW 290 H. H: VAT CF 100 gate valve. I: Adapter flange CF 40 to Swagelok, to attach the gas inlet system. The gold plated, stainless steel tube, with the rail and NEG cartridges, is positioned in the centre. Not shown are the second TMP (Turbovac SL 300) and the backing-pump Scrollvac SC 15 D.
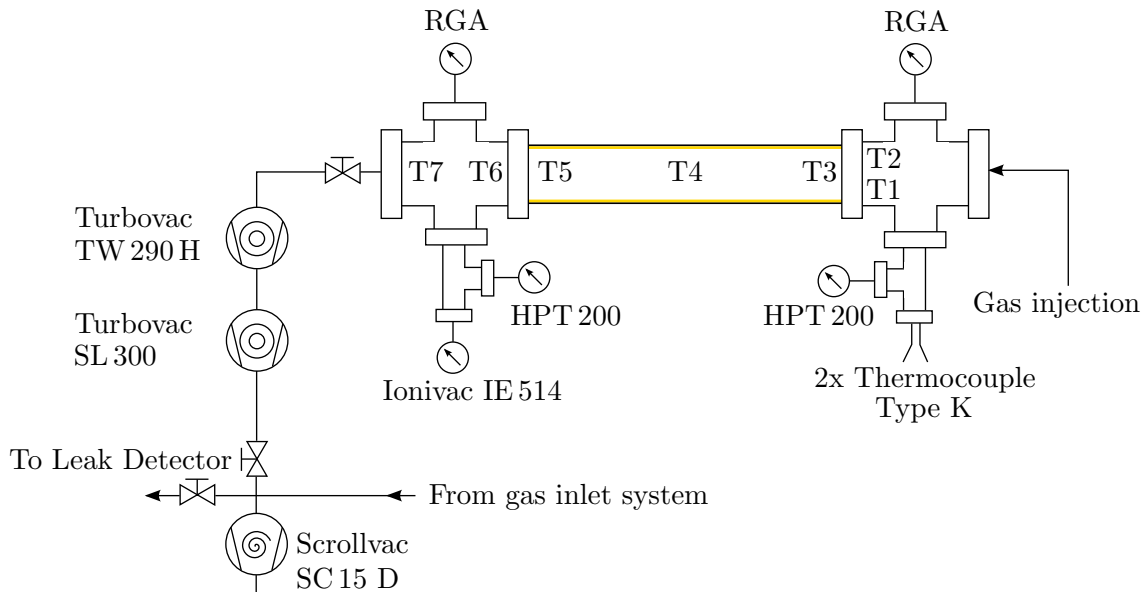
Figure 7.13.: Flow chart of the UHV chamber. This set-up is connected to the gas inlet system via the interfaces 'From gas inlet system' and 'Gas injection' (compare figure 7.14). Electric heating tapes, including PT 100 temperature sensors (T1 - T7), are wrapped around the two crosses and the gold plated tube. The pumped gas can be diluted with compressed air after the Scrollvac SC 15 D.

mode is $0°\text{C} < T < 150°\text{C}$. It is applicable in the pressure range below 10^{-4} mbar and bakeable at $200°\text{C}$ [172]. All measurements presented here have been performed with the Faraday detector.

- **Wide Range Pressure Gauge:** Pfeiffer HPT 200 (C and D in figure 7.12). The wide-range gauge is a fully metal-sealed unit and includes a Pirani ($9 \cdot 10^{-3}$ mbar $\leq p$ < 1000 mbar) and a Bayard-Alpert ($p < 9 \cdot 10^{-3}$ mbar) sensor. Its accuracy is $\pm 10\%$ in the range between $1 \cdot 10^{-8}$ mbar and 1 mbar, and $\pm 30\%$ between 20 mbar and 1000 mbar. The lowest measurable pressure is $5 \cdot 10^{-10}$ mbar. The pressure is measured in a 10 ms cycle. It can be operated between $5°\text{C}$ and $60°\text{C}$, while the maximal bake-out temperature is $180°\text{C}$ at the flange. [143]

- **Extractor gauge:** The Leybold Ionivac IE 514 (E in figure 7.12) can be operated between $0°\text{C}$ and $80°\text{C}$. The bake-out temperature of this unit must not exceed $350°\text{C}$ (cable disconnected). The X-ray limit is below 10^{-12} mbar, and hence the gauge is operating in a pressure range between 10^{-12} mbar $< p < 10^{-5}$ mbar. [173]

- **Two thermocouple sensors type K:** Each thermocouple consists of a 1 mm thick stainless steel housing, with a NiCr-Ni connection inside. Temperatures of up to $1200°\text{C}$ can be measured with a precision of ± 2.5 K. They are almost linear for temperatures between $0°\text{C} < T < 750°\text{C}$. Both thermocouple sensors (F in figure 7.12) have been fed through a CF 40 flange into the UHV chamber to measure the temperature inside.

The UHV of the set-up is generated by two cascaded TMPs of type Leybold Turbovac SL 300 and Leybold Turbovac TW 290 H (figure 7.12 G), lowering back diffusion of light gases into the chamber. The pump can be separated from the chamber via a VAT CF 100 gate valve (figure 7.12 H). Both SL 300 and TW 290 H provide a pumping speed of 190 ℓ/s ($\pm 20\%$) for hydrogen. The compression ratio is more than 10^{11} for nitrogen and about 10^5 for hydrogen. The cascaded TMPs can reach a final pressure of 10^{-10} mbar [174]. The TMPs are backed by a scroll pump of type Scrollvac SC 15 D from Leybold with a maxi-

mum pumping speed of $15\,\mathrm{m}^3/\mathrm{h}$ and a final pressure of $1.6 \cdot 10^{-2}\,\mathrm{mbar}$ [175]. Compressed air injection is provided at the output side of the scroll pump, which dilutes the pumped gas for safety reasons, when hydrogen is the predominant gas. Opposite the pumping station, a gas inlet is placed (figure 7.12 I). It is a simple CF 40 to Swagelok connection flange, where the gas inlet system, together with its valves and the buffer vessel, can be attached.

Three heating tapes are wrapped around the gold plated tube and the two vacuum crosses. Altogether seven PT 100-sensors are placed along the system to control ($T_{2,4,6}$) and to monitor (T_{1-7}) the temperature. The chamber can be baked at $400°\mathrm{C}$ with a programmable ramping speed. The default setting is $30\,\mathrm{K/h}$, as specified for the CPS. The construction is covered with layers of mineral wool and aluminium foil for thermal insulation.

Gas inlet system

The main part of the gas inlet system is a $15.6\,\ell$ buffer vessel. Its purpose is to provide a specific, well-known amount of gaseous hydrogen, to be injected into the UHV chamber for testing of the pumping and activation properties of the NEG cartridges. A flow chart is given in figure 7.14. The vessel can be evacuated via a TMP (type Turbovac TW 70 H from Leybold). The pumping speed for hydrogen is $49\,\ell/\mathrm{s}$. It reaches a final pressure of less than $10^{-9}\,\mathrm{mbar}$ [176] [177]. The scroll pump of the UHV chamber serves as the forepump for the gas inlet system as well. With a VAT CF 40 gate valve, the pump arrangement can be detached from the buffer vessel. Hydrogen, as well as any other gas, can be injected from a gas cylinder into the buffer vessel via a flow meter, mks Mass Flow Controller M 200 (flow range up to $2\,\mathrm{sccm} \approx 3.4\,\mathrm{mbar}\,\ell/\mathrm{s}$), or directly via a Swagelok valve. For the measurements (compare section 7.4.2) hydrogen was used as process gas. Since the flow rate from the gas inlet system into the UHV chamber was kept at a constant level during these measurements, the buffer vessel had to be stabilised in pressure. Therefore it was continuously refilled from the gas cylinder. Since the flow controller is calibrated with nitrogen (manufacturer configuration), it had to be characterised first with hydrogen. This was done via the increase in pressure inside the buffer vessel at different gas flow set points. Figure 7.15 shows the linear dependency between the measured gas flow (by the controller itself) and the calculated one via the pressure rise. The real hydrogen gas flow can thus be calculated with:

$$Q_{\mathrm{H_2}} = (-0.640 \pm 3.308) \cdot 10^{-4}\frac{\mathrm{mbar}\,\ell}{\mathrm{s}} + (1.088 \pm 0.017) \cdot Q_{\text{set point}} \quad . \qquad (7.8)$$

The outlet of the buffer vessel features a second flow meter of the same type (range $1\,\mathrm{sccm} \approx 1.7\,\mathrm{mbar}\,\ell/\mathrm{s}$)) and a bypass valve. Between the outlet and the inlet of the UHV chamber additional valves and bypasses, a control valve, and an aperture are placed to control the injection gas flow. Two capacitive, gas type independent pressure gauges (mks Baratron 690 A), with different pressure ranges are mounted at the buffer vessel. They allow a precise, gas independent, pressure measurement from atmospheric pressure ($1000\,\mathrm{mbar}$) down to $10^{-6}\,\mathrm{mbar}$. The standard accuracy is 0.12% (full scale range) [178].

NEG cartridges

The NEG cartridges are described in detail in section 7.2. The foldable rail is mounted permanently in the gold-plated tube. By opening the CF 160 flange at the gas inlet site, the getter cages can be placed on the rail and pushed to the centre of the UHV chamber. The two thermocouple sensors type K (1 mm in diameter) fit into the hollow tubes of the cartridges. They directly record the temperature of the getter cages. During measurements only two cartridges with an overall getter strip length of $(4.20 \pm 0.16)\,\mathrm{m}$ each, were inserted into the test set-up. The active getter surface is thus $A_{\text{exp.}} = (2268 \pm 86)\,\mathrm{cm}^2$. For
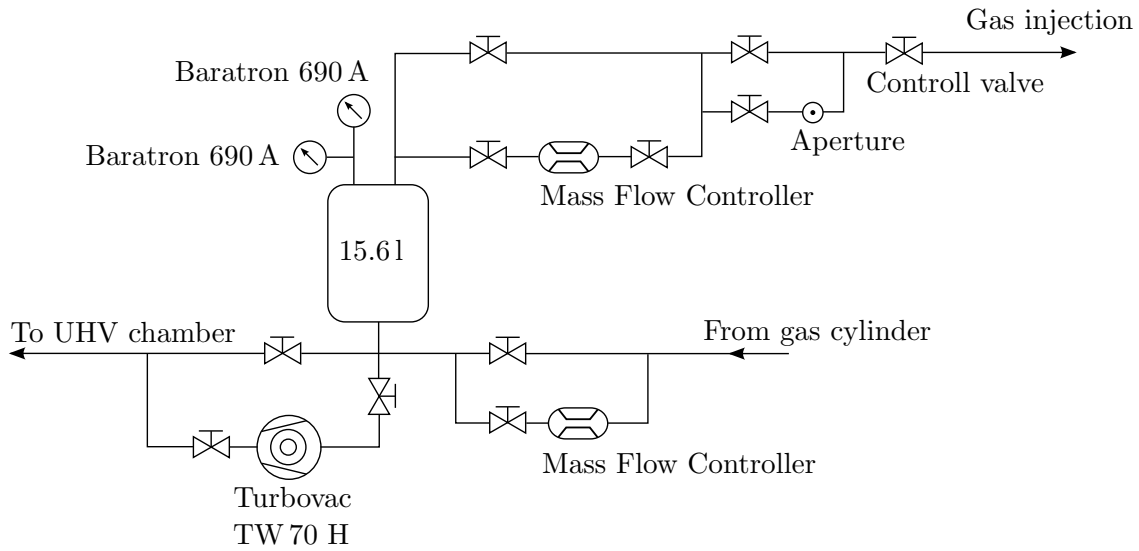
Figure 7.14.: Flow chart of the gas inlet system. The set-up is attached to the UHV chamber via the interface 'To UHV chamber' and 'Gas injection' (compare figure 7.13). The buffer vessel can be filled with any gas at the interface 'From gas cylinder'. Two PT 100 sensors are fixed to the vessel to monitor the temperature.
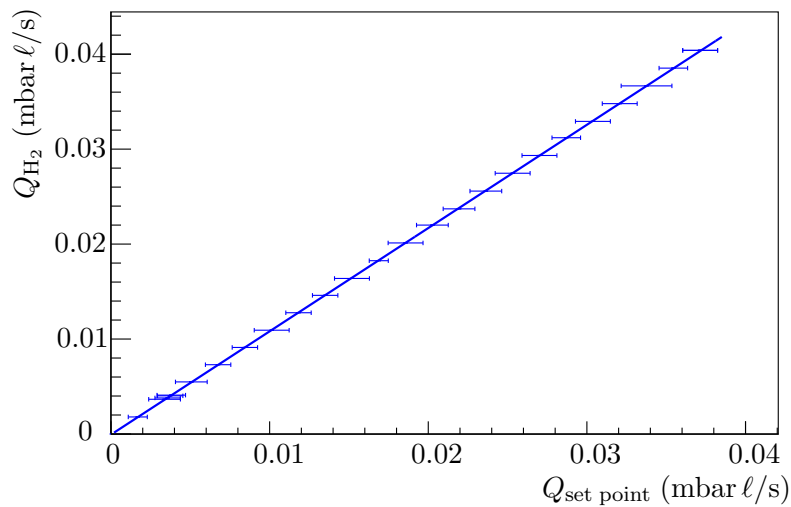
Figure 7.15.: Characterisation of the gas flow into the buffer vessel. By recording the pressure increase inside the buffer vessel, the incoming gas flow as a function of the set point of the flow controller was determined.
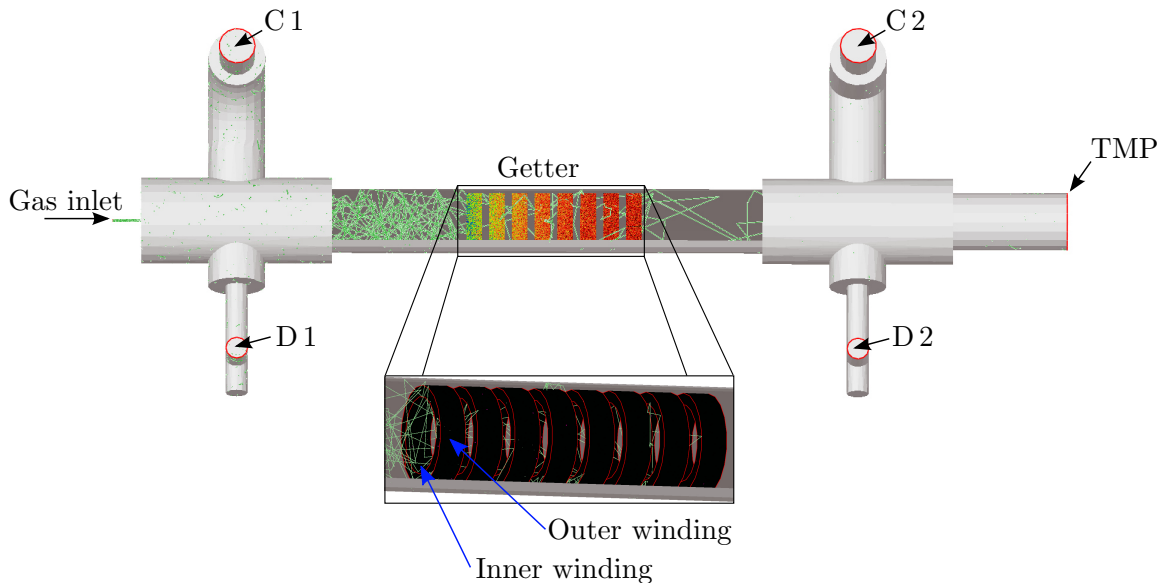
Figure 7.16.: Simulation model to determine the sticking coefficient of the NEG pump in the CPS. C 1 and C 2 represent the two RGA units, D 1 and D 2 the two pressure gauge units. The eight coloured cylinders illustrate the two NEG cartridges with four getter strips each.

calibration purposes the getter strips were replaced by stainless steel strips with identical geometric dimensions. The calibration cartridges exhibit a well-known sticking probability of zero and can thus be used to verify the simulations given in section 7.4.1.

The test stand is controlled by a LabView program optimised for this specific set-up. This program manages the read-out of all pressure and temperature sensors, and the control of the heating tapes. A detailed gas analysis can be done with the RGA specific software Pfeiffer Vacuum Quadstar.

7.4. Properties of the NEG-pump inside the test stand

The measurements were targeted to determine the sticking probability of the ST 707 getter material after an activation time of 24 h at a temperature regime of $(600 \pm 10)\,\mathrm{K}$ (compare figure 7.11). Two cartridges were placed inside the test stand and baked out at 600 K for 24 h. After cool down, hydrogen was injected into the UHV chamber, via the gas injection system. The pressures and partial pressures in front of and behind the NEG pump were measured during the injection. The ratio of both parameters was then compared with a detailed calibrated simulation to determine the sticking coefficient and hence the pumping speed. The simulation is described in section 7.4.1, whereas the measurements, including the calibration and results are detailed in section 7.4.2.

7.4.1. Theoretical pumping properties for different degrees of activation

The experimental determination of the sticking probability relies also on simulations in the molecular flow regime of the test set-up. These simulations are based on [179] and are adapted to the actual test set-up with MolFlow+. Figure 7.16 shows a screen shot during simulation. The surfaces C 1 and C 2 represent the two units RGA 1 and RGA 2 and are of equal size. The surfaces D 1 and D 2 represent the absolute pressure gauges. The gas inlet is a 12.6 mm^2 surface at the end of a 50 mm long tube, approximating the real inlet system at this location. At the opposite end, a facet with a non-vanishing sticking coefficient

Table 7.3.: Parametric sweep for the getter simulation inside the test stand, representing the range of uncertainties for the pumping speed S of the TMP, and the physical range of the sticking coefficient α [166].

Parameter	Range	Step-size
Pumping speed TMP	$152\,\ell/\text{s} < \text{S} < 228\,\ell/\text{s}$	$38\,\ell/\text{s}$
Sticking coefficient NEG	$0 < \alpha < 0.029$	0.001

Table 7.4.: Parameters for the fit given in equation 7.11 and figure 7.17.

Parameter	RGA ratio		Pressure gauge ratio	
	Value	Uncertainty	Value	Uncertainty
$c_0\ [10^{-1}]$	3.201	0.026	2.978	0.033
$c_1\ [10^{0}]$	-4.576	0.082	-3.871	0.100
$c_2\ [10^{-1}]$	4.219	0.023	4.471	0.029
$c_3\ [10^{2}]$	-1.304	0.012	-1.247	0.013

represents the TMP ($190\,\ell/\text{s} \pm 20\%$).

The geometrical dimensions, surfaces, and volumes are chosen to be identical to the real set-up. Since no special design elements, such as bellows, are implemented into the system, the Molflow+ model represents a very precise replication of the test experiment. The NEG pump is approximated by a set of cylinders with identical dimensions to the real getter strips, fixed in two cartridges with four two-sided double layers of getter material each. The active NEG surface is $A_{\text{sim.}} = 2350\,\text{cm}^2$. When comparing simulated and experimental data, this difference in active surface has to be taken into account. The end rings of each cartridge, the rail, and the thermocouple temperature sensor can be neglected, however.

In general, the pressure is proportional to the number of particles hitting a well-defined area A:

$$p \propto \frac{\text{Number of hits}}{A} \quad , \tag{7.9}$$

under isothermal conditions, and for a single gas species. By tracking particles which desorb from the gas inlet facet through the geometry and counting the number of hits on facets $C\,1$ and $C\,2$, the partial pressure ratio around the getter pump can be determined:

$$R = \frac{\text{Hits on C 2}}{A_2} \times \left(\frac{\text{Hits on C 1}}{A_1}\right)^{-1} = \frac{\text{Hits on C 2}}{\text{Hits on C 1}} \quad , \tag{7.10}$$

with equal surfaces $A_1 = A_2$. The same formula can be applied for the total pressure ratio with the facets $D\,1$ and $D\,2$.

The simulation contains two free parameters: the pumping speed of the TMP, and the sticking probability α of the getter strips. Both parameters were varied within their uncertainties (TMP) and physical range (α), the latter depending on the activation conditions of the NEG pump (see table 7.3). For each combination of parameters the ratio between the number of hits at the position of the RGAs and the pressure gauges, respectively, was recorded. The results are given in figure 7.17. The set of data can be parametrised by the function:

$$R = c_0 + c_1 \cdot \alpha + c_2 \cdot e^{(c_3 \cdot \alpha)} \quad , \tag{7.11}$$

with parameters given in table 7.4. The uncertainty in R has been calculated via the common Gaussian error propagation:

$$\sigma_R = \sqrt{\sigma_{c_0}^2 + \alpha^2 \cdot \sigma_{c_1}^2 + e^{(2c_3\alpha)} \cdot \sigma_{c_2}^2 + c_2^2 \cdot e^{(2c_3\alpha)} \cdot \alpha^2 \cdot \sigma_{c_3}^2} \tag{7.12}$$
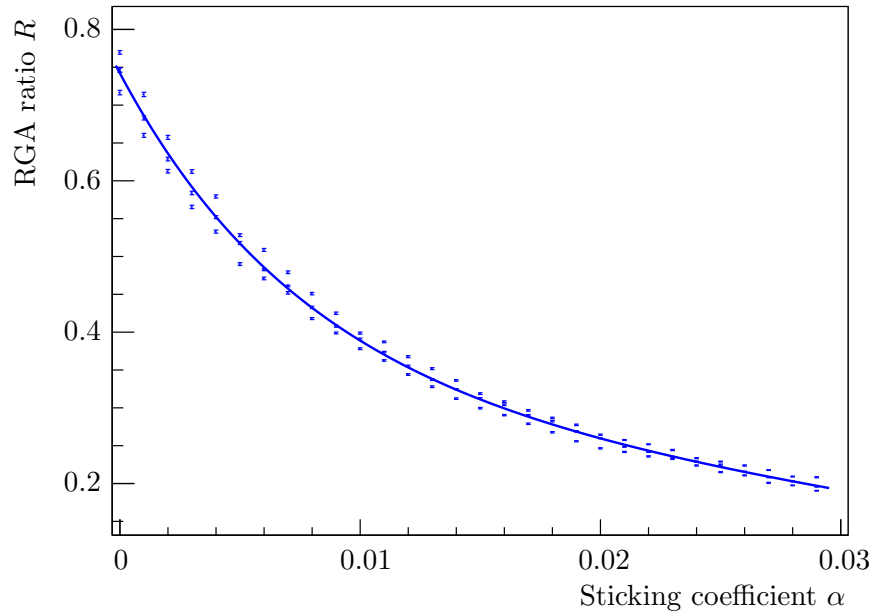
(a) RGA partial pressure ratio.
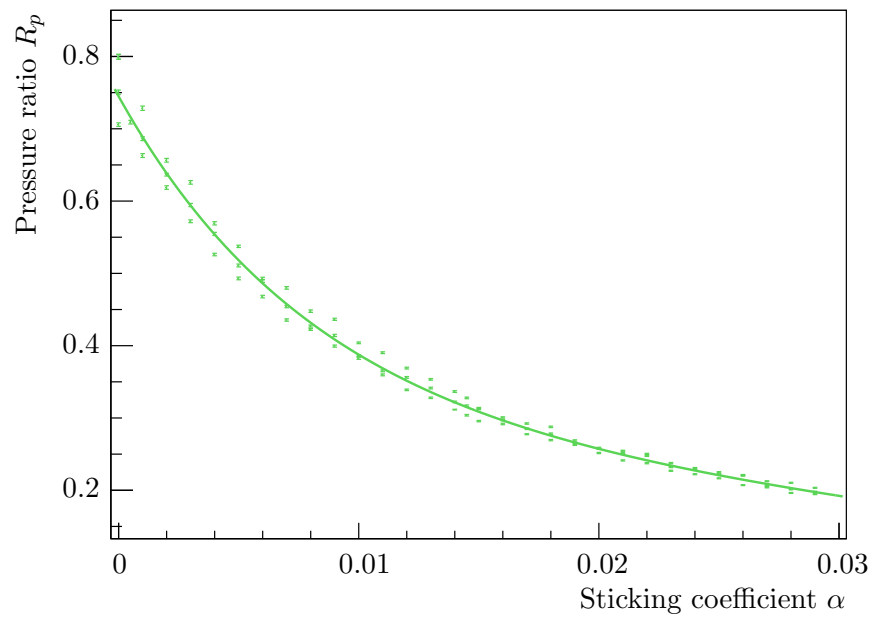
(b) Total pressure ratio.

Figure 7.17.: Simulation of the expected pressure ratios, measured (a) with the residual gas analysers (RGA) and (b) with the total pressure gauges around the NEG pump inside the test stand during hydrogen injection.

For calibration purposes, as described in the experimental section below, the (partial) pressure ratio with deactivated getter plays an important role. It can be calculated for a getter sticking coefficient of zero ($\alpha = 0$):

$$R_{\alpha=0} = c_0 + c_2 = 0.742 \pm 0.004 \tag{7.13}$$

$$R_{p\,\alpha=0} = 0.745 \pm 0.044 \quad . \tag{7.14}$$

The partial pressure ratio is described by R, the total pressure ratio by R_p.

Method of analysis

The experimental procedure provides two observables: a measured partial pressure ratio for the residual gas analysers (R_{RGA}), and a total pressure ratio for the wide-range pressure gauges (R_p):

$$R_{\mathrm{RGA}} = k \cdot \frac{RGA_2}{RGA_1}$$
$$R_p = k' \cdot \frac{p_2}{p_1} \quad , \tag{7.15}$$

with the calibration functions k and k'. The calibration functions are not constant, but depend on the pressure. Therefore they are parametrised by a function of RGA_1 and p_1, respectively. To determine both calibration functions, the following assumptions are made:

1. The calibration simulation without NEG pumping was defined to lead to the correct (partial) pressure ratios.

2. The RGA and the total pressure gauge in front of the NEG pumps were defined as references (RGA_1 and p_1).

The calibration functions were than be calculated in the following steps:

1. Expression of the RGA and the total pressure gauge behind the NEG pump (RGA_2 and p_2) via the reference gauges (RGA_1 and p_1) by a polynomial:

$$RGA_2 = \sum_n a_n \cdot RGA_1^n$$
$$p_2 = \sum_n b_n \cdot p_1^n \quad , \tag{7.16}$$

and determination of the coefficients a_n and b_n with the calibration measurements without NEG pump ($\alpha = 0$).

2. Determination of the calibration function by making use of the calibration measurements with a known (partial) pressure ratio, taken into account assumption (1) and equations 7.15 and 7.13:

$$R_{\alpha=0} = k \cdot \frac{RGA_2}{RGA_1}$$
$$\Longrightarrow k = 0.742 \cdot \frac{RGA_1}{RGA_2} \tag{7.17}$$
$$= 0.742 \cdot \frac{RGA_1}{\sum_{n=0}^{n=1} a_n \cdot RGA_1^n} \quad .$$

$$k' = 0.745 \cdot \frac{p_1}{\sum_{n=0}^{n=3} b_n \cdot p_1^n} \quad . \tag{7.18}$$

Then, via equation 7.11 and table 7.4, the measured (partial) pressure ratios (equation 7.15) can be converted into a sticking coefficient. The corresponding theoretical pumping probability now has to be corrected, since the active areas of the simulation ($A_{\text{sim.}} = 2350\,\text{cm}^2$) and experiment ($A_{\text{exp.}} = (2268 \pm 86)\,\text{cm}^2$) are not equal:

$$\alpha_{\text{exp.}} = \frac{A_{\text{sim.}}}{A_{\text{exp.}}} \cdot \alpha_{\text{sim.}} = (1.04 \pm 0.04) \cdot \alpha_{\text{sim.}} \quad . \tag{7.19}$$

The uncertainty in active area is caused by measurement uncertainties during the mounting of the NEG strips on the getter cartridges.

7.4.2. Experimental determination of the NEG sticking coefficient

The basic goal of the experiment was to determine the sticking coefficient α of the NEG cartridges under conditions similar to the CPS bake-out mode. Two cartridges have been used during these measurements. The experimental procedure was subdivided into the following steps:

1. **Calibration:** The two RGAs and the pressure gauges were calibrated relative to each other by inserting two cartridges into the UHV chamber with stainless steel strips instead of NEG strips ($\alpha = 0$). Subsequently, hydrogen was injected into the system. The pressure of each sensor was recorded continuously.

2. **Mounting the NEG pump:** The calibration cartridges were replaced by the NEG pumps. The thermocouple sensors were inserted into the hollow tubes of the cartridges.

3. **Getter activation:** The UHV chamber, including the getter pump, was baked out at 400°C for 24 h, with a constant ramping speed of 30 K/h. A temperature gradient along the set-up was necessary to protect the instrumentation from overheating (TMP < 90°C, RGA and HPT 200 < 120°C).

4. **Cool-down** to room temperature.

5. **Determination of the sticking factor:** Injection of hydrogen into the UHV chamber with a constant flow rate. Simultaneously the pressures and the partial pressures in front of and behind the getter pump were recorded and analysed according to the method given in section 7.4.1.

Relative calibration of the instrumentation

For calibration purposes, the cartridges with the stainless steel strips were mounted inside the UHV chamber. The evacuated buffer vessel of the gas inlet system was filled with hydrogen up to $p_{\text{buffer}} = 1\,\text{mbar}$. Subsequently the vessel was pumped out through the UHV chamber, via the TMPs installed there. The maximum pressure inside the UHV chamber was $1.8 \cdot 10^{-5}\,\text{mbar}$. Since no hydrogen was refilled into the buffer vessel, a continuous, but decreasing gas flow through the calibration cartridges was achieved. The residual gas analysers, as well as the absolute pressure gauges (hot cathodes) were continuously recording the (partial) pressure. The measurement targeted for the calibration functions given in equations 7.17 and 7.18. Since all pressure sensors operate with individual, internal electronic amplification, which depend on the determined pressure, a non-linear relation between the gauges in front of and behind the NEG pump was expected. Only the pressure region in which the later activation measurements took place was parametrised according to equation 7.16. Figure 7.18 shows the calibration for the residual gas analysers. Here, the H_2 partial pressure ratio in front of the cartridges (RGA_1) is plotted against the H_2 partial pressure behind the cartridges (RGA_2). The polynomial function, according to
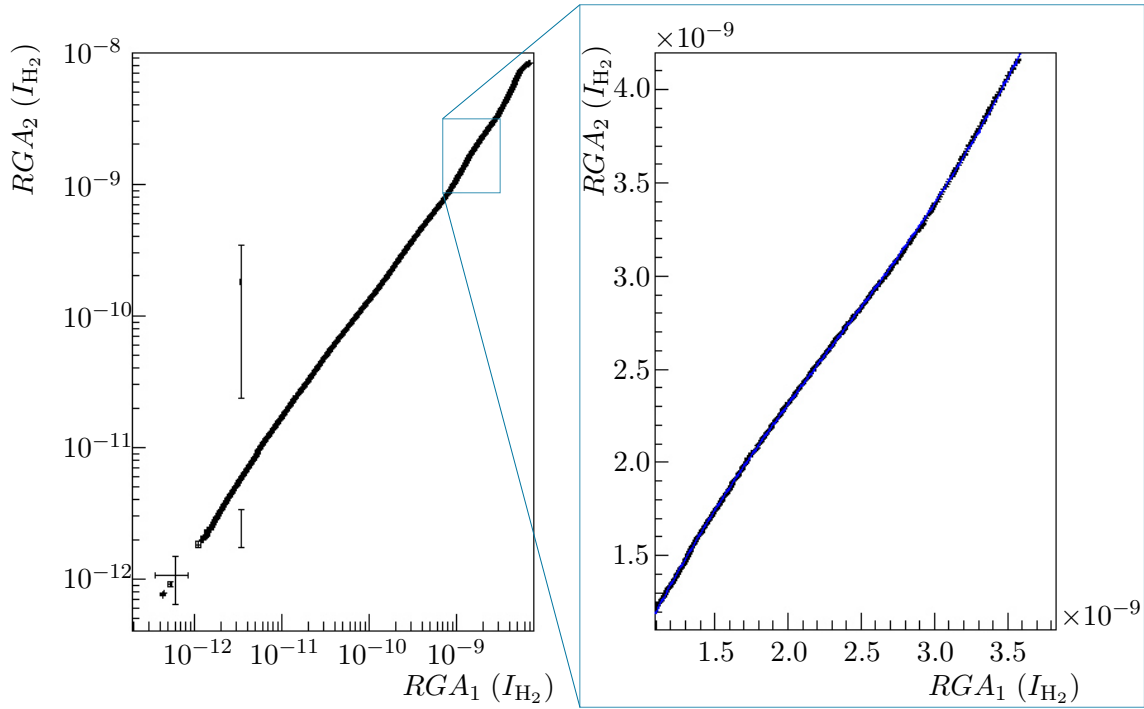
Figure 7.18.: Calibration measurement of the residual gas analysers RGA_1 (in front of the cartridges) and RGA_2 (behind the cartridges). Left: Complete measurement. Right: Parametrised interval. The units are given in ampere (ion current).

Table 7.5.: Fit parameters for the RGA (Pfeiffer Prisma QMS 200) calibration, according to equation 7.16 and figure 7.18.

Parameter	Value	Uncertainty	Unit
a_0 $[10^{-9}]$	-1.060	0.001	A
a_1 $[10^{0}]$	2.742	0.001	-
a_2 $[10^{8}]$	-7.450	0.006	A^{-1}
a_3 $[10^{17}]$	1.085	0.001	A^{-2}
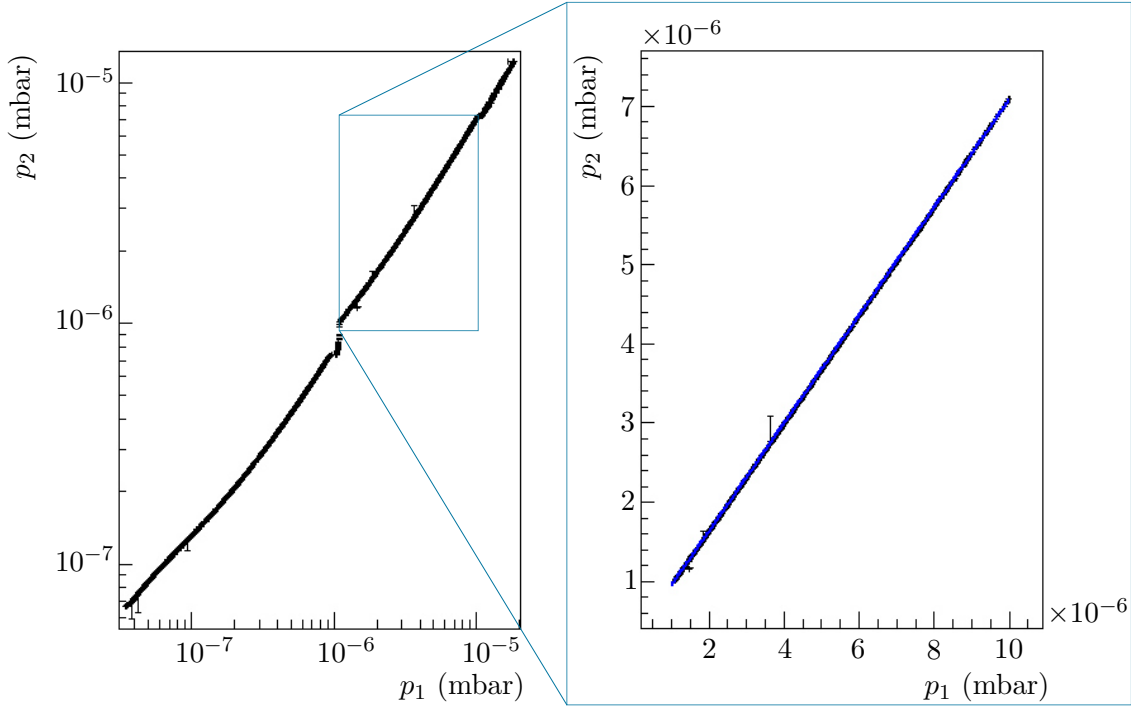
Figure 7.19.: Calibration measurement of the absolute pressure gauges (Pfeiffer HPT 200)
p_1 (in front of the cartridges) and p_2 (behind the cartridges). Left: Complete
measurement. Right: Fitted interval. The units are given in mbar.

Table 7.6.: Fit parameters for the absolute pressure gauges (Pfeiffer HPT 200) calibration,
according to the linear function in figure 7.19.

Parameter	Value	Uncertainty	Unit
b_0 [10^{-7}]	2.569	0.006	mbar
b_1 [10^{-1}]	6.811	0.001	-

equation 7.16, is given for the relevant ion current regime during activation measurements.
The associated parameters are listed in table 7.5.

The calibration function for the total pressure gauges was determined also by making use
of the recorded data given in figure 7.19. The pressure ratio is linear within one decade.
Between two orders of magnitude, a change in linearity was observed. This is due to the
different internal electronic amplifications. The important pressure range was parametrised
with a linear function. Parameters are given in table 7.6.

With the determined calibration parameters and equation 7.16, equation 7.15 turns into:

$$R_{RGA} = 0.742 \cdot \frac{RGA_2}{a_0 + a_1 \cdot RGA_1 + a_2 \cdot RGA_1^2 + a_3 \cdot RGA_1^3}$$

$$R_p = 0.745 \cdot \frac{p_2}{b_0 + b_1 \cdot p_1} \quad .$$

(7.20)

Determination of the CPS getter sticking coefficient

Two cartridges, with $(2268 \pm 86)\,\mathrm{cm}^2$ active getter surface, were placed in the centre of
the gold-plated tube inside the UHV chamber. One thermocouple type K sensor was fixed
in a hollow tube of one cartridge each. Subsequently the UHV chamber was baked-out
at a temperature of $T_4 = 400°C$, with $30\,\mathrm{K/h}$ ramping speed. At the outer region of
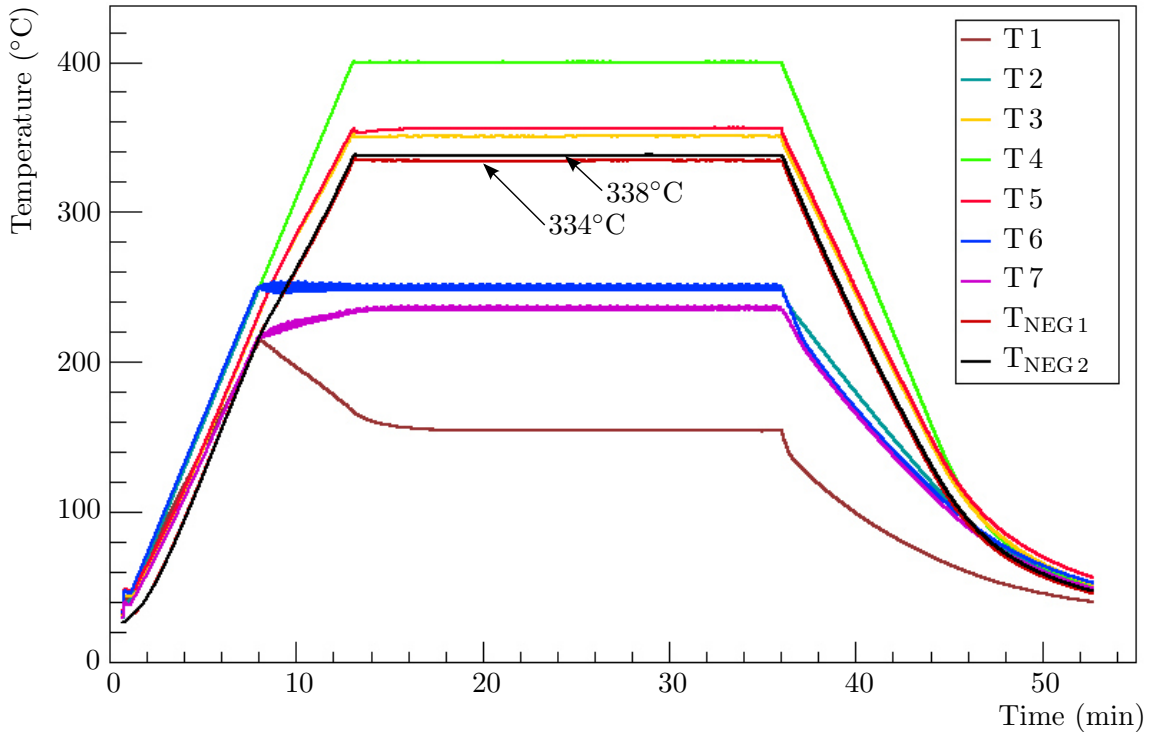
Figure 7.20.: Temperature evolution over time during the bake-out (activation) phase of the NEG pumps inside the test set-up. The position of the temperature sensors, identified with $T_1 - T_7$ are given in figure 7.13. $T_{NEG\,1}$ identifies the NEG cartridge close to the gas inlet system, $T_{NEG\,2}$ the one at the TMP side.

the set-up the maximum temperature was limited to $250°C$ ($T_{2,6}$) in order to protect the instrumentation. During bake-out, the system was continuously pumped out, via the cascaded TMPs ($190\,\ell/s$ for H_2 each). The temperature distribution over time was monitored (figure 7.20) and controlled via PT 100 sensors which were mounted along the apparatus, as illustrated in figure 7.13. Since the getter was activated indirectly by heat radiation only, the maximum temperature did not reach the full $400°C$. The two cartridges did reach an average temperature, equivalent to a condition of $336°C$ inside the CPS. The maximum temperature was kept for 24 h. Subsequently the getter pumps were cooled down via radiative heat loss.

During bake-out, chemisorbed particles at the getter ST707 surface were diffusing into the bulk material. Atoms, like hydrogen, that diffused to the surface, recombined to molecules, and were desorbed into the vacuum chamber. Correspondingly, the UHV chamber was cleaned during bake-out, since a significant part of molecules such as H_2O, H_2, CO_2, CO desorbed from the walls. After cool down, almost no residual gas could be detected with the residual gas analysers in the Faraday mode ($I < 10^{-13}\,A$).

To determine the getter sticking coefficient, the evacuated buffer vessel ($p_{buffer} \approx 10^{-6}\,mbar$) was filled with hydrogen to an initial pressure of $p_{buffer} = (0.95 \pm 0.10)\,mbar$. Subsequently the gas was injected into the UHV chamber. In order to achieve a constant injection flow, the buffer vessel was refilled with hydrogen via the inlet mass flow controller. The set point flow was adjusted (between $3.57 \cdot 10^{-3}\,mbar\,\ell/s$ and $4.42 \cdot 10^{-3}\,mbar\,\ell/s$), to keep the pressure of the buffer vessel at a constant level. A working pressure inside the UHV chamber in the region of $p \approx 10^{-6}\,mbar$ and $I_{RGA} \approx 10^{-9}\,A$ could be achieved. Figures 7.21 and 7.22 show the partial ion currents of the most common gases in the vacuum sys-

tem, during measurements. The measurement was subdivided into five time periods of 15 minutes gas injection and one long-term measurement for 15 hours. In each case, hydrogen was the dominant type of gas. Small amounts of other gases, such as N_2, O_2, Ar, etc., slowly increased over time. When comparing ion currents of both residual gas analysers one can observe that active gases such as O_2, CO, etc. are adsorbed by the getter as well. In figure 7.23 the ratio between both residual gas analysers and between the two total pressure gauges are plotted. In doing so, corrections according to equation 7.20 were applied. Injected molecules are partially adsorbed on the getter surface and partially pumped by the TMP. The surface coverage thus increases with the number of incoming particles, hence fewer particles are adsorbed and more particles are passing the getter pump, decreasing the measured ion current ratio, and total pressure ratio respectively. During the short-term injections as well as at the beginning of the long-term measurement, a constant ion current ratio was determined. The minimum ratio amounted to $R_{\mathrm{RGA, exp}} = 0.341$ with negligible statistical uncertainty. The total pressure remained very sensitive to different gas injection rates. Since the pressure inside the buffer vessel, and hence also the injection rate, varies slightly between individual measurement runs, a variation of the initial total pressure ratio was observed. For the first injection run, an average ratio of $R_{p, \mathrm{exp}} = (0.328 \pm 0.002)$ was determined with the absolute pressure gauges.

The sticking coefficients are determined with the help of the simulation shown in figure 7.17 and equation 7.19. For the calculation, the bisection method was used with a precision of 10^{-6}. The measured hydrogen ion current ratios yield a maximum sticking coefficient of $\alpha_{\mathrm{RGA, exp}} = (1.328 \pm 0.003) \cdot 10^{-2}$. From the total pressure ratios in the first run a similar sticking coefficient of $\alpha_{p, \mathrm{exp}} = (1.392 \pm 0.021) \cdot 10^{-2}$ is determined. Figure 7.24 shows the development of the sticking coefficients over time during the measurements. The sticking coefficient for hydrogen remains constant at the beginning. This fact indicates an equilibrium inside the UHV chamber between TMP pumping, getter pumping and gas injection. Reaching an equilibrium implies that the getter material has enough capacitiy for H_2 after activation at 336°C.

The same measurements were performed for a maximum activation temperature of 257°C over a period of 24 h. The heating and cooling rate remained the same as in the measurements described above. Three gas injection cycles were performed with flow rates between $3.6 \cdot 10^{-3}$ mbar ℓ/s and $3.7 \cdot 10^{-3}$ mbar ℓ/s for approximately ten minutes injection time. The short-term runs where followed by one long-term run with a hydrogen gas flow of $3.8 \cdot 10^{-3}$ mbar ℓ/s. The same calculation principle was used to determine the getter sticking probability. The results are shown in figure 7.25. The sticking probability for hydrogen was determined to be $\alpha_{\mathrm{exp.}} = (9.96 \pm 0.08) \cdot 10^{-3}$. The measurements with the total pressure gauges yield an experimental sticking coefficient of $\alpha_{\mathrm{exp.}} = (5.4 \pm 0.2) \cdot 10^{-3}$, which is about 60% less than observed after activation at 336°C. The sticking probability drops more quickly over time than during measurements after 336°C activation temperature. Hence, a smaller absorption capacity is reached in this case.

7.5. Impact of the measured pumping properties on the CPS reduction factor

The NEG pump is designed to serve as the final pumping stage inside section 7 of the CPS being the very last pumping unit to remove tritiated molecules before entering the tandem-spectrometer. This may occur if tritiated molecules pass through the cold stage or desorb from the cold gate valve.

When purging the CPS with helium, the contaminated argon frost layer will be evaporated in advance by heating up the beam tube system. The gaseous argon-tritium-helium mixture will then spread along beam tube elements 1-5, being separated from the spectrometer
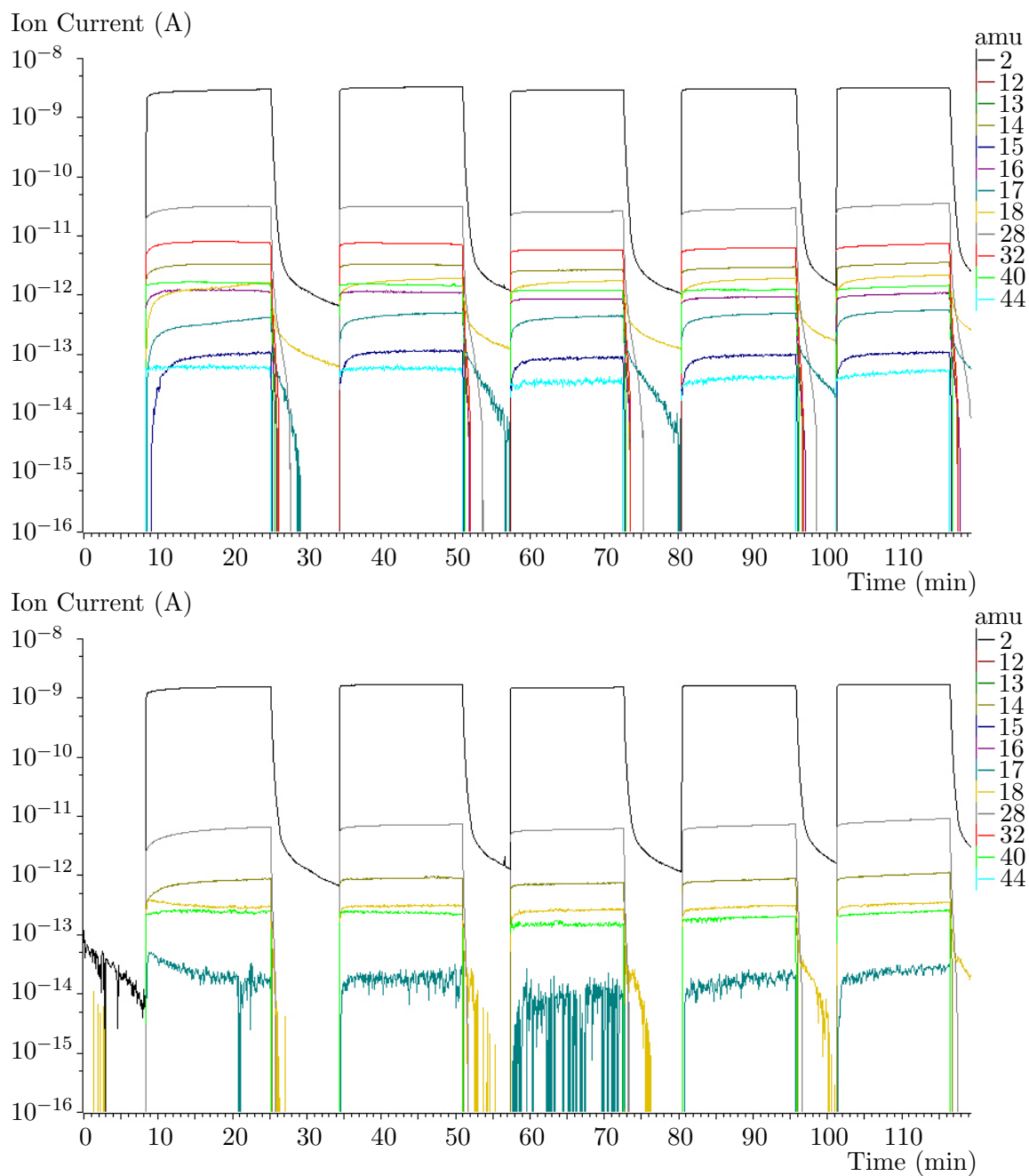
Figure 7.21.: Residual gas analysis during short-term run cycles, after getter activation at $T_{\mathrm{act.}} = 336°C$. Top: RGA in front of the NEG. Bottom: RGA behind the NEG.
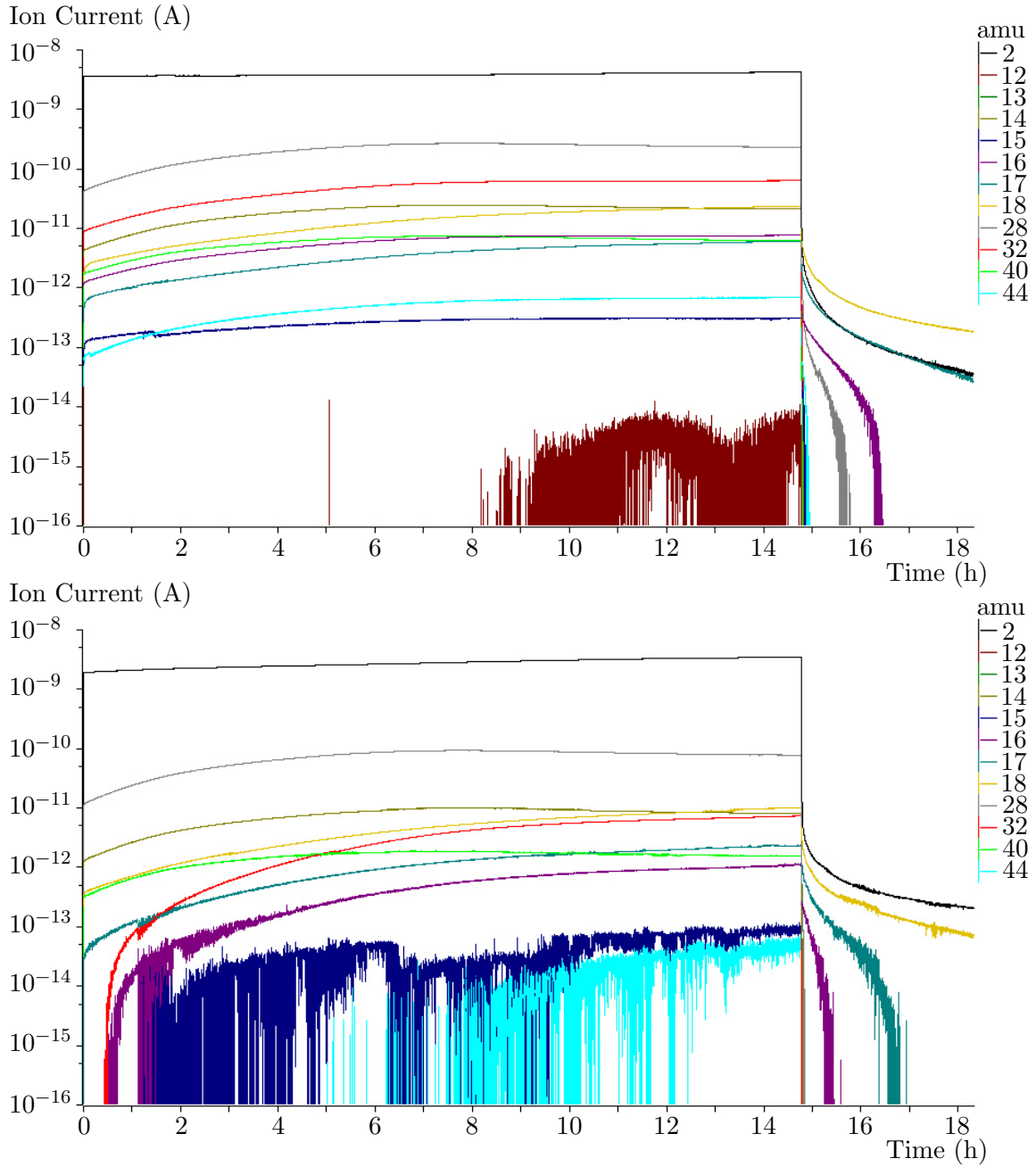
Figure 7.22.: Residual gas analysis during long-term run, after getter activation at $T_{act.} =$ 336°C. Top: RGA in front of the NEG. Bottom: RGA behind to the NEG.
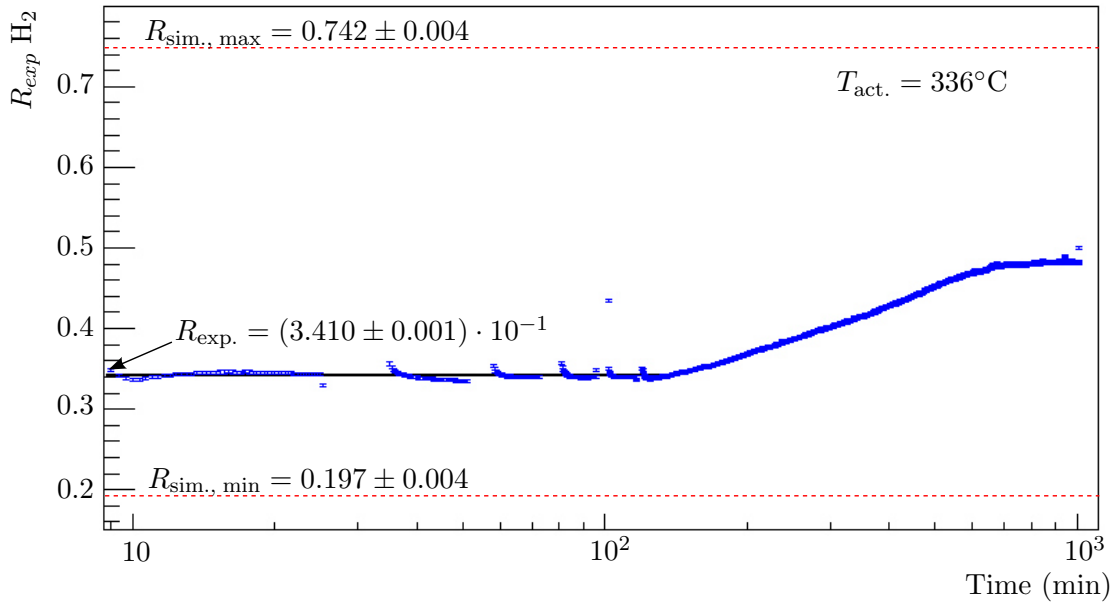
(a) H$_2$ ion current ratio.
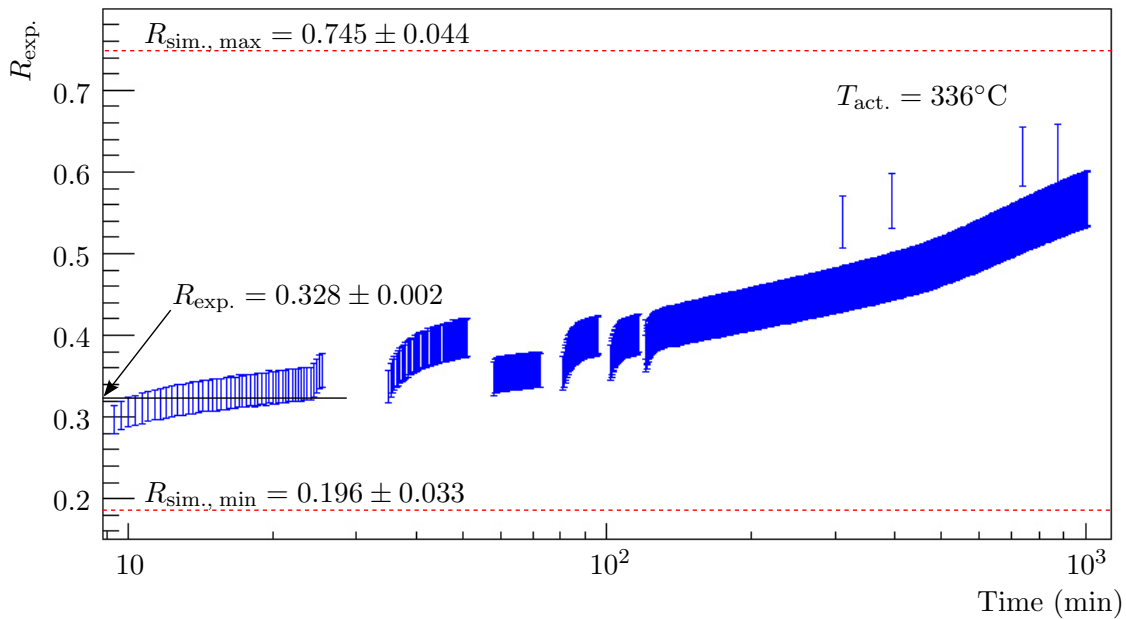
(b) Total pressure ratio.

Figure 7.23.: Ratios between the RGA H$_2$ ion currents (top) and between the total pressure gauges (bottom) during determination of the getter sticking coefficient after 24 h bake-out at $T_{act.} = 336°$C. Hydrogen was injected into the set-up, simultaneously the two (partial) pressure ratios in front of and behind the NEG pump were recorded.
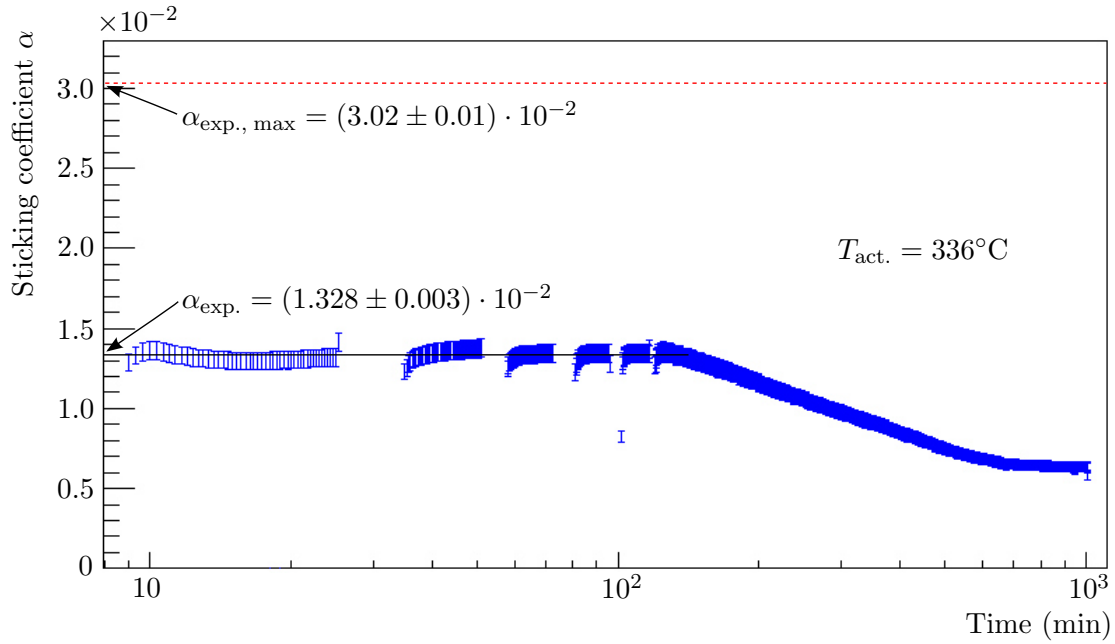
(a) NEG H_2 sticking coefficient, determined with the RGAs.
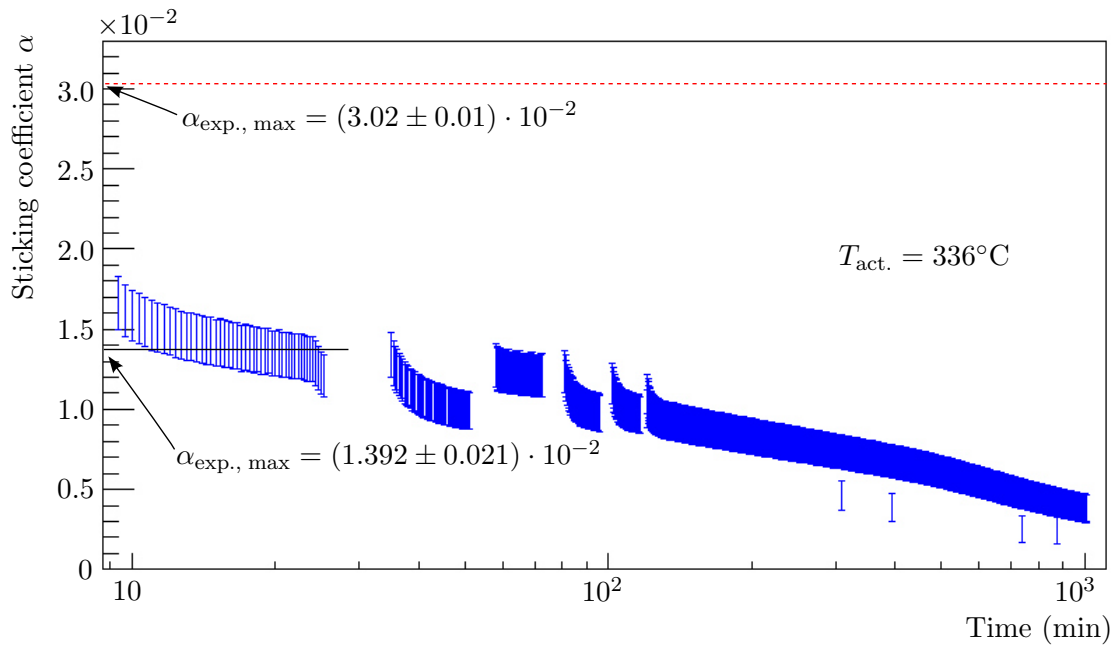
(b) NEG sticking coefficient, determined with the total pressure gauges.

Figure 7.24.: Sticking coefficients α over time of the CPS getter pump after activation at $T_{\text{act.}} = 336°\text{C}$ for $24\,\text{h}$, determined with the RGAs for hydrogen (top) and with the total pressure gauges (bottom) for the sum of all partial pressures inside the test set-up.
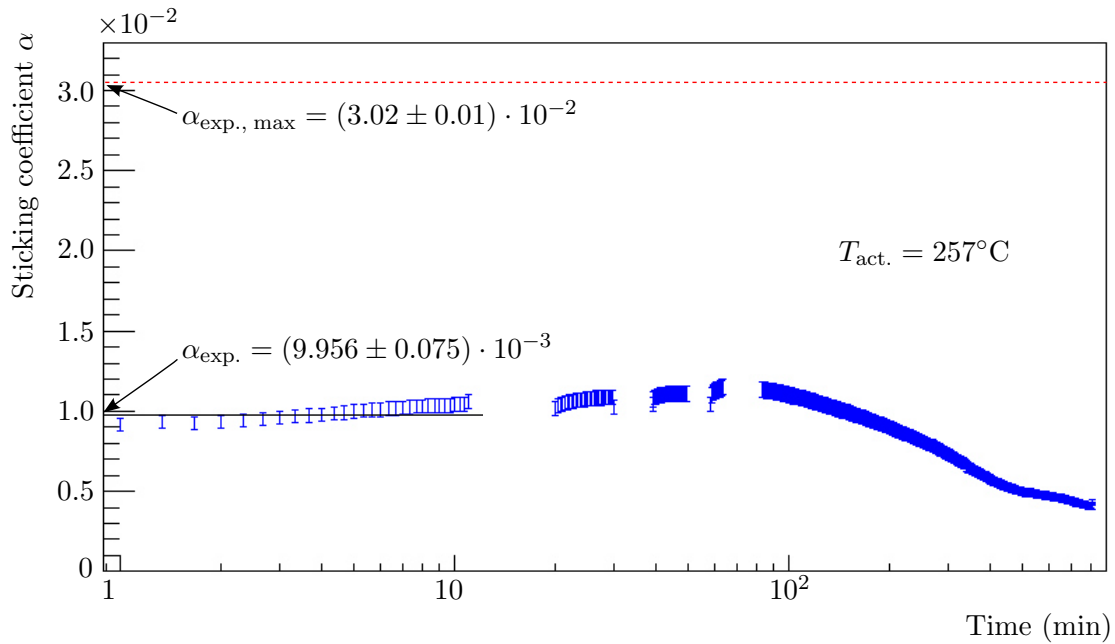
(a) NEG H_2 sticking coefficient, determined with the RGAs.
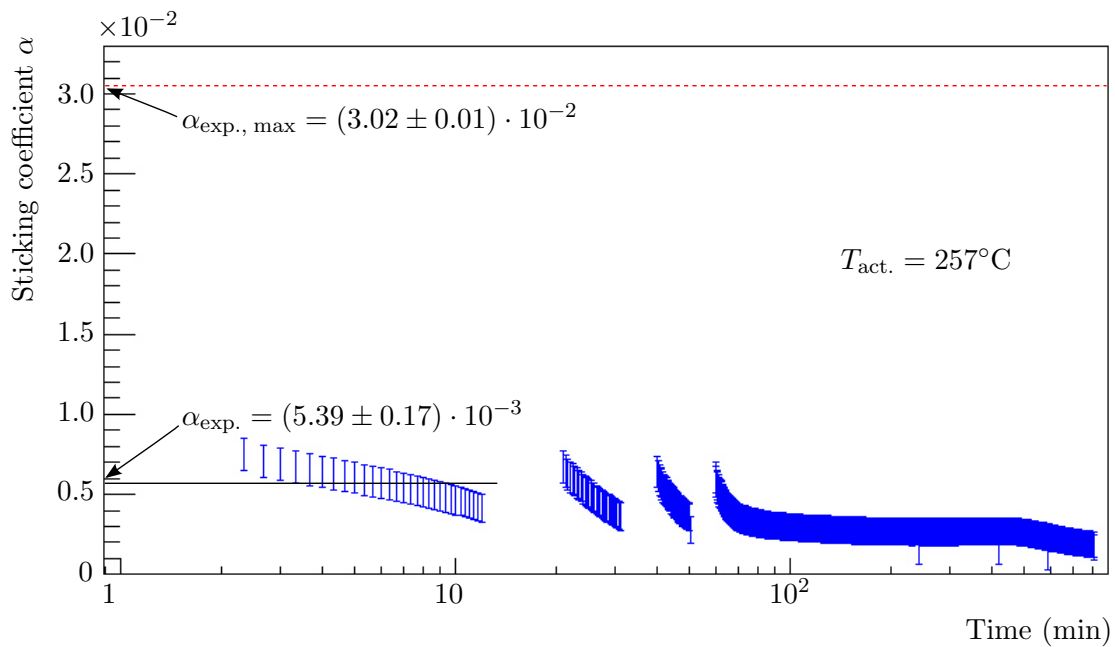
(b) NEG sticking coefficient, determined with the total pressure gauges.

Figure 7.25.: Sticking coefficients α over time of the CPS getter pump after activation at $T_{\text{act.}} = 257°C$ for 24 h, determined with the RGAs for hydrogen (top) and with the total pressure gauges (bottom) for the sum of all partial pressures inside the test set-up.
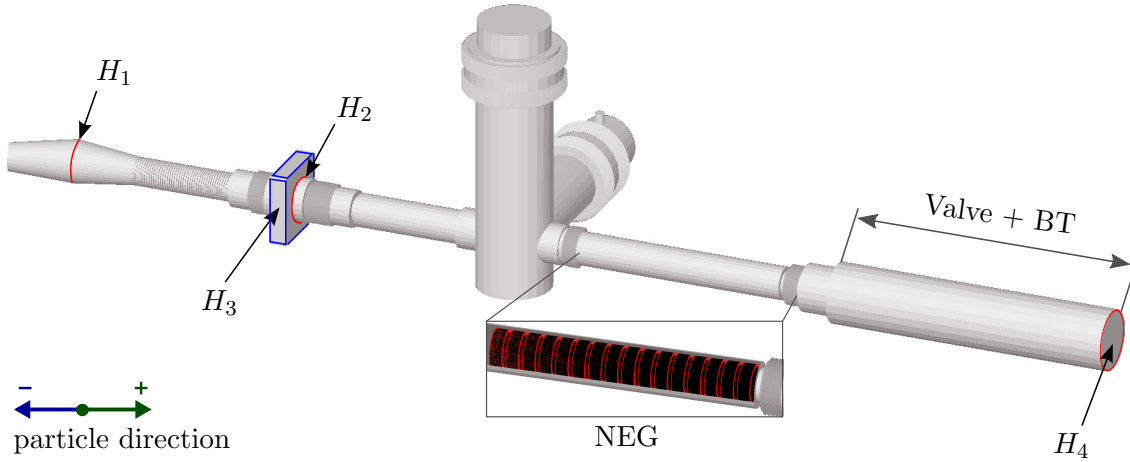
Figure 7.26.: Simulation model to evaluate the getter performance inside the CPS. In red: Analysing facets (desorption, adsorption, and hit counts). Blue: Desorption area for an opened cold gate valve. BT = beam tube between CPS and pre-spectrometer.

section by the closed cold gate valve. Small amounts of tritium will however be adsorbed onto the surface of the cold gate valve. When opening the valve again for standard operation, these small amounts will be pulled into the valve head where they can diffuse freely along the valve surfaces. Tritiated molecules will thus slowly desorb and might migrate into the spectrometer region. This migration effect can occur both in the opened and the closed state of the cold gate valve. The reduction factor of the getter pump, based on the measurements in section 7.4.2, has been investigated for all three cases (tritium from the cold stage, and from the opened and closed cold gate valve (CGV)).

Similar to the transmission probability simulation in chapter 6, a model has been implemented in Molflow+ as shown in figure 7.26. The model includes sections 5-7, the cold gate valve, pump port 2, and the beam tube (plus gate valve) between CPS and pre-spectrometer. The NEG pump is placed inside section 7. It consists of four cartridges with four double layers of getter strips each. The implemented active getter area was $4701.25 \, \mathrm{cm}^2$.

A sticking probability of 0.7 (argon frost) was defined for section 5. On the two facets H_1 and H_4, a sticking probability of unity was defined, thereby assuming negligible backscattering from the cold stage and the pre-spectrometer. Particles could desorb from facet H_1 (particles passing the cold stage), H_2 (desorption from the closed CGV), and from H_3 (desorption from opened CGV). The desorption distribution was chosen to be cosine-like. For each of the three desorption models, the getter sticking probability was set to its optimal value of 0.029 [166], to 0 (worst case), and to the experimentally determined sticking probabilities. In order to evaluate the pumping efficiency, a simulation without getter pumps was performed as a reference. In the simulations in which particles pass through the cold stage, the ratio between particles passing through facet H_2 in the + direction and particles adsorbed on facet H_4 was calculated:

$$P = \frac{H_{4+}}{H_{2+}} \pm \sqrt{\frac{\sigma_{H_{4+}}^2}{H_{2+}^2}} \quad . \tag{7.21}$$

A similar ratio was used for the simulation of the closed cold gate valve, replacing the hits H_{2+} by the number of desorbed particles from H_2.

In the cases where particles desorb from the opened cold gate valve, the ratio between the

Table 7.7.: Settings for the NEG evaluation simulations. The relation between indications and simulation model is given in figure 7.26. A sticking probability of 0.7 was defined on CPS section 5.

Number	Desorption	Sticking $\alpha = 1$	Sticking $\alpha_{\text{sim. NEG}}$	Description
Passing through cold stage				
1	H_{1+}	$H_1\,H_4$	-	Reference, no NEG
2	H_{1+}	$H_1\,H_4$	0	No getter activation
3	H_{1+}	$H_1\,H_4$	0.0290	Max. NEG activation
4	H_{1+}	$H_1\,H_4$	0.0127	NEG activation at 336 K
5	H_{1+}	$H_1\,H_4$	0.0096	NEG activation at 257 K
Desorption from closed CGV				
6	H_{2+}	H_4	-	Reference, no NEG
7	H_{2+}	H_4	0	No getter activation
8	H_{2+}	H_4	0.0290	Max. NEG activation
9	H_{2+}	H_4	0.0127	NEG activation at 336 K
10	H_{2+}	H_4	0.0096	NEG activation at 257 K
Desorption from opened CGV				
11	H_{3+}	$H_1\,H_4$	-	Reference, no NEG
12	H_{3+}	$H_1\,H_4$	0	No getter activation
13	H_{3+}	$H_1\,H_4$	0.0290	Max. NEG activation
14	H_{3+}	$H_1\,H_4$	0.0127	NEG activation at 336 K
15	H_{3+}	$H_1\,H_4$	0.0096	NEG activation at 257 K

number ob desorbed particles and particles adsorbed on facet H_4 was calculated:

$$P = \frac{H_{4+}}{H_{3+}} \pm \sqrt{\frac{\sigma^2_{H_{4+}}}{H^2_{3+}}} \quad . \tag{7.22}$$

Table 7.7 lists the settings, as defined in each simulation, while table 7.8 summarizes the results.

Summary: Particles passing through the cold stage

Even without any pumping properties, the NEG pump serves as a narrowing, and thus will reduce the gas flow to the pre-spectrometer by 17% with respect to the reference simulation, in which no getter pump is implemented in the CPS. With a maximum activated getter pump, the gas flow will be reduced by 82%. The transmission probability, with respect to the reference, does not change significantly when activating the getter pump at 336°C (72%) or at 257°C (68%). Since the differences in the transmission probability are marginal between an activation at low temperatures and a fully activated getter pump, one can conclude that the gas flow, coming from the cold stage, is extremely forward peaked, as only small amount of diffuse scattering, caused by particle-wall-interactions, will occur.

Table 7.8.: Results for the CPS NEG pump efficiency simulations. The setting are described in table 7.7, the model in figure 7.26. The transmission indicates the probability of particles reaching the pre-spectrometer.

Number	Hits H_{2+}/H_3	Hits H_{4+}	Transmission P	Description
Passing through cold stage				
1	168849	10185	$(6.03 \pm 0.06) \cdot 10^{-2}$	Reference, no NEG
2	202585	10229	$(5.05 \pm 0.05) \cdot 10^{-2}$	No getter activation
3	936111	10026	$(1.07 \pm 0.01) \cdot 10^{-2}$	Max. NEG activation
4	617487	10310	$(1.67 \pm 0.02) \cdot 10^{-2}$	NEG activation at $336\,\mathrm{K}$
5	561963	10906	$(1.94 \pm 0.02) \cdot 10^{-2}$	NEG activation at $257\,\mathrm{K}$
Desorption from closed CGV				
6	-	-	1	Reference, no NEG
7	-	-	1	No getter activation
8	181504	10126	$(5.58 \pm 0.06) \cdot 10^{-2}$	Max. NEG activation
9	82840	11906	$(1.44 \pm 0.01) \cdot 10^{-1}$	NEG activation at $336\,\mathrm{K}$
10	58262	11041	$(1.90 \pm 0.02) \cdot 10^{-1}$	NEG activation at $257\,\mathrm{K}$
Desorption from opened CGV				
11	87291	12065	$(1.38 \pm 0.01) \cdot 10^{-1}$	Reference, no NEG
12	87071	10219	$(1.17 \pm 0.01) \cdot 10^{-1}$	No getter activation
13	950960	10034	$(1.06 \pm 0.01) \cdot 10^{-2}$	Max. NEG activation
14	410888	10089	$(2.46 \pm 0.02) \cdot 10^{-2}$	NEG activation at $336\,\mathrm{K}$
15	313245	10083	$(3.22 \pm 0.03) \cdot 10^{-2}$	NEG activation at $257\,\mathrm{K}$

Summary: Particles desorbing from the closed CGV

Without an implemented NEG pump in case of vanishing sticking properties of the getter material, no final pumping mechanism inside the last two sections of the CPS will be available. In this case, the transmission probability into the spectrometer will be identical to unity for all desorbing particles. However, this gas flow will be reduced in case of a maximum activated getter pump by a fraction of 94%. As outlined above, the transmission probability does not vary much (86% to 81%) between the two experimentally determined getter sticking coefficients.

Summary: Particles desorbing from the opened CGV

Particles desorbing from the cold gate valve (CGV) body (opened status), can scatter backwards to the argon frost layer. This results in a theoretical transmission probability between CGV and the pre-spectrometer of 0.14, when no getter pump is installed. In case of a non-activated NEG pump, a reduction by 16% is achieved. Significantly fewer particles will reach the spectrometer for a maximum-activated getter pump (92% reduction). The difference in the sticking coefficient of the getter activated at 336°C or at 257°C is negligible with transmission probabilities of 82% and 77%, respectively.

Conclusions for the CPS NEG pump

When comparing different reduction factors, there is almost no difference between an activation of the CPS NEG pump at 336°C, the maximum specified bake-out temperature, and a case of 257°C. With respect to the pumping capacity, it is however still recommended to heat up the getter pump to a temperature regime as high as possible. The resulting impact can be clearly seen in figures 7.24 and 7.25, where the sticking coefficient remains constant for a considerably longer time after activation at the higher temperature. A corresponding statement with respect to the capacity during the test measurements is not possible, however, since one cannot differentiate between particles pumped by the TMP or by the getter pump.

Within the framework of simulations of this thesis it cannot be estimated whether a larger number of particles will desorb from the opened or the closed cold gate valve, or if more particles will pass through the argon frost layer. This has to be resolved during the first commissioning measurements by monitoring the exact residual gas composition at the end (pump port 2) of the CPS cryostat. A suite of test measurements, targeted at providing an estimate of the getter capacity are recommended as well.

7.6. Alternative mounting position for the CPS NEG pump

The mounting of a custom-made getter pump inside CPS section 7 is a rather challenging task. The unit has to fit into the beam tube, and it must be fixed in order not to be shifted due to eddy current forces, in case of a magnet quench. Finally it must not intersect the specified $191\,\mathrm{Tcm^2}$ magnetic flux tube. As shown in section 3.3.2, there remains a small safety margin only, when mounting the getter pump in this beam tube section. In order to investigate alternative positions for the NEG pump, where the risk of intersecting the flux tube would be much smaller, a simulation was performed similar to the simulations described above. Figure 7.27 shows a screen shot of the simulation, with the NEG pump placed in the horizontal pump port 2. Now, the NEG geometry consists of 8 cylinders with 2 layers of ST707 getter strips each, with an inner diameter of 150 mm and an outer diameter of 170 mm. The total active getter surface results in $A_{\mathrm{sim.}} = 4.34\,\mathrm{m^2}$. The simulation settings, as listed in table 7.9, are identical to the NEG pump inside section 7, presented above. A total of three cases were simulated, with particles
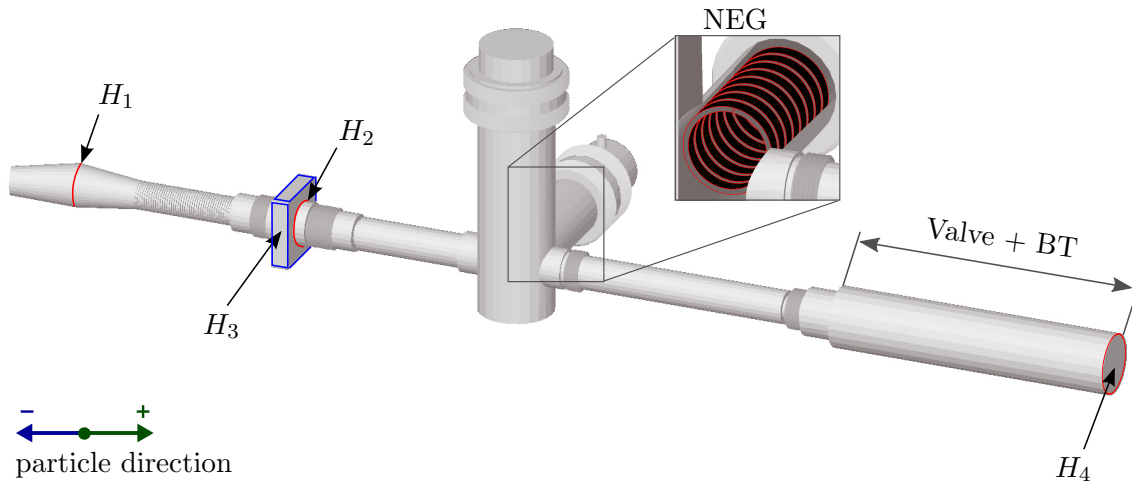
Figure 7.27.: 3D view of the simulation model to evaluate the getter performance inside the CPS at an alternative mounting position, now located in pump port 2. In red: Analysing facets (desorption, adsorption, and hit counts). Blue: Desorption area for an opened cold gate valve. BT = beam tube between CPS and pre-spectrometer.

1. passing through the cold stage,

2. desorbing from the closed cold gate valve, and

3. desorbing from the opened cold gate valve.

Since this is a design study, only the case with a maximum-activated NEG pump was considered. For each of the three cases the transmission ratios were calculated using equations 7.21 and 7.22. The results are listed in table 7.10. For the reference simulation the results given above are copied.

Summary: Efficiency of an alternative NEG position

Particles passing the argon frost layer have a transmission probability of 6% to reach the spectrometer section, if no getter pump is mounted. With a getter pump inside pump port 2 the probability will be reduced by 53%.

Each particle desorbed from the closed cold gate valve will reach the spectrometer section if no getter is installed inside the CPS, when mounting the NEG strips inside pump port 2 a flow reduction of 87% will occur.

If particles desorb from the opened cold gate valve, they will leave the CPS with a probability of 1.4%. Placing a NEG pump inside pump port 2 will reduce this probability by 76%.

When comparing the results from the simulations for a NEG pump mounted inside section 7 and inside pump port 2, one notices that the efficiency of the tritium flow reduction will be reduced by a factor of 3, if the getter pump is mounted inside pump port 2. The direct comparison is listed in table 7.11. Nevertheless, the risk of intersecting the flux tube will be considerably reduced when mounting the getter pump inside pump port 2. Also, this position offers easier access for maintenance. In addition, more getter material can be used since the vertical pump port 2 offers a larger volume and no weight limits are set for that position, and more getter material will improve the pump capacity. One may even implement both scenarios.

Table 7.9.: Settings for the NEG evaluation simulations for an alternative mounting position, according to the model shown in figure 7.27. A sticking probability of 0.7 was defined for CPS section 5.

Number	Desorption	Sticking $\alpha = 1$	Sticking $\alpha_{\text{sim. NEG}}$	Description
Passing through cold stage				
1	H_{1+}	$H_1\ H_4$	-	Reference, no NEG
2	H_{1+}	$H_1\ H_4$	0.029	Max. NEG activation
Desorption from closed CGV				
3	H_{2+}	H_4	-	Reference, no NEG
4	H_{2+}	H_4	0.029	Max. NEG activation
Desorption from opened CGV				
5	H_{3+}	$H_1\ H_4$	-	Reference, no NEG
6	H_{3+}	$H_1\ H_4$	0.029	Max. NEG activation

Table 7.10.: Results for the CPS NEG pump efficiency simulations for a NEG pump mounted inside pump port 2. The settings are described in table 7.9, the model in figure 7.27. Transmission indicates the probability of particles reaching the pre-spectrometer.

Number	Hits H_{2+}/H_3	Hits H_{4+}	Transmission P	Description
Passing through cold stage				
1	168849	10185	$(6.03 \pm 0.06) \cdot 10^{-2}$	Reference, no NEG
2	350440	10129	$(2.89 \pm 0.03) \cdot 10^{-2}$	Max. NEG activation
Desorption from closed CGV				
3	-	-	1	Reference, no NEG
4	79860	10367	$(1.30 \pm 0.01) \cdot 10^{-1}$	Max. NEG activation
Desorption from opened CGV				
5	87291	12065	$(1.38 \pm 0.01) \cdot 10^{-1}$	Reference, no NEG
6	306381	10099	$(3.30 \pm 0.03) \cdot 10^{-2}$	Max. NEG activation

Table 7.11.: Comparison between a NEG pump mounted in section 7 and in pump port 2. The transmission P describes the probability of desorbed particles to reach the spectrometer section.

Scenario	Mounting position	Transmission P
Passing through cold stage	No NEG	6%
	Section 7	1%
	Pump port 2	3%
Desorption from closed CGV	No NEG	100%
	Section 7	6%
	Pump port 2	13%
Desorption from opened CGV	No NEG	14%
	Section 7	1%
	Pump port 2	3%

8. Conclusions and Outlook

The KATRIN experiment, currently under construction at KIT (TLK), is targeted to determine the effective mass of the electron anti-neutrino with a sensitivity of $200\,\text{meV}/c^2$ (90% C.L.). In order to reach this ultimate goal the transport section is of utmost importance. It connects the tritium source with the spectrometer section where the energy analysis of β-decay electrons is performed. The transport section consists of two major functional units: a differential pumping part (DPS) and a cryogenic pumping part (CPS), using argon frost as adsorbent. The DPS is specified to reduce the tritium gas flow from the WGTS by five orders of magnitude. The CPS is specified to reduce the residual gas flow by another seven orders of magnitude. At the same time both components must guide the β-decay electrons adiabatically to the spectrometers. Both components are currently being assembled, and will be commissioned in 2015. In preparation for the commissioning phase of the CPS, this thesis has carried out extensive studies and R&D work with respect to the magnet safety system, the argon preparation, the getter activation, and the overall CPS pumping performance.

The most important part of the magnet safety system is formed by the by-pass diode stacks, which have to protect each superconducting coil. The diodes are mounted in parallel to the solenoids serving as an electric switch. In case of a magnet coil quench, the discharging of the stored magnetic energy has to proceed in a safe way. The diodes thus have to deal with a maximum amount of energy of $3.5\,\text{MJ}$ with currents up to $200\,\text{A}$. In order to protect the diodes from overheating, they have been sandwiched between massive copper heat sinks. This assembly was then stress-tested. The tests consisted of pre-selection tests, such as temperature cycling, electric tests, and five cycles of current endurance tests at $77\,\text{K}$ (non-adiabatic) and $4.5\,\text{K}$ (quasi-adiabatic) inside a wide-neck cryostat. The nominal current of $200\,\text{A}$ was applied to each diode for a time period of $253\,\text{s}$, which corresponds to the same amount of energy the diodes have do deal with during CPS operation, plus a 30% safety factor. All diodes passed the tests in liquid nitrogen, with diode temperatures less than $120\,\text{K}$. The temperature of the heat sinks remained below $80\,\text{K}$. It is important to note that these tests were performed with continuous cooling. With the quasi-adiabatic current endurance tests at $4.5\,\text{K}$ initial temperature, the operation conditions inside the CPS cryostat were simulated as closely as possible. Now the temperature of the diodes increased to $240\,\text{K}$, while the heat sink temperature still remained below $200\,\text{K}$. All seven plus two spare diode stacks were tested successfully and have been shipped to ASG for integration into the cryostat.

The CPS will be operated in cycles consisting of the steps of argon preparation, regular neutrino mass measurement runs (standard operation), and, after 1 Ci activity has been accumulated on the argon frost layer, of a specific regeneration, where the argon frost is renewed. The most critical phase of the entire cycle, the argon preparation, and in particular the argon injection phase through the nine capillaries, has been investigated within this thesis. Therefore the injection geometry was copied in a dedicated test set-up on a scale of one to one. Subsequently, the gas flow properties of this capillary were tested in a vacuum test-stand. Under isothermal conditions the conductance and the gas throughput, for argon and helium, were determined and were found to be in good agreement with simulations. These results were then applied to the CPS as a whole. First, the temperature distribution along a capillary during argon preparation was simulated. The temperature profile shows distinct variations, depending on the heat load at the capillary anchorage inside the CPS. At the electrically heated gas inlet, a temperature of $76 \, \text{K}$ will be reached. At the opposite end the temperature will vary between $17 \, \text{K}$ (maximum thermal contact) and $69 \, \text{K}$ (no thermal contact). Since the anchorage is a loosely pressed contact, the heat load at that point can be assumed to be negligible, thus the most likely temperature regime there will be $60 \, \text{K} - 69 \, \text{K}$.

The temperature distribution was then used as input for non-isothermal gas flow simulations of argon through the capillary in the molecular flow regime. It turned out that the pressure inside the capillary drops significantly from the first to the last orifice, i.e close to a factor of 100. Hence an inhomogeneous argon frost layer inside each beam tube segment 2-5 has to be expected. However, on the beneficial side, this pressure drop avoids freezing of argon inside the capillary, since the vapour pressure is at all times above the pressure along the capillary. There is even a safety factor of at least two orders of magnitude in pressure. This is of central importance for the KATRIN experiment in view of an efficient argon frost layer preparation, which typically will have to be performed about a handful of times per calendar year.

A total of $1000 - 3000$ layers of frozen argon have to be prepared in the central CPS beam tube elements. With a maximum throughput in the order of $10^{-3} \, \text{mbar} \, \ell/\text{s}$ (molecular flow regime) through all 9 capillaries, the argon preparation would take about 3-4 weeks. In order to shorten this time, the inlet pressure has to be increased by up to two orders of magnitude to a value beyond the molecular flow regime, thereby entering the transitional flow. Since calculations in the transitional flow regime are only estimates the exact argon preparation procedure, with respect to the injection time, has to be determined by experiment during CPS commissioning.

Within this thesis the reduction factor of the differential pumping section was simulated as well. A reduction factor of $4.5 \cdot 10^5$ for the stand-alone conductance was calculated for a fully instrumented DPS. This key KATRIN design parameter thus fulfils the specifications. From this the gas load onto the CPS is in the specified order of magnitude as well ($10^{12} \, \text{T}_2/\text{s}$). Based on literature data it was shown in the thesis at hand, that the sorption capacity of the CPS is sufficiently large to accumulate 60 Ci. Hence, a safety factor of 60 will be achieved during operation, which is essential in view of the long-term fail-safe operation of the transport section.

The transmission probability of the CPS for incoming tritium was simulated. When neglecting time-dependent desorption processes and the diffusion by radioactive decays, a maximum ideal transmission probability of the order of 10^{-17} is achieved, again, according to the definition of a stand-alone conductance. This optimistic theoretical transmission probability was compared with results obtained in the TRAP experiment, a former test set-up to investigate pumping with argon frost. With a calculated probability in the order

of 10^{-10}, a reduction by seven orders of magnitude from the ideal case is obtained. However, it has to be noted that the temperature of the CPS will be significantly lower than the operation temperature of the former TRAP experiment. Hence the real transmission probability for the CPS is expected to be in the range from 10^{-17} up to 10^{-10}. This interval suggests that the CPS is at least three orders of magnitude better than specified, again this considerably safety factor is essential in view of a fail-safe tritium retention. The exact reduction value has to be determined by experiment during commissioning of the CPS.

The final stage of tritium pumping inside the transport section will be a unit based on non-evaporable getter (NEG) strips placed in the most downstream section of the CPS. This pump will be activated indirectly during bake-out of the CPS via thermal radiation. Thermal simulations were performed in order to deduce the maximum activation temperature and the thermal operation conditions of the getter pump. The maximum activation temperature will be $336°C$, while the average operation temperature is expected to be at a value of $-23°C$. The sticking coefficient for the simulated activation temperature was determined with a dedicated complex test facility, yielding a maximum sticking probability of $\alpha = 0.013$. Note that the maximum possible sticking coefficient is 0.029. Lowering the activation temperature to a value of $260°C$ will lead to a smaller sticking coefficient of 0.010.

In order to verify which activation temperature is the most reasonable one, the impact of the NEG pump on the CPS gas flow reduction was investigated by simulations. It turned out that there is a negligible difference in the reduction factor when the NEG pump is activated at $336°C$ (maximum) or at $260°C$. Both scenarios will thus improve the reduction factor by about half an order of magnitude. For capacitive reasons, the pump should however be activated at temperatures as high as possible. Therefore it is recommended to redesign the NEG pump of the CPS. By widening its inner radius, the risk of intersecting the transported magnetic flux tube will be lowered. In addition the pump should be equipped with an electric heater, which would enable higher local activation temperatures and thus reduce the thermal stress on the complex CPS beam tube system.

This thesis thus has characterised the most important operating and physic parameters of the entire KATRIN transport system, both by dedicated test experiments as well as by specific simulations over a vast range of absolute pressures, ranging from transitional to the free molecular flow. With two large pumping units, the DPS and the CPS cryostats now being in the final stage of assembly, all data for a successful tritium retention with optimised performance are at hand. Without this, a tritium retention by more than 14 orders of magnitude, which has never been reached before, will not be possible and sub-eV neutrinos could not be measure by the KATRIN experiment.

Appendix

A. Simplification of bellows in heat transfer simulations

Bellows are characterized by a thin wall thickness and a high absolute length. This causes a low thermal conductivity. Bellows are used to separate two regions with different temperatures from each other. Due to its geometry, tensions of a non-isothermal system are reduced by a bellow. These effects occur especially in the temperature-stabilised vacuum systems of the two big cryostats in the KATRIN experiment, namely WGTS and CPS.

Thermal simulations of systems with bellows are a challenge when using the finite element method (FEM). In FEM simulation, the geometry (here the bellow) is discretised by a mesh. Since the bellow geometry is very complex, a huge number of mesh elements is required for the discretisation, consuming computation power and calculation time. In order to reduce the calculation time and the computation power, especially memory, the geometry has to be simplified. Bellows offer a good opportunity for simplifications. The following sections describe a method of simplification. Therefore the thermal properties of a 2D axial symmetric model of a bellow are simulated with COMSOL Multiphysics.

A.1. Simplification of the bellow geometry

In order to demonstrate how a bellow can be simplified and how this simplification influences the thermal properties, a specific bellow of the CPS section 7 was implemented in COMSOL Multiphysics. Figure A.1 shows a partial section of this specific bellow and its simplification.

(a) Bellow.

(b) Simplified bellow.
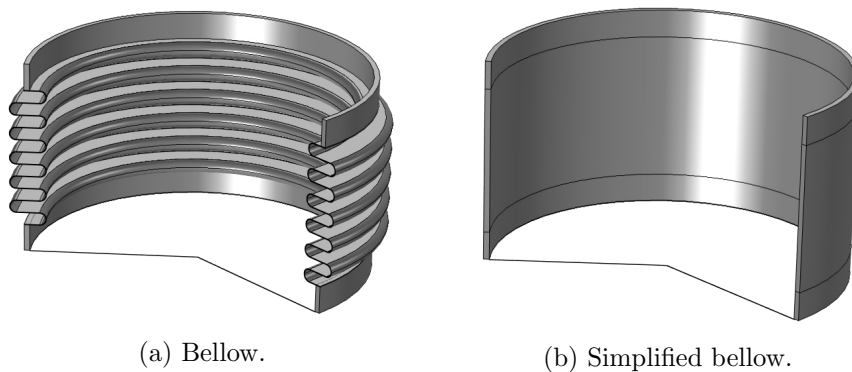
Figure A.1.: Partial section of a bellow (a) and a simplified (b). The curved part has been replaced by a tube.

The thin, curved part was replaced by a tube with the same inner and outer dimensions as the subsequent connection tubes and with the effective length (l_{eff}) of the bellow. The effective length is the direct connection line between both connection tubes. In order to achieve an equal thermal conductivity of the simplified bellow and the bellow itself, the physical properties have to be modified in the simulation.

A.2. Modification of the physical properties

Thermal processes can be described via a few simple equations [123]:

$$Q_{\text{cond.}} = k \cdot \frac{A}{l} \cdot \Delta T \qquad \text{(Conductive heat load)}, \qquad (8.1)$$

$$Q_{\text{rad.}} = \epsilon \cdot \sigma \cdot \Delta(T^4) \qquad \text{(Radiative heat load)}, \qquad (8.2)$$

$$Q_{\text{conv.}} = h \cdot A \cdot \Delta T \qquad \text{(Convective heat load)}, \qquad (8.3)$$

with the thermal conductivity k, the emission coefficient ϵ, the Stefan-Boltzmann constant σ, and the convective heat transfer coefficient h. Equation 8.2 assumes a grey surface, where the irradiation coefficient α equals the emission coefficient ϵ. This is a basic assumption in heat transfer simulations with COMSOL Multiphysics. Equation 8.3 is negligible, when simulating bellows under vacuum conditions, for example bellows in the CPS cryostat.

By replacing the curved part of a bellow by a simple tube, the thermal conductivity has to be adjusted by multiplying it with a dimensionless factor c which compensates the geometrical differences. This factor can be determined via:

$$Q_{\text{cond./bellow}} = Q_{\text{cond./tube}}$$
$$k \cdot \frac{A}{l} \cdot \Delta T = k \cdot c \cdot \frac{A_{\text{tube}}}{l_{\text{eff}}} \cdot \Delta T \qquad (8.4)$$
$$c = \frac{A}{l} \cdot \frac{l_{\text{eff}}}{A_{\text{tube}}} \quad ,$$

with the effective length of the bellow l_{eff}, the real length of the bellow l, the cross-section area of the bellow wall A, and the cross-section area of the simplified bellow wall A_{tube}. The length of a bellow is easy to calculate by adding up the length of every boundary. However, the area A of a bellow is not constant, since the inner and outer radii vary along the curved part. Thus, this area has to be approximated with the following approach. If r_{min} is the minimal inner radius of the bellow, and r_{max} the maximal outer radius, the mean area can be estimated by:

$$A = \pi \cdot \left[\left(\bar{r} + \frac{d}{2} \right)^2 - \left(\bar{r} - \frac{d}{2} \right)^2 \right] \quad , \qquad (8.5)$$

here $\bar{r} = (r_{\text{min}} + r_{\text{max}})/2$ is the mean radius and d the wall thickness.

With these assumptions the bellow and its approximation, shown in figure A.1, have been simulated. The results are presented in the following section.

A.3. Thermal simulation of a bellow and its simplification

The main focus was given to the temperature gradient along and the thermal radiation through a bellow. In order to investigate the thermal radiation, a disc was added to the simulation at one end (the colder end) of the bellow. There was a tiny space between disc and bellow to avoid a direct thermal contact. The temperature of the disc was fixed to 0 K, the emission coefficient to 0 and the absorption probability to unity. Hence, the disc had no influence on radiation and conduction of the bellow, but it absorbed the radiation coming from the inner surface of the bellow or its simplification completely. Thus the thermal radiation profile is equal to the irradiation profile on this particular disc. All simulation

Table A.1.: Settings and boundary conditions for the thermal simulation of a bellow.

Parameter	Value	Description
T_1	293.15 K	Temperature at the top end of the bellow / simplification
T_2	77 K	Temperature at the bottom end of the bellow / simplification
ϵ	0.2	Emission coefficient of the inner surface (polished stainless steel)
ϵ_D	0	Emission coefficient of the disc
a_D	1	Absorption probability of the disc
c	0.03621	Scaling of thermal conductivity of the simplified bellow (compare equation 8.4)

settings are listed in table A.1. In addition the radiative heat exchange between the inner surface and the ambient was defined to be zero. This is comparable to a closed system, such as the CPS cryostat.

Figure A.2 shows the temperature distribution and the radiation profile. The asymmetry in the simplified model is due to lighting effects of COMSOL Multiphysics graphical output and not a physical effect.

Figure A.3a shows the temperature distribution along the bellow in comparison to its simplification. As expected, the temperature gradient fits very well. The maximum deviation is about 5.5 K, which is located in the lower (colder) third of the curved part. The deviations in temperature at the beginning and at the end of the curved part are less than 1 K.

Figure A.3b shows a plot ot the thermal irradiation on the disc for both geometries. The radiative power is plotted as a function of the radius of the analysing disc, since the geometry is axial symmetric. By integrating the irradiation over the whole surface of the analysing disc the overall radiation from the inside of the bellow, and its simplification can be determined. In numbers, there is an outgoing radiative power of 0.26 W from the bellow and 0.24 W from its simplification in this particular simulation. This leads to a deviation of less than 8%.

This simulation shows that bellows can be approximated by simple tubes, if the physical properties, especially the thermal conductance, are adjusted. Simplifying bellows reduces significantly the calculation time, since fewer mesh elements are required for the finite element simulation. The number of mesh elements in the simulation presented here was reduced by a factor of 6 for the 2D axial symmetric model. In a real 3D model this factor will increase significantly up to 150. The simulation of the approximated bellow reduced the computation time by nearly 90%.

(a) Temperature of bellow in K.

(b) Radiation of bellow in W/m^2.

(c) Temperature of simplification in K.

(d) Radiation of simplification in W/m^2.
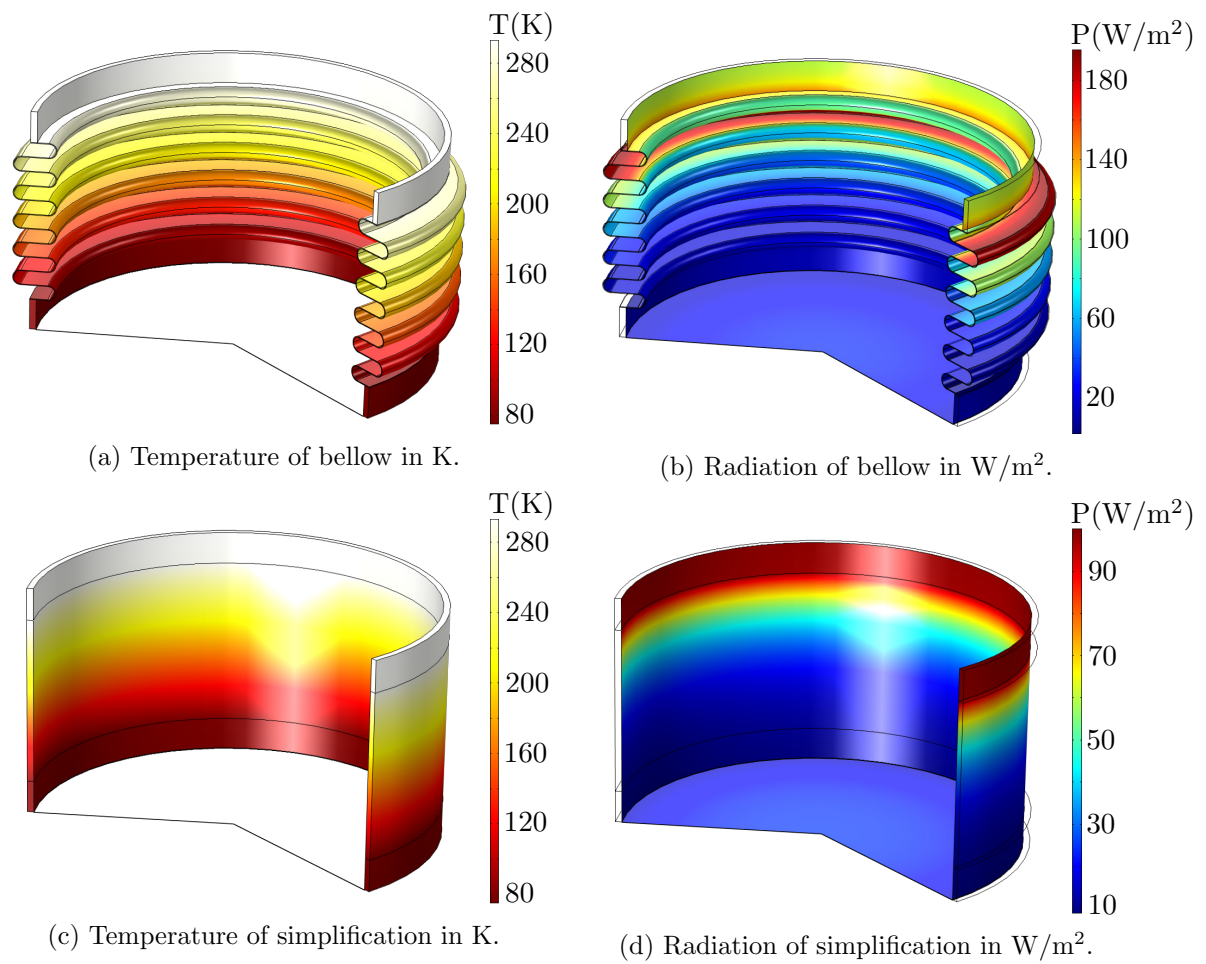
Figure A.2.: Results of the thermal simulation of a bellow. The temperature gradient (in K) is shown on the left side, with the bellow on top (A.2a) and its simplification on bottom (A.2c). The radiation (in W/m^2) is shown on the right, again with the bellow on top (A.2b) and the simplified bellow on bottom (A.2d). The analysing disc can be seen on the radiation images.
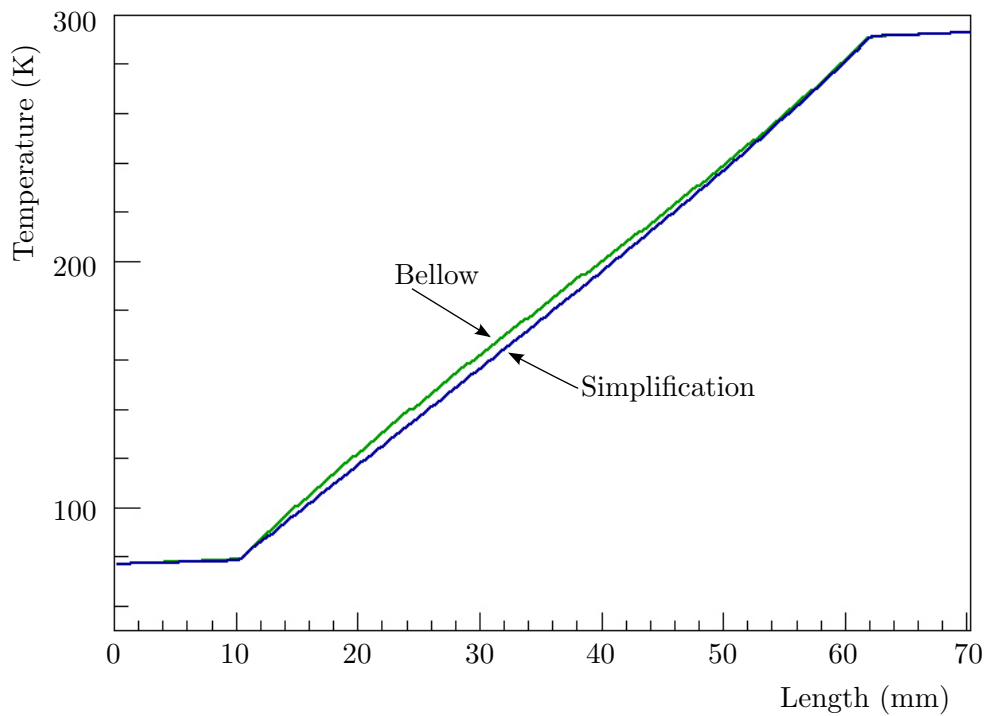
(a) Temperature gradient.
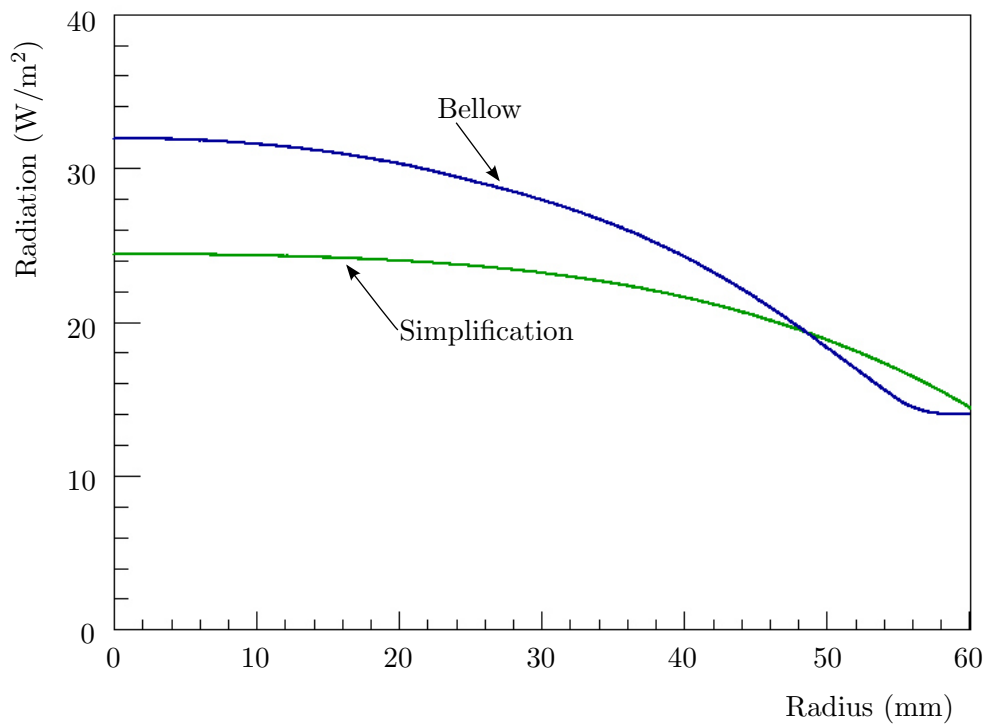
(b) Irradiation on the analysing disc.

Figure A.3.: Plotted results of the thermal simulation of a bellow. The temperature gradient in K along the length of the bellow and its simplification, respectively, is shown on top, and the irradiation in W/m^2 onto the analysing disc is shown on bottom.

B. Technical data of the instrumentation used in the test-stands

Technische Daten

Produkt: TURBOVAC SL 300
Katalog-Nr.:   800170V3006

Anschlussflansch Saugseite:	DN 100 CF	
Anschlussflansch Druckseite:	DN 16 ISO-KF	
Saugvermögen		
N_2 - Stickstoff:	270 l/s	
Ar - Argon:	260 l/s	
He - Helium:	255 l/s	
H_2 - Wasserstoff:	190 l/s	
Gasdurchsatz		
N_2 - Stickstoff:	2,9 mbar x l/s	
Ar - Argon:	2,0 mbar x l/s	
He - Helium:	1,9 mbar x l/s	
H_2 - Wasserstoff:	0,9 mbar x l/s	
Kompressionsverhältnis		
N_2 - Stickstoff:	$> 1,0 \times 10^{11}$	
Ar - Argon:	$> 1,0 \times 10^{11}$	
He - Helium:	$1,0 \times 10^{7}$	
H_2 - Wasserstoff:	$2,0 \times 10^{5}$	
Enddruck:	$< 1,0 \times 10^{-10}$ mbar	$< 7,5 \times 10^{-11}$ Torr
Max. Vorvakuumdruck für N_2 :	8,0 mbar	6,0 Torr
Nenndrehzahl:	$60000 \ \text{min}^{-1}$	60000 rpm
Hochlaufzeit:	$\approx 4,0$ min	
Max. Leistungsaufnahme:	115 W	
Leistungsaufnahme bei Enddruck:	18 W	
Schutzart:	IP 20	
Zulässige Umgebungstemperatur:	15 - 45°C	59 - 113°F
Kühlung standard:	Konvektion	
Kühlung optional:	Luft / Wasser	
Kühlwasseranschluss:	G 1/8", Innengewinde / 8 mm Schlauchwelle	
Kühlwasserverbrauch:	30 - 60 l/h	
Zulässiger Kühlwasserdruck:	3 - 7 bar	
Zulässige Kühlwassertemperatur:	15 - 35°C	59 - 95°F
Abmessungen:	siehe Maßblatt	
Gewicht:	$\approx 7,4$ kg	$\approx 16,3$ lbs

Technische Änderungen vorbehalten

Figure B.4.: Technical data sheet for the Leybold Turbovac SL 300. Taken from [174].

Technische Daten

Produkt: SCROLLVAC SC 15 D
Katalog-Nr.:   133001

Anschlussflansch Saugseite:	DN 25 ISO-KF	
Anschlussflansch Druckseite:	DN 16 ISO-KF	
Nennsaugvermögen bei 50 Hz:	15,0 m^3/h	8,8 cfm
Nennsaugvermögen bei 60 Hz:	18,0 m^3/h	10,6 cfm
Saugvermögen bei 50 Hz:	13,0 m^3/h	7,7 cfm
Saugvermögen bei 60 Hz:	15,5 m^3/h	9,1 cfm
Endtotaldruck ohne Spülgas:	1,6 x 10^{-2} mbar	1,2 x 10^{-2} Torr
Endtotaldruck mit Spülgas:	1,6 x 10^{-2} mbar	1,2 x 10^{-2} Torr
Wasserdampfverträglichkeit bei 50/60 Hz:	0,11 mbar	0,08 Torr
Wasserdampfkapazität bei 50/60 Hz:	1,04 g/h	
Spülgasmenge:	10 l/min	
Schallpegel nach DIN 45 635		
ohne Spülgas:	≤ 58 dB(A)	
mit Spülgas:	≤ 66 dB(A)	
Leckrate:	1,0 x 10^{-6} mbar l/s	
Netzanschluss:	1-ph, 200-230 V, 50/60 Hz	
Motorleistung:	400 W	0,54 HP
Motordrehzahl bei 50 Hz:	1.450 min^{-1}	1.450 rpm
Motordrehzahl bei 60 Hz:	1.730 min^{-1}	1.730 rpm
Motorschutzart:	IP 20	
Zulässige Umgebungstemperatur:	+5 bis +40°C	+41 bis +104°F
Abmessungen:	siehe Maßblatt	
Gewicht:	25,0 kg	55,2 lbs

Technische Änderungen vorbehalten

Figure B.5.: Technical data sheet for the Leybold Scrollvac SC 15 D. Taken from [175]

Specifications and Ordering Information

Configuration	Absolute, single-ended
Full Scale Ranges	1 Torr through 25,000 Torr (mmHg) (0.02 psia through 500 psia)
Accuracy (including non-linearity, hysteresis, and non-repeatability)	0.5% of Reading
Response Time	< 20 msec
Temperature Coefficients	
Zero	0.008% of F.S./°C (10 Torr through 25,000 Torr); 0.020% of F.S. (1 and 2 Torr)
Span	0.04% of Rdg./°C
Ambient Operating Temperature	0° to 50°C (32° to 122°F), 15° to 40°C (59° to 104°F) (1 and 2 Torr only)
Overpressure Limit	45 psia or 2x F.S., whichever is greater
Burst Pressure	10x F.S. or 100 psi, whichever is greater
Materials Exposed to Gases	Inconel® (Optional Fittings: 316SS)
Power	
Input	0 to 10 Volt output, +13 VDC to +32 VDC @ 10 mA max. (For drop-in replacements of 122A and B which have a ±15 VDC input, use Input/Output Ordering Code 2. See below.)
	0 to 5 Volt output, +10.8 VDC to +32 VDC @ 10 mA max (regulated if below 13 VDC)
Output	0 to 10 VDC into > 10K ohms load
	0 to 5 VDC into > 10K ohms load
Electromagnetic Compatibility	Fully compliant to EMC Directive 2004/108/EC[1]
Restriction of Hazardous Substances	Fully compliant to RoHS Directive 2002-95-EC
Electrical Connectors	9-pin Type "D", 15-pin high density Type "D", 15-pin Type "D" on 4.70" (118mm) ±0.5" (12.7mm) cable, 4-pin bayonet type, Bendix® -compatible, 5-pin terminal strip
Fittings	
Standard	½" tube
Optional	¼" VCR® female, 8 VCR female, NW 16 KF[2], mini-CF

[1] For CE Compliance, an overall metal braided shielded cable, properly grounded at both ends, is required.
[2] NW 16 KF fittings cannot be used on units with a pressure range of 10,000 mmHg and higher.
For units with a pressure range of 5,000 mmHg, an HPS Overpressure ring must be used.

Dimensional Drawing —
Note: Unless otherwise specified, dimensions are nominal values in inches (mm referenced).

LOW CAPACITANCE MANOMETER PRESSURE UP TO 1000 TORR

HIGH CAPACITANCE MANOMETER > 1000 TORR THROUGH 25,000 TORR

Ordering Code Example: 722B12TCE2FJ

Type 722B	Code	Configuration
Type 722B	722B	722B
Pressure Range Full Scale (mmHg)		
1	01T	
2	02T	
10	11T	
20	21T	
30	31T	
50	51T	
100	12T	
250	RDT	12T
500	52T	
1,000	13T	
2,000 (must be ordered with a fitting)	23T	
5,000 (must be ordered with a fitting other than NW16KF)	53T	
10,000 (must be ordered with a fitting other than NW16KF)	14T	
20,000 (must be ordered with a fitting other than NW16KF)	24T	
25,000 (must be ordered with a fitting other than NW16KF)	RCT	
Fittings		
¼" VCR Female	CD	
½" Tube	BA	
8 VCR female	CE	CE
Mini-CF, rotable	HA	
NW 16 KF	GA	
Input/Output		
+13 to +32 VDC/0-10 VDC	2	2
+13 to +32 VDC/0-5 VDC	3	
Accuracy		
0.5% of Reading	F	F
Connectors		
9-pin Type "D"	A	
15-pin high density Type "D"	C	
4-pin bayonet type, Bendix® -compatible	D	J
5-pin terminal strip	J	
15-pin Type "D" on 6-inch cable	K	
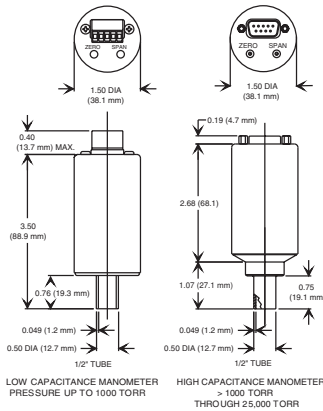
MKS Global Headquarters

2 Tech Drive, Suite 201
Andover, MA 01810

Tel: 978.645.5500
Tel: 800.227.8766 (in U.S.A.)
Web: www.mksinst.com

722B_RoHS - 8/12
© 2009 MKS Instruments, Inc.
All rights reserved.

Some Baratron® products may not be exported to many end user countries without both US and local government export licenses under ECCN 2B230.

Specifications are subject to change without notice. Baratron® is a registered trademark of MKS Instruments, Inc., Andover, MA. VCR® is a registered trademark of Swagelok® Co., Solon OH. Inconel® is a registered trademark of Inco Alloys International, Inc., Huntington, WV. Bendix® is a registered trademark of Amphenol Corp., Bendix Connector Operations, Sydney, NY.

Figure B.6.: Fraction of the technical data sheet for the mks Baratron 722 B. Taken from [180].

Specifications and Ordering Information

Full Scale Ranges	0.02, 0.05, 0.1, 1, 2, 10, 20, 100, 1000, 2000, 5000, 10000, 15 000, 20000, 25000 Torr
Resolution	0.001% of F.S. (0.002% of F.S. for 0.02 and 0.05 Torr)
Accuracy	0.12% of Reading (including non-linearity, hysteresis, and non-repeatability), 0.15% for 0.1 and 0.05 Torr, 0.25% for 0.02 Torr
Temperature Coefficients	
Zero	0.002% of F.S./°C for 1 - 25000 Torr range; 0.005% F.S./°C for 0.1 Torr, 0.015% F.S./°C for 0.05 Torr, 0.03% F.S./°C for 0.02 Torr
Span	0.02% of Rdg./°C
Ambient Operating Temperature	15°C to 40°C
Volume	6.3 cc
Warm-Up Time	2 hours for 25000 Torr F.S., 4 hours for 0.1 Torr F.S. and lower
Overpressure Limit	45 psia (310 kPa) or 120% F.S., whichever is greater
Materials Exposed to Gases	Inconel®
Input Power Required	±15 VDC ±5% @ 0.25 Amps (max.)
Output Signal	Pressure: 0 to +10 VDC into >10K Ω load
Optional Features LED's and Switches	Temperature status: one semiconductor switch will turn "ON" and corresponding green LED will be "ON" when the instrument is at temperature. Heater status: second semiconductor switch will turn "OFF" when heater failure occurs and corresponding bi-color LED will be blinking red, otherwise light will remain green.
Electromagnetic Compatibility	Fully CE Compliant to EMC Directive 89/336/EEC
Fittings	Optional: 8 VCR® female, NW 16 KF, Mini-CF

Specifications for Semiconductor Switch

Current Charge Capacity	120mA max.
Switch on Resistance	20 Ω max. @ 120mA, 50°C
Open Circuit Voltage	28V max.
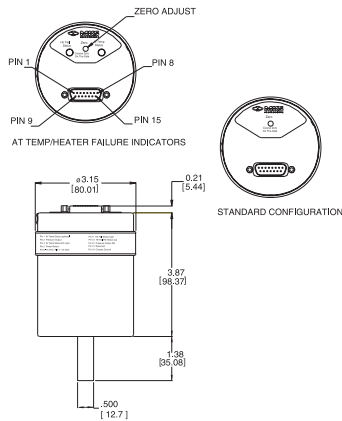
Ordering Code Example: 627B01TBC1B	Code	Configuration
Type 627B	627B	627B
Pressure Range Full Scale		
0.02	U2T	
0.05	U5T	
0.1	.1T	
1	01T	
2	02T	
10	11T	
20	21T	
100	12T	01T
1000	13T	
2000	23T	
5000	53T	
10000	14T	
15000	RBT	
20000	24T	
25000	RCT	
Fittings		
8 VCR female	B	
Mini-CF, rotable (pressure limited to bolt strength)	C	B
NW 16KF (only for 5000T or lower)	D	
Accuracy		
0.12% of Reading	C	
0.15% of Reading	D	C
0.25% of Reading	E	
Options		
Standard Configuration	1	
Optional Temperature/Heater Status	2	1
Connector		
15 pin Type "D" with Thread Lock	B	
15 pin Type "D" with Slide Lock	P	B

Dimensional Drawing —

Note: Unless otherwise specified, dimensions are nominal values in inches (mm referenced).

ZERO ADJUST

PIN 1   PIN 8
PIN 9   PIN 15

AT TEMP/HEATER FAILURE INDICATORS

STANDARD CONFIGURATION

⌀3.15 [80.01]   0.21 [5.44]

3.87 [98.37]

1.38 [35.08]

.500 [12.7]

∴∴mks

Technology for Productivity

Bulletin 627B - 08/02
© 2002 MKS Instruments, Inc.
All rights reserved.

Global Headquarters

90 Industrial Way
Wilmington, MA 01887-4610

Tel: 978.284.4000
Tel: 800.227.8766 within U.S. only
Web: www.mksinst.com

Specifications are subject to change without notice.
Baratron® is a registered trademark of MKS Instruments, Inc., Wilmington, MA.
VCR® is a registered trademark of Swagelok® Co., Solon OH.
Inconel® is a registered trademark of Inco Alloys International, Inc., Huntington, WV.

Figure B.7.: Fraction of the technical data sheet for the mks Baratron 627 B. Taken from [181].

HPT 200, DN 40 CF-F, RS-485, Profibus

- 5 · 10⁻¹⁰ to 1000 hPa
- High security by two filaments
- High accuracy
- Profibus DP Interface (optional)
- Analog output and set points (optional)

PB = additionally with Profibus-DP interface

AR = additionally with analogue output and two switch-points

Similar Image

Dimensions

145

66   45   Ø 70
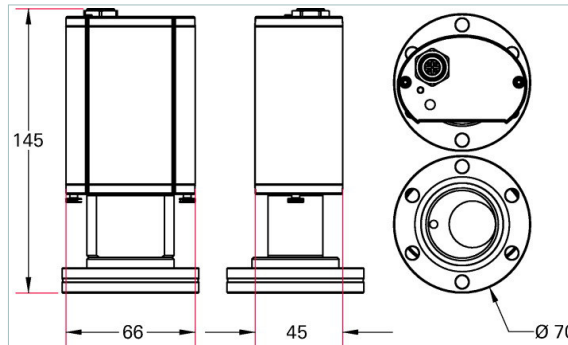
DN 1   DN 40 CF-F

Technical Data	HPT 200, DN 40 CF-F, RS-485, Profibus
Accuracy: % of measurement	1 · 10⁻⁸ – 1 hPa: ± 10 %, 20 – 1000 hPa: ± 30 %
Bakeout temperature max. at the flange	180 °C | 356 °F | 453 K
Filament	Iridium yttriated, twice
Flange (in)	DN 40 CF-F
Interface: Connection	Digital RS-485, M12 f, 5-pole, Profibus DP, M12 f, 5-pole
Materials in contact with media	Tungsten, stainless steel, nickel, glass, ceramics
Measurement range max.	1,000 hPa | 750 Torr | 1,000 mbar
Measurement range min.	5 · 10⁻¹⁰ hPa | 3.75 · 10⁻¹⁰ Torr | 5 · 10⁻¹⁰ mbar
Measuring cycle	10 ms
Method of measurement	Pirani/Bayard-Alpert
Number of filaments	2
Pressure max.	4,000 hPa | 3,000 Torr | 4,000 mbar
Protection category	IP 54
Repeatability: % of measurement	1 · 10⁻⁸ – 1 · 10⁻² hPa: ± 5%; 1 · 10⁻² – 10 hPa: ± 2 %
Seal	Metal
Sensor cable length max.	100 m
Supply: Voltage	24 V DC
Temperature: Operating	5-60 °C | 41-140 °F | 278-333 K
Temperature: Storage	-40-65 °C | -40-149 °F | 233-338 K
Weight	670 g

Order number	
Pirani/Bayard-Alpert combination HPT 200 (5 · 10⁻¹⁰ – 1000 hPa)	**PT R39 352**

Figure B.8.: Fraction of the technical data sheet for the Pfeiffer HPT 200. Taken from [182].

C. CPS argon capillary drawings
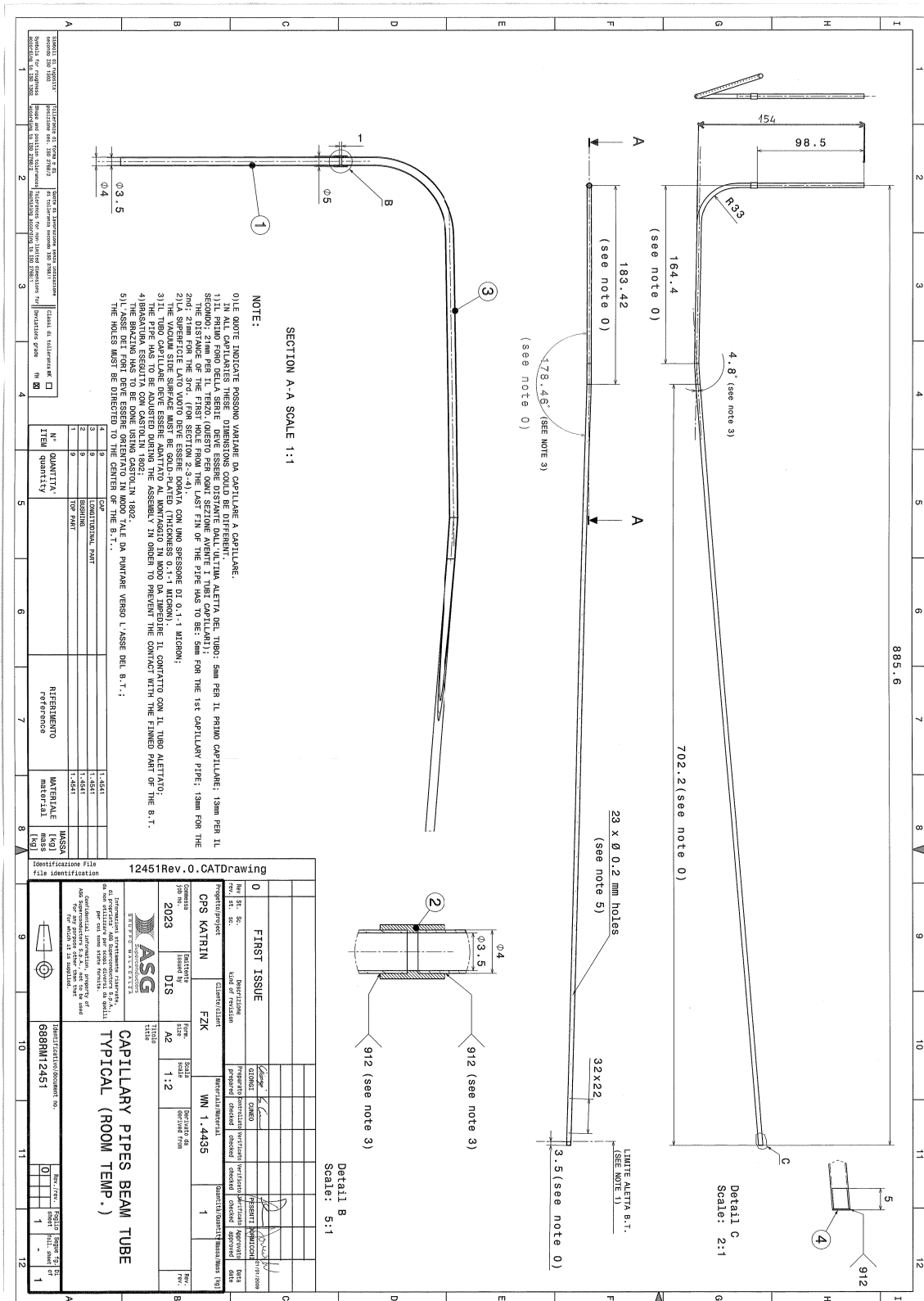
Figure C.9.: Technical drawing (by ASG) of the argon capillaries.

Figure C.10.: Technical drawing (by ASG) of the argon capillary feedthrough.

Table D.2.: CPS modes of operation. Given are the internal components of the CPS with the corresponding temperatures in K. Taken from [118].

Component	Bake-Out	Cool-Down	Argon-Preparation	Standby	Standard Operation	Regeneration	Warm-Up	CKrS Calibration
Outer Radiation Shield	300±20	300→77	77+5	77+5	77+5	77+5	77→300	77+5
Solenoids	300±20	300→4.5	4.5±0.1	4.5±0.1	4.5±0.1	4.5±0.1	4.5→300	4.5±0.1
Beam Tube Section 1	500±20	300→77	77+10	77+10	77+10	> 100	77→300	77+10
Pump Port 1	500±20	300→77	77+10	77+10	77+10	> 100	77→300	77+10
Beam Tube Sections 2-5	500±20	300→4.5	6±1	3.0-3.5	3.0-3.5	3→100	> 100→300	3.0-3.5
Inner Argon Gas Injection Capillaries	500±20	300→4.5	> 40	3.5	3.5	3→100	> 100→300	3.5
Cold Gate Valve Body	500±20	300→4.5	4.5±0.1	4.5±0.1	4.5±0.1	4.5→100	> 100→300	4.5±0.1
Beam Tube Section 6	620±20 (24 h)	300→77	77+10	77+10	77+10	77+10	77→300	77+10
Pump Port 2	< 620	300→77	77+10	77+10	77+10	77+10	77→300	77+10
Beam Tube Section 7	620±20 (24 h)	300	300	300±20	300±20	300	300	77+10
Inner Radiation Shield	300-400	300→77	77+5	77+5	77+5	77+5	77→300	77+5

E. Vapour pressure of cryogenic liquids

Table E.3.: Vapour pressure of ^{4}He. Data taken from [141].

^{4}He (K)	Pressure (mbar)	^{4}He (K)	Pressure (mbar)	^{4}He (K)	Pressure (mbar)
4.507	1300	3.524	480	2.890	200
4.416	1200	3.489	450	2.858	190
4.319	1100	3.452	440	2.825	180
4.269	1050	3.415	420	2.791	170
4.230	**1013.25**	3.377	400	2.755	160
4.216	1000	3.337	380	2.718	150
4.162	950	3.295	360	2.679	140
4.106	900	3.252	340	2.638	130
4.048	850	3.208	320	2.594	120
3.988	800	3.161	300	2.549	110
3.925	750	3.137	290	2.500	100
3.859	700	3.112	280	2.448	90
3.790	650	3.087	270	2.392	80
3.717	600	3.061	260	2.331	70
3.687	580	3.035	250	2.298	65
3.656	560	**3.008**	**240**	2.263	60
3.624	540	2.979	230	2.227	55
3.591	520	2.951	220	2.087	40
3.558	500	2.921	210		

Table E.4.: Vapour pressure of Argon. Data taken from [141], based on [183] (between 1013.25 K and 83.945 K), and from [59], based on [144] (below 83.945 K).

Ar (K)	Pressure (mbar)	Ar (K)	Pressure (mbar)	Ar (K)	Pressure (mbar)
87.302	**1013.25**	61.300	1.0E+01	26.600	1.0E-08
87.178	1.0E+03	53.500	1.0E+00	25.000	1.0E-09
86.696	9.5E+02	47.500	1.0E-01	23.500	1.0E-10
86.195	9.0E+02	42.700	1.0E-02	22.400	1.0E-11
85.672	8.5E+02	38.800	1.0E-03	21.200	1.0E-12
85.124	8.0E+02	35.400	1.0E-04	20.200	1.0E-13
84.550	7.5E+02	32.800	1.0E-05	19.300	1.0E-14
83.945	7.0E+02	30.300	1.0E-06		
71.700	1.0E+02	28.400	1.0E-07		

F. Wiring diagram of pulse generator
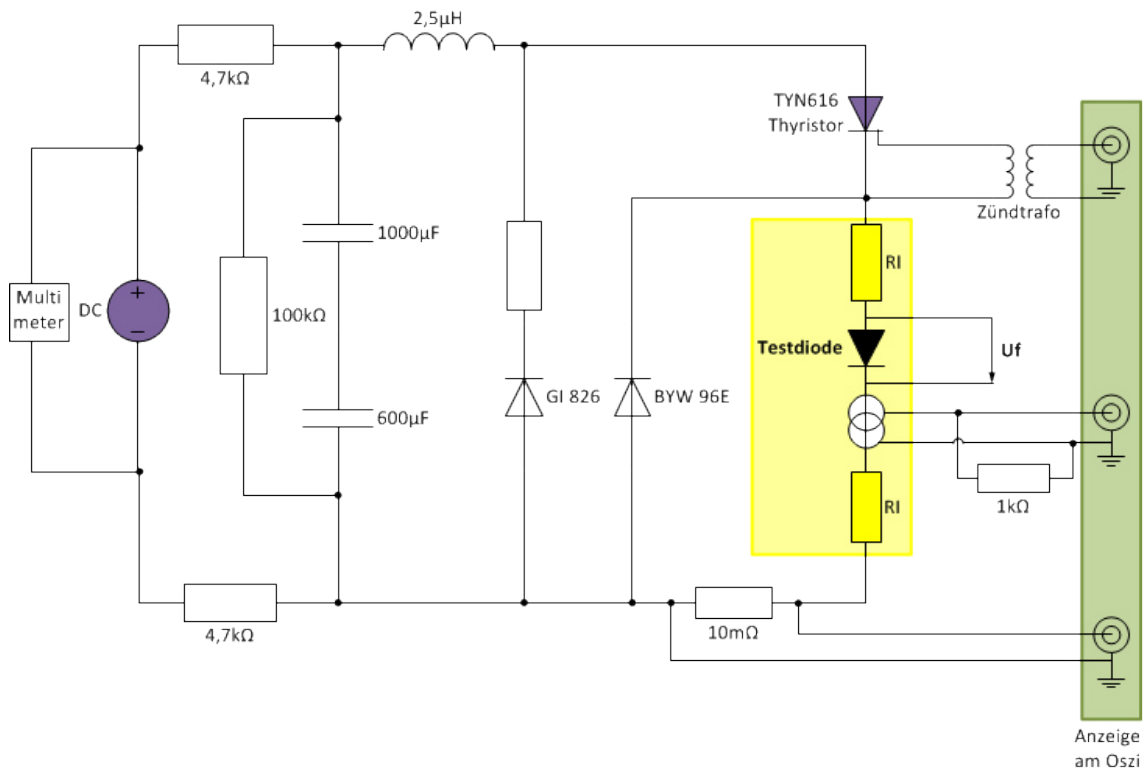
Figure F.11.: Current pulse generator used for the characterisation tests of the CPS bypass diode stacks.

G. Thermal conductance of solid/solid interfaces
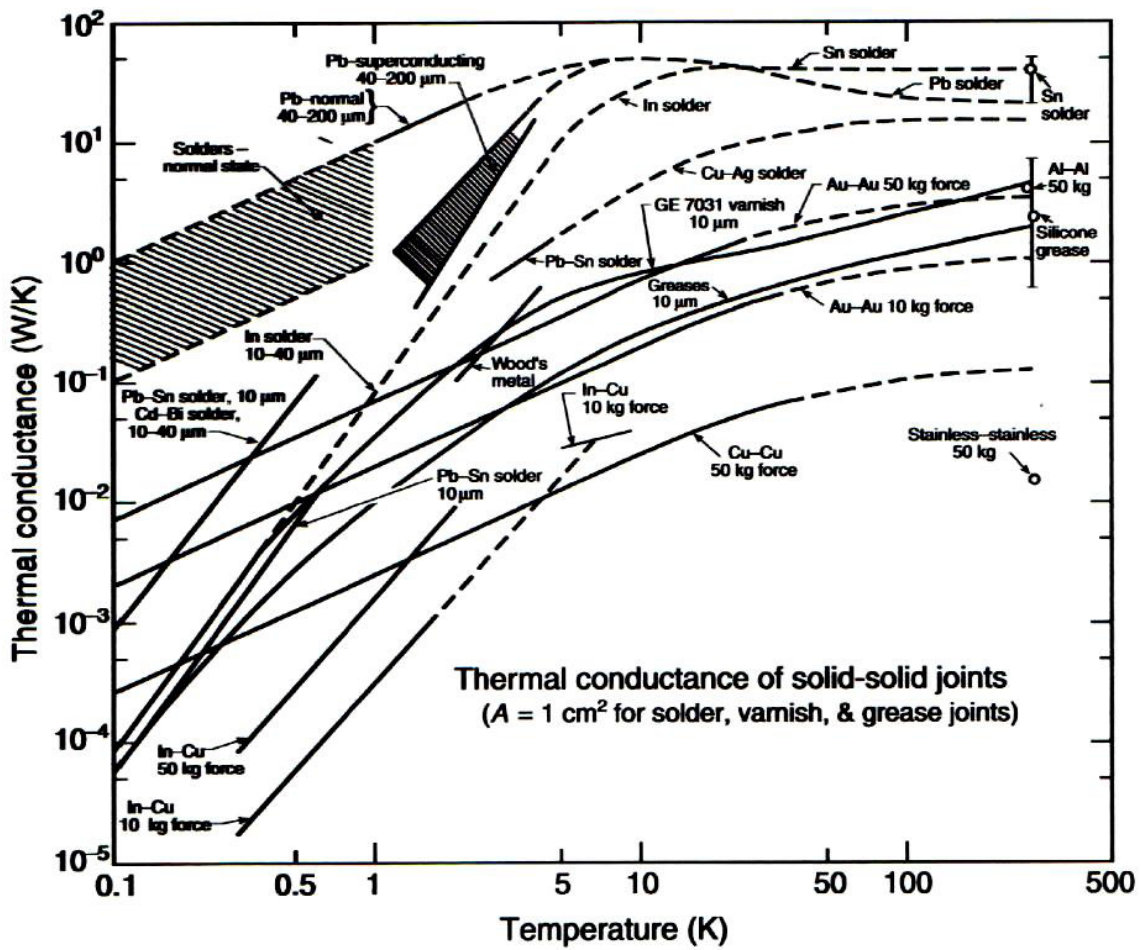
Figure G.12.: Thermal conductance for solid/solid interfaces. Taken from [141].

Bibliography

[1] KATRIN Collaboration. KATRIN Design Report. 2004.

[2] W. Pauli. Offener Brief an die Gruppe der Radioaktiven bei der Gauvereins-Tagung zu Tübingen. 4. Dezember 1930.

[3] E. Fermi. Versuch einer Theorie der β-Strahlen. *Zeitschrift für Physik*, 88:161–177, 1934.

[4] F. Reines and C. Cowan. Detection of the Free Neutrino. *Phys. Rev.*, 92:830–831, 1953.

[5] G. Danby, J-M. Gaillard, K. Goulianos, L. M. Lederman, N. Mistry, M. Schwartz, and J. Steinberger. Observation of high-energy neutrino reactions and the existence of two kinds of neutrinos. *Physical Review Letters*, 9, 1962.

[6] K. Kodama et al. Observation of tau neutrino interactions. *Physics Letters B*, 504 (3):218 – 224, 2001.

[7] K. Bethge and U. E. Schröder. *Elementarteilchen und ihre Wechselwirkungen.* WILEY-VCH, third edition, 2006.

[8] K.A. Olive et al. (Particle Data Group). Review of particle physics. *Chinese Physics C*, 38, 2014.

[9] J. Lesgourgues and S. Pastor. Massive neutrinos and cosmology. *Phys.Rept.*, 429: 307–379, 2006.

[10] W. D. Apel et al. The KASCADE-Grande experiment. *Nuclear Instruments and Methods in Physics Research Section A*, 620(2-3):202–216, 2010.

[11] D. Zavrtanik. The Pierre Auger observatory. *Nuclear Physics B - Proceedings Supplements*, 85(1-3):324–331, 2000.

[12] K. Hirata, T. Kajita, M. Koshiba, M. Nakahata, Y. Oyama, N. Sato, A. Suzuki, M. Takita, Y. Totsuka, T. Kifune, T. Suda, K. Takahashi, T. Tanimori, K. Miyano, M. Yamada, E. Beier, L. Feldscher, S. Kim, A. Mann, F. Newcomer, R. Van, W. Zhang, and B. Cortez. Observation of a neutrino burst from the supernova SN1987A. *Phys. Rev. Lett.*, 58:1490–1493, 1987.

[13] Raymond Davis, Don Harmer, and Kenneth Hoffman. Search for Neutrinos from the Sun. *Phys. Rev. Lett.*, 20:1205–1209, 1968.

[14] John Bahcall. Solar Neutrino Cross Sections and Nuclear Beta Decay. *Phys. Rev.*, 135:B137–B146, 1964.

[15] John Bahcall. Solar Neutrinos. I. Theoretical. *Phys. Rev. Lett.*, 12:300–302, 1964.

[16] J. N. Bahcall and R. Davis. Solar Neutrinos: A Scientific Puzzle. *Science*, 191: 264–267, 1976.

[17] GALLEX Collaboration. GALLEX solar neutrino observations: results for GALLEX IV. *Physics Letters B*, 447(1):127–133, 1999.

[18] J. N. Abdurashitov et al. Solar neutrino flux measurements by the Soviet-American Gallium Experiment (SAGE) for half the 22-year solar cycle. *Journal of Experimental and Theoretical Physics*, 95:181–193, 2002.

[19] GNO Collaboration. Complete results for five years of GNO solar neutrino observations. *Physics Letters B*, 616(3 - 4):174 – 190, 2005.

[20] Y. Fukuda et al. Solar Neutrino Data Covering Solar Cycle 22. *Phys. Rev. Lett.*, 77:1683–1686, 1996.

[21] Y. Fukuda et al. Measurements of the Solar Neutrino Flux from Super-Kamiokande's First 300 Days. *Phys. Rev. Lett.*, 81:1158–1162, 1998.

[22] Q. R. Ahmad et al. Measurement of the Rate of $\nu_e + D \rightarrow p + p + e^-$ Interactions Produced by ^8B Solar Neutrinos at the Sudbury Neutrino Observatory. *Phys. Rev. Lett.*, 87:071301, 2001.

[23] Q. R. Ahmad et al. Direct Evidence for Neutrino Flavor Transformation from Neutral-Current Interactions in the Sudbury Neutrino Observatory. *Phys. Rev. Lett.*, 89:011301, 2002.

[24] Y. Fukuda et al. Evidence for Oscillation of Atmospheric Neutrinos. *Phys. Rev. Lett.*, 81:1562–1567, 1998.

[25] K. Zuber. *Neutrino Physics*. CRC Press, second edition, 2011.

[26] A. Yu. Smirnov. The MSW effect and Matter Effects in Neutrino Oscillations. *Physica Scripta*, 2005:57–64, 2004.

[27] S. Abe et al. Precision Measurement of Neutrino Oscillation Parameters with KamLAND. *Phys. Rev. Lett.*, 100:221803, 2008.

[28] F. P. An et al. Observation of Electron-Antineutrino Disappearance at Daya Bay. *Phys. Rev. Lett.*, 108:171803, 2012.

[29] J. K. Ahn et al. Observation of Reactor Electron Antineutrinos Disappearance in the RENO Experiment. *Phys. Rev. Lett.*, 108:191802, 2012.

[30] Y. Abe et al. Indication of Reactor $\overline{\nu}_e$ Disappearance in the Double Chooz Experiment. *Phys. Rev. Lett.*, 108:131801, 2012.

[31] P. Adamson et al. Improved Measurement of Muon Antineutrino Disappearance in MINOS. *Phys. Rev. Lett.*, 108:191801, 2012.

[32] K. Abe et al. First muon-neutrino disappearance study with an off-axis beam. *Phys. Rev. D*, 85:031103.

[33] D. J. Fixsen. The temperature of the Cosmic Microwave Background. *ApJ 709*, 2009.

[34] A. A. Penzias and R. W. Wilson. A Measurement of Excess Antenna Temperature at 4080 Mc/s. *Astrophysical Journal*, 142:419–421, 1965.

[35] Planck Collaboration. Planck 2013 results. XVI. Cosmological parameters. *Astronomy & Astrophysics*, 571, 2014.

[36] Steen Hannestad. Neutrino physics from precision cosmology. *Progress in Particle and Nuclear Physics*, 65:185–208, 2010.

[37] S. Schoenert et al. GERDA - The GERmanium Detector Array for the search of neutrinoless $\beta\beta$ decays of ^{76}Ge at LNGS. *Nuclear Physics B - Proceedings Supplements*, 145:242–245, 2005.

[38] M. Auger et al. Search for Neutrinoless Double-Beta Decay in ^{136}Xe with EXO-200. *Phys. Rev. Lett.*, 109:032505, 2012.

[39] M. Agostini et al. Results on Neutrinoless Double-β Decay of ^{76}Ge from Phase I of the GERDA Experiment. *Phys. Rev. Lett.*, 111:122503, 2013.

[40] V. N. Aseev, A. I. Belesev, A. I. Berlev, E.V. Geraskin, A. A. Golubev, N. A. Likhovid, V. M. Lobashev, A. A. Nozik, V. S. Pantuev, V. I. Parfenov, A. K. Skasyrskaya, F.V. Tkachov, and S.V. Zadorozhny. Upper limit on the electron antineutrino mass from the Troitsk experiment. *Physical Review D*, 84, 2011.

[41] K. Assamagan, Ch. Brönnimann, M. Daum, H. Forrer, R. Frosch, P. Gheno, R. Horisberger, M. Janousch, P. Kettle, Th. Spirig, and C. Wigger. Upper limit of the muon-neutrino mass and charged-pion mass from momentum analysis of a surface muon beam. *Phys. Rev. D*, 53:6065–6077, 1996.

[42] R. Barate et al. ALEPH Collaboration. An Upper limit on the tau-neutrino mass from three-prong and five-prong tau decays. *Eurupean Physical Journal C2*, pages 395–406, 1998.

[43] Ch. Kraus, B. Bornschein, L. Bornschein, J. Bonn, B. Flatt, A. Kovalik, B. Ostrick, E.W. Otten, J.P. Schall, Th. Thümmler, and Ch. Weinheimer. Final results from phase II of the Mainz neutrino mass search in tritium β decay. *The European Physical Journal C*, 40:447–468, 2005.

[44] Guido Altarelli and Klaus Winter. *Neutrino Mass*. Springer, 2003.

[45] Stefan Goerhardt. *Background Reduction Methods and Vacuum Technology at the KATRIN Spectrometers*. Phd thesis, Karlsruhe Institute of Technology, 2014.

[46] M. Babutzka, M. Bahr, .J Bonn, B. Bornschein, A. Dieter, G. Drexlin, K. Eitel, S. Fischer, F. Glück, S. Grohmann, M. Hoetzel, T. M. James, W. Kaefer, M. Leber, B. Monreal, F. Priester, M. Roellig, M. Schlösser, U. Schmitt, F. Sharipov, M. Steidl, M. Sturm, H. H. Telle, and N. Titov. Monitoring of the operating parameters of the KATRIN Windowless Gaseous Tritium Source. *New Journal of Physics*, 14, 2012.

[47] Michael Sturm. *Aufbau und Test des Inner-Loop-Systems der Tritiumquelle von KATRIN*. Phd thesis, Karlsruhe Institute of Technology, 2010.

[48] Laura Kuckert. *Simulation of the KATRIN tritium source and first measurements with the windowless gaseous tritium sourse (WGTS)*. Ongoing phd thesis, Karlsruhe Institute of Technology.

[49] Markus Hötzel. *Simulation and analysis of source-related effects for KATRIN*. Phd thesis, Karlsruhe Institute of Technology, 2012.

[50] S. Grohmann. Stability analyses of the beam tube cooling system in the KATRIN source cryostat. *Cryogenics*, 49:413–420, 2009.

[51] S. Grohmann. A new method for flow measurement in cryogenic systems. *Cryogenics*, 60:9–18, 2014.

[52] S. Grohmann, T-Bode, H. Schoen, and M. Suesser. Precise temperature measurement at 30 K in the KATRIN source cryostat. *Cryogenics*, 51:438–445, 2011.

[53] S. Grohmann. Demonstrator test results, 2011. 20th KATRIN Collaboration Meeting, Internal Talk.

[54] F. Glück. Positive ions and dipole electrodes in DPS2-F, 2007. Institute for Nuclear Physics, Karlsruhe Institut of Technology, Internal Talk.

[55] F. Glück. Tritium ion concentrations in WGTS and transport system, 2010. Internal Report.

[56] F. Glück. Electrons and ions in KATRIN STS, 2010. Internal Talk.

[57] F. Glück. Background from positive ions, 2006. Internal Talk.

[58] E. Cavanna, S. Cuneo, O. Dormicchi, G. Drago, L. Giorgi, G. Murru, and M. Tassisto. KATRIN CPS - TDR. Technical design report, ASG Superconductors GRUPPO MALACALZA, 2009.

[59] R.A. Haefer. *Kryo-Vakuumtechnik*. Springer, 1981.

[60] Florian Habermehl. *Electromagnetic measurements with the KATRIN pre-spectrometer*. Phd thesis, Karlsruhe Institute of Technology, 2009.

[61] G. Drexlin, V. Hannen, S. Mertens, and C. Weinheimer. Current Direct Neutrino Mass Experiments. *Advances in High Energy Physics*, 2013, 2013.

[62] Florian M. Fraenkle. *Background Investigations of the KATRIN Pre-Spectrometer*. Phd thesis, Karlsruhe Institute of Technology, 2010.

[63] Susanne Mertens. *Study of Background Processes in the Electrostatic Spectrometers of the KATRIN Experiment*. Phd thesis, Karlsruhe Institute of Technology, 2012.

[64] N. Wandkowsky, G. Drexlin, F. M. Fraenkle, F. Glück, S. Groh, and S. Mertens. Validation of a model for radon-induced background processes in electrostatic spectrometers. *Journal of Physics G: Nuclear and Particle Physics*, 40, 2013.

[65] S. Mertens, G. Drexlin, F.M. Fraenkle, D. Furse, F. Glück, S. Goerhardt, M. Hoetzel, W. Kaefer, B. Leiber, T. Thuemmler, N. Wandkowsky, and J. Wolf. Background due to stored electrons following nuclear decays in the KATRIN spectrometers and its impact on the neutrino mass sensitivity. *Astroparticle Physics*, 41:52–62, 2013.

[66] Johannes S. Schwarz. *The Detector System of the KATRIN Experiment - Implementation and First Measurements with the Spectrometer*. Phd thesis, Karlsruhe Institute of Technology, 2014.

[67] Fabian Harms. *Assembly and First Results of the KATRIN Focal-Plane Detector System at KIT*. Diploma thesis, Institute for Experimental Nuclear Physics, Karlsruhe Institute of Technology, 2012.

[68] J. F. Amsbaugha et al. Focal-plane detector system for the KATRIN experiment. *Journal of Instrumentation*, 2014.

[69] Martin Babutzka. *Design and development for the Rearsection of the KATRIN experiment*. Phd thesis, Karlsruhe Institute of Technology, 2014.

[70] M. Schlösser, T. M. James, S. Fischer, R. J. Lewis, B. Bornschein, and H. H. Telle. Evaluation method for Raman depolarization measurements including geometrical effects and polarization aberrations. *Journal of Raman Spectroscopy*, 44:453–462, 2013.

[71] M. Schlösser, H. Seitz, S. Rupp, P. Herwig, C. G. Alecu, M. Sturm, and B. Bornschein. In-Line Calibration of Raman Systems for Analysis of Gas Mixtures of Hydrogen Isotopologues with Sub-Percent Accuracy. *Analytical Chemistry*, 85:2739–2745, 2013.

[72] Sebastian Fischer. *Laser Raman Spectroscopy for the KATRIN experiment.* Phd thesis, Karlsruhe Institute of Technology, 2014.

[73] Moritz G. Erhardt. *Untersuchung der Langzeitstabilitaet des nuklearen Standards fuer die Energieskala des KATRIN-Experiments.* Diploma thesis, Institute for Experimental Nuclear Physics, Karlsruhe Institute of Technology, 2012.

[74] Miroslav Zbořil. *Solid electron sources for the energy scale monitoring in the KATRIN experiment.* Phd thesis, Westfälische Wilhelms-Universität Münster, 2011.

[75] M. Slezák, S. Bauer, O. Dragoun, M. Erhard, K. Schlösser, S̆palek, D. Vénosb, and M. Zbořilc. Electron line shape of the KATRIN monitor spectrometer. *Journal of Instrumentation*, 8, 2013.

[76] Marco Kleesiek. *A Data-Analysis and Sensitity-Optimization Framework for the KATRIN Experiment.* Phd thesis, Karlsruhe Institute of Technology, 2014.

[77] V.N. Aseev et al. Energy loss of $18\,\mathrm{keV}$ electrons in gaseous T_2 and quench condensed D_2 films. *The European Physical Journal D*, 10:39–52, 2000.

[78] Wolfgang Kaefer. *Sensitivity Studies for the KATRIN experiment.* Phd thesis, Karlsruhe Institute of Technology, 2012.

[79] Benjamin Jung. *Simulation des Myon-induzierten Untergrundes und dessen Speicherwahrscheinlichkeit am KATRIN Hauptspektrometer.* Diploma thesis, Institute for Experimental Nuclear Physics, Karlsruhe Institute of Technology, 2011.

[80] F.M. Fraenkle, L. Bornschein, G. Drexlin, F. Glück, S. Goerhardt, W. Kaefer, S. Mertens, N. Wandkowsky, and J. Wolf. Radon induced background processes in the KATRIN pre-spectrometer. *Astroparticle Physics*, 35:128–134, 2011.

[81] Richard Bottesch. *Set-up of the motion control and characterization of the ablation laser for the condensed $^{83\mathrm{m}}$Kr conversion electron source of the KATRIN experiment.* Diploma thesis, Westfälische Wilhelms-Universität Münster, 2012.

[82] Pfeiffer Vacuum GmbH. The Vacuum Technology Book, Volume II, 2013. Band 2 - Know-how Book.

[83] Karl Jousten. *Wutz Handbuch Vakuumtechnik.* Vieweg+Teubner, 2010.

[84] John F. O'Hanlon. *A User's Guide to Vacuum Technology.* Wiley, second edition edition, 1989.

[85] Marton Ady and Roberto Kersevan. MolFlow+ user guide, 3 June 2014. Version 2.4.1.

[86] Pfeiffer Vacuum. Arbeiten mit Turbomolekularpumpen, Einführung in die Hoch- und Ultrahochvakuum-Erzeugung. 2003.

[87] Sebastian Riegel. *Die Erwärmung von Turbomolekularpumpen in verschiedenen Betriebszuständen.* Diploma thesis, Karlsruhe Institute of Technology, Institute for Experimental Nuclear Physics, 2011.

[88] Alexander Jansen. *Modellierung der Rotortemperatur von Turbomolekularpumpen in Magnetfeldern mit unterschiedlichen Gasflüssen.* Diploma thesis, Karlsruhe Institute of Technology, Institute for Experimental Nuclear Physics, 2012.

[89] Franz Dinkelacker. *Untersuchung Magnetischer Abschirmung für Turbomolekularpumpen der DPS am KATRIN-Experiment.* Bachelor thesis. Karlsruhe Institute of Technology, Institute for Experimental Nuclear Physics. 2013.

[90] Robin Groessle. *Konzeptionierung und Systematik der Hochspannungsversorgung für das KATRIN Experiment.* Diploma thesis, Karlsruhe Institute of Technology, Institute for Experimental Nuclear Physics, 2010.

[91] Jan Bondy. *Modellierung und Messung der Rotortemperatur einer Turbomolekularpumpe in einem externen Magnetfeld.* Bachelor thesis, Karlsruhe Institute of Technology, Institute for Experimental Nuclear Physics, 2013.

[92] Norio Ogiwara, Kenichiro Kanazawa, Takashi Inohara, and Kaoru Wada. Influence of magnetic field on turbo-molecular pumps. 84, 2009.

[93] G. Drexlin, R. Gehring, R. Groessle, S. Horn, N. Kernert, S. Riegel, R. Neeb, A. Wagner, J. Wolf, and B. Bornschein. Investigation of turbo-molecular pumps in strong mangetic fiels. 86, 2011.

[94] Oerlikon Leybold Vacuum. Fundamentals of Vacuum Technology. 2007.

[95] MolFlow+ - A Monte-Carlo Simulator package developed at CERN, 2014. URL `http://test-molflow.web.cern.ch/`.

[96] COMSOL Multiphysics Reference Manual, November 2013. Version 4.4.

[97] Oerlikon Leybold Vacuum GmbH. Technical Data: TURBOVAC MAG W 2800. 2012.

[98] Moritz Hackenjos. *Aufbau und Inbetriebnahme der DPS Module (preliminary).* Ongoing master thesis, Karlsruhe Institute of Technology, Institute for Experimental Nuclear Physics.

[99] J. Wolf. Scientific collaborator, Institute for Experimental Nuclear Physics (IEKP), Karlsruhe Institute of Technology.

[100] Florian Joerg. *Simulation magnetischer Abschirmungen für Turbomolekularpumpen am KATRIN-Experiment.* Bachelor thesis, Karlsruhe Institute of Technology, Institute for Experimental Nuclear Physics, 2014.

[101] Norio Ogiwara, Toru Yanagibashi, Yusuke Hikichi, Masaaki Nishikawa, Junichiro Kamiya, and Kaoru Wada. Development of a turbo-molecular pump with a magnetic shield function. *Vacuum*, 98:18–21, 2013.

[102] Stahl Electronics. D-67582 Mettenheim, Hauptstrasse 15.

[103] Marta Ubieto Dîaz. *Off-line commissioning of a non-destructive FT-ICR detection system for monitoring the ion concentration in the KATRIN beamline.* Phd thesis, Ruperto-Carola University of Heidelberg, 2012.

[104] Hendrik Golzke. *Accuracy determination of the KATRIN FT-ICR mass spectrometers using ^{6}Li and ^{7}Li.* Diploma thesis, Karlsruhe Institute of Technology in corporation with Max-Planck-Institute for Nuclear Physics Heidelberg, 2012.

[105] Michael Heck. *Investigations of various excitation and detection schemes of stored ions in a Penning trap.* Phd thesis, Ruperto-Carola University of Heidelberg, 2013.

[106] Stefan Stahl. KATRIN-FT-ICR Introduction and User Guide. 2013.

[107] Stefan Stahl, P. Ascher, K. Blaum, B. Cacirli, M. Ubieto-Diaz, H. Golzke, M. Heck, S. Naimi, and D. Rodriguez. Commissioning of the KATRIN DPS-Penning Traps in Heidelberg, 2013. KATRIN Internal Talk.

[108] M. Heck, P. Ascher, R.B. Cakirli, H. Golzke, D. Rodîguez, S. Stahl, U. Ubieto-Díaz, and K. Blaum. An online FT-ICR Penning-trap mass spectrometer for the DPS2-F section of the KATRIN experiment. *Nuclear Instruments and Methods in Physics Research A*, 757:54–61, 2014.

[109] Alexander Windberger. *Berechnung und Simulation zum Verhalten von Ionen in der differenziellen Pumpstrecke des KATRIN-Experiments*. Diploma thesis, Karlsruhe Institute of Technology, Institute for Experimental Nuclear Physics, 2011.

[110] Andreas Kosmider. *Tritium Retention Techniques In The KATRIN Transport Section And Commissioning Of Its DPS2-F Cryostat*. Phd thesis, Karlsruhe Institute of Technology, 2012.

[111] Stefan Reimer. *Ein elektrostatisches Dipolsystem zur Eliminierung von Ionen in der DPS2-F des KATRIN Experimentes*. Diploma thesis, Karlsruhe Institute of Technology, Institute for Experimental Nuclear Physics, 2009.

[112] Rodolphe Combe. *Design Optimization of the KATRIN Transport Section and Investigations of Related Background Contribution (preliminary)*. Ongoing master thesis, Karlsruhe Institute of Technology, Institute for Experimental Nuclear Physics.

[113] ASG Superconductors S.p.A. URL `http://www.as-g.it/`. Genova - Italy C.so F. M. Perrone, 73r.

[114] VAT Vakuumventile AG. URL `http://www.vatvalve.com/home`. 9469 Haag, Seelistrasse, Switzerland.

[115] Udo Schmidt. *Entwicklung eines Monitordetektors fuer das KATRIN-Experiment*. Phd thesis, Karlsruhe Institute of Technology, 2008.

[116] Beatrix Ostrick. *Eine kondensierte $^{83\mathrm{m}}$Kr Kalibrationsquelle für das KATRIN-Experiment*. Pdh thesis, Westfälische Wilhelms-Universität Münster, 2008.

[117] ASG Superconductors. Inspection Report - CPS Beam Tube coil module assembly, 07 October 2014. Rev. 4.

[118] J. Bonn, B. Bornschein, R. Gehring, W. Gil, S. Grohmann, O. Kazachenko, M. Keilhauer, J. Kleinfeller, H. Krause, K. Mueller, S. Putselyk, C. Heinheimer, and C. Weiss. Technical Specification - Cryogenic Pumping Section (CPS). 2008.

[119] Michael Sturm. Bericht: Konzepte für das Heliumspülen zur Regeneration der CPS, 17 July 2013. KATRIN Internal Report.

[120] G. Gergelya, A. Konkola, M. Menyharda, B. Lesiakb, A. Jablonskib, D. Vargac, and J. Tothc. Determination of the inelastic mean free path (IMFP) of electrons in germanium and silicon by elastic peak electron spectroscopy (EPES) using an analyser of high resolution. *Vacuum*, 48:621–624, 1997.

[121] Martin Babutzka. *Untersuchung eines verfahrbaren Monitordetektors zur Überwachung der Aktivität des β-Zerfalls in der kryogenen Pumpstrecke des KATRIN-Experiments*. Diploma thesis, Karlsruhe Institute of Technology, Institute for Experimental Nuclear Physics, 2010.

[122] Bastian Beskers. *Messung und Optimierung der Eigenschaften des Monitordetektors fuer keV-Elektronen in der kryogenen Pumpstrecke bei KATRIN*. Diploma thesis, Karlsruhe Institute of Technology, Institute for Experimental Nuclear Physics, 2011.

[123] Theodore L. Bergman. *Introduction to heat transfer*. Wiley, Hoboken, NJ, 6th edition, 2011.

[124] Stephan Bauer. *Energy calibration and stability monitoring of the KATRIN experiment*. Pdh thesis, Westfälische Wilhelms-Universität Münster, 2013.

[125] Michael Sturm for the KATRIN Collaboration. DPS: New concept for the differential pumping section, 2012. XXIIIth KATRIN Collaboration Meeting.

[126] D. Hagedorn. Advisor for KATRIN from CERN, LHC-Division, CH-1211 Geneva 23.

[127] A. Hervé. Advisor for KATRIN from CERN, LHC-Division, CH-1211 Geneva 23.

[128] SEMIKRON. Rectifier diode SKN 240, SKR 240, 05.04.2004. Data sheet.

[129] W. Gil. Scientific collaborator, Institute for Nuclear Physics (IKP), Karlsruhe Institute of Technology.

[130] A. Hervé. Review of CPS Parameters, 27.01.2012. KATRIN Internal report.

[131] A. Hervé. Regrouping KATRIN protection Schemes, 15.03.2012. KATRIN Internal report.

[132] Theo Schneider. KATRIN - WGTS: Diodenmessungen am KIT, 17.08.2010. KATRIN Internal Report.

[133] G. Drexlin. Diode Protection System for DPS-2F, CPS and WGTS, 24.08.2011. Internal Report - Version 2.0.

[134] W. Gil, H. Bolz, A. Jansen, M. Steidl, and D. Hagedorn. Tests of By-Pass Diodes at Cryogenic Temperatures for the KATRIN Magnets. volume 1574, pages 274–280. AIP Conference Proceedings, 2014.

[135] V. Berland, D. Hagedorn, and F. Rodriguez-Mateos. Testing of High Current By-pass Diodes for the LHC Magnet Quench Protection. *IEEE Transactions on Magnetics*, 32(4), 1996.

[136] D. Brown, A. Della Corte, C. Fiamozzi Zignani, A. Gharib, D. Hagedorn, S. Turtu, and C. Rout. Cryogenic Testing of High Current By-pass Diode Stacks for the Protection of the Superconducting Magnets in the LHC. 2004. CERN LHC Project Report 686.

[137] Experimental Analysis and Modeling of the Electrical and Thermal Transients of the Diode-By-pass for the LHC-Magnet protection at Cryogenic Temperatures. 1998. CERN LHC Project Report 268.

[138] REGATRON AG. DC-Netzgerät TopCon Serie - Manual Modell TC.P Quadro, 2011. V04.51.

[139] ITK Engineering AG. URL http://www.itk-engineering.de/. Luipoldstrasse 59, D-76863 Herxheim.

[140] M. Schwarz. Dokumentation KATRIN Diodenprüfstand. Technical report, ITK Engineering AG, 27.11.2012. Version 1.2.0.

[141] Jack W. Ekin. *Experimental techniques for low temperature measurements : cryostat design, materials, and critical-current testing.* Oxford Univ. Press, 2007.

[142] ASG Superconductors GRUPPO MALACALZA. TDR Diodes reworking on CPS magnetic system, 2012. Internal Report.

[143] Pfeiffer Vacuum GmbH. HPT 200 Pirani/Bayard-Alpert Transmitter - Betriebsanleitung. 2014.

[144] R.E. Honig and H.O. Hook. *RCA Review 21*, 1960.

[145] Oleg Kazachenko. CPS Ar - Injection System, 30.01.2009. KATRIN Internal report.

[146] Frank Eichelhardt. *Measurement of the Tritium Pumping Properties of 4.2 K Argon Condensate for the Cryogenic Pumping Section of KATRIN.* Phd-thesis, 2009.

[147] O. Kazachenko, B. Bornschein, L. Bornschein, F. Eichelhardt, N. Kernert, and H. Neumann. TRAP-a cryo-pump for pumping tritium on pre-condensed argon. *Nuclear Instruments and Methods in Physics Research Section A: Accelerators, Spectrometers, Detectors and Associated Equipment*, 587(1):136 – 144, 2008.

[148] F. Eichelhardt, B. Bornschein, L. Bornschein, O. Kazachenko, N. Kernert, and M. Sturm. First Tritium Results of the KATRIN Test Experiment Trap. *Fusion Science and Technology*, 54(2):615–618, August 2008.

[149] O. G. Peterson, D. N. Batchelder, and R. O. Simmons. Measurements of X-Ray Lattice Constant, Thermal Expansivity, and Isothermal Compressibility of Argon Crystals. *Physical Review*, 150, Number 2, 1966.

[150] E. R. Dobbs, D. F. Figgins, G. O. Jones, D. C. Piercey, and D. P. Riley. Density and Expansivity of Solid Argon. *Nature*, No. 4531, 1956.

[151] Sergej A. Nepijko, Irene Rabin, and Wilfried Schulze. Morphology of Frozen Rare-Gas Layers. *ChemPhysChem - A European Journal of Chemical Physics and Physical Chemistry*, 6:235–238, 2005.

[152] H. Abe and W. Schulze. The Sorption Capacity of Solid Rare Gas Layers. *Chemical Physics*, 41:257–263, 1979.

[153] E.R. Dobbs and G.O. Jones. Theory and Properties of Solid Argon. *Reports on Progress in Physics*, 20, 1957.

[154] O. Knacke and I.N. Stranski. Die Theorie des Kristallwachstums. *Ergebnisse der Exakten Naturwissenschaften*, 26:383–427, 1952.

[155] A.L. Hunt, C.E. Taylor, and J.E. Omohundro. *Advances in Cryogenic Engineering*, 8, 1963.

[156] R.T. Brackmann and Wade L. Fite. Condensation of Atomic and Molecular Hydogen at Low Temperatures. *The Journal of Chemical Physics*, 34, Number 5:1572–1579, 1961.

[157] J. O. Hirschfelder, C. F. Curtiss, and R. B. Bird. *Molecular theory of gases and liquids.* New York, London, Sydney, J. Wiley and Sons, 1967.

[158] R.W.G. Wyckoff. *Crystal Structures.* Wiley, 1963.

[159] K. Becker, G. Klipping, W.D. Schoenherr, W. Schulze, and K. Toelle. Proceedings: Cryogenic Engineering Conference. 4, 1972.

[160] J. Wolf and M. Krause. Paper in progress: Investigations on modelling the conductance of bellows. 2014. Karlsruhe Institute of Technology, Institute for Experimental Nuclear Physics.

[161] C. Boffito, B. Ferrario, L. Rosai, and F. Doni. Gettering in cryogenic applications. *Journal of Vacuum Science and Technology A 5*, pages 3442–3445, 1987.

[162] SAES Getters Group, 2014. URL `http://www.saesgetters.com`.

[163] SAES Getters Group. ST707 - Non Evaporable Getters Activable at Low Temperatures. Booklet.

[164] Antonia Lange. *Analyse zur indirekten Aktivierung einer NEG-Pumpe in der CPS des KATRIN-Experimentes.* Bachelor Thesis, Karlsruhe Institute of Technology, Institute for Experimental Nuclear Physics, 2014.

[165] LEM Laboratorium für Elektronenmiskroskopie, Karlsruhe Institute of Technology, 2013.

[166] Ch. Day, X. Luo, A. Conte, A. Bonucci, and P. Manini. Determination of the sticking probability of a Zr-V-Fe nonevaporable getter strip. *Journal of Vacuum Science and Technology A*, 25:824, 2007.

[167] C. Benvenuti and P. Chiggiato. Pumping Characteristics of the St707 Non-Evaporable Getter (Zr 70-V 24.6-Fe 5.4 wt%). *Journal of Vacuum Science & Technology*, A 14:3278–3282, 1996.

[168] Uwe Kraemer. Simulation und Messung mit dem Prototyp einer elektrisch aktivierbaren NEG-Pumpe am KATRIN Testzylinder. Bachelor thesis, Karlsruhe Institute of Technology, Institute for Experimental Nuclear Physics, 2013.

[169] VAT Deutschland GmbH. VAT Vakuumventile 2016. Product catalog.

[170] Felix Bachmann. *Aufbau und Inbetriebnahme des CPS-Test Aufbaus*. Bachelor Thesis, Karlsruhe Institute of Technology, Institute for Experimental Nuclear Physics, 2012.

[171] Carsten Röttele. *Optimierung der Aktiverungstemperatur der CPS Getterpumpe im KATRIN Experiment*. Bachelor Thesis, Karlsruhe Institute of Technology, Institute for Experimental Nuclear Physics, 2013.

[172] Pfeiffer Vacuum. QMS 200 Quadrupol-Massenspektrometer PRISMA^{TM}. 1999. Manual.

[173] Leybold Vacuum. IE 414/IE514 IONIVAC Sensors. 2001/2002. Leybold Vacum Products and Reference Book.

[174] Oerlikon Leybold Vacuum GmbH. Technical Data TURBOVAC SL 300. As at 15.12.2011. URL `http://www.oerlikon.com/leyboldvacuum/de/`.

[175] Oerlikon Leybold Vacuum GmbH. Technical Data Scrollvac SC 15 D. As at 20.08.2013. URL `http://www.oerlikon.com/leyboldvacuum/de/`.

[176] Leybold Vacuum GmbH. Technical Data TURBOVAC TW 70 H. 2001.

[177] Oerlikon Leybold Vacuum GmbH. Technical Data TURBOVAC SL 80 H. 2014. URL `http://www.oerlikon.com/leyboldvacuum/de/`.

[178] MKS Instruments GmbH. MKS Type 690A Absolute and Type 698A Differential High Accuracy Pressure Transducers. 2009. URL `http://www.mksinst.com/`.

[179] Marcel Krause. *Simulation des Testaufbaus für eine Getter-Vakuumpumpe*. Bachelor Thesis, Karlsruhe Institute of Technology, Institute for Experimental Nuclear Physics, 2013.

[180] MKS Instruments GmbH. Baratron general purpose absolute capacitance manometer - Type 722B. As at 07.01.2015. URL `http://www.mksinst.com/`.

[181] MKS Instruments GmbH. Baratron temperature regulated capacitance manometer - Type 627B (45°C). As at 07.01.2015. URL `http://www.mksinst.com/`.

[182] Pfeiffer Vacuum GmbH. Pirani/Bayard-Alpert combination HPT 200 ($5 \cdot 10^{-10} - 1000\,$hPa). As at 07.01.2015. URL `http://www.pfeiffer-vacuum.de/`.

[183] C. Tegeler, R. Span, and W. Wagner. A New Equation of State for Argon Covering the Fluid Region for Temperatures from the Melting Line to $700\,$K at Pressures up to $1000\,$MPa. *J. Phys. Chem. Ref. Data*, 28(3):779–850, 1999.

Acknowledgement / Danksagung

An dieser Stelle möchte ich mich bei allen bedanken, die mich während der Promotionszeit und bei der Fertigstellung meiner Arbeit unterstützt haben. Ein besonderer Dank geht dabei an:

Prof. Dr. Guido Drexlin, der es mir ermöglicht hat meine Dissertation am KATRIN-Experiment zu verfassen. Vielen Dank für die Korrekturen und die wissenschaftliche Unterstützung.

Prof. Dr. Ulrich Husemann, der sich als Zweitgutachter die Zeit genommen hat meine Arbeit zu korrigieren und zu bewerten.

Dr. Joachim Wolf und **Dr. Markus Steidl** für die wissenschaftliche Unterstützung, für die Zeit bei Problemen, und natürlich auch für die Zeit, die sie sich genommen haben um meine Dissertation zu korrigieren.

Der Aufbau, die Optimierung, und die Inbetriebnahme der Testexperimente wäre ohne die Hilfe einiger Personen nicht möglich gewesen. Für die Unterstützung bei allen mechanischen, vakuumtechnischen und elektronischen Herausforderungen möchte ich mich deshalb bedanken bei: Norbert Kernert, Luisa LaCasio, Klaus Müller, Antonia Lange, der Werkstattgruppe von Herrn Horn, insbesondere bei Klaus Mehret und Monika Kaiser, Jürgen Grimm, Arne Felden und vor allem bei Steffen Jokisch. Ohne euch wäre vieles nicht möglich gewesen.

Auf der wissenschaftlichen Seite möchte ich mich außerdem noch bei Woosik Gil, Michael Sturm, Ferenc Glück und Lutz Bornschein bedanken, sowie bei Michaela Meloni, Karin Vogt und Steffen Lichter für die Bereitstellung vieler CAD Zeichnungen.

Neben den technischen Versuchen, waren es vor allem die vielen Arbeitskollegen und -Kolleginnen, die meine Arbeit am Institut immer spannend gestaltet haben. Deswegen möchte ich mich bei allen bedanken, die immer für ein positives Arbeitsklima gesorgt haben. Insbesondere sind dabei Philipp Reiher, Laura Kuckert, Daniel Hilk, Birgit Adams, Sebastian Ziegler, Stefan Görhardt, Stefan Groh und Marcel Krause zu erwähnen.

Bedanken möchte ich mich außerdem bei Rainer Gumbsheimer, der neben der technischen Koordination auch immer ein offenes Ohr für Probleme und Fragen hatte.

Ein großer Dank geht an Heike Bolz, nicht nur weil ich eine Menge von ihr im praktischen Umgang mit Elektronik gelernt habe, sondern viel mehr wegen ihrer offenen, ehrlichen und hilfsbereiten Art, die mir über weite Strecken meiner Arbeit sehr geholfen hat.